Journal of
Materials Chemistry A

Materials for energy and sustainability

Accepted Manuscript

Journal of
Materials Chemistry A

Materials for energy and sustainability

rsc.li/materials-a

ISSN 2050-7488

COMMUNICATION
Zhenhai Wen *et al*
An electrochemically neutralized energy-assisted low-cost acid-alkaline electrolyzer for energy-saving electrolysis hydrogen generation

Volume 6
Number 12
28 March 2018
Pages 4883-5230

ROYAL SOCIETY
OF CHEMISTRY

This is an Accepted Manuscript, which has been through the Royal Society of Chemistry peer review process and has been accepted for publication.

Accepted Manuscripts are published online shortly after acceptance, before technical editing, formatting and proof reading. Using this free service, authors can make their results available to the community, in citable form, before we publish the edited article. We will replace this Accepted Manuscript with the edited and formatted Advance Article as soon as it is available.

You can find more information about Accepted Manuscripts in the Information for Authors.

Please note that technical editing may introduce minor changes to the text and/or graphics, which may alter content. The journal's standard Terms & Conditions and the Ethical guidelines still apply. In no event shall the Royal Society of Chemistry be held responsible for any errors or omissions in this Accepted Manuscript or any consequences arising from the use of any information it contains.

ROYAL SOCIETY
OF CHEMISTRY

rsc.li/materials-a

Journal of Materials Chemistry A Accepted Manuscript

1
2 **Synergistic Impacts on Properties, Stability, and Applications of MXenes via Polymer Integration**

3
4 Sunil Kumar[#*1], Syed Muhammad Zain Mehdi[#1,2], Manish Taunk[3], Sanjeev Kumar[3], Amit Aherwar[4], Sudhanshu Singh[5], Tej Singh[6]

5 [1]*Department of Nanotechnology and Advanced Materials Engineering and HMC, Sejong University, Seoul-05006,*
6 *South Korea*
7 [2]School of Chemical, Biological and Battery Engineering, Gachon University, 1342 Seongnam-daero, Sujeong-gu,
8 Seongnam-si, Gyeonggi-do 13120, Republic of Korea
9 [3]*Department of Physics, Chandigarh University, Gharuan, Mohali-140413, India*
10 [43]*Department of Mechanical Engineering, School of Automobile, Mechanical & Mechatronics Engineering,*
11 *Manipal University, Jaipur 303007, India*
12 [5]*Department of Computer Science and Engineering, Parul University, Vadodara, Gujarat, 391760, India.*
13 [6]*Savaria Institute of Technology, Faculty of Informatics, ELTE Eötvös Loránd University, Szombathely 9700,*
14 *Hungary*
15 [*]*Corresponding author: skumar@sejong.ac.kr (Sunil Kumar)*
16 [#]*Equal 1st authors/ Equal contribution*

17 **Abstract**

18 MXenes are known for their exceptionally high electrical conductivity, mechanical resilience, and

19 versatile surface chemistry. However, these tend to oxidize under ambient conditions, posing a

20 major hurdle in their performance in various applications. Contrary to these, polymers are mostly

21 stable under ambient conditions, making these ideal materials to combine with MXenes to create

22 MXene-polymer nanocomposites with enhanced higher stability against oxidation and improving

23 MXenes functionality. This synergy can also enhance the mechanical strength, thermal stability,

24 surface properties, and other characteristics of MXenes improving the overall performance of

25 MXenes. This review focuses on the role of polymers in improving the properties of MXenes and

26 mitigating their oxidation under various conditions. Polymers serve as protective barriers and

27 improve interfacial interactions, maintaining various properties of MXenes for longer periods. The

28 review also highlights MXene-polymer nanocomposite fabrication techniques, like solution

29 blending, layer-by-layer assembly, in-situ polymerization, electrospinning, etc., for their effective

30 integration. The review also explores MXene-polymer nanocomposite applications in different

31 areas, including energy storage devices, electronics, sensors, filtration membranes, biomedical

32 applications, etc. Finally, the review also outlines various challenges and opportunities in

33 synthesizing MXene-polymer nanocomposites for diverse applications, emphasizing the potential

34 of MXene-polymer synergy to open new opportunities in future hybrid materials.

35 ***Keywords:*** MXene; Polymer nanocomposites; Oxidation stability; Synthesis strategies;

36 Synergistic effects; Applications.

1. Introduction

Nanocomposites have been identified as a promising way to meet the growing global demands in various sectors including energy. The combination of nanoparticles, nanofillers, and a polymer matrix material leads to improved properties like strength, conductivity, catalytic activity, etc. in these materials[1]. The potential of nanocomposites lies in their ability to revolutionize energy storage, conversion, and transportation technologies, which can offer more efficient and sustainable solutions for the future[2]. Polymers are the most popular for nanocomposite synthesis due to their versatility, easy processing, and ability to incorporate various nanofillers[3]. Different materials can be used as filler for the synthesis of polymers-based nanocomposites[4]. In this perspective, 2D MXenes are now recognized as a promising candidate[5]. MXenes originate from *MAX* phases, which are compounds of transition metals, by undergoing an etching process using HF or LiF/HCl acids[6]. Following the etching process, the *A* component is removed from the *MAX* phases, and the resulting MXenes are thoroughly washed with DI water. MXenes possess surface terminal groups such as -OH, -O, -Cl, or -F, and are commonly denoted as $M_{n+1}X_nT_x$, where M denotes a transition metal element, X typically denotes carbon/nitrogen/carbonitrides, and T_x represents surface functionalities as terminal groups[7].

MXenes have remarkable features such as high electrical conductivity[8, 9], hydrophilicity[10], electrochemical characteristics[11, 12], adjustable band gap[13, 14], and substantial surface area[15]. These characteristics make MXenes versatile materials having applications in fields such as energy storage[8, 11, 15, 16-18], fuel cells[19, 20], photodetectors[14, 21], sensors[22], conductive ink[23], 3D printing[24, 25, 26], smart windows[27], electromagnetic interference (EMI)[28, 29], etc. $Ti_3C_2T_x$ MXene stands out as the most widely recognized member of the MXene family. High electrical conductivity, tailored surface, thermal stability, mechanical strength, etc. make it the favorite member of the MXene family. In addition to $Ti_3C_2T_x$, the MXene family includes other potential members, such as Ti_2CT_x[30], V_2CT_x[18, 31, 32], Nb_2CT_x[33], etc. These MXenes, each having unique characteristics, offer a wide range of properties useful in diverse potential applications[34]. MXenes, including Ti_2C, V_2C, Nb_2C, Mo_2TiC_2, and $Mo_2Ti_2C_3$, showcase distinctive characteristics distinguishing them from the widely studied Ti_3C_2. For example, Ti_2C has thinner layers, offering a slightly larger bandgap and rapid ion transport, making it suitable for photothermal therapy[35], energy storage applications[36], electrocatalysts for water splitting[37], etc. V_2C demonstrates Superior redox properties due to the

1 variable oxidation states of vanadium, improving its performance in pseudo capacitors and

2 catalytic reactions[38]. Similarly, Nb_2C is known for its superior electrochemical durability in

3 aqueous and organic electrolytes, making it highly suitable for robust energy storage[39, 40], and

4 photocatalytic applications[41]. Additionally, Nb_2C MXene demonstrates good electrical

5 conductivity and improved wettability, attributed to its lower Fermi energy level relative to

6 Ti_3C_2[39]. In the case of dual-transition metal MXenes ($M_2'M''C_2$), structurally stable Mo_2TiC_2

7 combines the enhanced catalytic performance of Mo with the structural integrity of Ti, offering

8 improved HER/OER performance[42] and N_2 reduction reaction activity[43]. Similarly, $Mo_2Ti_2C_3$,

9 with its thicker multilayer structure, offers tunable conductivity and thermal stability, positioning

10 it as a promising material for thermal management and electronics. $Mo_2Ti_2C_3$ MXene manifests

11 elevated photothermal conversion efficiency due to its substantial optical absorption across a wide

12 spectral range, and layered structure, which facilitates efficient heat transfer and energy

13 dissipation[44]. Partially oxidized $Mo_2Ti_2C_3$ MXene has demonstrated significant potential for

14 energy storage applications due to its enhanced electrochemical properties and structural

15 stability[45].

16 MXenes boast various remarkable properties, however, these are vulnerable to oxidative

17 degradation when exposed to ambient conditions or during processing, which restricts their

18 practical application[46]. Therefore, enhancing oxidation stability is crucial for their broader

19 adoption in real-world uses. Various methods have been proposed to enhance the oxidation

20 stability of MXenes. These methods include storing MXenes at low temperatures in Ar

21 atmosphere[47], or in eutectic solvents[48], using sodium L-ascorbate[49], or integrating MXenes into

22 polymer blends[50, 51]. The use of polyanions for preservation has shown promising results in

23 minimizing the MXenes oxidation, as this process usually begins at the edges of the material[52].

24 MXenes treated with antioxidants have demonstrated better stability under ambient conditions,

25 allowing their use in energy storage applications for more than 80 days[53]. Among these

26 approaches, MXene-polymer hybrids or nanocomposites stand out most favorably as they provide

27 various functionalities to these hybrid materials. However, the techniques of passivation or

28 blending may lead to decreased electrical conductivity compared to pure MXenes.

29 Polymers are recognized for their outstanding capability to be processed and shaped. Incorporating

30 MXenes into polymers can enhance and customize their characteristics for particular uses. MXene-
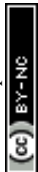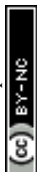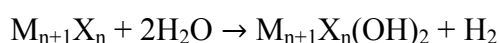
1 polymer nanocomposites can improve mechanical attributes, including flexibility, tensile strength,

2 and toughness[54, 55]. MXenes are prone to oxidation and deterioration in typical environmental

3 conditions[56] but polymers can form a protective barrier around the MXene flakes, which increases

4 their stability against oxidation[50, 51]. Additionally, the polymers mixed with MXenes provide

5 numerous possibilities for functionalization and alteration[57]. MXene-polymer nanocomposites

6 have found applications in flexible electronics[24, 58-60], self-healing sensors[61], 3D printing[62-64],

7 energy storage[50, 65], anti-corrosion[66, 67], fire retardants[68], water purification/treatment[69-71], solar

8 cells[72, 73], and antibacterial applications[74-76].

9 MXene-polymer nanocomposites can be prepared using methods, such as solution casting[68, 77],

10 solution blending[78], electrospinning[79, 80], in-situ polymerization[81, 82], thin film coatings or polymer

11 lamination[50] or fibers[83, 84], etc. Some of the popular polymers which are hybridized with MXene

12 include polyvinyl alcohol (PVA)[85], Polydimethylsiloxane (PDMS)[86], poly(3,4-

13 ethylenedioxythiophene) polystyrene sulfonate (PEDOT:PSS)[87, 88], polyaniline (PANI)[89],

14 polypyrrole (PPy)[90], etc. The polymers can serve as intercalants or spacers within MXene-polymer

15 nanocomposites[16, 91].

16 Some earlier reviews on MXene-polymer composites are available; however, these primarily focus

17 on synthesis and general applications[92, 93], or the role of MXenes as fillers[94], and a few are

18 outdated[95]. This article uniquely highlights the synergistic effects of MXene-polymer integration,

19 showcasing enhancements in mechanical strength, conductivity, and thermal stability. By

20 emphasizing these synergistic effects and the latest advancements, this review provides a

21 comprehensive and up-to-date perspective on their advanced applications, filling the gaps left by

22 previous studies.

23 **2. MXenes synthesis**

24 The synthesis of 2D MXenes was first achieved in 2011 by etching Ti_3AlC_2 using a highly

25 concentrated acid. This top-down approach involves removing the "A" layer from the MAX

26 phases. A strong acid like HF effectively breaks the M-A metallic bond leading to the formation

27 of layered MXene structures. The reaction mechanism of selective etching using HF is as

28 follows[96]:

29 $$M_{n+1}AX_n + 3HF \rightarrow M_{n+1}X_n + AlF_3 + 1.5H_2$$

30 $$M_{n+1}X_n + 2H_2O \rightarrow M_{n+1}X_n(OH)_2 + H_2$$

1 $$M_{n+1}X_n + 2HF \rightarrow M_{n+1}X_n F_2 + H_2$$

2 During the HF etching process, Al (A layer) removal causes surface terminations, leading to the

3 functionalization of the M layer. The chemical etching in an acidic medium inevitably results in

4 defect sites in synthesized MXene flakes. These defect sites play a key role in the oxidation of

5 MXenes and reduce their self-life to a few days in an ambient environment, limiting their extensive

6 use. Later many synthesis routes were developed but selective etching methods using fluoride-

7 containing agents in an acidic medium were widely used[97]. The reaction time, temperature, and

8 acid concentration affect the quality and quantity of resultant MXenes.

9 Despite the successful synthesis of MXenes using concentrated HF etching, environmental

10 concerns and the need for a safer, simpler method have prompted the use of mild etching agents

11 like HCl with various fluoride salts for large-scale production. The HCl and fluoride salts mixture

12 forms in-situ HF for etching the "A" layer in the MAX phases (Figure 1a). The MXenes

13 synthesized using HCl have high yields, fewer defects, and resulted in higher electrical

14 conductivity. However, the MAX phase's purity is also a crucial factor in deciding the resultant

15 properties of MXenes[98]. Natu et.al reported a water-free synthesis method using polar solvents

16 along with ammonium dihydrogen fluoride[99]. The etching process in this method is reported to be

17 very slow but surprisingly the resultant MXene has only the -F group as the termination species.

18 One of the major issues associated with MXene synthesis is the use of hazardous chemicals, such

19 as HF or in situ-produced HF from fluoride salts and strong acids, which pose significant

20 ecological and health hazards. These chemicals can lead to hazardous waste, requiring meticulous

21 management and disposal processes. To address these issues, researchers have been exploring

22 environmentally friendly or less harmful methods for MXene synthesis. Recently, fluoride-free

23 synthesis methods including the electrochemical method[100], molten salts assisted etching[101], the

24 alkali etching method[102], chemical vapor deposition (CVD) synthesis approach[103], etc., have been

25 developed to minimize hazardous byproducts. These methods not only mitigate safety and

26 environmental concerns but also allow the alteration of the MXene structure and surface chemistry,

27 making them promising approaches for scalable and eco-friendly MXene production.

1
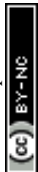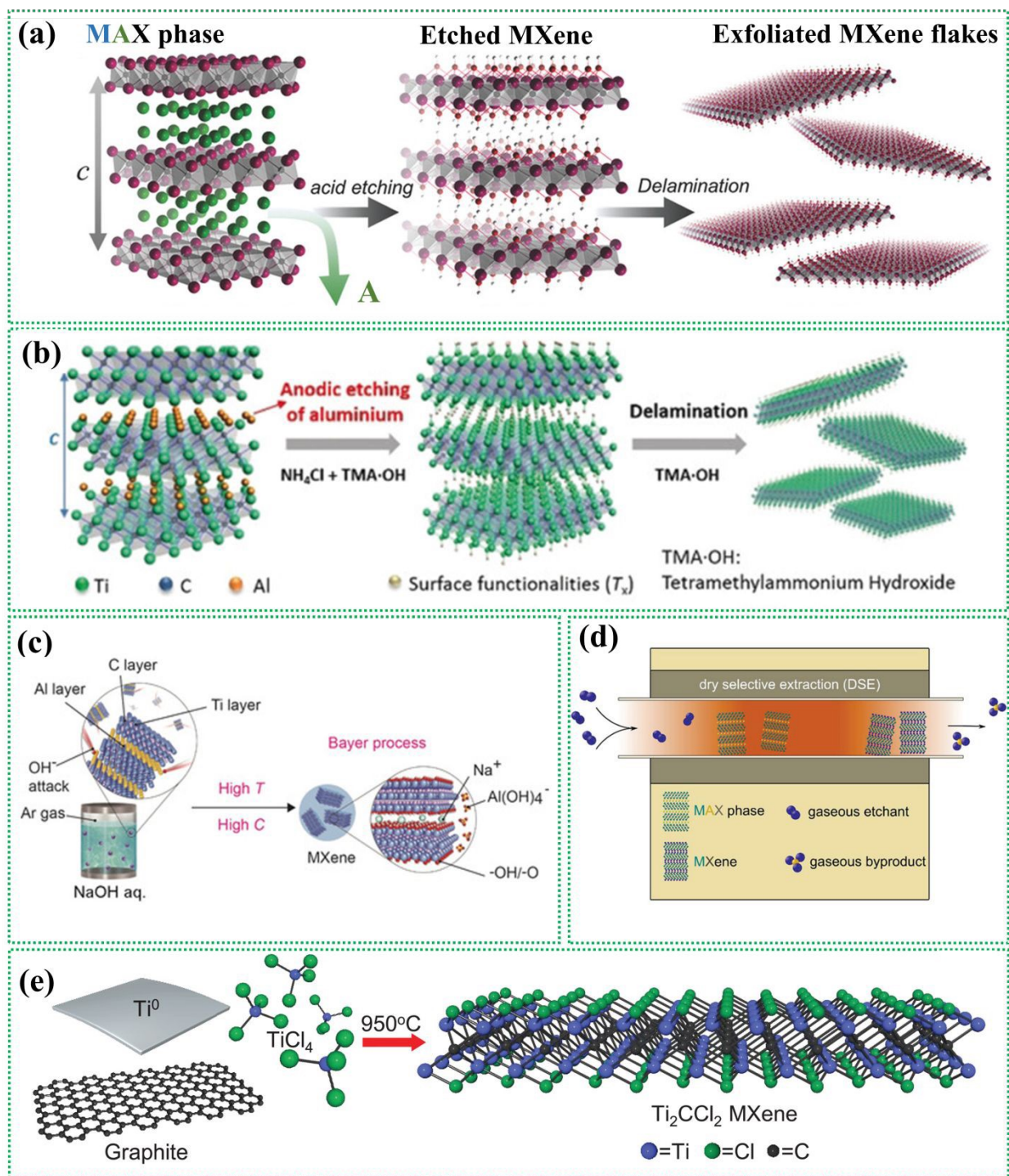
Figure 1. MXene synthesis strategies. (a) MXene etching by fluorine-based etchants. Reproduced with permission from ref.[104]. Copyrights 2016, Wiley. (b) Electrochemical etching method. Reproduced with permission from[100]. Copyrights 2018, Wiley. (c) Alkali-assisted etching method. Reproduced with permission from ref.[102]. Copyrights 2018, Wiley. (d) Dry selection extraction approach. Reproduced with permission from[105]. (e) CVD method-based MXene synthesis using Ti, graphite, and TiCl$_4$. Reproduced with permission from ref.[103]. Copyrights 2023, The American Association for the Advancement of Science.

1   The electrochemical etching method selectively removes the "A" layer from the MAX phase using

2   non-acidic electrolytes, making it safer and more environmentally friendly than traditional acid-

3   based methods. In a two-electrode system (Figure 1b), the bulk MAX phase (like Ti_3AlC_2) serves

4   as both the anode and counter electrode, with an electrolyte including ammonium chloride and

5   tetramethylammonium hydroxide (TMAOH, pH > 9). The anode undergoes etching at room

6   temperature, under a constant potential while the electrolyte is stirred. After a few hours, the

7   electrolyte becomes grey-white with a gelatinous precipitate, and black powders (stacked $Ti_3C_2T_x$)

8   settle at the bottom.

9   The alkali etching method employs alkali solutions (like NaOH or KOH) to selectively remove the

10   "A" layer from the MAX phase, resulting in the synthesis of layered MXenes (Figure 1c). In this

11   method, an alkaline solution is dissolved in argon-purged deionized water before adding the MAX

12   phase powder. The mixture is transferred to an autoclave, sealed, and subjected to heating under

13   an argon atmosphere for 12 hours. After the hydrothermal process, the resulting suspension is

14   filtered, thoroughly rinsed, and dried under vacuum, producing MXene with minimal impurities

15   and a high degree of purity. This method is considered safer and more straightforward than

16   fluorine-based acidic etching but may yield lower amounts of MXene or require extended reaction

17   times depending on the alkali concentration and reaction conditions.

18   These methods lead to MXene formation but exhibit low yield and are more time-consuming than

19   fluoride-based synthesis approaches. Recently, a new approach called dry selective extraction has

20   been proposed theoretically[105]. In this method, a glass ampoule filled with a known quantity of

21   MAX phase is placed in a tube furnace at an elevated temperature (Figure 1d). Iodine vapors are

22   then passed through the ampoule containing the MAX phase at 350°C, acting as an etchant to

23   remove the A layer and leaving behind MXenes. It was reported that the reaction does not occur

24   below 350°C and temperatures above 400°C result in over-etching.

25   The bottom-up synthesis methods allow precise control over material chemistry thus enabling

26   tailored customization of material design. The bottom-up approaches include CVD method[103]

27   (Figure 1e) and direct solid-state synthesis. In a recent article, Wang et al. reported Ti-based and

28   Zr-based MXenes by combining Ti metal and graphite powder with the desired quantity of

29   $TiCl_4$[103]. The sealed ampoules containing this mixture were placed in a furnace at 950°C for 2 h to

30   obtain MXenes. The process involved methane or N_2 gas reacting with $TiCl_4$ on the titanium

1 surface, resulting in Cl-terminated Ti_2CCl_2 or Ti_2NCl_2 MXenes. The proposed method is shown to

2 have the potential for bulk production.

3 Besides these, the salt-template MXene synthesis was reported by Xiao et al. to synthesize

4 molybdenum nitride[106]. In this method, a 2D template of MoO_3 is prepared and coated with NaCl

5 by annealing in an Ar atmosphere. The NaCl-coated 2D MoO_3 mixture was heated to 650 ℃ in

6 NH_3 atmosphere to yield MoN MXene. Ding et al. introduced a chemical scissor–mediated method

7 for precise structural editing of layered transition metal carbides to synthesize MXene[107]. This

8 method uses chemical scissors to open non-van der Waals gaps in MAX phases, followed by

9 atomic replacement via diffusion of metal ion intercalants into interlayer vacancies. The scissors

10 are also used for termination removal.

11 ### 3. MXenes structure and surface chemistry

12 MXenes exhibit a surface-rich chemistry which provides it unique properties and potential

13 applications[108]. In MXene synthesis, when the "A" layer is selectively etched from the precursor

14 MAX phase the interlayer spaces are generated between the MXene layers, where solvent

15 molecules or functional groups are developed (Figure 2a). These surface terminations on

16 the MXene surface play an important role in defining the properties of MXenes[109]. The nature of

17 the surface terminations can be altered during the synthesis of MXenes to tailor the surface

18 chemistry of MXenes[110]. The layered structure of MXenes, combined with their tunable surface

19 chemistry and properties, allows various applications in electronics, energy storage, catalysis,

20 sensing, medicines, and more[111, 112].

21 MXenes typically possess surface terminations, such as -OH, -O, -Cl, or -F, resulting from the

22 etching process used to synthesize them. During acidic etching, mainly containing fluoride ions,

23 MXenes typically exhibit –F and –O/–OH groups (Figure 2b). F terminations can be modulated

24 by adjusting acid concentrations, while their complete replacement with –O/–OH groups can be

25 achieved through alkaline treatments using KOH, NaOH, or TBAOH [113] [114]. The molten salt

26 etching (like $ZnCl_2$) facilitates Lewis acid-base reactions between cations and the A layer,

27 substituting it with Zn and then followed by –Cl terminations[115]. Variation in the composition of

28 molten salts during MAX phase etching facilitates the incorporation of halogen terminations, such

29 as –Cl, –Br, and –I. In addition to these, a wide range of terminations, such as –S, –Se, –Te, –P,

30 and –Sb, can be uniformly introduced onto MXene surfaces, enabling tailored surface

31 functionalities for diverse applications (Fig. 2b). Heating MXenes under reactive gases further

1   allows the formation of uniform –O and –C terminations. The molten salt method also produces –

2   Cl or –Br terminated MXenes like $Ti_3C_2Cl_2$, Nb_2CBr_2 etc., which can act as templates for post-

3   synthesis modifications, yielding MXenes terminated with –S, –Se, –Te, –NH, –O, or bare/–H

4   groups (Figure 2b).

5
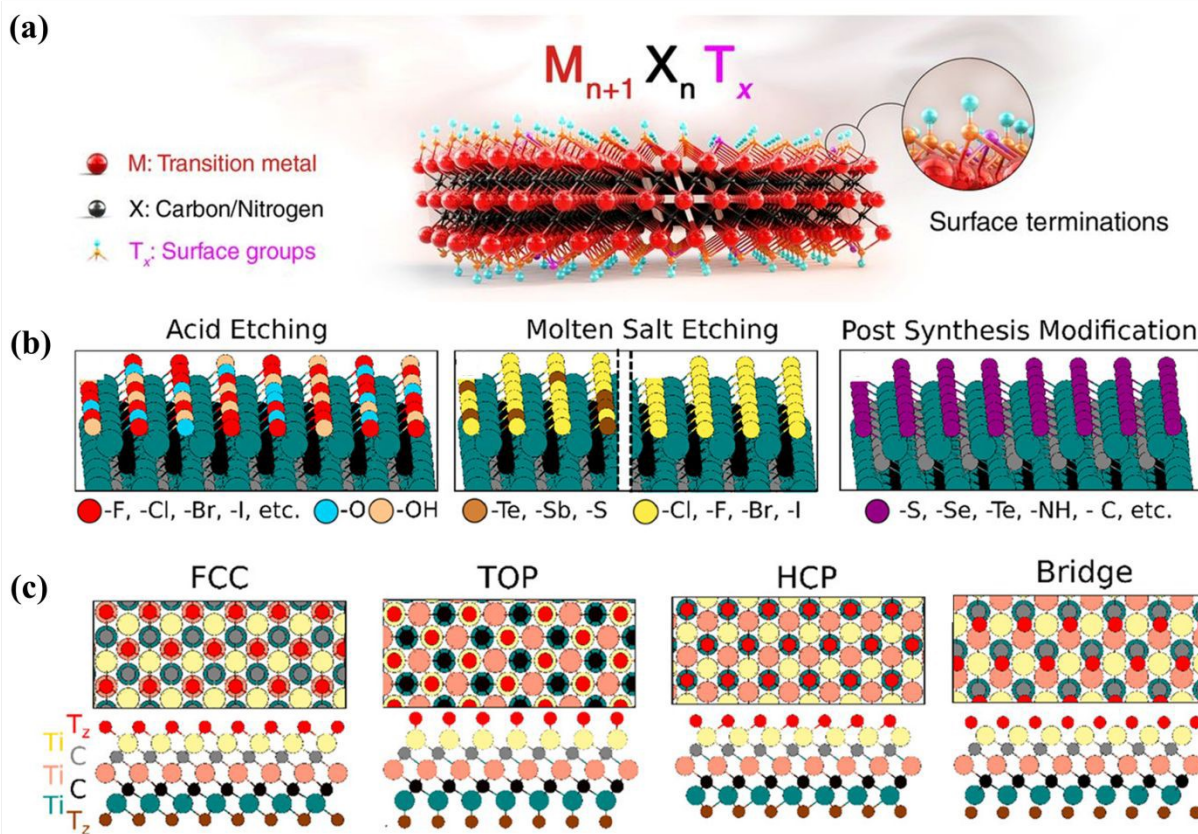
6   **Figure 2.** MXenes surface terminations. (a) A schematic representation of the MXene structures,
7   indicating the surface terminations of the outer metal layers. Reproduced with permission from
8   Ref.[111]. Copyrights 2021, The American Association for the Advancement of Science. (b) MXene
9   termination scenarios: (i) Halogen and −O/–OH terminations from the acidic etching of MAX
10   phases, (ii) Surface terminations from molten salts, (iii) Surface terminations via molten salts via
11   altered treatment, (iv) Post-synthesis modification introduce uniform terminations. (c) Surface
12   terminations: (i) FCC sites, (ii) "Top" positions on surface Ti, (iii) HCP sites, and (iv) Bridge sites
13   between Ti atoms. Reproduced with permission from Ref.[116]. Copyrights 2023, American
14   Chemical Society.

15   Theoretical investigations show that MXene surface terminations occupy distinct crystallographic

16   sites[117]. For $Ti_3C_2T_x$ MXene, terminations above middle Ti atoms align with FCC sites, while those

17   above surface Ti atoms adopt a "top" configuration, and those above C atoms occupy "HCP" sites.

18   Terminations between Ti atoms form a "bridge" configuration (Figure 2c). FCC sites are

19   energetically most favorable among these, with most terminations preferring these positions.

1 These terminations play a significant role in determining the surface chemistry, stability, and

2 interactions of MXene with other materials[118]. The surface terminations of MXenes offer

3 opportunities for functionalization[119]. The presence of water-loving polar surface terminations,

4 particularly -OH groups, leads to a strong affinity for water molecules and promotes wetting of the

5 MXene surface[119]. This hydrophilicity can be advantageous for applications such as water

6 treatment and filtration[120]. The surface chemistry of MXenes influences their solubility and

7 interactions with solvents. MXenes are generally not soluble in common organic solvents but are

8 dispersible in water-based solutions due to their hydrophilic nature[121]. This solubility behavior

9 enables their use in solution processing techniques and the fabrication of MXene-based films,

10 coatings, and composites.

11 **3.1 MXenes oxidation and its factors**

12 MXenes oxidize when exposed to ambient conditions or elevated temperatures, transforming into

13 their corresponding oxides. For example, $Ti_3C_2T_x$ MXene evolves into a $Ti_3C_2T_x/TiO_2$ and

14 eventually forms carbon-supported TiO_2 nanoparticles[122, 123]. It has been reported earlier that the

15 MXene oxidation starts at the edges of MXene flakes and advances toward the interior basal

16 planes[124, 125].

17 The oxidation can be observed through color changes; fresh $Ti_3C_2T_x$ MXene dispersed in water

18 has a dark green, which is converted to a translucent, cloudy hue as oxidation progresses with time

19 (Figure 3a). The MXenes oxidation is relatively faster in aqueous suspensions than in organic

20 dispersions[108, 126]. MXene hydrolysis is crucial in transforming MXenes into respective oxides in

21 aqueous suspensions, a process that can be inhibited in organic solvents. For instance, no oxidation

22 was observed in iso-propanol solutions of MXenes stored under an O_2 atmosphere for a same

23 duration[126] (Figure 3b). TEM analysis of freshly prepared MXenes shows clean surfaces and edges

24 (Figure 3c), with high-resolution TEM images revealing single-crystalline nanosheets (Figure

25 3f)[47]. The SAED pattern confirms a hexagonal atomic structure (Inset: Figure 3f). After one week

26 of exposure to air at room temperature, MXene edges display "branch-like" features, and

27 crystalline nanoparticles form on the basal planes of the flakes (Figure 3d, g), identified as anatase

28 in the fast Fourier transform (FFT). After 30 days, MXenes completely decompose into anatase

29 clumps and disordered carbon (Figure 3e, h). The presence of dissolved oxygen and water leads to

30 a reaction with the active edges of the flakes, resulting in TiO_2 formation. MXene oxidation is
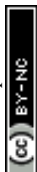
1   influenced by various factors. For example, the chemical etching process used to synthesize

2   MXenes in strong acids creates surface defects in MXene flakes[127, 128]. Under ambient conditions

3   or in aqueous suspension, these defect-rich sites ease oxidative degradation, which in turn impact

4   the properties of MXenes[129]. Environmental factors, such as exposure to air or immersion in water,

5   further contribute to MXene degradation. The stability and reactivity of MXenes are significantly

6   influenced by factors like the pH of the dispersion[130, 131], storage temperature[131], MXene

7   concentration[132, 133], flake size, etc[125, 132].

8
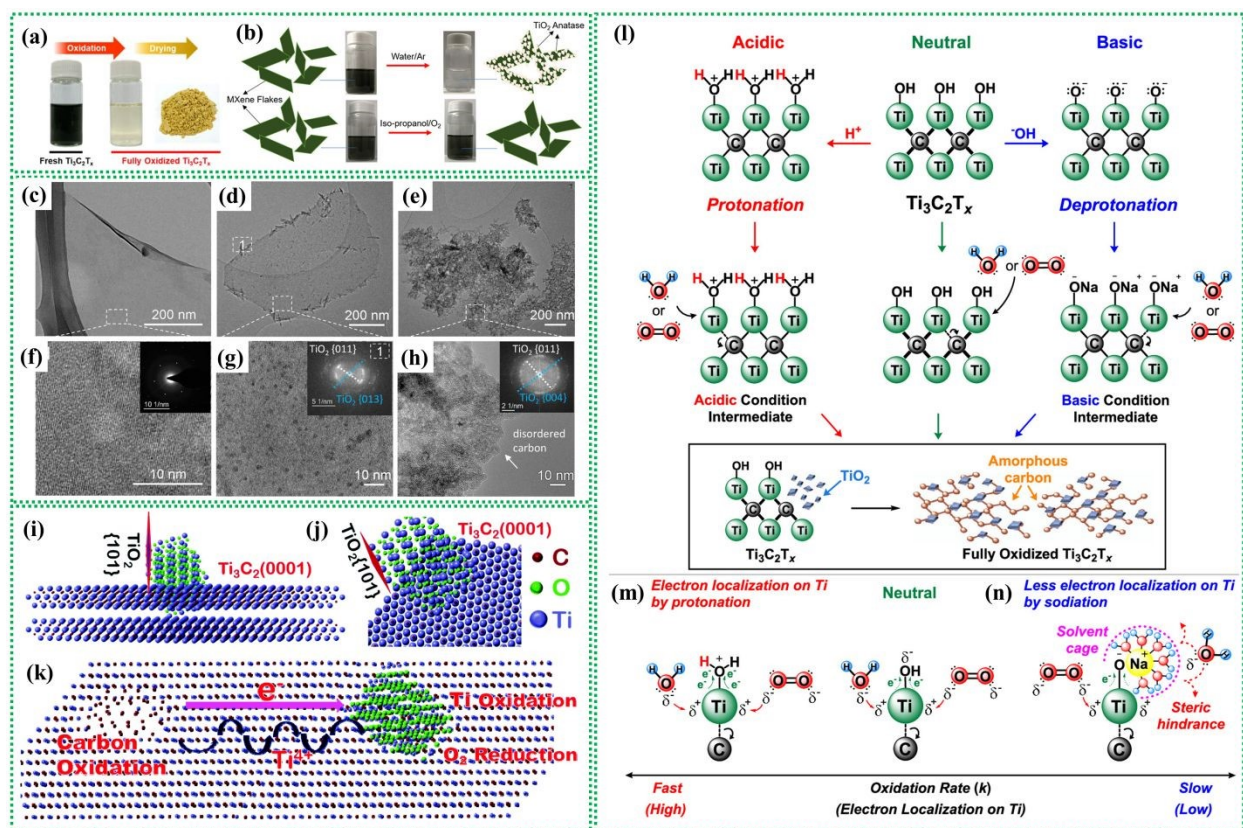
Figure 3. (a) Digital images of $Ti_3C_2T_x$ suspensions before and after oxidation. Reproduced with
permission from ref.[123]. Copyrights 2021, American Chemical Society. (b) MXene dispersion
impact in water and isopropanol. Reproduced with permission from ref.[134]. Copyrights 2019,
American Chemical Society. TEM images of (c) MXene flakes of fresh $Ti_3C_2T_x$ solution and
solutions stored at room temperature in the air after (d) 7 days and (e) 30 days. (f-h) HRTEM
images corresponding to panels c-e, respectively. In Figure f, the inset shows the corresponding
SAED pattern, while Figures g and h display the respective FFT patterns. Reproduced with
permission. Reproduced with permission from ref.[47]. Copyright 2017, American Chemical
Society. Defects in MXenes: (i)-(j) Depiction of TiO_2 cluster bonding with Ti_3C_2, highlighting the
TiO_2-(101) plane-oriented perpendicular to the MXene basal plane (0001). (k) Schematic
illustrating Ti_3C_2 oxidation, showing carbon oxidation at the positive side and Ti-ion oxidation at
the negative side of the internal electric field. Rapid electron transport to the convex area and slow
Ti-ion diffusion create the internal electric field. Reproduced with permission from ref.[127].

1 Copyright 2022, The Royal Society of Chemistry. Effect of pH on MXenes oxidation: (l) Proposed

2 mechanism for the oxidation reaction in $Ti_3C_2T_x$ mixtures under (m) Acidic and (n) Basic

3 conditions. Reproduced with permission.[123] Copyright 2021, American Chemical Society.

4 During sonication-assisted delamination, maintaining a constant temperature and using Ar can

5 prevent oxidation. Storing solutions in Ar-sealed vials or refrigeration reduces oxidation. Using

6 mild etchants like tetraethylammonium hydroxide (TMAOH) avoids fluorine by-products,

7 enhancing the stability of MXenes[135]. MXenes should be protected from UV exposure as

8 prolonged exposure leads to faster oxidation[136]. Synthesis methods determine surface terminations,

9 with HF-etching resulting in more -F terminations compared to those synthesized with LiF-HCl[137].

10 Etching MAX phases with alkali and molten salts prevents MXenes oxidation and hydrolysis[101,

11 [138]. HF etching introduces defects, accelerating degradation to TiO_2. Relatively mild acids like

12 HCl/LiF and fluorine-free etchants like TMAOH, NaOH, or KOH reduce the MXene defects.

13 Defects in MXenes also facilitate oxidation. Defects in MXenes, created during etching, drive

14 oxidation and affect reactivity, structural changes, conductivity, and functional group formation[128,

15 [139]. Adjusting etchants concentration can control defects which can also boost the resistance

16 against oxidation as well as the performance in desired applications. In Ti_3C_2 MXene, Ti atoms

17 form TiO_2 nanoparticles while the remaining carbon atoms cluster to produce amorphous carbon,

18 resulting in $C@TiO_2$ heterojunctions[127]. During oxidation at room temperature, the anatase TiO_2

19 (101) plane is oriented perpendicular to the Ti_3C_2 basal plane (Figure 3i, j). The rotation of the

20 TiO_2-(101) lattice plane during nucleation depletes Ti^{3+} in adjacent Ti_3C_2 crystals, creating Ti

21 vacancies and excess carbon atoms. Ti vacancies are commonly found in the surface layer of

22 MXenes prepared via exfoliation methods. Ti-vacancies in Ti_3C_2 MXenes create an internal

23 electric field that drives electron flow, carbon cluster nucleation, and Ti-cation diffusion. This field

24 enhances carbon oxidation, forming TiO_2 nanoparticles and amorphous carbon. Ti-vacancies also

25 facilitate O_2 entry into the lattice, promoting TiO_2 nucleation and growth. Wrinkles and atomic

26 steps act as nucleation sites for oxidation, with Ti-vacancies promoting carbon oxidation and TiO_2

27 formation (Figure 3k).

28 Temperature and pH significantly influence MXene oxidation by affecting its reaction kinetics and

29 pathways[52, 87]. Higher pH slows oxidation at 20 °C, while increased temperature accelerates it.

30 The oxidation mechanism of aqueous $Ti_3C_2T_x$ MXene dispersions starts at -OH group sites, with

31 pH significantly impacting reaction intermediates (Figure 3l). Acidic conditions protonate surface

32 hydroxyls, enhancing Ti atom electrophilicity and promoting nucleophilic addition reactions with

1   H$_2$O or O$_2$. In basic conditions, excess OH- deprotonates hydroxyls, form sodiated intermediates

2   and bulky solvent cages that hinder oxidation due to steric effects and reduced electrophilicity

3   (Figure 3m-n).

4   **4. MXene-polymer hybrids for oxidation prevention**

5   MXene-polymer nanocomposites are increasingly recognized for their ability to prevent MXene

6   oxidation, as polymers serve as protective layers that shield MXenes from environmental

7   degradation. The polymers can preserve MXenes for more than 180 days[140]. These

8   nanocomposites can preserve MXenes not only at room temperature but also under higher

9   temperatures and moist conditions[141]. This integration not only enhances the stability of MXenes

10   but also improves their overall performance in various applications. Table 1 summarizes some

11   MXene-polymer combinations investigated to enhance MXene stability over different periods.

12   **Table 1.** MXene-polymer nanocomposites for MXene stability improvement

S. No.	MXene-polymer composition	MXene etchant	Preventive measure	Stability duration	Ref.
1	MXene/poly(tannic acid)	LiF/HCl	Oxygen-rich macromolecule	60 days	142
2	MXene/melamine	LiF/HCl	Nanocomposite	60 days	143
3	MXene/PVA-CA hydrogel	LiF/HCl	Nanocomposite	30 days	144
4	MXene/polymer	-	Nanocomposite	42 days	145
5	MXene/polyacrylamide	-	Nanocomposite	15 days	146
6	MXene/aramid nanofiber (ANF)	LiF/HCl	Nanocomposite	-	147
7	MXene/polystyrene	LiF/HCl	Nanocomposite	180 days	140
8	MXene/dopamine	LiF/HCl	Nanocomposite	13 hours at 170 °C	148
9	MXene/Bentonite	LiF/HCl	Nanocomposite	2 hours at 600 °C	149
10	MXene/Sodium alginate	LiF/HCl	Nanocomposite	30 days	150
11	MXene/PVA	LiF/HCl	Nanocomposite	50 days	151
12	MXene/PET	LiF/HCl	Nanocomposite	200 hours at 70 °C	141
13	MXene/polymer	LiF/HCl	Nanocomposite	180 days	152

13   **4.1 Polystyrene/MXene for oxidation improvement**

14   To address the issue of MXene oxidation, a *'particle manufacturing technique'* (Figure 4a) was

15   employed to develop polystyrene/MXene (PS/MXene) composites with a 3D conductive network

16   structure[140]. The material conductivity reached 3846.15 S/m when the filler content was merely

1   1.81 vol%. Due to the compact and ordered structure of fabricated PS/MXene composite, it holds

2   53.4% of its initial conductivity after 180 days.

3
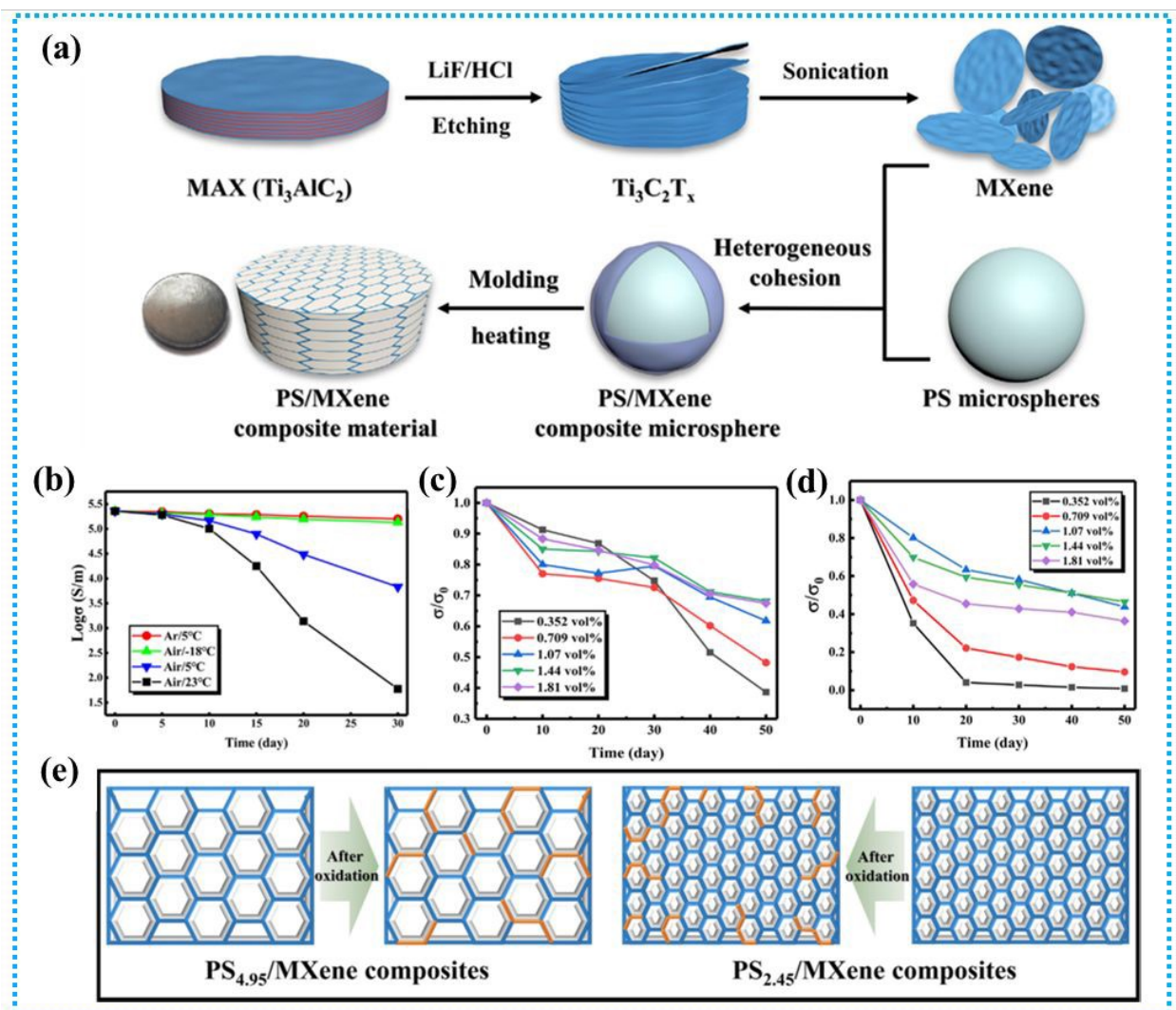
Figure 4. (a) Schematic showing the exfoliation of $Ti_3C_2T_x$ MXene and fabrication of composites
with a three-dimensional conductive network framework, (b) Storage environment effects on
MXene's intrinsic conductivity. (c-d) Impact of environmental factors on conductivity during the
composite material is being prepared, and (e) Schematic of the oxidation mechanism in MXene-
polymer composite. Reproduced with permission from ref.[140]. Copyright 2021, Elsevier Ltd.

9   The fundamental procedure for exfoliating $Ti_3C_2T_x$ MXene and creating PS/MXene composites

10   with a 3D ordered structure through "particle construction". [153]. Firstly, this work used the

11   conventional technique of manufacturing MXene because of its benefits, which include large

12   lamellae, fewer flaws, and good electrical conductivity when created by LiF/HCl etching [154]. The

13   electrical conductivity of freshly prepared MXene sheets was initially measured at 2.28×10^5 S/m,

14   as shown in Figure 4b. This conductivity remained stable over 30 days in an argon atmosphere or
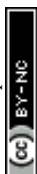
1 at low temperatures. However, in the air at room temperature, MXene's conductivity dropped

2 drastically, retaining only 0.026% of its initial value, highlighting its rapid oxidation and reduced

3 practicality. The interaction between conductivity and storage time for PS/MXene composites is

4 illustrated in Figure 4c-d. Key findings include: (1) Composites with higher MXene content

5 maintain conductivity better over time compared to those with lower MXene content, showing

6 slower degradation. (2) Larger particle composites exhibit greater conductivity loss than those with

7 smaller particles, regardless of MXene concentration. Additionally, smaller PS microspheres

8 create a denser conductive network, providing superior protection for MXene, as depicted in

9 Figure 4e. At larger microspheres, the conductive network is not well established while smaller

10 microspheres can form a much denser network, that certainly offers superior MXene protection.

11 **4.2 Polymer passivation**

12 Polymer passivation is a technique used to improve the oxidation stability of MXenes, particularly

13 against oxidation. By applying a polymer coating, such as polydopamine, the surface of MXenes

14 is protected from environmental factors that can lead to degradation. This passivation method

15 effectively reduces the oxidation rate and maintains the electrical properties of MXenes over

16 time[152]. Under ambient conditions, pristine MXene begins to oxidize at room temperature. FE-

17 SEM images of untreated MXene after 30 days (Figure 5a) reveal powdery particles around the

18 edges, indicating early oxidation. This process starts at edges and imperfections, progressing

19 inward as shown in Figure 5b, where oxidized TiO_2 (orange) replaces the MXene flakes (greenish).

20 Prior reports have indicated that the smaller the MXene flake, the higher the oxidation rate

21 [155]. Even in its dry state, MXene will eventually oxidize, nevertheless, the rate of oxidation is

22 slower under ambient circumstances than in humid environments or DI water[151]. To prevent

23 oxidation, a MXene film was coated with a 1% polymer solution in acetone. The polymer layer

24 thickness was ~50 nm. Sheet resistance (R) was measured over 180 days to evaluate oxidation

25 stability, with percentage changes (Figure 5c). The results showed obvious proof that polymer

26 passivation preserves MXene from oxidization. Even 180 days later, the relative resistance change,

27 $(R-R_0/R_0)$%, is ~20% in polymer-passivated MXene as compared to 800% in pristine MXene. The

28 UV–Vis spectra of pristine MXene film after 30 days show the same transmittance as on day 1,

29 however, the transmittance rises to ~89% after 180 days (Figure 5d). The high transmittance may

30 be associated with TiO_2 formation due to the oxidized $Ti_3C_2T_x$ MXene[151]. Contrary to this, a

31 negligible change in transmittance was noticed in the passivated MXene film 180 days (Figure
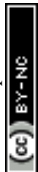
1   5e), indicating that almost no TiO_2 is formed and MXene oxidation is suppressed due to polymer

2   passivation.

3   In another study, a polymer laminated MXene (PL-MXene) electrode was fabricated to analyze

4   the impact of polymer lamination on electronic applications[141]. MXene flakes dispersed in water

5   were spin-coated on a glass substrate silanized with a self-assembled monolayer of (3-

6   aminopropyl)triethoxysilane (APTES).
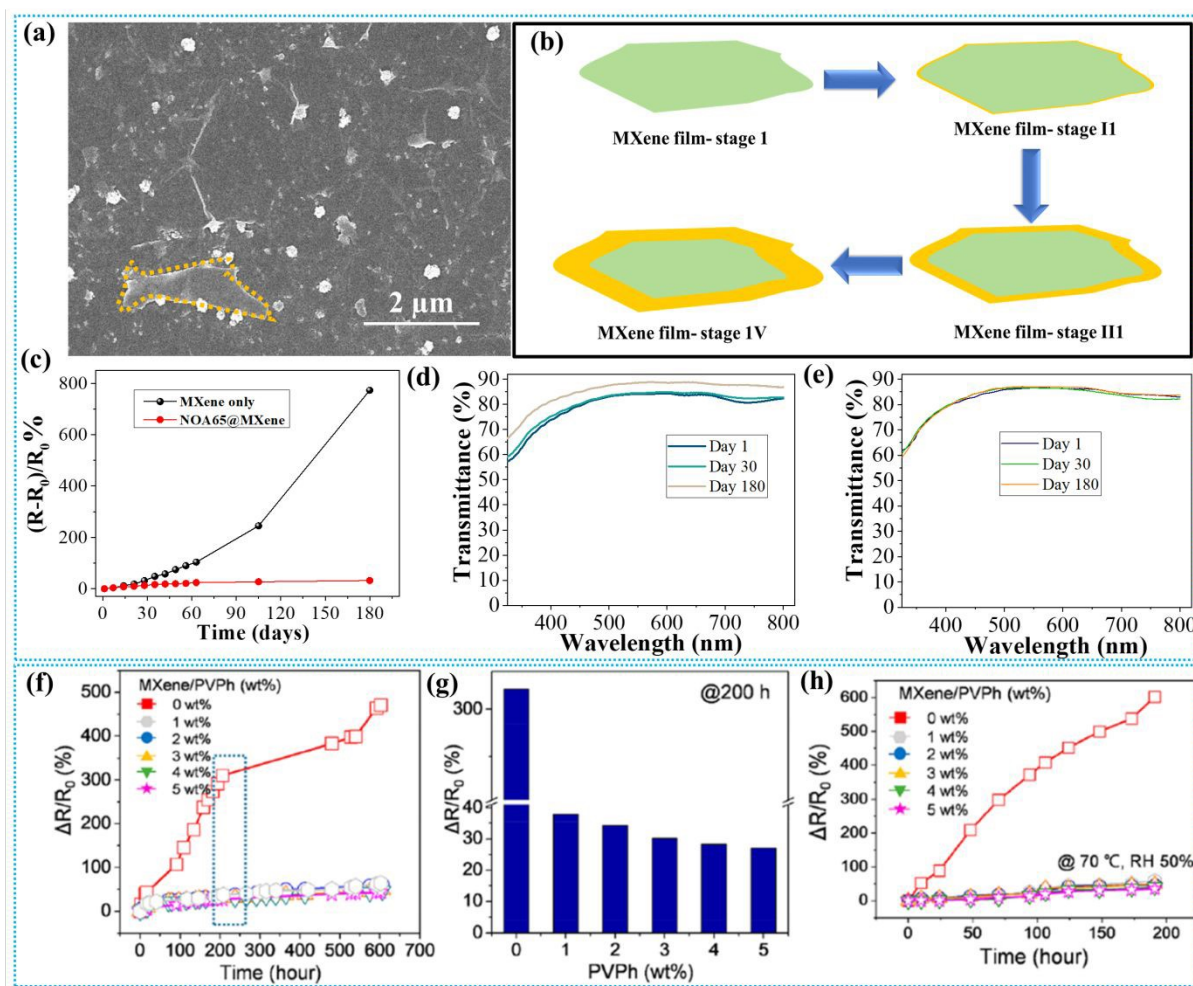
7

8   **Figure 5.** MXene passivation by polymers. (a) FE-SEM image of MXene sheet after 30 days
9   exposure in ambient circumstances. The MXene flake that has been highlighted indicates the start
10   of oxidation, (b) An illustration of the oxidation phases of MXene flakes. (c) The ratio of resistance
11   change $(R-R_0/R_0)\%$ for treated and non-treated MXene films up to 180 days, where R_0 is the initial
12   sheet resistance. UV-Vis spectra of MXene films (d) non-treated and (e) treated at varying times.
13   Reproduced with permission from ref.[152]. Copyright 2022, Elsevier Ltd. (f) PL-MXene electrode's
14   oxidation stability in comparison to the thin MXene layer. (g) The resistance decrease (ΔR) and
15   initial resistance (R_0) of the PL-MXene electrode are shown against time and PVPh concentration,
16   200 hours after exposure to air oxidation, (h) Evolution of the resistance variations over time of

1   the PL-MXene electrode under oxidation stability tests at 50% humidity and 70 °C. Reproduced

2   with permission from ref.[141]. Copyright 2021, American Chemical Society.

3   Subsequently, poly(4-vinyl phenol) (PVPh) was prepared as a barrier layer on the MXene film [141].

4   The PL-MXene film, coated with a PVPh layer (~60 nm) on an MXene layer (~18 nm), exhibits a

5   very smooth surface with an RMS roughness of ~1.4 nm. After 200-600 hours of air exposure, the

6   resistance of bare MXene increases by 310% and 470%, respectively (Figure 5f). In contrast, PL-

7   MXenes with PVPh coatings showed minimal resistance change, between 27% and 38% after 200

8   hours, with only slight increases after 600 hours, demonstrating excellent oxidation resistance

9   (Figure 5g). Even at 70 °C temperature and 50% relative humidity, PL-MXenes with PVPh

10 coatings maintained good stability, showing a $\Delta R/R_0$ change of 35% to 60% after 200 hours, while

11 bare MXene showed a drastic increase to 600% (Figure 5h).

12 **4.3 MXene-sodium alginate nanocomposites**

13 Sodium alginate (SA) effectively stabilizes MXenes against oxidation. The alginate-stabilized

14 MXenes maintain their conductivity and offer improved oxidation resistance. These MXene-

15 alginate nanocomposites are particularly useful in flexible EMI shielding applications. Figure 6(a)

16 shows the schematic illustrating the fabrication process of the MXene-SA composite[150]. Linen

17 fabric, chosen for its eco-friendly properties, was used as a substrate for MXene composite

18 modification. Before applying the composite, the fabric was treated with decontamination powder

19 to ensure effective loading. Hydrogen bonding between SA and MXene was achieved via

20 functional groups on the MXene surface, enhancing the composite's mechanical strength and

21 oxidation stability. MXene-SA composites and MXene alone were subjected to acid and base

22 conditions to assess environmental stability and oxidation resistance. After 30 minutes in HCl (pH

23 = 1), the sheet resistance of MX10@S$_1$-10 (MXene with SA) increased to 20.4 ± 0.7 Ω/sq, whereas

24 MX10-10 (MXene without SA) showed a much higher increase to 58.63 ± 0.047 Ω/sq (Figure 6b).

25 In NaOH (pH = 14), MX10@S$_1$-10's resistance rose to 155.33 ± 7.02 Ω/sq after 25 minutes,

26 compared to a significant rise to 867.67 ± 66.38 Ω/sq for MX10-10 (Figure 6c). This demonstrates

27 that the MXene-SA composite offers superior protection against oxidation in both acidic and basic

28 environments. The results manifest that $MX_{10}@S_1$-10 has much better stability than MX_{10}-10 even

29 in harsh conditions such as acidic and alkaline. The coating of MXene sheets with SA inhibited

30 the direct interaction of ambient oxygen, moisture, or corrosive solutions resulting in improved

31 oxidation stability.
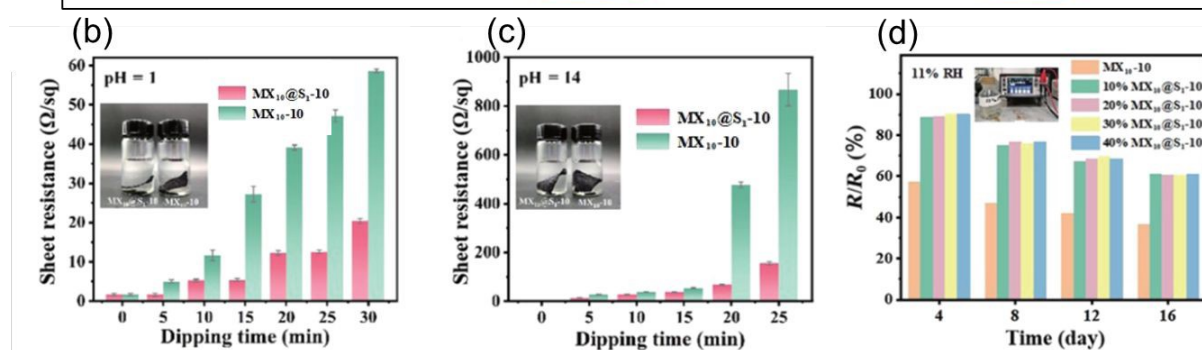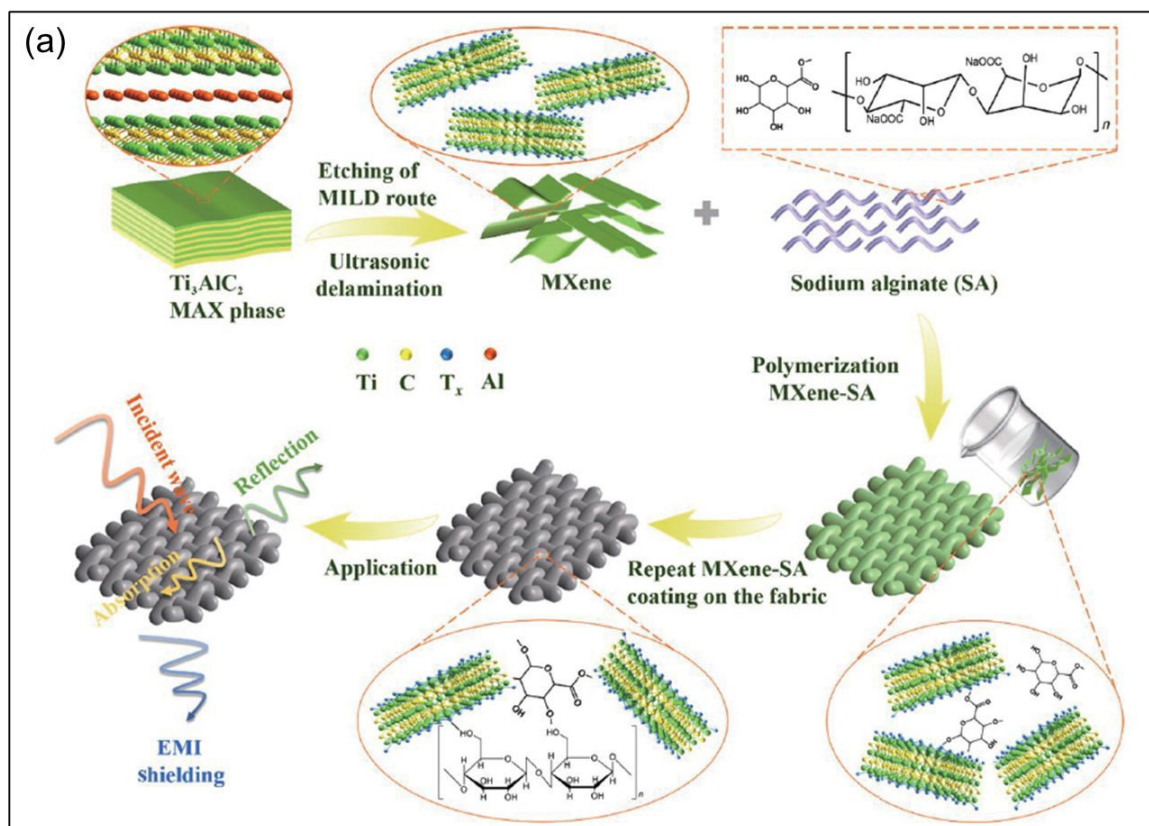
Figure 6. (a) Schematic synthesis of MXene and illustration for single-step fabrication strategy for sodium alginate-MXene film, Sheet-resistance (R/R_0) variation by treating in (b) HCl (pH = 1), (c) NaOH (pH = 14), and (d) change in R /R_0 for MX_{10}-10 and $MX_{10}@S_1$-10 with varying SA content at 11% of RH at 25°C. Reproduced with permission from ref.[150]. Copyright 2024, Springer Nature.

The oxidation stability of fabricated MXene composites was further studied by measuring their sheet resistance after storing in humid conditions at ambient temperature (25°C). MX_{10}-10 and $MX_{10}@S_1$-10 were stored in humid conditions (RH) of 11%, 33%, 75.5%, and 97.6% with varied SA amounts of 10%, 20%, 30%, and 40% for evaluating the stability. There is a change in resistance of MX_{10}-10 composite with time at 11% RH ambient, with the resistance ratio decreasing to 36.67% from 57.48%. The resistance ratio decreased from 88.56% to 60.99% for

1   MX$_{10}$@S$_1$-10 upon the 10% addition of SA (Figure 6d). MX$_{10}$@S$_1$-10 has a higher resistance ratio

2   than MX$_{10}$-10 indicating that MX$_{10}$@S$_1$-10 has a higher stability under varied humid and corrosive

3   conditions.

4   **4.4 Mussels-derived dopamine polymerization**

5   Researchers addressed the oxidation vulnerability of MXene-based materials by utilizing mussel-

6   derived dopamine polymerization[148]. Dopamine derived from mussels effectively overcomes

7   oxidation by enhancing interfacial interaction and ordering in MXene film. Dopamine forms a thin

8   sticky layer at the surfaces of MXene flake by in situ polymerization and binding caused by

9   spontaneous interfacial charge transfer. Effective oxygen and moisture screening also significantly

10   increases the ambient stability of MXene films. It's interesting to note that angstrom thick

11   polydopamine enhances MXene films' inherent high electrical conductivity. Figure 7a shows the

12   fabrication procedure and morphological distinction between pure- and polydopamine-treated

13   MXene (PDTM) film. SEM cross-sectional images show that pure MXene has random, misaligned

14   layers, while PDTM5 films exhibit well-aligned, consistent MXene sheets (Figure 57b, c).

15   Neighboring MXene flakes are aligned in their organized stacking by the polydopamine nano

16   binder, which bridges them together and creates the highly ordered MXene structure [156]. After

17   applying polydopamine coating, internal voids, and misfits could be mostly eliminated [157]. As a

18   result, dopamine coating increased the apparent density of hybrid films resulting in in-plane

19   electron transfer. Furthermore, dopamine hybridization enhances MXene's electrical conductivity;

20   PDTM5 has the greatest conductivity of 5141 S/cm Figure 7d. The enhanced flake alignment,

21   enhanced film densification, and increased electron density all contribute to in-plane electron

22   transport [158]. Polydopamine-treated MXene films exhibit significantly reduced oxidation at

23   ambient conditions and elevated temperatures, as shown in Figure 7(e). The PDTM5 film

24   experiences a much smaller increase in sheet resistance at 170°C compared to the pure MXene

25   film, which shows a five-fold resistance increase in 13 hours. The PDTM10 film demonstrates

26   even lower resistance, likely due to thermally induced crystallization of the polydopamine layer,

27   which also limits oxygen and moisture infiltration.
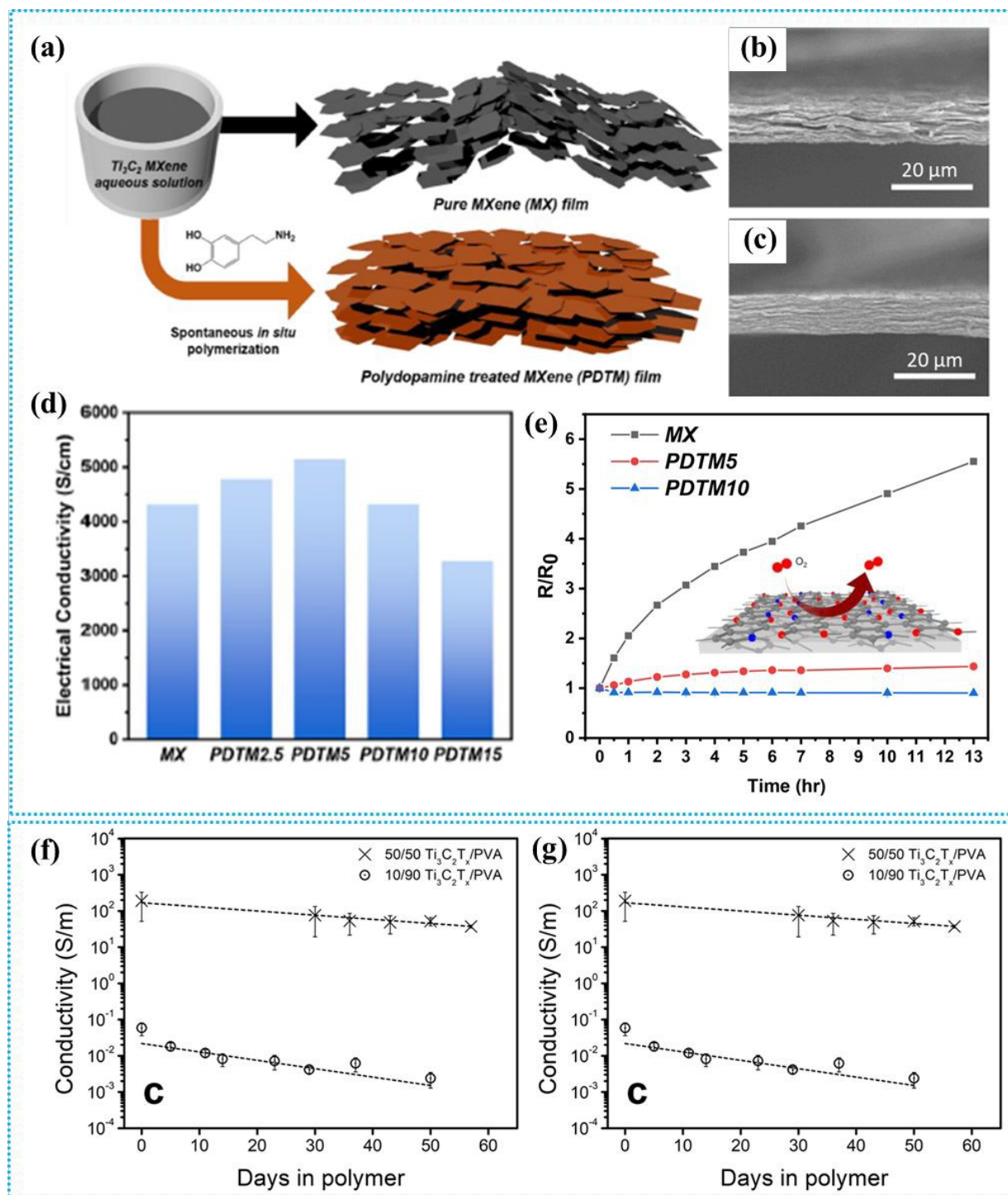
1

2   **Figure 7.** (a) Schematic showing the production process and the morphological changes between
3   pure and polydopamine-treated MXene film, (b) and (c) Cross-sectional SEM images of pure- and
4   PDTM-treated MXene, (d) electrical conductivity of MXene film with varied PDTM concentration
5   (0-15%), (e) Change in electrical resistance during heating (170 °C) in air. Reproduced with
6   permission from ref.[148]. Copyright 2020, American Chemical Society. The conductivity variation
7   of (f) Pristine MXene films and (g) MXene/PVA films in air[151].

1

2 The thin dopamine layer protects MXene from oxidation while maintaining electrical performance

3 and enhancing interfacial contact.

4 **4.5 Can all polymers prevent MXene oxidation?**

5 As discussed above, while most polymers support MXene stability, not all polymers can

6 effectively prevent oxidation. Polymers with a hydrophilic nature are mostly unable to prevent

7 oxidation in MXenes as hydrophilicity allows water and oxygen molecules to penetrate the

8 composite and the MXene surface. Habib et al. studied the oxidation stability of vacuum-filtered

9 $Ti_3C_2T_x$ films MXenes/PVA films and used the electrical conductivity as an indicator to estimate

10 their stability[151]. The study monitored the decline in electrical conductivity of $Ti_3C_2T_x$/PVA

11 composites over time and compared it with pristine MXene films exposed to air (Figure 7f-g). Two

12 different weight ratios of PVA were used to assess the impact of polymer concentration on the

13 stability of MXenes: 50–50 wt% $Ti_3C_2T_x$ to PVA and 10–90 wt% $Ti_3C_2T_x$ to PVA. The study

14 reported that the pristine MXene maintained only 2% of its initial conductivity in air after 9 weeks

15 (Figure 7f). The conductivity of the 50–50 wt% sample decreased to about 40% of its original

16 value by day 30 and 20% by day 57, while the 10–90 wt% sample dropped to roughly 7% by day

17 29 and 4% by day 50 (Figure 7g). Both samples exhibited a rapid decline in conductivity during

18 the first four weeks, followed by a slower decrease, indicating a reduction in oxidation rates due

19 to diminishing reactive sites. This consistent trend across both composite samples and the $Ti_3C_2T_x$

20 film suggests that the oxidation mechanism is mostly unaffected by polymer content, and the

21 hydrophilic PVA does not provide an effective protective barrier against oxidation.

22 **5. Synergistic effects on nanocomposite properties**

23 Typically, the main benefit of composite membranes lies in their tailored properties, allowing the

24 use of specific materials for particular applications. MXene materials can serve as optimal

25 nanofillers, enhancing MXene/polymer membranes with a range of properties such as increased

26 mechanical strength[159], better thermal performance[160], and enhanced conductivity[161], etc.

27 Moreover, the oxidation of MXene materials is significantly reduced due to their effective

28 encapsulation within the polymer[162]. MXenes can be combined with two types of polymers:

29 cationic and neutral[163]. The cationic polymer (e.g. PDDA) can form electrostatic interactions with

30 negatively charged MXene nanosheets, resulting in a relatively loose structure with some voids,

31 similar to the MXene-only film. In contrast, the neutral polymer (e.g. PVA) can rely on hydrogen
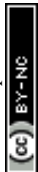
1 bonding, leading to a compact layered structure (Figure 8a). Using negatively charged polymers

2 can enhance the dispersion of MXene nanosheets due to electrostatic repulsion. Molecular

3 dynamics simulations reveal the synergy of hydrogen and ionic bonding agents in effectively

4 transferring local stress while providing substantial slippage space for MXene nanosheets[164].
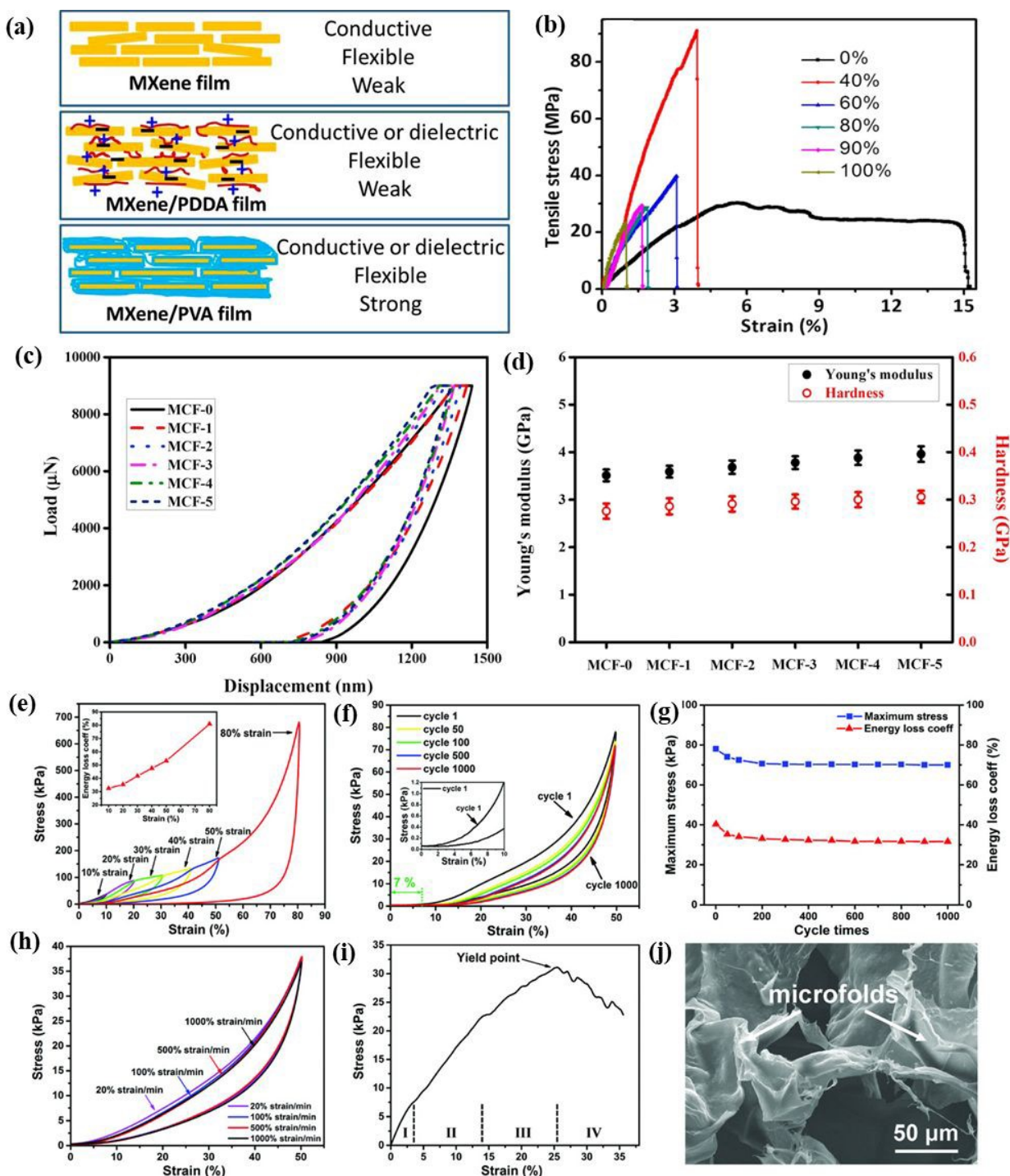
5 **5.1 Mechanical properties**

6 The mechanical properties represent a crucial factor for polymer-based composites, which can be

7 effectively enhanced by incorporating inorganic fillers. The distinctive characteristics and

8 nanostructures of nanomaterials, along with their reactivity, have made them appealing candidates

9 as fillers to strengthen polymer-based membranes across various types of polymers. Usually, free-

10 standing MXenes often experience inadequate mechanical characteristics and weak interactions

11 among the nanosheets, which can lead to structural failure due to capillary forces during the

12 polymer impregnation process. Introducing 10 wt% PVA improves the tensile strength of the

13 $Ti_3C_2T_x$/PVA film by 34%, reaching 91 ± 10 MPa, around fourfold that of the pure $Ti_3C_2T_x$ film,

14 when PVA loading was increased to 60 wt%[163] (Figure 8b). The enhanced stiffness and strength

15 indicate effective stress transfer to the embedded $Ti_3C_2T_x$ nanosheets, suggesting some interfacial

16 bonding, likely aided by the OH group terminations on $Ti_3C_2T_x$. The Young's modulus of

17 $Ti_3C_2T_x$/PVA films can be adjusted by varying the $Ti_3C_2T_x$-to-PVA ratio. The hollow cylinders

18 made from these films can support substantial weights, with a 6 mm diameter and 10 mm high

19 cylinder supporting about 4,000 times its weight ($\sim$1.3 MPa), and a similar cylinder with 90 wt%

20 $Ti_3C_2T_x$/PVA supporting approximately 15,000 times its weight ($\sim$2.9 MPa).

21 To explore this issue in greater depth, researchers have created MXene composite frameworks by

22 adding crosslinking agents to connect MXene nanosheets. Researchers combined resorcinol and

23 formaldehyde with $Ti_3C_2T_x$ to form a composite framework[165]. The organic precursors

24 polymerized on hydrophilic $Ti_3C_2T_x$, creating a crosslinked $Ti_3C_2T_x$/C foam (MCF) structure after

25 pyrolysis. This framework exhibited a well-connected structure with impressive mechanical

26 strength, supporting 500 times its weight. Using a similar polymer impregnation method with

27 epoxy precursors, a dense $Ti_3C_2T_x$/C/epoxy film structure was also produced. The MCF samples

28 were labeled as MCF-0 to MCF-5, with increasing $Ti_3C_2T_x$ MXene content from 0 to 1.64 wt%,

29 respectively. The SEM images show that adding $Ti_3C_2T_x$ MXene to the MCF resulted in a

1   reduction of cell density due to crosslinked, folded sheets, while further MXene addition increased

2   cell density and decreased sheet size.

3

4   **Figure 8.** Mechanical properties of MXene-polymer nanocomposite. (a) Schematic representation
5   of MXene-based functional films demonstrating tunable mechanical characteristics of flexible,
6   free-standing $Ti_3C_2T_x$, $Ti_3C_2T_x$/PVA, and $Ti_3C_2T_x$/PDDA films. (b) Stress–strain curves
7   illustrating the performance of $Ti_3C_2T_x$/PVA films with varying $Ti_3C_2T_x$ content[163]. (c) Load-

1 displacement curves showcasing the performance of the MCF/epoxy EMI shielding
2 nanocomposites; (d) Hardness and Young's modulus measurements for the MCF/epoxy EMI
3 shielding nanocomposites, illustrating their mechanical properties. Reproduced with permission
4 from ref.[165]. Copyright 2019, Elsevier Ltd. (e) Compressive stress-strain (σ–ε) curves for the
5 aerogel (MXene to PAA ratio 1:4) at various strains, with an inset showing energy loss coefficients
6 at these strains. (f) Fatigue performance of the aerogel (MXene to PAA ratio 1:1) subjected to
7 1000 cycles at 50% strain. (g) Changes in elastic stress and energy loss coefficients over 1000
8 cycles at 50% strain. (h) Stress-strain curves of the aerogel (MXene to PAA ratio 2:1) evaluated
9 at different compressive strain rates (20, 100, 500, and 1000% min^{-1}). (i) Tensile stress-strain curve
10 for the aerogel (MXene to PAA ratio 2:1); (j) SEM image illustrating the fracture morphology of
11 the MXene/PI aerogel. Reproduced with permission from ref.[166]. Copyright 2018, Wiley.

12 The polymerization of resorcinol and formaldehyde on hydrophilic $Ti_3C_2T_x$ MXene effectively

13 fused the carbon structure and MXene, enhancing crosslinking density and carbon junctions. The

14 load-displacement curves (Figure 8c) show that increasing $Ti_3C_2T_x$ MXene content reduces the

15 indentation depth of MCF/epoxy EMI shielding nanocomposites, enhancing their resistance to

16 indentation. As $Ti_3C_2T_x$ MXene content increases, Young's modulus and hardness improve by 13%

17 and 11%, respectively, due to the superior mechanical properties of MXenes and the improved

18 stress transfer within the cross-linked MCF network (Figure 8d). The higher cell density from

19 additional MXene further strengthens the cross-linked structure, boosting the mechanical

20 performance of the nanocomposites. Liu et al. improved the flexibility and mechanical stability of

21 $Ti_3C_2T_x$/PI foam by using polyimide (PI) to bridge $Ti_3C_2T_x$ nanosheets, achieving compressibility

22 and stretchability through freeze-drying $Ti_3C_2T_x$/poly(amic acid) (PAA) followed by

23 polymerization[166]. An aqueous solution of hydrophilic PAA and $Ti_3C_2T_x$ was freeze-dried,

24 followed by thermal annealing to polymerize PAA into PI. Strong polar interactions between PI

25 and $Ti_3C_2T_x$ tightly bonded the two components, resulting in a durable $Ti_3C_2T_x$/PI foam with

26 excellent mechanical properties, including compression, torsion, and 180° bending. The MXene/PI

27 aerogel demonstrates strong interfacial bonding between MXene and PI, resulting in superior

28 mechanical properties compared to neat MXene aerogel. Figure 8e shows the compressive stress-

29 strain curves, where the MXene/PI aerogel exhibits excellent reversible compressibility up to 80%

30 strain (MXene to PAA ratio 1:4), unlike the pristine MXene aerogel, which suffers from

31 irreversible deformation due to weak interactions between its layers. The MXene/PI aerogel also

32 has a high energy loss coefficient (η), reaching 80.9% at 80% strain, indicating strong energy

33 absorption. This makes it highly effective for shock absorption, as demonstrated by its ability to

34 protect a glass plate from fracturing after a heavy impact while maintaining its original shape. The

1   MXene/PI aerogel was tested for fatigue resistance through long-term compression-release cycles.

2   After pre-stabilizing the aerogel with several loading-unloading cycles, it maintained over 90% of

3   maximum stress and only 7% volume deformation after 1000 cycles at a fixed strain of 50%

4   (Figure 8f), indicating excellent structural robustness. While the maximum stress and energy loss

5   coefficient slightly decreased during initial cycles, they stabilized over 1000 cycles (Figure 8g).

6   Additionally, the aerogel retained its compressibility at various strain rates (20, 100, 500, and

7   1000% min^{-1}), with stress-strain curves showing close overlap (Figure 8h). Uniaxial tensile tests

8   show that the MXene/PI aerogel achieves a tensile strain of 26% and a maximum stress of 31.1

9   kPa, attributed to enhanced sheet-to-sheet interactions with PI (Figure 8i). The tensile stress-strain

10 curve consists of four stages: (1) elastic deformation, where stress increases linearly with strain;

11 (2) densification, marked by continuous stress increase as the porous network compacts; (3) a

12 plateau region with slower stress increases due to friction and adhesion; and (4) fracture,

13 characterized by decreasing stress with fluctuations, indicating structural failure. Fractured

14 surfaces with pleated cell walls illustrate the role of micro folds in tolerating cyclic tensile

15 deformation (Figure 8j). Some of the mechanical properties of MXene-polymer nanocomposites

16 are summarized in Table 2.

17 **Table 2. Mechanical properties of MXene-polymer nanocomposites**

S. No.	Polymer	MXene	MXene Concentration	Mechanical property (MPa)	Improvement percentage (%)	Ref.
1	Natural rubber	$Ti_3C_2T_x$	6.71 vol. %	~ 18 (tensile stress)	700	[167]
2	Epoxy resin	$Ti_3C_2T_x$	1.0 wt.%	98 (flexural strength)	66	[168]
3	PEDOT:PSS	$Ti_3C_2T_x$	$Ti_3C_2T_x$: polymer (3:1)	30.18 (tensile strength)	503.6	[169]
4	Polyvinyl alcohol (PVA)	$Ti_3C_2T_x$	2 wt.%	~ 48 (tensile stress)	77.8	[170]
5	Polyurethane (PU)	$Ti_3C_2T_x$	0.5 wt.%	~ 18 (tensile strength)	20	[171]
6	Thermoplastic polyurethane (TPU)	$Ti_3C_2T_x$	0.5 wt.%	20.6 (tensile strength)	47.1	[172]
7	PVC	$Ti_3C_2T_x$	15 wt.%	57.3 (tensile strength)	174.1	[173]
8	PVA	$Ti_3C_2T_x$	0.5 wt.%	13 (tensile strength)	-	[174]

9	Epoxy	Ti_3CN	90 wt.%	12.8 GPa (Young's modulus)	-	175
10	Epoxy	$Ti_3C_2T_x$	15 wt.%	4.32 GPa (Young's modulus)	20.8	176
11	Epoxy	$Ti_3C_2T_x$	4.25 wt.%	3.96 GPa (Young's modulus)	13	165
12	Polypropylene	$Ti_3C_2T_x$	2.0 wt.%	18.4 (tensile strength)	35.3	177
13	PVA	$Ti_3C_2T_x$	40	91 (tensile strength)	313.6	163

5.2 Electrical properties

In any device application, conductivity is a crucial property, and MXenes excel in this regard, achieving an impressive electrical conductivity of ~24,000 S/cm.[178] Among the MXenes, $Ti_3C_2T_x$ stands as a pinnacle, characterized by its exceptional electrical conductivity and multifaceted utility across diverse applications. Most polymers are insulators, but adding MXene flakes can improve their electrical conductivity. The addition of MXenes to the polymers can separate the layers of MXenes and promote bonding at the molecular level between MXene and the polymer. It was found that found that the electrical conductivity of PVA increases from 0.04 to 2.2×10^4 S/m when the MXene ($Ti_3C_2T_x$) content varies from 40 wt% to 90 wt% in the polymer matrix[163]. The relationship between the MXene content in polymer matrix e.g. polyacrylamide (PAM) and electrical conductivity is expressed as[179]:

$$\sigma = k(m - m_{th})^\alpha$$

In this equation, σ represents the electrical conductivity of nanocomposite ($Ti_3C_2T_x$/PAM membranes, k is a constant, m denotes the MXene loading amount, m_{th} is the percolation threshold required for conductivity enhancement, and α is the scaling exponent.

The role of MXene in inducing electrical conductivity in MXene-polymer nanocomposites has been theoretically predicted for various nanocomposites like polypropylene (PP)/MXene, nitrile butadiene rubber (NBR)/MXene, natural rubber (NR)/MXene, polystyrene (PS)/MXene, and polyacrylamide (PAM)/MXene[180]. A proposed model predicts electrical conductivity, assuming

1   the MXene nanosheet thickness ~500 nm. The percolation threshold (φ_p), calculated using the

2   interphase thickness aligns with experimental values. The φ_p is given by equation:

$$\varphi_p = \frac{(40t)^2}{(D + 20t_i)^2}$$

4   where t is the thickness, t_i the interphase depth, and D the MXene diameter. Uniform MXene

5   dispersion lowers the percolation threshold, while clustering increases it. Based on theoretical

6   predictions, the interphase thickness for NBR/MXene, PP/MXene, PS/MXene, NR/MXene, and

7   PAM/MXene nanocomposites are 10, 10, 34, 17, and 5 nm, respectively. The proposed model

8   yields a tunneling distance of 0.76 to 7.5 nm, which is below the 10 nm maximum threshold for

9   tunneling conductivity. For all MXene-based nanocomposites, the theoretical calculations match

10   with experimental values (Figure 9a-d).
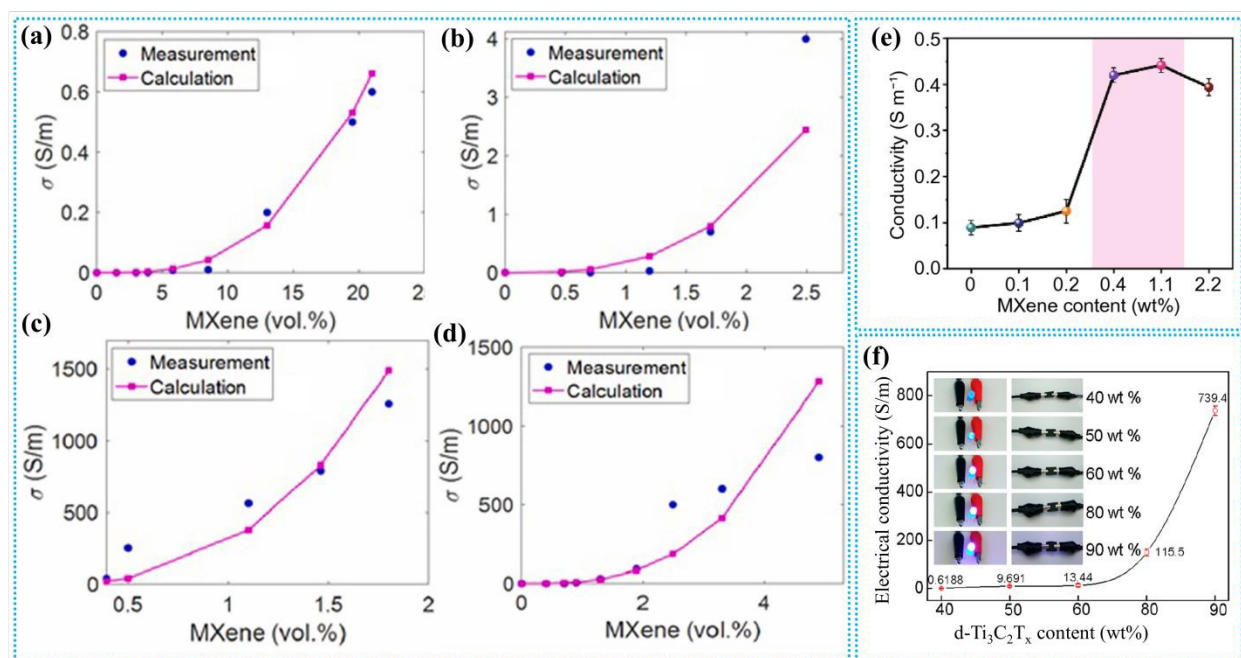
Figure 9. Electrical properties of MXene-polymer nanocomposites. (a-d) Empirical findings and conductivity predictions for NBR/MXene, PP/MXene, PS/MXene, and NR/MXene nanocomposites, respectively. Reproduced with permission from ref.[180]. Copyright 2024, Elsevier Ltd. (e) Conductivity variation of MXene hydrogel with MXene content[181]. (f) Electrical conductivity *vs*. d-Ti$_3$C$_2$T$_x$ content for d-Ti$_3$C$_2$T$_x$/CNF composite sheets. Reproduced with permission from ref.[182]. Copyright 2018, American Chemical Society.

18   Yu et al. developed an MXene organohydrogen incorporating glycerol (Gly), featuring an MXene

19   network for electron conduction, binary solvent channels for ion conduction, and multiple solvent-

20   polymer-MXene interfaces for EMI applications[181]. The conductivity of the MXene hydrogel rises

1 sharply from 0.099 to 0.442 S m^{-1} with increasing MXene content from 0.1 to 2.2 wt%, before

2 slightly decreasing to 0.394 S m^{-1}. (Figure 9e). This trend reflects the balance between enhanced

3 electron transport and reduced ion conduction due to smaller ion channels at higher MXene

4 concentrations.

5 MXenes, when combined with cellulose nanofibers (CNFs), form a composite paper that

6 demonstrates significant improvements in electrical conductivity[182]. As the d-$Ti_3C_2T_x$ content

7 increases, the conductivity rises sharply, reaching 739.4 S m^{-1} at 90 wt%. Even at 50 wt%, the

8 conductivity is 9.691 S m^{-1}, exceeding the 1 S m^{-1} required for effective EMI shielding

9 applications (Figure 9f). While the insulating nature of CNFs slightly reduces the overall

10 conductivity compared to pure d-$Ti_3C_2T_x$, their one-dimensional structure aids in the alignment of

11 MXene nanosheets, ensuring a connected and efficient conductive network. This nanocomposite

12 exhibits a tensile strength of 135.4 MPa, a fracture strain of 16.7%, and a high folding endurance

13 of up to 14,260 cycles.

14 MXene-based nanocomposites display both isotropic and anisotropic electrical properties,

15 depending on their structural alignment and processing conditions. When hybridized with

16 materials like CNTs and PVDF, these composites can exhibit anisotropic conductivity, with high

17 in-plane conductivity and lower through-plane conductivity in films, while achieving isotropic

18 conductivity in foams. Le et al. prepared PVDF/CNT/MXene films and introduced foam structures

19 using CO_2-assisted foaming at various saturation temperatures (T_{sat}) and different MXene content

20 levels. CNTs intertwine with MXenes to form a 3D conductive network, further improving

21 electrical performance. PVDF is selected for its pyroelectric effect, high dielectric constant,

22 mechanical stiffness, and thermal stability. The in-plane conductivity ($\sigma_\parallel$) and through-plane

23 conductivity ($\sigma_\perp$) of PVDF/CNT/MXene films initially increase with MXene content but level off

24 due to contact resistance between fillers. At 1 wt% MXene, $\sigma_\parallel$ reaches a peak value (~17 S/m) due

25 to optimal MXene alignment, while $\sigma_\perp$ remains lower due to poor conductivity between layers.

26 Higher MXene content (12 wt%) leads to aggregation, reducing $\sigma_\parallel$ and increasing $\sigma_\perp$ slightly.

27 Composite foams, prepared at T_{sat} = 171 °C, show increased $\sigma_\perp$ and decreased $\sigma_\parallel$ compared to

28 films, with more random filler orientation enhancing through-plane connectivity. Larger cell sizes

29 at higher T_{sat} reduce filler contact, lowering both conductivities. Some of the electrical properties

30 of MXene-polymer nanocomposites are summarized in Table 3.

1 **Table 3. Electrical properties of MXene-polymer nanocomposites**

| S. No.	Polymer	MXene	MXene Concentration	Electrical Conductivity (S/m)	Ref.
1	Natural rubber	$Ti_3C_2T_x$	6.71 vol. %	1400	[167]
2	PEDOT:PSS	$Ti_3C_2T_x$	88 wt.%	340.5	[169]
3	Epoxy	$Ti_3C_2T_x$	15 wt.%	105	[176]
4	Epoxy	$Ti_3C_2T_x$	4.25 wt.%	184	[165]
5	PDMS	$Ti_3C_2T_x$	2.5 vol%	550	[183]
6	PVA	$Ti_3C_2T_x$	90 wt.%	22433	[163]
7	PEO	$Ti_3C_2T_x$	1 % wt.%	210×10^{-6}	[184]
8	PAM	$Ti_3C_2T_x$	6 wt.%	3.3×10^{-2}	[185]
9	PVA	$Ti_3C_2T_x$	0.14 wt.%	590×10^{-6}	[186]
10	Polystyrene	$Ti_3C_2T_x$	0.26%	1081	[187]
11	PVDF-TrFE-CFE@	$Ti_3C_2T_x$	19.5 wt.%	37.4	[188]

2 @poly(vinylidene fluoride-trifluoro ethylene) (PVDF-TrFE)

3 **5.3 Thermal Properties**

4 MXenes display anisotropic properties due to their structural makeup, with strong covalent bonds

5 within the basal plane providing high in-plane strength, while weaker interlayer forces allow easy

6 exfoliation[189]. This anisotropy results in higher thermal conductivity within the plane, making

7 MXenes ideal for heat dissipation in different applications[190]. MXenes, particularly Ti_3C_2, have

8 thermal conductivities that often surpass those of many metals, making them ideal for enhancing

9 heat transfer in composites. When incorporated into polymers, MXenes improve thermal

10 conductivity by forming interconnected networks that facilitate efficient heat conduction. The

11 effectiveness of these composites depends on the polymer type; those that form hydrogen bonds

12 with MXenes, like PVA and PVDF, enhance thermal transfer through better interfacial bonding.

13 The loading amount of MXenes also influences conductivity, with significant improvements

14 occurring when a continuous network is established at higher concentrations. First-principles

15 density functional calculations show that MXenes exhibit thermal conductivities greater than most

16 metals and low-dimensional semiconductors, making them promising additives for enhancing the

17 thermal conductivity of polymer composites. Earlier studies demonstrate that a $Ti_3C_2T_x$/PVA

18 membrane (12.71 wt% PVA) demonstrated a thermal conductivity of 47.6 W m^{-1}·K^{-1}, which,

1   while lower than that of pristine Ti_3C_2 (55.8 W m^{-1}·K^{-1})[191]. Cao et al. found that the thermal

2   conductivity of $Ti_3C_2T_x$/PVDF membranes exhibited minimal increase at low MXene loading

3   (<1.0 wt%) but surged at higher levels[192]. This increase is attributed to the extensive surface area

4   of Ti_3C_2 flakes and the formation of hydrogen bonds with PVDF, which effectively reduce

5   interfacial thermal resistance and enhance thermal conductivity.
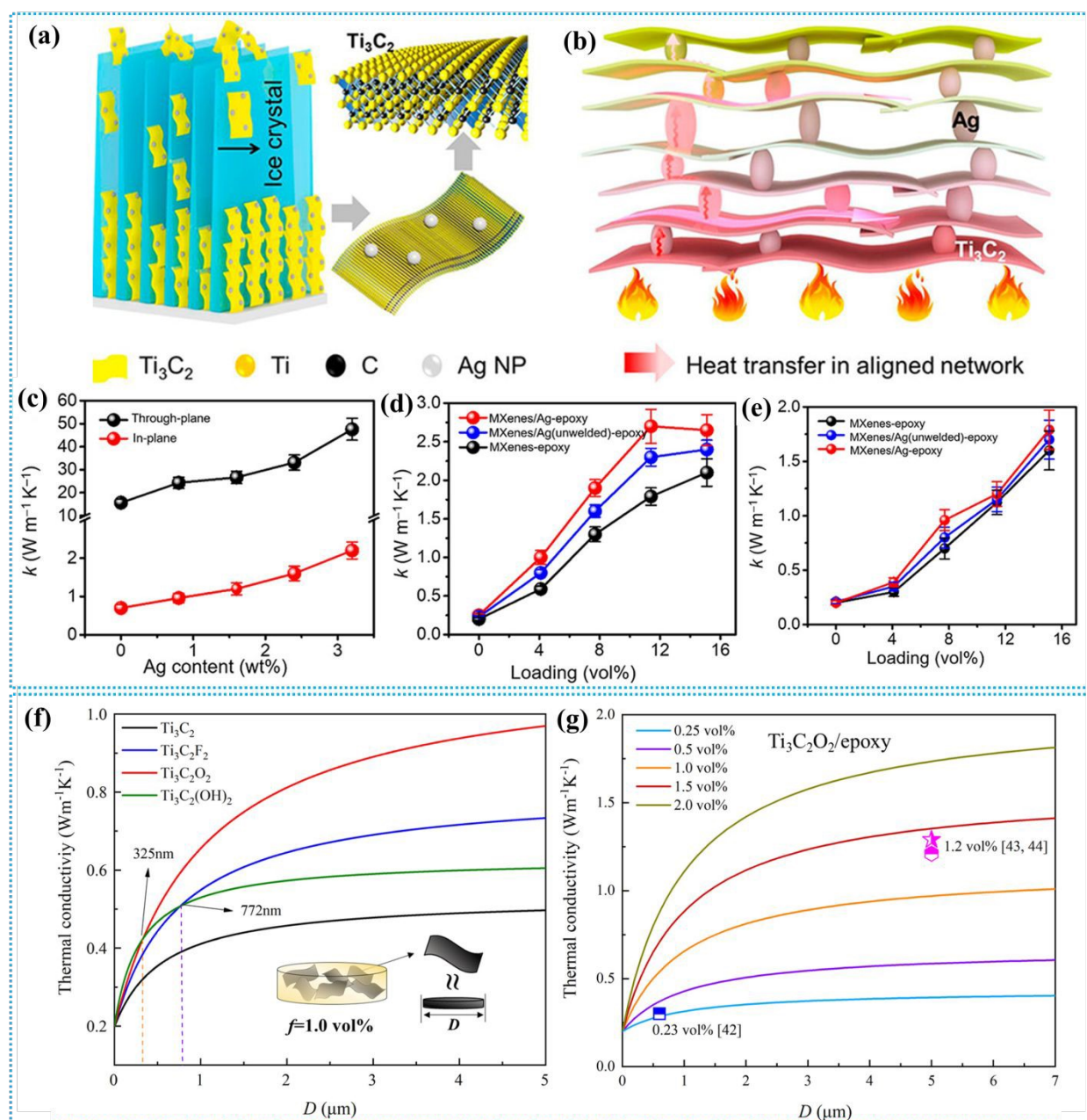
6

7   **Figure 10.** Thermal properties of MXene-polymer nanocomposites. (a) Illustration of the ice-
8   template technique for aligning MXene/Ag nanofillers. (b) Effective heat transfer in both in-plane
9   and through-plane directions within the welded MXene/Ag aerogel skeleton due to material and

1 structural synergy. (c) Thermal conductivities of MXene films with varying Ag loadings. (d)
2 Through-plane conductivity comparisons of MXene-epoxy, MXene/Ag (unwelded)-epoxy, and
3 MXene/Ag-epoxy nanocomposites. (e) In-plane conductivity comparisons of MXene-epoxy,
4 MXene/Ag (unwelded)-epoxy, and MXene/Ag-epoxy nanocomposites. Reproduced with
5 permission from ref.[193]. Copyright 2020, American Chemical Society. (f) Thermal conductivity of
6 $Ti_3C_2T_x$/epoxy composites at 1.0 vol% filler content. (g) Thermal conductivities of $Ti_3C_2O_2$/epoxy
7 composites with varying volume content and filler size. Reproduced with permission from ref.[194].
8 Copyright 2022, Elsevier Ltd.

9 To improve the thermal conductivity of the MXene/epoxy nanocomposites Ji et al. designed 3D
10 MXene/Ag aerogels using the ice templating method (Figure 10a) as heat transfer skeletons for
11 epoxy nanocomposites by in situ decorating Ag nanoparticles on exfoliated MXene nanosheets to
12 improve contact[193] (Figure 10b). The vertically aligned MXenes, with a high through-plane
13 thermal conductivity of 472 W m^{-1} K^{-1}, form a thermally conductive network when combined
14 with Ag, which has a thermal conductivity of 430 W m^{-1} K^{-1} and low soldering temperature. The
15 resulting MXene/Ag/epoxy nanocomposite exhibits a through-plane thermal conductivity of 2.65
16 W m^{-1} K^{-1}, a 26.2% increase compared to the MXene-epoxy nanocomposite, along with improved
17 mechanical and thermal expansion properties. The films demonstrate distinct thermal conductive
18 behaviors in the in-plane and through-plane directions, with in-plane thermal conductivity rising
19 to 47.57 W m^{-1} K^{-1} at 3.2 wt% Ag nanoparticles loading compared to 15.64 W m^{-1} K^{-1} for pristine
20 MXene films. In the through-plane direction, the thermal conductivity increases from 0.7 to 2.2 W
21 m^{-1} K^{-1} (Figure 10c), enhancing efficient heat dissipation in practical applications; however, Ag
22 nanoparticles loading beyond 3.2 wt% leads to film fragility. The thermal conductivities of
23 MXene/Ag/epoxy nanocomposites, measured via the laser flash technique, exhibited
24 enhancements in both in-plane (Figure 10d) and through-plane (Figure 10e) directions upon
25 incorporating MXene/Ag fillers. The through-plane thermal conductivity reaches 2.65 W m^{-1} K^{-1}
26 at 15.1 vol% filler loading, representing a >1200% increase compared to pure epoxy resin. This
27 suggests that Ag nanoparticles improve thermal conductivity by promoting effective heat transfer
28 channels within the nanocomposite. The observed anisotropic thermal behavior is attributed to the
29 two-dimensional structure of MXenes, which results in distinct heat transfer mechanisms along
30 the horizontal and vertical orientations of the film.

31 Terminal groups on MXenes can impact thermal conductivity by reducing phonon scattering and
32 enhancing interfacial interactions with epoxy matrices[194, 195]. Wang et al. used molecular dynamics
33 and effective medium theory to analyze four MXenes-Ti_3C_2, $Ti_3C_2F_2$, $Ti_3C_2O_2$, and $Ti_3C_2(OH)_2$-

1 and their epoxy composites[194]. The study found that $Ti_3C_2O_2$ achieves the highest thermal

2 conductivity of 140.25 W m^{-1} K^{-1}, while $Ti_3C_2(OH)_2$ exhibits the lowest interfacial thermal

3 resistance (ITR), improving composite conductivity at optimal flake sizes (Figure 10f). The study

4 assumes MXene flakes as disk shapes with a diameter and thickness of 0.98 nm. It was proposed

5 that the effective thermal conductivities of the nanocomposites initially increase sharply with the

6 lateral size of fillers, eventually leveling off after reaching a critical size. Among the composites,

7 $Ti_3C_2O_2$/epoxy demonstrates the highest thermal conductivity, while Ti_3C_2/epoxy exhibits the

8 lowest due to its intrinsic thermal conductivity and high ITR. The results indicate two intersections

9 between $Ti_3C_2(OH)_2$/epoxy and the -O and -F terminated MXenes, suggesting that below critical

10 sizes (325 nm for -O and 772 nm for -F), interfacial thermal conductance plays a more significant

11 role in enhancing thermal performance. Additionally, in the $Ti_3C_2O_2$/epoxy system, filler volume

12 content below 2 vol% is optimal to avoid agglomeration, with thermal conductivity increasing

13 linearly before reaching a plateau as the MXene size increases (Figure 10g). Some of the thermal

14 properties of MXene-polymer nanocomposites are summarized in Table 4.

15 **Table 4. Thermal properties of MXene-polymer nanocomposites**

S. No.	Polymer	MXene	MXene Concentration	Thermal Conductivity (W/mK)	Improvement percentage (%)	Ref.
1	PVA	$Ti_3C_2T_x$	2 wt.%	-	18.7	170
2	Thermoplastic polyurethane (TPU)	$Ti_3C_2T_x$	1 wt.%	-	8.4	172
3	PVC	$Ti_3C_2T_x$	15 wt.%	3.45	~1050	173
4	PVA	$Ti_3C_2T_x$	2 wt.%	-	8.2	174
5	Epoxy	Ti_3CN	5 wt.%	-	2.7	175
6	Epoxy resin	$Ti_3C_2T_x$	1.0 wt.%	-	-0.55	168
7	Polypropylene	$Ti_3C_2T_x$	2.0 wt.%	-	11.8	177
8	PDMS	$Ti_3C_2T_x$	2.5 vol%	0.694	220	183
9	PVDF	$Ti_3C_2T_x$	5 wt.%	0.363	100	196
10	PVA	$Ti_3C_2T_x$	-	47.6	-	197
11	Epoxy	$Ti_3C_2T_x$	15 wt.%	7.60	~100	198
12	Epoxy	$Ti_3C_2T_x$	1 wt.%	0.587	141.3	199

16 **6. MXene-polymer nanocomposites- synthesis strategies**

1   MXenes can be integrated with a wide range of polymers, facilitating the tailoring of

2   nanocomposite materials for specific applications. The interaction force between the MXene

3   matrix and polymers in nanocomposite synthesis primarily involves hydrogen bonding, van der

4   Waals interactions, electrostatic interactions, and π-π stacking, depending on the functional groups

5   present on both MXene surfaces and the polymer chains[94]. The MXene surface terminations (e.g.,

6   –O, –OH, –F,) can form hydrogen bonds with polymers containing polar groups like –OH, –

7   COOH, –NH$_2$, etc. Additionally, electrostatic interactions may occur when charged polymers are

8   used, especially in systems where MXenes have surface charges[92]. Van der Waals forces contribute

9   to non-covalent binding, while polymers with aromatic groups can engage in π-π interactions with

10   MXene layers. These interactions are key to enhancing compatibility, mechanical strength, and

11   functional properties in MXene-polymer nanocomposites. MXene-polymer composites can be

12   fabricated using different processing techniques, such as solution casting[68, 77], melt blending[200, 201],

13   or electrospinning[80], etc., allowing for the production of complex shapes, thin films, coatings, or

14   fibers. This versatility in processing enables the integration of MXenes into a wide range of devices

15   and structures[202, 203, 204, 205].

16   **6.1 Surface grafting/modification of MXenes**

17   Due to the abundant functional groups at the surface of MXenes, it becomes easier to functionalize

18   these with different organic molecules. First-principles calculations revealed that unmodified

19   Ti$_3$C$_2$ MXene can cleave and decompose monomers effectively. In contrast, surface-functionalized

20   Ti$_3$C$_2$F$_2$, Ti$_3$C$_2$FO, and Ti$_3$C$_2$O$_2$ bind weakly with monomers due to van der Waals forces, while

21   Ti$_3$C$_2$(OH)$_2$ shows a stronger binding affinity[206]. In the surface modification process, MXene

22   sheets are functionalized or chemically modified to introduce specific groups or moieties on their

23   surfaces. These modified MXene sheets are then mixed or dispersed within a polymer solution or

24   melt. During polymerization or crosslinking, the functionalized MXene sheets become covalently

25   bonded or physically intertwined with the polymer chains, leading to the formation of

26   nanocomposite material[207, 208]. A protein-inspired supramolecular elastomer was developed for

27   intelligent sensing applications, utilizing self-healable Ti$_3$C$_2$ MXene blended with rubber (serine-

28   grafted epoxidized natural rubber) (S-ENR) latex[209]. The study created a self-healing elastomer

29   inspired by proteins for smart sensing. MXene nanosheets were esterified with serine using EDC

30   and DMAP at 100°C for 3 hours to produce S-MXene (Figure 11a). Serine-modified epoxidized

31   natural rubber (ENR) latex was synthesized by reacting serine with ENR latex at 100°C for 3

1   hours. S-MXenes/S-ENR nanocomposites were prepared by combining S-MXene with S-ENR

2   latex, stirring, sonicating, and drying to form a 3D network film (Figure 11b). Besides this, another

3   surface modification technique involving the covalent attachment of polyethylene glycol

4   carboxylic acid (PEG6-COOH), onto MXenes through esterification chemistry was introduced.

5   The surface modification of $Ti_3C_2T_x$ using PEG6-COOH with high ligand loading significantly

6   improves the dispersibility of MXene flakes in a wide range of non-polar organic solvents (e.g.,

7   2.88 mg/mL in chloroform) without inducing oxidation or altering the structural ordering of

8   $Ti_3C_2T_x$ two-dimensional layers[208]. Besides these, there are other reports on the MXenes surface

9   modifications for MXene-polymer hybridization[208, 210].

6.2 Solution blending

11 In this method, MXenes and polymers are dispersed in a compatible solvent, and mixed via

12 stirring, ultrasonication, or high-shear mixing. Then the solvent is removed by evaporation,

13 vacuum drying, or freeze-drying to form a solid MXene-polymer composite. Carey et.al conducted

14 a study where they prepared a dispersion of alkylated 2D MXene in nonpolar solvents using the

15 blending method[201]. The study investigated the pseudocapacitive behavior of the resulting

16 nanocomposite material. In this process, after the MXene etching, the Li^+ ions present inside the

17 multilayers are ion-exchanged with di(hydrogenated tallow)benzyl methyl ammonium chloride

18 (DHT) (Figure 11c). The resulting multilayers can be easily dispersed in nonpolar solvents. These

19 can be easily processed with linear low-density polyethylene nanocomposite (LLDPE) for many

20 applications. The good part of this hybrid assembly is that these remain dispersed for more than

21 10 days without sedimenting even in nonpolar solvents. Jiao et.al conducted a study to prepare

22 photothermal healable, stretchable, and conductive $Ti_3C_2T_x$ MXene composite films using the

23 vacuum filtration method, to achieve efficient EMI shielding[211]. To determine the optimal ratio

24 between waterborne polyurethane (WPU) and natural rubber latex (NR latex), a series of

25 composite films were prepared with varying WPU: NR mass ratios. These composite films were

26 respectively denoted as WNM as these contain WPU, NR, and MXene. The next step involved

27 obtaining WPU/NR composite emulsions by mixing specific proportions of WPU and NR latex

28 emulsions in an ice bath. Subsequently, a $Ti_3C_2T_x$ suspension was gradually introduced into the

29 WPU/NR composite emulsions. This step allowed the incorporation of $Ti_3C_2T_x$ at various volume
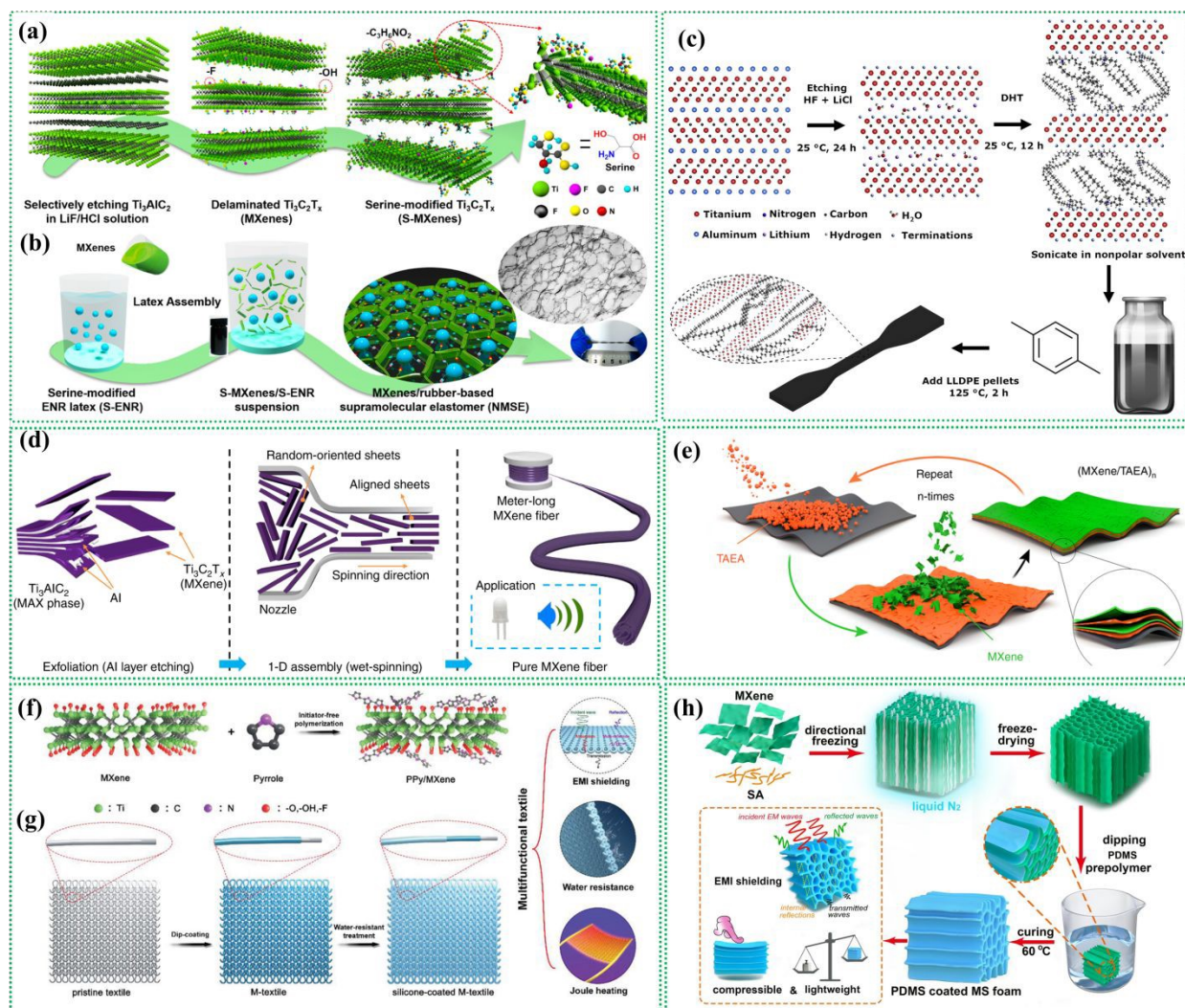
30 fractions.

Figure 11. MXene-polymer nanocomposites synthesis. (a) The surface modification of MXene nanosheets is achieved through an esterification reaction with serine. (b) MXene network in NMSE is constructed using the latex assembly method. Reproduced with permission from ref.[209]. Copyright 2020, American Chemical Society. (c) MXene-polymer blending. MXene multilayers are then treated with DHT to enhance their functionality. The functionalized MXene nanosheets are dispersed in a nonpolar solvent and subsequently utilized in the solution processing of LLDPE[201]. (d) Electrospinning technique. MXene material is concentrated in an aqueous solution and then assembled into a fiber. This fiber was aligned in the axial direction using a wet-spinning process[212]. (e) The process of LBL self-assembly of (MXene/TAEA)n multilayer films on planar substrates is depicted schematically[213]. (f) In-situ polymerization MXene-polymer hybrids. Schematic illustration of the modification process of MXene with in situ polymerized PPy. (g) Fabrication of PPy/MXene-decorated PET textile, along with the subsequent process of creating the multifunctional silicone-coated M-textile. Reproduced with permission from ref.[82]. Copyright 2018, Wiley. (h) The schematic shows the process of making an MXene/SA hybrid aerogel and its subsequent PDMS-coated MXene/SA foam. Reproduced with permission from ref.[214]. Copyright 2024, Elsevier Ltd.

1 The WNM films were obtained through vacuum filtration, followed by natural drying. Recently,

2 Pan et al. have reported a wearable and flexible MXene and PEDOT: PSS conducting polymer

3 nanocomposite for continuous noninvasive monitoring of sweat glucose[215]. The addition of 0.1 %

4 mass fraction of MXene has significantly improved the conductivity of the composite. In this

5 study, ethylene glycol has been utilized to increase the cross-linking and film-forming properties

6 of nanocomposite. The nanocomposite hydrogel sensor showed a sensitivity of 21.7 $\mu A \cdot mM^{-1}$

7 cm^{-2} within the concentration range of 1–94 μM and a sensitivity of 8.3 $\mu A \cdot mM^{-1} cm^{-2}$ within the

8 range of 94–1294 μM. Importantly, this glucose biosensor demonstrated outstanding

9 electrochemical performance in sweat, which was highly correlated with the corresponding

10 findings of the glucometer.

11 **6.3 Electrospinning method**

12 The electrospinning technique can prepare polymer fibers with diameters in the nanoscale range.

13 MXene-polymer nanocomposites can be effectively synthesized using electrospinning

14 techniques[80, 216]. MXene fibers can also be synthesized using the wet-spinning technique. Eom et

15 al. devised a technique for producing pure MXene fibers without additional binders[212]. This

16 method involves a large-scale wet-spinning assembly, where MXene sheets are dispersed in water

17 at high concentrations, preventing aggregation or phase separation issues (Figure 11d). The

18 coagulation process plays a pivotal role in the fabrication of these fibers. By introducing

19 ammonium ions during coagulation, the researchers have assembled MXene sheets into highly

20 flexible, meter-long fibers. These fibers exhibit an exceptionally high level of electrical

21 conductivity, making them promising candidates for various applications in advanced materials.

22 Besides, MXenes can be incorporated into polymer solutions used for electrospinning to produce

23 MXene-polymer composite nanofibers. Recently, a study was conducted on an electrospun

24 flexible triboelectric nanogenerator that utilized metallic MXene nanosheets and poly(vinyl

25 alcohol) (PVA)[217]. To prepare the PVA-MXene solution, a 10% (w/v) PVA solution, 1.0 g of PVA

26 was mixed with 10 mL of distilled water at 90 °C while stirring for ~1 h. Subsequently, MXene

27 was added to the PVA aqueous solution and stirred thoroughly to achieve a homogeneous

28 PVA/MXene mixture. Electrospinning was performed using a 5 mL syringe and needle with a 0.68

29 mm inner diameter at an applied voltage of 18 kV. The combination of MXene nanosheets and

30 PVA in the composite material imparts outstanding electrical properties, enhancing its

31 electronegativity and conductivity. For the positive friction layer, silk fibroin (SF) was selected as

1 the material for electrospinning nanofiber film due to its biocompatibility, biodegradability, and

2 significant triboelectric properties.

3 **6.4 Layer-by-layer (LBL) assembly**

4 This method involves the sequential deposition of alternating layers of $Ti_3C_2T_x$ MXenes and

5 polymers onto a substrate. The MXene and polymer layers are formed through techniques such as

6 dip coating, spin coating, spray deposition, etc. The coating process can be repeated to achieve the

7 desired thickness and control the MXene-to-polymer ratio in the composite. A method for the

8 vacuum-assisted LBL self-assembly of pillared two-dimensional multilayers comprising MXene

9 and a small molecule called tris(2-aminoethyl) amine (TAEA) was developed[213]. In this process,

10 (MXene/TAEA)n multilayers were prepared, where n represents the number of bilayers formed in

11 the self-assembled structure. In this method, $Ti_3C_2T_x$ MXene and TAEA solutions with a

12 concentration of 1 g L^{-1} were used. Porous substrates were placed on a cellulose membrane fixed

13 in an adjustable-flow vacuum system. Using airbrushes, atomized solutions were sprayed onto the

14 substrates. The cycle of spraying TAEA, rinsing with water, and then spraying MXene was

15 repeated to create (MXene/TAEA)n films of the desired thickness (Figure 11e). For larger surfaces

16 of 3D CNF aerogel and melamine foam, a rapid-LBL assembly method was used. MXene and

17 TAEA solutions were poured on top of the aerogel or foam and forced through by applying vacuum

18 pressure. (MXene/TAEA)n multilayer films can be prepared through LBL self-assembly onto

19 fibers and foams. Another study was conducted titled LBL assembly of polyaniline nanofibers

20 (PNF) and $Ti_3C_2T_x$ MXene electrodes for electrochemical energy storage[218]. In this research, the

21 LBL assembly technique was used to create thin-film electrodes by stacking PNF and $Ti_3C_2T_x$

22 MXene materials. The resulting electrodes were intended for applications in electrochemical

23 energy storage, aiming to enhance the performance of energy storage devices such as batteries or

24 supercapacitors.

25 **6.5 In-situ polymerization**

26 In this method, the monomers of the polymer are introduced into a solution containing MXene,

27 and polymerization occurs in situ, meaning within the same environment as the MXene particles[81,]

28 [82, 214]. This leads to the formation of a homogeneous mixture of MXene and polymer, creating a

29 nanocomposite material with MXene uniformly dispersed throughout the polymer matrix[219]. The

30 choice of polymer depends upon the end requirement. If a conducting polymer is chosen it will

31 result in a nanocomposite which may have applications as active electronic material whereas, an

1 insulating polymer will result in a final product with limited or reduced conductivity. In a study

2 reported by Wang et al., the fabrication of MXene-decorated multifunctional and water-resistant

3 textiles with remarkable electromagnetic interference (EMI) shielding and Joule heating

4 performances were investigated. To achieve this, PPy modified MXene sheets using in-situ

5 polymerization (Figure 11f) were utilized, which were deposited onto poly(ethylene terephthalate)

6 textiles[82]. Subsequently, a silicone coating was applied to the textiles to enhance their conductivity

7 and hydrophobicity. Highly conductive and water-resistant textiles exhibited high EMI shielding

8 efficiency and excellent Joule heating performance (Figure 11g). In another study, Wu and co-

9 workers developed compressible, durable, and conductive PDMS-coated MXene/sodium alginate

10 (SA) foams (MS) for high-performance electromagnetic interference (EMI) shielding. The

11 researchers used MXene and SA to fabricate the foam and then coated the foam with PDMS to

12 enhance its properties for EMI shielding[214]. $Ti_3C_2T_x$/SA hybrid aerogels were fabricated as

13 follows: $Ti_3C_2T_x$ suspension (20 mg mL^{-1}) was added to different amounts of SA (0, 4, 12, 28, and

14 48 mg) with stirring at 500 rpm for 5 h to achieve homogeneous and high viscosity suspensions.

15 The resulting suspensions were poured into Teflon molds and rapidly frozen on a copper cylinder

16 immersed in liquid nitrogen. Subsequently, the directionally frozen samples were freeze-dried at -

17 60 °C under 10 Pa for 48 h to yield unidirectional aerogels. These MS porous architectures were

18 coated with PDMS by vacuum-assisted impregnation method. To create the PDMS-coated MS

19 foam, a mixture of 10 g PDMS prepolymer, 1 g curing agent, and 30 mL n-hexane was thoroughly

20 mixed in a beaker for 30 min. The resulting mixture was cured at 60 °C for 12 h, resulting in the

21 formation of a thin PDMS layer on the MXene nanosheets of the MS aerogel, creating the PDMS-

22 coated MS foam (Figure 11h). The resulting PDMS-coated MXene/SA foam exhibited excellent

23 compressibility, durability, and electrical conductivity, making it a promising candidate for

24 effective EMI shielding applications. Besides these, Table 5 summarizes different polymers

25 utilized in MXene-polymers nanocomposite synthesis, along with their respective applications.

26 **Table 5.** MXene-polymer nanocomposites and their applications.

S. No.	MXene	Polymer used	Synthesis technique	MXene concentration	Application of nanocomposite	Reference
1	$Ti_3C_2T_x$	PEDOT:PSS	Electrogelation method	0 to 60wt%	Sensing	220
2	$Ti_3C_2T_x$	PEDOT:PSS	Ice templating method	0, 1, and 3 wt %	Electrical stimulation	221
3	$Ti_3C_2T_x$	PEDOT:PSS	Mixing/blending	10-90 wt.%	EMI shielding	222

4	$Ti_3C_2T_x$	PEDOT:PSS	LBL assembly	-	Energy storage/capacitive sensors	88
5	$Ti_3C_2T_x$	PEDOT:PSS	LBL assembly (spray)	29- 76.6 wt%	Multifunctional	223
6	V_2CT_x	PEDOT:PSS	Mixing/blending	-	Solar cells	224
7	Nb_2CT_x	PEDOT:PSS	Solution mixing	MXene:PEDOT:PSS (1:5, 1:7, and 1:9)	Solar cells	225
8	$Ti_3C_2T_x$	PDMS	Dip-coating and curing	1, 3, and 5 wt.%	EMI shielding skins	226
9	$Ti_3C_2T_x$	PDMS	Mixing/curing	20-50%	Pressure sensor	227
10	V_2CT_x	PDMS	Coating	-	EDL transistor	228
11	$Ti_3C_2T_x$	PU#	Mixing	1:1	EMI shielding	229
12	$Ti_3C_2T_x$	PU#	LBL assembly	-	EMI shielding and Joule Heating	230
13	$Ti_3C_2T_x$	Epoxy	Coating	0-2wt.%	Anti-corrosion	231
14	$Ti_3C_2T_x$	Polypyrrole	In situ polymerization	MXene:PPy (9:1, 8:2 and 7:3)	Supercapacitors	232
15	$Ti_3C_2T_x$	Doxorubicin	Surface modification	1:2	Tumor targeting	233
16	$Ti_3C_2T_x$	Chitosan	Electrospinning	0- 0.75 wt.%	Antibacterial	234
17	$Ti_3C_2T_x$	Silane	Surface modification	1:1	Water purification	235
18	$Ti_3C_2T_x$	PANI/PU	Electrospinning	0- 10%	Zn-ion batteries	236
19	$Ti_3C_2T_x$	Polypyrrole	Polymerization	1:1 and 2:1	Pseudocapacitive electrodes	81
20	$Ti_3C_2T_x$	PEG	3D printing	-	Tissue engineering	237
21	$Ti_3C_2T_x$	PVA	Blending	40-90%	Flexible electronics	16
22	$Ti_3C_2T_x$	PVA	Solvent exchange	2.50%	Strain sensors	238
23	$Ti_3C_2T_x$	SA	Ultrasonic mixing	5-30 mg mL-	Flexible electronic sen	239
24	$Ti_3C_2T_x$	Polypropylene	Hot-pressing	25%, 56%, and 70%	Flame-retarding/ EMI shielding	240
25	$Ti_3C_2T_x$	TAEA*	LBL self-assembly	-	Supercapacitors	213

1   * Tris(2-aminoethyl) amine (TAEA), #polyurethane (PU)

2   Combining MXenes with a wide variety of polymers makes it possible to enhance and tailor the

3   properties of MXenes and these can alter the properties of the resulting composite material as

4   desired[241, 242, 243].

5   **7. Applications of MXene-polymer nanocomposites**

1 The addition of polymers to MXenes can significantly improve their performance and expand their

2 applications in various fields. By incorporating polymers with good mechanical strength and

3 flexibility, the resulting MXene-polymer hybrids exhibit enhanced mechanical properties, making

4 them suitable for applications requiring flexibility, stretchability, and impact resistance[54, 244, 245].

5 This includes flexible electronics, wearable devices, and flexible coatings[60, 83, 202, 246]. Polymers

6 can enhance the electrochemical performance of MXenes in energy storage devices. The

7 combination of MXenes' high electrical conductivity with polymers' ion transport properties can

8 enhance the charge storage capacity of these devices[247, 248]. Polymers enhance MXene dispersion,

9 prevent restacking, and improve synergy, boosting overall material properties[249].

10 **7.1 MXene-polymers for energy storage applications**

11 MXene-polymer composites offer several advantages in energy storage devices. Polymers can

12 provide mechanical stability to the electrode materials. This improved mechanical stability leads

13 to enhanced cycling performance and a longer lifespan of energy storage devices[250]. Due to van

14 der Waals forces, MXenes layers tend to restack and agglomerate, resulting in reduced accessible

15 surface area and hindered ion diffusion due to lack of active sites[91, 251]. Polymers in MXene-

16 polymer composites help to disperse and stabilize MXene layers, preventing restacking and

17 preserving the high surface area of MXenes[16]. Polymers can facilitate ion diffusion within the

18 electrode materials[252]. Polymers can enhance the compatibility of MXene electrodes with different

19 electrolyte systems. Certain polymers can act as ion-conductive additives or binders that promote

20 ion transport and enhance the stability of electrolyte-electrode interfaces. The performance of the

21 electrodes, which were fabricated using PEDOT (poly(3,4-ethylene dioxythiophene)) deposited

22 $Ti_3C_2T_x$ sheets, exhibited an improvement compared to the electrodes made with pristine

23 $Ti_3C_2T_x$[253].

24 Polyaniline@MXene-based positive electrodes have been investigated for asymmetric

25 supercapacitor applications[250]. The electrode is prepared by casting a homogenous polyaniline

26 layer onto a 3D porous $Ti_3C_2T_x$ MXene. This enabled the stable operation of MXene at positive

27 potential due to the increased work function after combining with polyaniline. The resulting

28 flexible polyaniline@MXene positive electrode offers a high volumetric capacitance of 1632 F

29 cm^{-3} at 5000 mV s^{-1}. In another study, pseudocapacitive electrodes were developed by performing

30 oxidant-free polymerization of PPy between the layers of $Ti_3C_2T_x$ MXene[81]. Hybrid electrodes of

31 $Ti_3C_2T_x$ and PPy achieved up to 416 F g^{-1} capacitance in 1 M H_2SO_4.
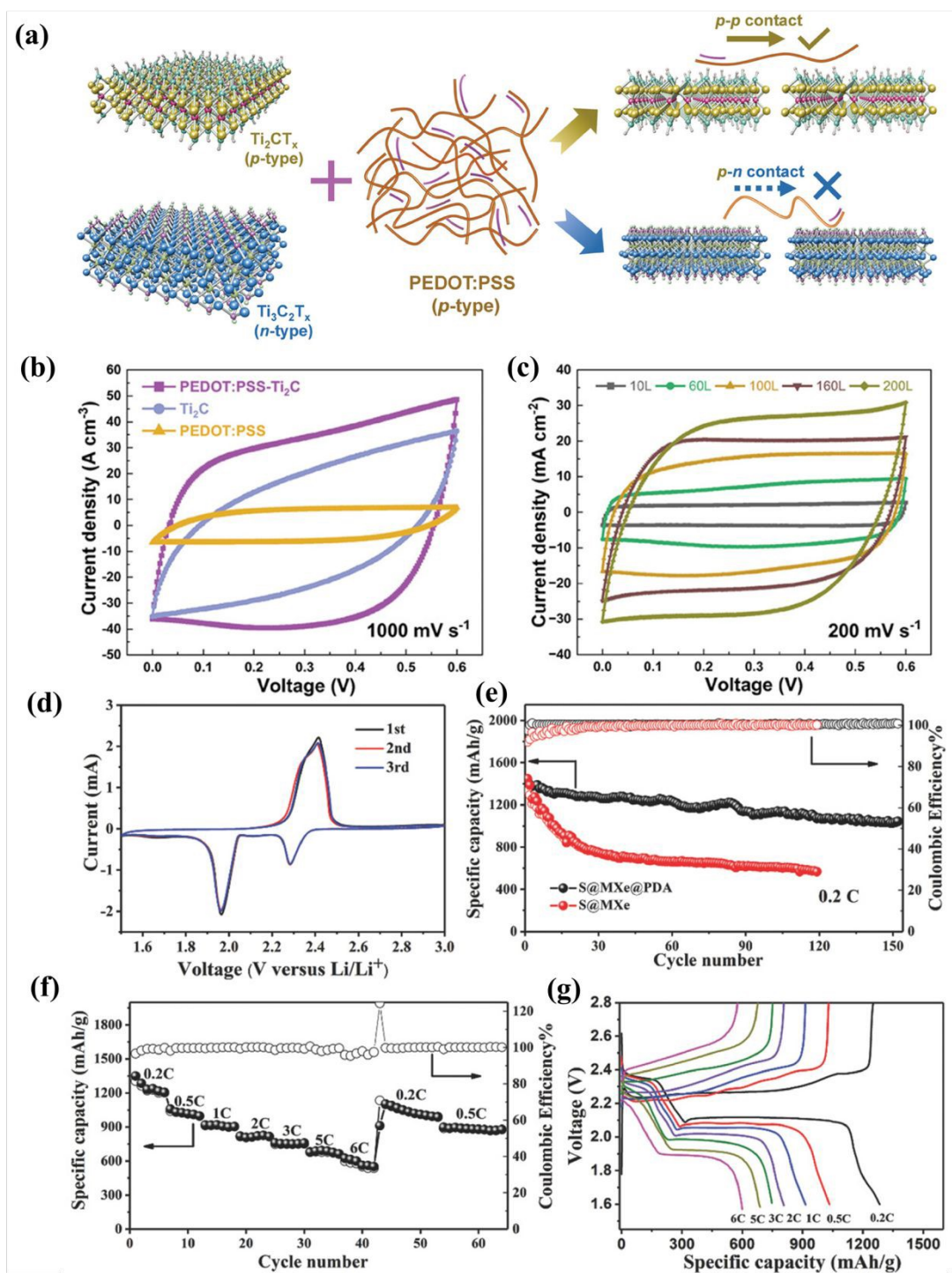
Figure 12. (a) Schematic of interactions between PEDOT:PSS and MXenes (Ti$_2$C and Ti$_3$C$_2$). (b) CV curves of 10L MSCs with Ti$_2$C, PEDOT:PSS, and PEDOT:PSS-Ti$_2$C electrodes. (c) CV curves of PEDOT:PSS-Ti$_2$C MSCs at 200 mVs^{-1} with different layer numbers[254]. (d) CV curves of S@MXene@PDA at 0.2 mV s^{-1} (first three cycles). (e) Cycling performance of S@MXene@PDA vs. S@MXene at 0.2 C. (f, g) Rate performance and voltage profiles at 0.2–6 C. Reproduced with permission from ref.[255]. Copyright 2018, Wiley.

1   MXene/PPy (2:1 and 1:1 ratios) nanocomposites, prepared by mixing delaminated $Ti_3C_2T_x$ and

2   PPy, were utilized for supercapacitor applications. Cyclic voltammetry (CV) curves of the hybrid

3   samples revealed a strong pseudocapacitive behavior. The supercapacitors based on a 2:1 ratio

4   nanocomposite demonstrated higher capacitance than those of pristine MXene and the 1:1 ratio

5   due to optimized composition. These supercapacitors outperformed PVA-$Ti_3C_2T_x$ electrodes,

6   achieving ~99% Coulombic efficiency and 92% capacitance retention over 25,000 cycles. Nyquist

7   plots confirmed good ionic conductivity, with slightly higher diffusion resistance in PPy-

8   containing films, attributed to robust bonding, effective ion/electron transport, and protective role

9   of MXene.

10   Besides $Ti_3C_2T_x$ MXene Ti_2C MXene has also demonstrated excellent energy storage capabilities.

11   Xue et al. developed ultrafast, metal-free, on-paper micro-supercapacitors (MSCs) using a

12   composite of conductive PEDOT: PSS and capacitive Ti_2C MXene[254]. They developed a more

13   effective direct ink writing (DIW) by combining PEDOT: PSS with Ti_2CT_x, leveraging its higher

14   specific capacitance and compatibility with PEDOT: PSS's hole transport paths (Figure 12a).

15   Unlike $Ti_3C_2T_x$, this blend avoids conductivity degradation, enabling improved conductivity,

16   reduced restacking, and high-rate electrochemical performance even with thick electrodes. At 1000

17   mV s^{-1} scan rate, PEDOT: PSS-Ti_2C MSCs (10 layers, ≈5 μm thick) achieved a volumetric

18   capacitance of ≈30.6 F cm^{-3}, which is nearly double that of pure Ti_2C MSCs and 6 times higher

19   than PEDOT: PSS MSCs, confirming their synergistic interaction. CV curves maintained excellent

20   rectangularity, and capacitance increased linearly with layer count at lower scan rates (Figure 12b-

21   c). These MSCs retained >96% of their capacitance after 10,000 cycles at a high scan rate of 1000

22   mV s^{-1}. They also exhibited an extended voltage window of up to 6 V and maintained outstanding

23   performance even at ultrafast scan rates of 10 V s^{-1}. This work highlights the potential of Ti_2C

24   when integrated with polymers for eco-friendly, high-performance power sources for paper-based,

25   portable, and wearable electronics. Additionally, flexible solid-state micro-supercapacitors can be

26   fabricated by electrochemically polymerizing MXene-facilitated PEDOT composite films, and

27   these composite films can be utilized along with MnO_2 to create pseudocapacitive asymmetric

28   micro-supercapacitors[256].

29   MXene-polymer nanocomposites also offer advantages in batteries, as demonstrated by Yaio et al.

30   in Li–S batteries with MXene-polydopamine (S@Mxe@PDA) cathodes[255]. The dual polysulfide

1 confinement strategy effectively suppresses shuttling, supports high sulfur loading, and ensures

2 strong conductivity and lithium polysulfide adsorption for improved performance. The polar amine

3 sites of the PDA layer enable strong chemical adsorption of polysulfides, localizing them on the

4 electrode surface. Additionally, the PDA enhances electrolyte wetting, uptake, and ionic

5 conductivity, improving Li^+ transport. Figure 12d shows the CV curves of the S@Mxe@PDA

6 cathode at 0.2 mV s⁻¹, with reduction peaks at 2.27 and 1.98 V corresponding to the formation of

7 Li_2Sx and Li_2S_2/Li_2S. Figure 12e displays long-term cycling stability at 0.2 C, with

8 S@Mxe@PDA achieving 1044 mAh g⁻¹ after 150 cycles (73% retention), outperforming S@Mxe

9 (565 mAh g⁻¹, 39% retention) due to better polysulfide confinement. Figure 12e,f demonstrates

10 the rate performance of S@Mxe@PDA, showing stable capacities at 1349–624 mAh g⁻¹ from 0.2

11 to 6 C, with minimal capacity loss when returning to lower rates, indicating fast kinetics and

12 stability.

13 Besides these, MXene-polymer hybrids can also be utilized for all-solid-state batteries and fuel

14 cells[19, 205, 257, 258].

7.2 MXene-polymer nanocomposites in sensors and flexible electronics

16 MXene-polymer nanocomposites offer several advantages over MXene-only systems in the field

17 of sensors[32, 60, 259, 260]. The incorporation of polymers in MXene-based sensors can improve the

18 sensing performance by enhancing selectivity, flexibility, sensitivity, and response time depending

19 upon their sensing nature[261-263]. Polymers can provide a selective environment for target analytes

20 by interacting with specific molecules, gases, or ions[264, 265]. The integration of MXene-polymer

21 nanocomposites has shown significant promise in enhancing the performance of pressure and gas

22 sensors due to the higher conductivity and surface area of MXenes. In a study, a bioinspired

23 interlocked structure was developed to achieve high deformability in 2D MXene/natural

24 microcapsule-based flexible pressure sensors using polyimide (PI) and PDMS[262]. To prepare Ti_3C_2

25 MXene/natural microcapsule nanofilm, a 0.2 g portion of natural microcapsule (NMC) was

26 dispersed in 10 mL of ethanol to create a well-mixed solution. 10 ml of Ti_3C_2 MXene solution was

27 then added to the NMC solution, and the mixture was stirred for 2 hours to ensure uniform

28 dispersion of Ti_3C_2 MXenes and NMC. The mixture was subsequently filtered through a

29 polypropylene membrane to create a composite film. This film was air-dried for 30 minutes at

1   room temperature and carefully peeled off from the polypropylene membrane, resulting in a

2   flexible Ti_3C_2/NMC composite film (Figure 13a).

3   Polymeric $Ti_3C_2T_x$ MXene nanocomposites have exhibited promising applications in room-

4   temperature ammonia gas sensing[265]. The PEDOT: PSS/MXene composites were prepared via a

5   simple in situ polymerization process in/on $Ti_3C_2T_x$ MXene and subsequently utilized to fabricate

6   a gas sensor on a PI substrate. The synthesis involved adding EDOT to the appropriate amount of

7   $Ti_3C_2T_x$ MXene suspension, followed by the introduction of ammonium persulfate (APS) and

8   poly(4-styrene sulfonate) (PSS). The mixture was stirred for 24 hours at room temperature and

9   1000 rpm, producing a black PEDOT: PSS/MXene composite solution (Figure 13b). These

10   MXene-polymer nanocomposites are used to create wearable capacitive pressure sensors, with

11   $Ti_3C_2T_x$ MXene and poly(vinylidene fluoride-trifluoro ethylene) (PVDF-TrFE) as the dielectric

12   layer between PEDOT: PSS and polydimethylsiloxane electrodes, facilitating reliable human

13   physiological signal acquisition[261]. MXene powder in DMF was sonicated for 1 hour to form a

14   homogeneous suspension, mixed with PVDF-TrFE to create a solution with up to 13 wt % MXene,

15   and electro-spun into nanofibers. For the sensor, PDMS was spin-coated and cured on glass,

16   followed by PEDOT: PSS spin-coating and DMSO treatment. The PEDOT: PSS film was peeled

17   off, with CNS placed between two PEDOT: PSS layers, and carbon tape electrodes added (Figure

18   13c).

19   Self-healing sensors based on MXene-polymer nanocomposites have attracted significant attention

20   due to their unique capabilities in autonomously repairing damage and restoring functionality[266].

21   Polymers provide flexibility and conformability to MXene-based sensors, enabling their

22   integration into various form factors and substrates. These composites combine the exceptional

23   properties of MXene, such as high electrical conductivity and mechanical strength, with the self-

24   healing properties of polymers[267]. A study recently developed a conductive MXene nanocomposite

25   hydrogel with healable and degradable properties for advanced epidermal sensors[267]. The hydrogel

26   was created by combining MXene, poly(acrylic acid) (PAA), and amorphous calcium carbonate

27   (ACC). In the synthesis, PAA and calcium chloride were dissolved in water and stirred, followed

28   by the addition of an MXene solution. A carbonate solution was then added, forming the MXene-

29   PAA-ACC hydrogel. After formation, the hydrogel was washed thoroughly until the water was

30   clear.

31

Journal of Materials Chemistry A Accepted Manuscript
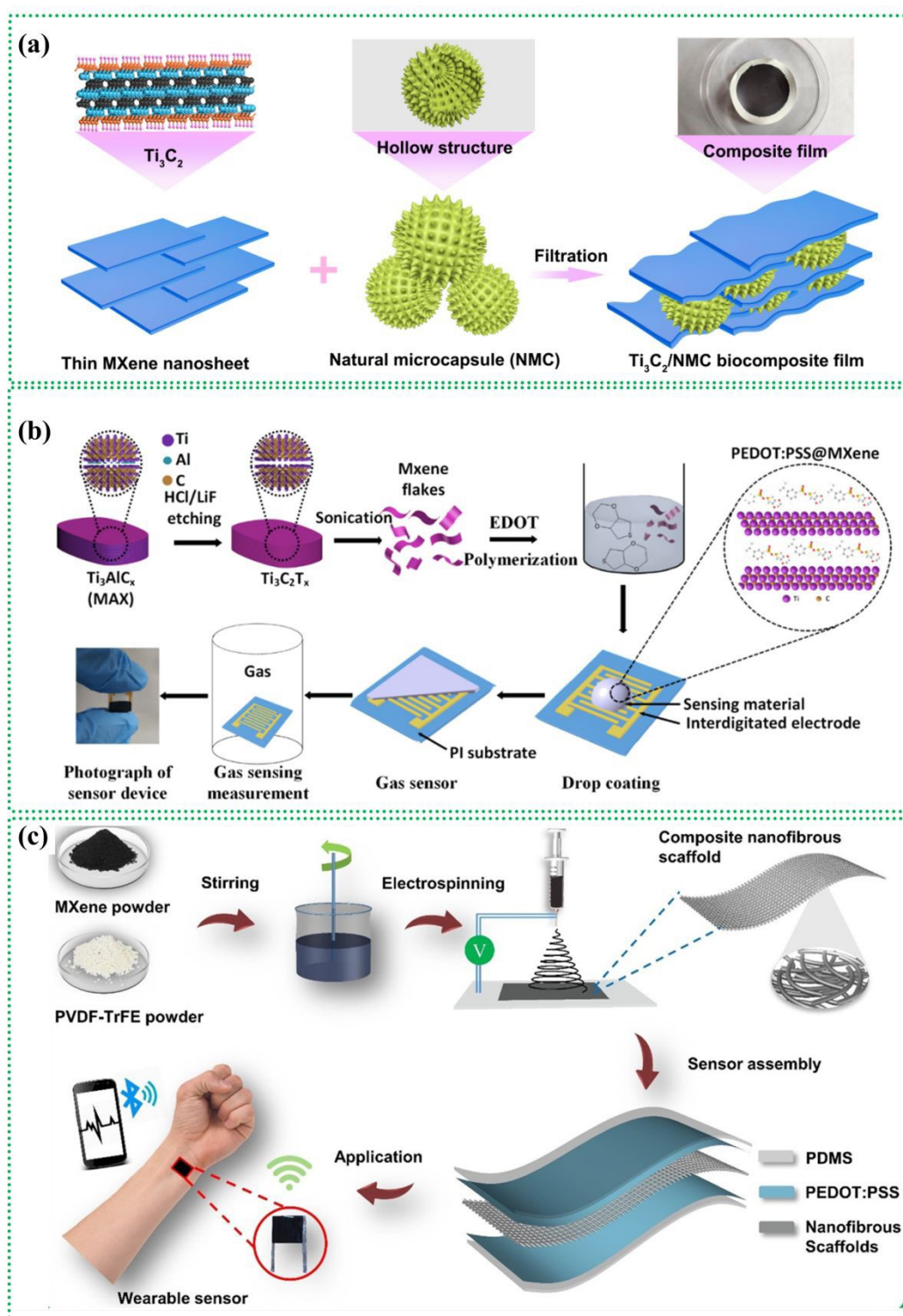
Figure 13. MXene-polymer nanocomposites-based sensors. (a) Schematic diagram illustrating the fabrication process of the Ti$_3$C$_2$/NMC bio-composite film. Reproduced with permission from ref.[262]. Copyright 2019, American Chemical Society. (b) The schematic illustration depicts the synthesis process of PEDOT: PSS/MXene composites and the subsequent fabrication process of the gas sensor based on these composites. Reproduced with permission from ref.[265]. Copyright 2020, American Chemical Society. (c) Schematic diagram illustrating the fabrication process of
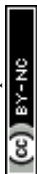
1   the composite nanofiber scaffolds (CNS)-based pressure sensor. Reproduced with permission from

2   ref.[261]. Copyright 2020, American Chemical Society.

3   Besides these, there are many other reports on MXene-polymer composites given in Table 6 with

4   diverse applications[32, 243, 260, 268].

5   Table 6. The comparison of several MXene-based composites as sensors.

6

| Sr.	Components	MXene contents (wt.%)	Fabrication technique	Structure type	Sensor type	Mechanical strength	Gauze factor	Ref.
1	$Ti_3C_2T_x$/PDMAEMA	78	Surface modification	Accordion	Temperature	-	-	[269]
2	$Ti_3C_2T_x$/Poly(N-isopropylacrylamide)/Polyacrylamide	-	In situ polymerization	Porous network	Temperature and Strain	0.4 MPa	-	[270]
3	$Ti_3C_2T_x$/PDADMA/BPEI	90.7	Physical mixing	Layer-by-layer	pH	-	116 kΩ pH^{-1}	[271]
4	$Ti_3C_2T_x$/PEDOT/PVDF	5	In situ polymerization	Sandwich	Pressure	-	0.51 kPA^{-1}	[261]
5	$Ti_3C_2T_x$/PVA/PDMS	0.2	Physical mixing	Sandwich	Pressure	-	1.5 kPA^{-1}	[272]
6	$Ti_3C_2T_x$/PVDF-TrFE	38	Physical mixing	Sandwich	Pressure	-	2213.68 kPa^{-1}	[273]
7	$Ti_3C_2T_x$/PDA/AgNWs	16.7	Physical mixing	Brick-and-mortar	strain	-	200	[274]
8	$Ti_3C_2T_x$/PVA/Poly(vinylpyrrolidone)	1	Physical mixing	Porous network	strain	300 kPa	19.18	[275]
9	$Ti_3C_2T_x$/Poly(acrylic acid)(PAA)/Amorphous calcium carbonate (ACC)	0.07	Physical mixing	Porous network	strain	180 kPA	10.79	[276]
10	$Ti_3C_2T_x$/PAA	2	Physical mixing	Porous network	strain	30 kPa	0	[277]

7

8

9

1 MXene-polymer composites can lead to the development of flexible electronic devices having

2 lightweight, flexible, and high-performance devices with enhanced mechanical properties, tailored

3 electrical conductivity, and improved protection against environmental factors[16, 59]. The

4 synergistic effects between MXenes and polymers can be used in next-generation flexible

5 electronic devices with diverse applications, including wearable electronics, flexible displays, EMI

6 shielding, conformable sensors, and piezoelectric applications [50, 60, 278, 279, 280, 281] . Zhang et al.

7 investigated a flexible MXene-decorated fabric (M-CF) featuring interwoven conductive

8 networks. The study explored the fabric's multifunctional capabilities, specifically focusing on

9 integrated Joule heating, electromagnetic interference shielding, and strain-sensing

10 performances[59]. By incorporating MXene into the fabric's structure, the researchers aimed to

11 enhance its electrical and thermal properties, making it a versatile material for various applications

12 related to heating, shielding, and sensing. After etching the MXene inks were uniformly sprayed

13 onto the surface of pretreated cotton fabrics (Figure 14a). To achieve different loading contents of

14 MXene on the fabric, they adjusted the spray-drying cycles. By varying the MXene content in the

15 cotton fabric, they aimed to optimize and find the most suitable MXene loading for achieving the

16 desired multifunctional applications like EMI shielding, Joule heating, sensing, etc. (Figure 14b).

17 The EMI shielding properties of the samples were studied within a frequency range of 8-12 GHz,

18 employing a waveguide method. The average EMI shielding effectiveness of the 2 wt% MXene-

19 based sample is ~25 dB, while for the 4 and 6 wt.%, it measured 33 and 36 dB, respectively. The

20 sensors based on 2 wt% MXene led to maximum resistance change under the same bending strain,

21 making the nanocomposite ideal for detecting small human activities. The optimized 2 wt.% M-

22 CF sensor maintained consistent resistance change for more than 5000 cycles of bending and

23 releasing. Attached to a finger, the MXene-based sensor consistently detected resistance changes

24 during bending movements and accurately recorded a pulse rate of 80 beats per minute.

25 Polymer lamination can effectively mitigate MXene oxidation as evidenced by their application in

26 various devices. Lee et al. demonstrated that laminating a thin poly(4-vinylphenol) (PVPh) layer

27 as a protective film on MXene (PL-MXene) protects it from the external environment[50]. This

28 combination was utilized for the electroluminescent (EL) display whose structure is demonstrated

29 in Figure 14(c). The relative luminance variance ($\Delta L/L_0$) of devices with PL-MXene and bare

30 MXene electrodes over time is shown in Figure 14(d). Besides these, there are many other reports
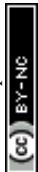
1   on the usage of MXene-polymers nanocomposites in the domain of flexible devices with a wide

2   variety of applications[244, 248, 256, 258, 279, 282, 283].

3   MXene-polymer nanocomposites are also studied for piezoelectric applications. Piezoelectric

4   sensors can transform the plentiful mechanical energy that surrounds us into electrical energy,

5   mechanical energy harvesters are seen to be one of the most appealing energy harvesting

6   technologies. Nevertheless, their poor electrical performance is preventing it from being used

7   practically. Because the electrical performance of the energy harvester may be enhanced by

8   harvesting the applied mechanical energy in two harvesters concurrently, hybridization of the two

9   distinct mechanical energy harvesters such as MXene and any other piezoelectric material may

10 offer a solution to this problem.

11 An overall schematic representation of the hybridization generator integrating MXene and barium

12 titanate as conductive fillers in the PDMS matrix (HG-MBP) is shown in Figure 14e [284]. The HG-

13 MBP was made of MXene/BaTiO$_3$, polyimide (PI), and aluminum (Al), as seen in Figure 14e.

14 The electrode, substrate, piezoelectric layer, and triboelectric layer are all PDMS (MBP) composite

15 films. As seen in the inset photographic image of Figure 14e, the superior flexibility of HG-MBP

16 was verified with a high bending angle using a bending test. This resulted from the intrinsic

17 property of the MBP composite film, which has a thickness of 125 ± 10 μm and contains 2D and

18 nano-scaled materials, such as MXene sheets and BaTiO$_3$ nanoparticles, inside the PDMS matrix

19 with high elasticity. Schematic of MXene is shown in Figure 14g (*i*). Additionally, an X-ray

20 diffraction (XRD) examination was performed to verify that MXene was successfully synthesized.

21 As shown in Figure 14g (*ii*). A high open-circuit voltage of 80 V, a short-circuit current of 14 μA,

22 and a power density of 13.5 W/m^2 were achieved after determining the ideal MXene concentration.

23 An example of this is the successful control of a 3D printer-modeled robot hand using the finger

24 joint motions of a real hand that has HG-MBPs attached. The k-mean clustering approach was also

25 used in the development of the object recognition system, which distinguishes between various

26 materials with a high classification accuracy of 93.33%. These findings demonstrate the great

27 potential of the suggested HG-MBP as a material detection sensor and human gesture manipulation

28 system, which is anticipated to be used as a next-generation e-skin in the human-machine interface.

29   MXene exhibits a better piezoelectric effect on poly(vinylidene fluoride-co-trifluoroethylene)

30 (PVDF-TrFE) compared to polyvinylidene fluoride (PVDF). Generally (beta-phase) β-phase in

31 PVDF crystals exhibit the best piezoelectric properties, although achieving this phase in PVDF is

1   still challenging [285] [286]. However, PVDF-TrFE inherently possesses a larger content of the

2   electroactive β-phase than PVDF due to its higher steric hindrance [287]. The incorporation of MXene

3   into PVDF-TrFE further promotes the nucleation of this phase, leading to improved piezoelectric

4   properties [288]. This enhancement is less significant in PVDF due to its lower initial β-phase content.

5   The dielectric constant is significantly increased, and dielectric loss is decreased in PVDF-TrFE

6   as a result of the interaction between the polymer matrix and the surface functional groups of

7   MXene. PVDF-TrFE/MXene composites exhibit enhanced mechanical flexibility and durability,

8   making them more suitable for applications in flexible electronics and wearable devices. Fatemeh

9   M. et al. [288] reported the fabrication of acoustic energy harvesters using electrospinning of the

10   piezoelectric polymer PVDF-TrFE onto fabric-based electrodes. The incorporation of $Ti_3C_2T_x$

11   MXene flakes effectively induced polarization locking within the electro-spun PVDF-TrFE,

12   optimizing its electromechanical performance. The resulting device was mechanically robust,

13   lightweight, and flexible, enabling efficient energy harvesting and sound detection within the 50

14   to 1000 Hz frequency range and at sound pressure levels between 60 and 95 dB. The device

15   demonstrated an impressive sensitivity of 37 VPa^{-1}, outperforming previous PVDF-based acoustic

16   harvesters. It achieved a peak output power of 19 mW/cm³ at 200 Hz and 95 dB. This advancement

17   highlights the potential of MXene-enhanced PVDF-TrFE composites in powering small electronic

18   devices, including implantable biomedical devices, smart wearables, and remote Internet-of-things

19   (IoT) systems. The comparison of PVDF/MXene and PVDF-TrFE/MXene composites is given in

20   Table 7. Numerous studies that reported the applications of PVDF-TrFE/MXene-based

21   piezoelectric nanogenerators can be found here [289] [290] [291] [292].

22

23

24

1   Table 7. The comparison of several MXene-based composites as piezoelectric nanogenerators.

| Components	MXene contents (wt.%)	Device dimensions	Source	Fabrication technique	Sensitivity	Power density	Ref.
$PVA/Ti_3C_2T_x$	-	8×8 mm^2	0.5 H	Electrospinning	-	42 mW m^{-2}	[293]
$Glycine/Nb_2CT_x$	-	100 mm^2	0.6 Hz, 10 N	Crystallization	5 pC N^{-1}	-	[294]
$PVDF/Ti_3C_2T_x$	-	1×1 cm^2	96.5 dB, 0.2 N	Crystallization	0.4 nA kPa^{-1}	-	[295]
$PVDF/Ti_3C_2T_x$	0.4wt.%	2.5 cm $\times$ 3.0 cm	1–3 Hz	Electrospinning	43 pCN^{-1}	-	[281]
$PVDF/Ti_3C_2T_x$	1.0 wt.%	2×20 mm	1–10^7 Hz	Microinjection Molding		18.9 µWcm^{-2}	[280]
$PVDF/Ti_3C_2T_x$	0.01-0.05 g/L	2 cm $\times$ 2 cm	4.7 N, 5 Hz	Spin- and spray-coating	-	14 µWcm^{-2}	[296]
$PVDF/Ti_3C_2T_x$	5-25 wt%	20 mm $\times$ 20 mm	1-8 Hz	Electrospinning	-	11.213 Wm^{-2}	[297]
$PVDF/CNT/Ti_3C_2T_x$	0.05-0.2 wt %	2×1.5 cm^2	1–500 MΩ	Electrospinning	-	18.08 W m^{-2}	[298]
$PVDF-TrFE/Ti_3C_2T_x$	0.05- 0.2 wt%	12.56 cm^2	200 Hz, 95 dB	Electrospinning	37 V Pa^{-1}	0.207 mWm^{-2}	[288]
$PVDF-TrFE/Ti_3C_2T_x$	0.02-0.5 wt.%	2.4 cm^2	5 kPa, 1 Hz	Printing	-52.0 pC N^{-1}	-	[299]
$PVDF-TrFE/Ti_3C_2T_x$	2.0 wt%	1×1 cm^2	20 N, 1 Hz	Electrospinning	-	3.64 mWm^{-2}	[285]
$PVDF-TrFE/Ti_3C_2T_x$	16% (w/v)	15×1.3 mm	7 N, 6 Hz	Electrospinning	-	4.02 W/m^2	[289]

2

3
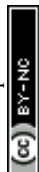
1
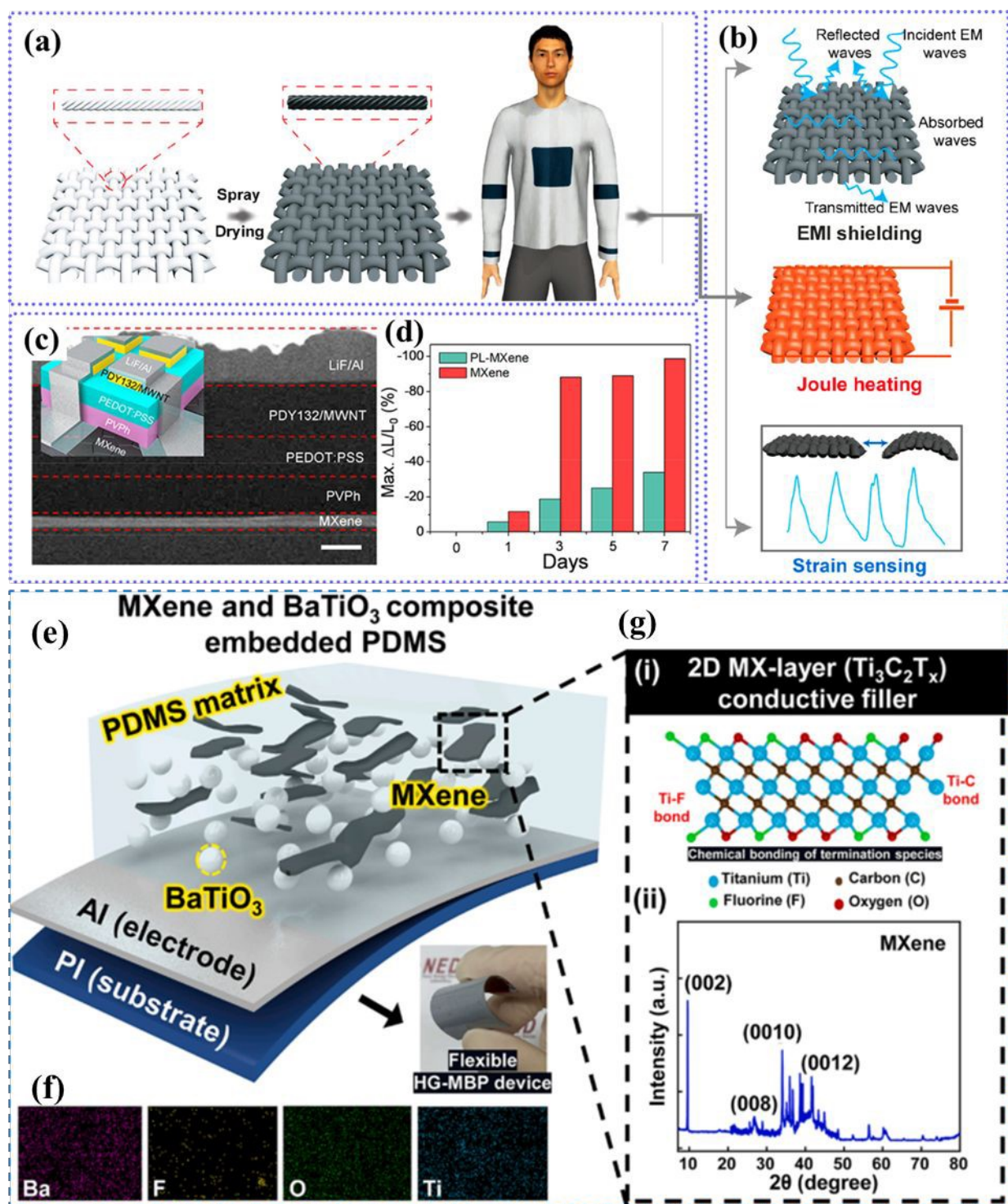
2

3

4   **Figure 14.** MXene-polymers nanocomposites in flexible electronics. (a). Multifunctional MXene-
5   decorated cotton woven fabrics fabricated by employing the spray-coating method, where the
6   MXene material is applied to the cotton woven fabric to impart its multifunctional properties like
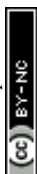
1 EMI shielding, Joule heating and strain sensing, etc. (b) Demonstration indicating the applications
2 of MXene coated flexible fabrics in different areas. Reproduced with permission from ref.[59].
3 Copyright 2020, American Chemical Society. (c) SEM image showing the cross-sectional view of
4 an organic AC-EL display with a PL-MXene electrode (scale bar: 50 nm). The inset provides a
5 schematic representation of the PL-MXene organic AC-EL display. (d) Maximum ΔL (luminance
6 change) to L_0 (initial luminance) ratio of bare MXene and PL-MXene organic AC-EL displays as
7 a function of air exposure duration (days). [50]. Copyright 2020, American Chemical Society. (e)
8 General schematic representation of the manufactured HG-MBP with the Al electrode connected
9 to the PI substrate spin-coated with MBP composite film. The inset graphic illustrates the
10 constructed HG-BMP's flexibility. (f) MXene and BaTiO3 particles implanted in the PDMS matrix
11 as shown in a cross-sectional EDX picture. (g) (*i*) MXene's schematic chemical bond structure and
12 (*ii*) XRD result [284].

13 Zhao and colleagues used rolling [281], hot pressing, and electrospinning techniques to create a high-

14 performance MXene/PVDF composite film with a β-phase of more than 95 weight percent. The

15 MXene/PVDF-based sensor showed exceptional voltage sensitivity, up to 0.0480 V N^{-1}. It is

16 important to remember that the MXene used in this work was generated via HF etching, which left

17 it with rich surface groups. The favorable impact may be primarily ascribed to the hydrogen

18 bonding interaction that favors all trans planar conformation (β-phase) during PVDF

19 crystallization and is brought about by the –OH groups of the MXene and F atoms of PVDF chains.

20 The directed distribution and regular stack of MXene flakes, which facilitated the transfer, storage,

21 and release of electric charge, were further examined by Han and colleagues [280]. Furthermore, this

22 paper mentioned the -F groups of the MXene with interfacial compatibility, which are typically

23 thought of as a type of significant surface group.

24 Even though adding MXenes to composites increases their piezoelectricity for improved sensing

25 properties, if the MXene level is over the percolation threshold, the composite's performance

26 drastically declines [300, 301]. This may be explained by the fact that when the amount of conductive

27 MXene is too high, many connections are created that degrade the performance. Increased MXene

28 content may result in additional β phases but a conductive route inside the composite. Additionally,

29 a lower MXene content results in fewer β phases. One important component for improving

30 performance is the percolation threshold. Li and colleagues used molecular dynamics to simulate

31 MXene/PVDF composite material systems with varying MXene levels based on the Forcite model

32 [302]. They then computed the free volume fraction (FFV) to demonstrate the impact of MXene

33 sheets. On the shape of the macromolecular chain. The space between molecules is known as free

34 volume. When a suitable quantity of MXene sheets was introduced into the PVDF polymer system,

1 the polymer system's FFV dropped to its lowest value, indicating that there was less room for

2 macromolecular chains to move. Additionally, the optimized sensor demonstrated a sensitivity of

3 up to 55.42 mV kPa^{-1}.

4 Due to their varied inherent characteristics, MXenes give composite materials new functions in

5 addition to improving piezoelectric performance. In addition to their electrical benefits, MXenes

6 are biocompatible, which makes them appropriate for a range of biomedical applications [303, 304, 304].

7 MXene-based composites can be employed safely in settings that call for interactions with

8 biological systems thanks to their biocompatibility. MXenes is a promising material for advanced

9 composite technologies because of its improved piezoelectricity and bio-friendly qualities, which

10 help to close the gap between high-performance materials environmentally, and biologically

11 compatible solutions. By using MXenes' high electrical conductivity to increase electron transfer

12 rates, Fu and colleagues were able to generate and transport electrical charges under mechanical

13 stress, improving the piezoelectric response [305]. Furthermore, the composite's MXenes not only

14 generated sufficient heat to eradicate bacteria while simultaneously producing singlet oxygen,

15 which may also have a highly effective sterilizing effect. This suggests that it has a lot of promises

16 for use in biomedical and self-powered body monitoring applications. Comparison of several

17 MXene-polymer composites in field of piezoelectric nanogenerators is given in Table 7.

18 **7.3 MXene-polymer nanocomposites in 3D/4D printing**

19 MXene polymer composites offer great promise for 3D/4D printing applications, integrating

20 MXene's exceptional properties of high electrical conductivity and mechanical strength with the

21 versatility and tunability of polymers [26, 64, 306]. Enabled by 3D/4D printing technology, these

22 composites showcase dynamic and shape-changing capabilities in response to external stimuli,

23 paving the way for advanced engineering and smart applications [307, 308].

24 The programmable micro-supercapacitors can be developed using 3D printing of composite ink

25 consisting of PEDOT: PSS/MXene/ethylene glycols (PME)[26]. In Figure 15a, the design and

26 preparation procedure of 3D printed PME gel composites for micro-supercapacitors is illustrated.

27 By mixing MXene and ethylene glycol (EG), and PEDOT: PSS solution an ink was prepared.

28 During the fabrication process, the ink was transferred to a syringe and extruded under pressure

29 through a needle to construct thick interdigitated electrodes for the MSCs. To achieve controlled

30 solidification and form a 3D highly interconnected framework, a freezing technology utilizing a

1 cold plate was applied during the printing process. In this process PEDOT: PSS (Figure 15b) plays

2 a significant role, and by appropriately bridging the PEDOT structures an integrated porous

3 structure is created for the optimization of ion/electron transport kinetics in the fabricated gel

4 (Figure 15c).

5 In addition to the development of 3D printing, the development of 4D printed hydrogels using

6 MXene and PEDOT: PSS, showcasing high-efficiency pseudocapacitive energy storage

7 capabilities[309].
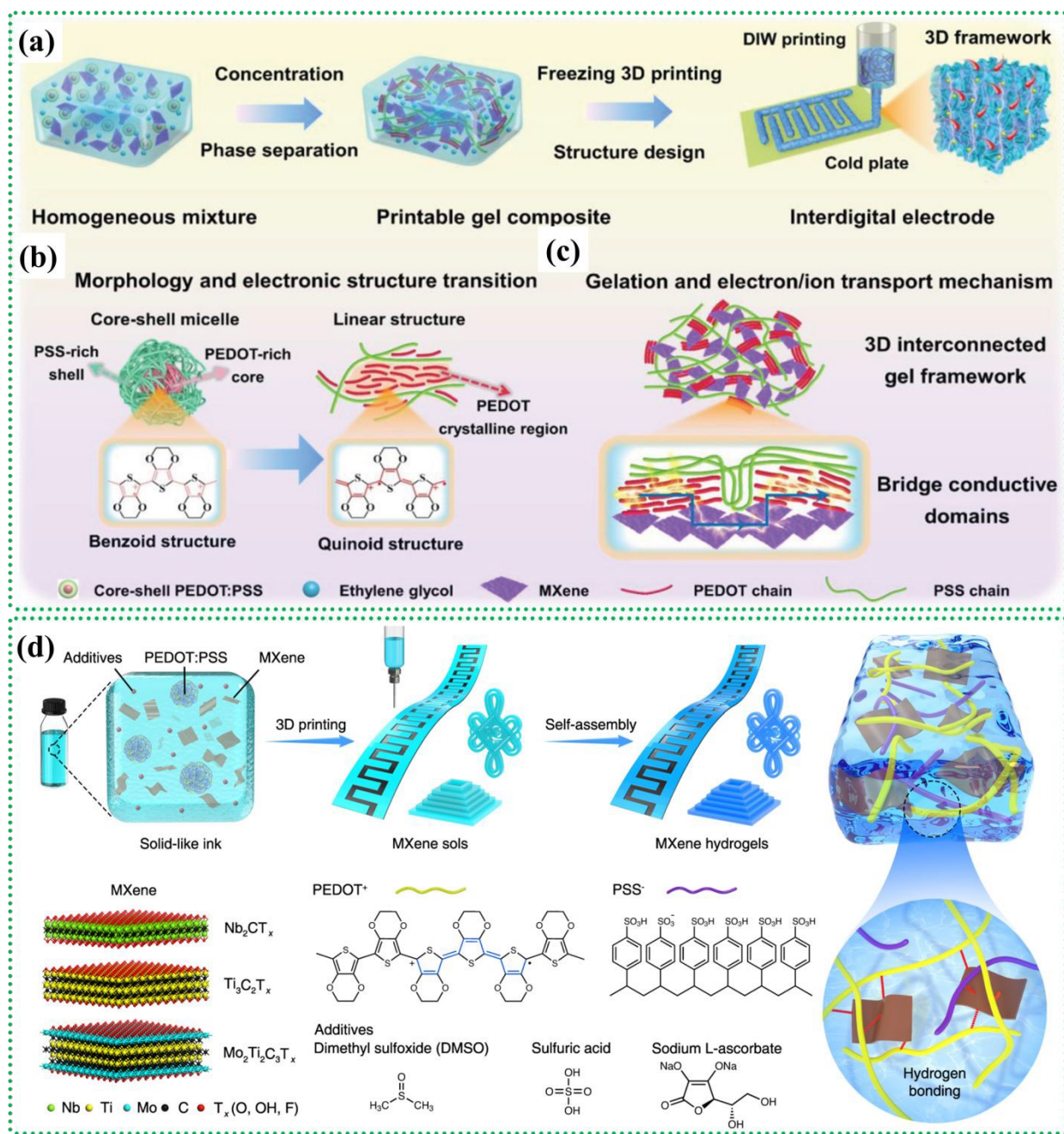
Figure 15. 3D/4D printing applications. (a) The preparation of the 3D printable PME gel composite inks and interdigital electrodes is depicted in a schematic illustration. (b) The morphology and electronic structure transition of PEDOT:PSS within the PME gel composites is shown. (c) A schematic illustration illustrates the gelation process and the mechanism for enhancing electron/ion transport in the PME gel composites. Reproduced with permission from ref.[26]. Copyright 2023, Wiley. (d) Composite inks comprising MXenes, PEDOT: PSS, and additives are utilized for 3D printing designed patterns. Through a self-assembly process, these inks transform into MXene hydrogels[309].

1 MXene hydrogels were prepared via self-assembly by mixing $Ti_3C_2T_x$ MXene suspension with

2 PEDOT suspension, followed by sonication. A solution containing DMSO, sulfuric acid, sodium

3 L-ascorbate, and deionized water was added and stirred. The mixture was then poured into molds

4 and heated to form Ti3C2Tx MXene hydrogels. These hydrogels were further treated with sulfuric

5 acid to improve mechanical strength and washed to remove impurities. The optimization involved

6 adjusting MXene content, DMSO volume, sulfuric acid concentration, and sodium L-ascorbate

7 ratio. The method offers numerous advantages, especially its remarkable versatility and feasibility

8 in synthesizing various MXenes such as Nb_2CT_x, $Ti_3C_2T_x$, and $Mo_2Ti_2C_3T_x$.

9 An approach to 3D printing using MXene and poly(vinyl alcohol) (PVA) composites using

10 MXene-surfactant ink has also been proposed for energy storage applications. Through the

11 controlled deposition of highly conductive MXene particles onto a PVA matrix, the fabricated

12 sample exhibited conductive behavior[63]. In a separate study, Li et al. demonstrated the production

13 of elastic nanocomposites by encapsulating 3-(trimethoxysilyl)propyl methacrylate-modified

14 MXene nanosheets within a photocurable polyurethane acrylate resin (PAR) matrix using digital

15 light processing 3D printing. By adjusting the MXene content in the PAR, the mechanical

16 properties of the elastomers were tailored. The resulting MXene-PAR nanocomposites, containing

17 0.1% w/w fillers, exhibited remarkable tensile strength and elongation at a break of 23.3 MPa and

18 404.3%, respectively, representing a significant increase of 100.8% and 37.8%, compared to the

19 control[310]. Some other reports on MXene-polymer composites in 3D/4D printing are also available

20 in the literature[307, 311].

21 **7.4 MXene-polymer nanocomposites in EMI shielding**

22 EMI shielding is the most explored area among the applications of MXene-polymer

23 nanocomposites. These composites offer several advantages in the field of EMI shielding [312, 313].

24 MXene-polymer composites exhibit lightweight, conductivity, and improved mechanical

25 properties making them highly suitable for EMI shielding applications[313, 314]. Polymers provide

26 the advantage of tunability in MXene-polymer composites, allowing the customization of EMI

27 shielding performance for specific applications or requirements[29, 313]. By selecting appropriate

28 polymers with specific dielectric properties, the composite's overall electrical conductivity and

29 impedance matching can be tailored to provide optimal shielding performance within desired

30 frequency ranges[29, 204]. Polymers in MXene-polymer composites provide chemical resistance and

1 durability, enhancing the longevity and performance of EMI shielding materials. The polymer

2 matrix acts as a protective layer, shielding the MXene flakes from environmental factors such as

3 moisture, chemicals, or oxidation[315].

4 Different structures of MXene/polymer composites offer distinct mechanisms for EMI shielding

5 depending on various factors[315]. In multilayer MXene/polymer composites, multiple MXene layers

6 are stacked within the polymer matrix (Figure 16a). The interlayer spacing and alignment influence

7 the EMI shielding. Electromagnetic waves penetrate the composite and get reflected or scattered

8 at the interfaces between the MXene layers and the polymer. This multiple reflection and scattering

9 lead to effective EMI attenuation. Porous MXene/polymer composites have voids or pores within

10 the material (Figure 16b). These voids can trap and dissipate electromagnetic waves, reducing their

11 propagation. The interconnected porous network of MXene also enhances the electrical

12 conductivity, further improving the EMI shielding efficiency. In segregated MXene/polymer

13 composites, MXene and polymer phases exist as distinct domains within the material (16c). The

14 MXene domains act as conductive pathways, while the polymer regions provide structural support.

15 This phase separation enhances electrical conductivity and enables effective EMI shielding by

16 creating a conductive network to dissipate electromagnetic energy. Some MXene/polymer

17 composites include magnetic particles or other conductive additives (Figure 16d). MXene/polymer

18 composites with conductive and magnetic fillers show excellent EMI-shielding performance. The

19 conductive network inculcates an impedance mismatch at the composite/air interface, leading to a

20 high reflection. Magnetic materials enhance impedance matching at the conductive filler/air

21 interface, increasing EMW absorption. These additives enhance the electromagnetic absorption

22 and scattering properties of the composite.

23 To address the challenges posed by harsh freezing and high-humidity environments for polymeric

24 EMI shielding materials, Chang et al. developed ultrathin, flexible MXene/Ag nanowires/PEDOT:

25 PSS composite coatings[316]. Fabricated via drop-casting and hydrophobic spraying, these coatings

26 achieve an EMI shielding effectiveness of 31.5 dB at ~10 μm thickness. These nanocomposite

27 coatings also offer excellent electro/photo-thermal properties, water repellency, interfacial

28 adhesion, and mechanical durability, making them suitable for cold and damp conditions. The

29 shielding mechanism of the MXene/AgNWs/PEDOT: PSS coating is shown in Figure 16(e).
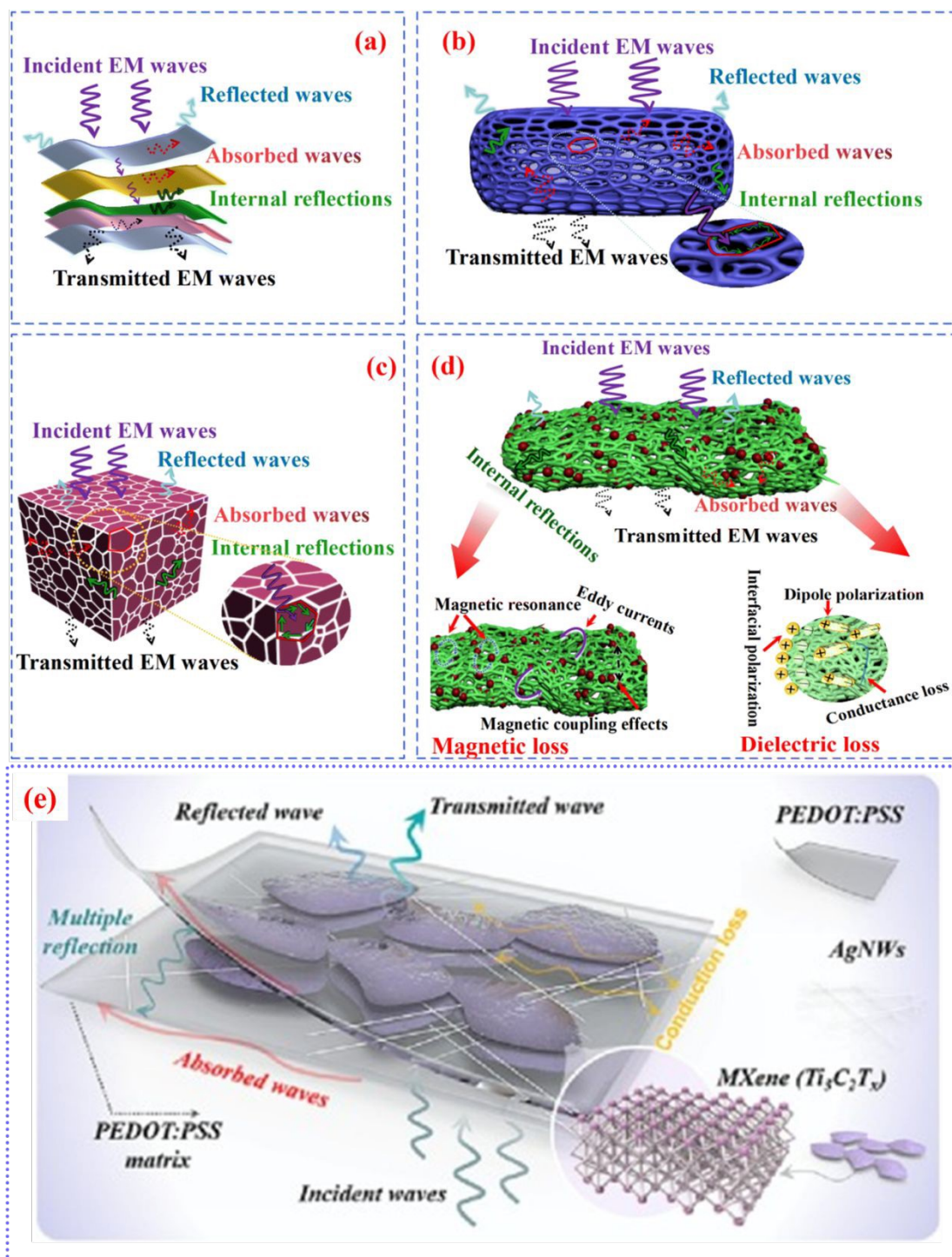
Figure 16. EMI shielding mechanisms vary among different structures of MXene/polymer composites. (a) Multiple MXene layers lead to reflection and scattering, effectively attenuating EMI. (b) The interconnected MXene network and voids trap and dissipate electromagnetic waves, reducing their propagation. (c) Separate MXene and polymer domains create conductive pathways, ensuring efficient EMI shielding. (d) The inclusion of magnetic or conductive fillers enhances impedance matching, improving EMI absorption[315]. (e) Diagram depicting electromagnetic

1 microwave dissipation in the MXene/AgNW/PEDOT:PSS coating. Reproduced with permission
2 from ref.[316]. Copyright 2023, Elsevier Ltd.

3 As an electromagnetic wave strikes the MXene/AgNWs/PEDOT: PSS coating, most of it reflects

4 due to impedance mismatch. The penetrating portion interacts with dense charge carriers, leading

5 to significant polarization and conduction losses. The 1D AgNWs bridge the gaps between MXene

6 nanosheets, creating conduction networks that enhance electron hopping and migration, thus

7 increasing conduction losses. Additionally, the lamellar microstructures cause the wave to bounce

8 between MXene layers, further dissipating energy due to impedance mismatch at the PEDOT:

9 PSS/MXene interfaces.

10 In a recent study, $Ti_3C_2T_x$ MXene composite films were developed for efficient EMI shielding,

11 featuring photothermal healing, stretchability, and high conductivity[211]. By increasing the MXene

12 content in the waterborne polyurethane (WPU), natural rubber, and MXene-based composite

13 (WNM) composite films the conductivity increased sharply which led to the high EMI shielding

14 for WNM composite exhibiting the EMI shielding efficiency (SE) of 76.1 dB at a thickness of 336

15 $\pm$ 15 μm for X-band, whereas, for Ku-band the EMI SE value is ~80 dB. The EMI shielding

16 mechanism in the composite films is based on induced polarization due to the MXene functional

17 groups. The local dipoles between Ti and surface groups (-F and -OH), especially -F on MXene

18 surfaces, induce dipole polarization, leading to attenuation of penetrated EMWs through interfacial

19 polarization loss. Additionally, polarized interfaces between the honeycomb-like MXene network

20 and the polymeric matrix enhance polarization loss, further improving EMI shielding performance.

21 The honeycomb-like MXene network structure contributes to the exceptional EMI shielding

22 performance of the WNM films across a wide frequency range.

23 These advantages of MXene-polymer composites in EMI shielding make them highly attractive

24 for various industries, including flexible electronics[317], telecommunications[318], aerospace[319],

25 where effective protection against electromagnetic interference is crucial[320]. The synergistic

26 effects between MXenes and polymers enable the development of lightweight, flexible, and high-

27 performance EMI shielding materials with improved properties and capabilities.

28 **7.5 MXene-polymers nanocomposites for anti-corrosion applications**

29 The exceptional characteristics of $Ti_3C_2T_x$, such as its unique layered structure and large specific

30 surface area, along with remarkable electrical and mechanical properties, make it highly promising

1 for anti-corrosion applications[66, 321, 322]. To utilize the inherent anticorrosion properties of pristine

2 $Ti_3C_2T_x$ nanosheets these were incorporated in the form of single- to few-layer Ti3C2Tx

3 nanosheets into a waterborne epoxy coating (WEC) through a simple physical mixing. Zhang et

4 al. conducted a study on the surface functionalization of $Ti_3C_2T_x$ and its application in aqueous

5 polymer nanocomposites to enhance corrosion protection[322]. In this approach, they utilized [3-(2-

6 Aminoethyl) aminopropyl] trimethoxy silane (AEAPTES), a silane coupling agent, to modify the

7 $Ti_3C_2T_x$ MXene. This modification aimed at adjusting the wettability of $Ti_3C_2T_x$ to improve its

8 compatibility with the polymer matrix in the nanocomposites.

9 In another study, a few-layer amino-functionalized $Ti_3C_2T_x$ nanosheets (k-Ti_3C_2) were combined

10 with an interpenetrating polymer network (IPN) to create k- Ti_3C_2/IPN composite coatings and

11 examined the tribological characteristics of these coatings[323] (Figure 16a). The wear rates of the

12 k- Ti_3C_2-0.75 (0.75 wt.% amino functional $Ti_3C_2T_x$) composite coating decreased by 82.41%

13 before UV aging and 74.55% after UV aging, compared to the pure IPN coating, under dry friction

14 conditions. Additionally, during the tribo-corrosion test in a 3.5 wt% NaCl solution, the k- Ti_3C_2-

15 0.75 composite coating exhibited the highest open circuit potential (OCP) and the lowest

16 coefficient of friction (COF) among all coatings, both before and after UV aging.

17 In a recent study, the anticorrosion and anti-wear behavior of an inorganic-organic multilayer

18 protection system consisting of an epoxy coating incorporating $Ti_3C_2T_x$ MXene. The researchers

19 designed and prepared this protective system to enhance its effectiveness against corrosion and

20 wear[66]. The hydrophilic nature of $Ti_3C_2T_x$ allowed it to maintain stable dispersions within the

21 epoxy matrix. This characteristic played a vital role in creating an effective physical barrier for

22 anti-corrosion purposes. The Ti_3C_2/epoxy coatings with different Ti_3C_2 content (0.5, 1, and 2 wt.

23 % $Ti_3C_2T_x$/epoxy) were obtained via the curing reaction of epoxy resin with an amine curing agent

24 (Figure 17a). The mechanism of protection from corrosion with Ti_3C_2 content was proposed as

25 demonstrated in Figure 17b-c. With no MXene content the corrosion probability is high and as the

26 MXene content is increased the corrosion inhibition efficiency increases. But as the Ti_3C_2 content

27 was raised to 2.0 wt. %, irregular corrosion particles began to accumulate once more and corrosion

28 inhibition efficiency decreased. This indicates that beyond the optimal content, MXene tends to

29 agglomerate, adversely impacting the anti-corrosion performance. Hence, Ti_3C_2 nanosheets can

30 effectively enhance the corrosion resistance of the coatings, but only when added in the optimal

1   amount. The Tafel plots display the corrosion behavior of the uncoated Q345 sample (polished

2   steel), pure epoxy, and $Ti_3C_2T_x$ /epoxy composites with different $Ti_3C_2T_x$ ratios (Figure 17d).
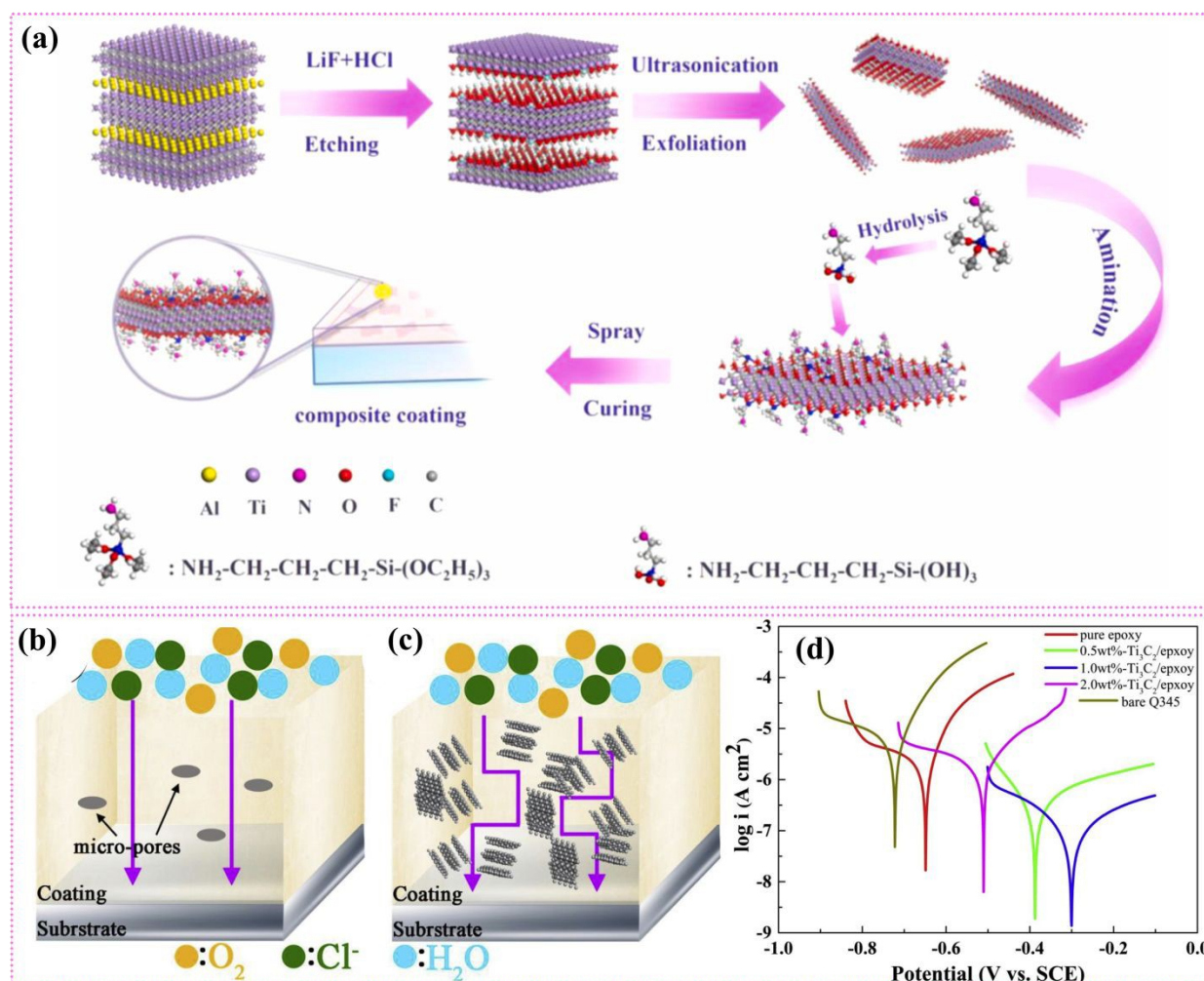
3

4   **Figure 17.** The anti-corrosion performance of MXene-polymer composites. (a) Synthesis of k-
5   Ti_3C_2/IPN coatings. Reproduced with permission from ref.[323]. Copyright 2021, Elsevier Ltd.
6   Schematic representation of the corrosion process in two scenarios: (b) Without Ti_3C_2 contained
7   epoxy coating and (c) With Ti_3C_2 contained epoxy coating. (d) Tafel plots of the samples immersed
8   in 3.5% NaCl for 96 hours. Among the uncoated and coated samples, the 1 wt. %-coated sample
9   exhibited the most superior protection. This was evident from the substantial positive shift in
10   potential value (E_{corr}) and the lowest corrosion current (I_{corr}). The potential was measured relative
11   to the saturated calomel electrode, utilized as the reference electrode. Reproduced with permission
12   from ref.[66]. Copyright 2019, Elsevier Ltd.

13   Following a 96-hour immersion in a 3.5% NaCl solution, it was observed that the $Ti_3C_2T_x$ provided

14   enhanced corrosion protection on the steel substrates compared to pure epoxy coatings. This

15   improvement in anti-corrosion properties was attributed to MXene flakes in an optimized

16   concentration, acting as thin film barriers that hindered the diffusion of electrolytes and provided

1 effective corrosion protection to the substrate. The anti-corrosion performance can also be

2 achieved through well-dispersed MXene-polymer composite coatings, made possible by covalent

3 modification and ambient electron-beam curing[241].

4 **7.6 MXene-polymers nanocomposites in biomedical applications**

5 Polymer-functionalized MXenes exhibit exceptional properties that make them highly valuable for

6 various applications in the medical sector. The big advantage is that the polymers have better

7 compatibility, hence these nanocomposites can also be applied to numerous biomedical

8 applications[282, 324]. The applications include antimicrobial treatments, photothermal therapy (PTT),

9 drug delivery systems, diagnostic imaging techniques, biosensors, and bone regeneration

10 processes. MXene polymer nanocomposites have shown great promise in biomedical applications.

11 These nanocomposites combine the unique properties of MXene materials, such as excellent

12 conductivity, high surface area, and antibacterial activity, with the versatility and biocompatibility

13 of polymers. They hold potential for various biomedical uses, including tissue engineering[237, 325],

14 cancer therapy[326, 327, 328], drug delivery systems[207, 329], biosensors[330], and antimicrobial coatings[331,

15 332]. MXene polymer nanocomposites offer exciting opportunities for advancing medical

16 technologies and improving healthcare outcomes.

17 **7.6.1 Antimicrobial applications**

18 The hydrophilic nature and anionic surface properties of MXenes enhance their interaction with

19 bacterial cell membranes. Through hydrogen bonding, the functional groups of MXenes interact

20 with lipopolysaccharide molecules on the cell membrane, leading to cell inactivation. This

21 interaction hinders nutrient intake, effectively inhibiting bacterial growth. Additionally, the

22 formation of a conductive bridge over the lipid bilayer facilitates the transfer of reactive electrons

23 from the bacterial cell to the external environment, ultimately causing cell death[74, 75]. The

24 application of $Ti_3C_2T_x$, a high aspect ratio material, as a coating on PVDF membranes resulted in

25 notable improvements in hydrophilicity, as evidenced by a reduced contact angle of 37°.

26 Additionally, the presence of large pores in the membrane was mitigated. As a result, the viability

27 and growth of E. coli (Gram-negative bacteria) were reduced by approximately 73%, while B.

28 subtilis (Gram-positive bacteria) experienced a growth inhibition of around 67%[74].

29 A study on the tunable antibacterial activity of a polypropylene (PP) fabric coated with $Ti_3C_2T_x$

30 MXene flakes, coupling the nano-blade effect with reactive oxygen species (ROS) generation was
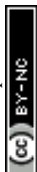
1 conducted[75]. In this study, an antibacterial medical fabric using a straightforward self-assembly

2 process was developed, wherein delaminated $Ti_3C_2T_x$ MXene flakes were arranged on the surface

3 of PP fibers (Figure 18a). By varying the amount of MXene in the coating solution from 1 to 32

4 mg/mL, they achieved edge-on assembly of MXene flakes on the PP surface, allowing the

5 monitoring of band gap evolution for a restacked structure. Characterization of the PP/$Ti_3C_2T_x$

6 nanocomposite revealed highly effective antibacterial properties, a robust coating, and excellent

7 chemical/thermal stability. In-vitro microbiological studies against both Gram-positive

8 Staphylococcus aureus as well as Gram-negative Escherichia coli demonstrated that PP/$Ti_3C_2T_x$

9 reduced bacterial viability up to 100%. This effect was attributed to a synergistic combination of

10 physical contact causing membrane stress and light-induced ROS generation. The antibacterial

11 mechanism in PP/ $Ti_3C_2T_x$ fabrics involved synergistic membrane stress mediated by the physical

12 contact of sharp edges (nano-blade effect) of MXene flakes, along with the generation of ROS

13 (Figure 18b). Before this, $Ti_3C_2T_x$ MXene exhibited antibacterial properties. Rasool et al.

14 investigated $Ti_3C_2T_x$ against E. coli and B. subtilis using bacterial growth curves and agar plates[74].

15 $Ti_3C_2T_x$ showed higher antibacterial efficiency against both E. coli and B. subtilis compared to

16 graphene oxide. The concentration-dependent antibacterial activities of $Ti_3C_2T_x$ in aqueous

17 suspensions (Figure 18c). The top frame (Right side-top, Figure 18c (A-F)) shows photographs of

18 agar plates where after a 4-hour treatment, the E. coli bacterial cells were subjected to recultivation

19 with different concentrations of $Ti_3C_2T_x$: 0 μg/mL (A), 10 μg/mL (B), 20 μg/mL (C), 50 μg/mL

20 (D), 100 μg/mL (E), and 200 μg/mL (F). The bottom frame (Right side-down, Figure 18c(A-F))

21 shows photographs of agar plates with B. subtilis bacterial cells treated similarly. At a

22 concentration of 200 μg/mL, $Ti_3C_2T_x$ resulted in over 98% bacterial cell viability loss within 4

23 hours of exposure, as validated by regrowth curve analysis and colony forming unit (CFU).

24 Electron microscopic analysis and lactate dehydrogenase (LDH) release assay revealed damage to

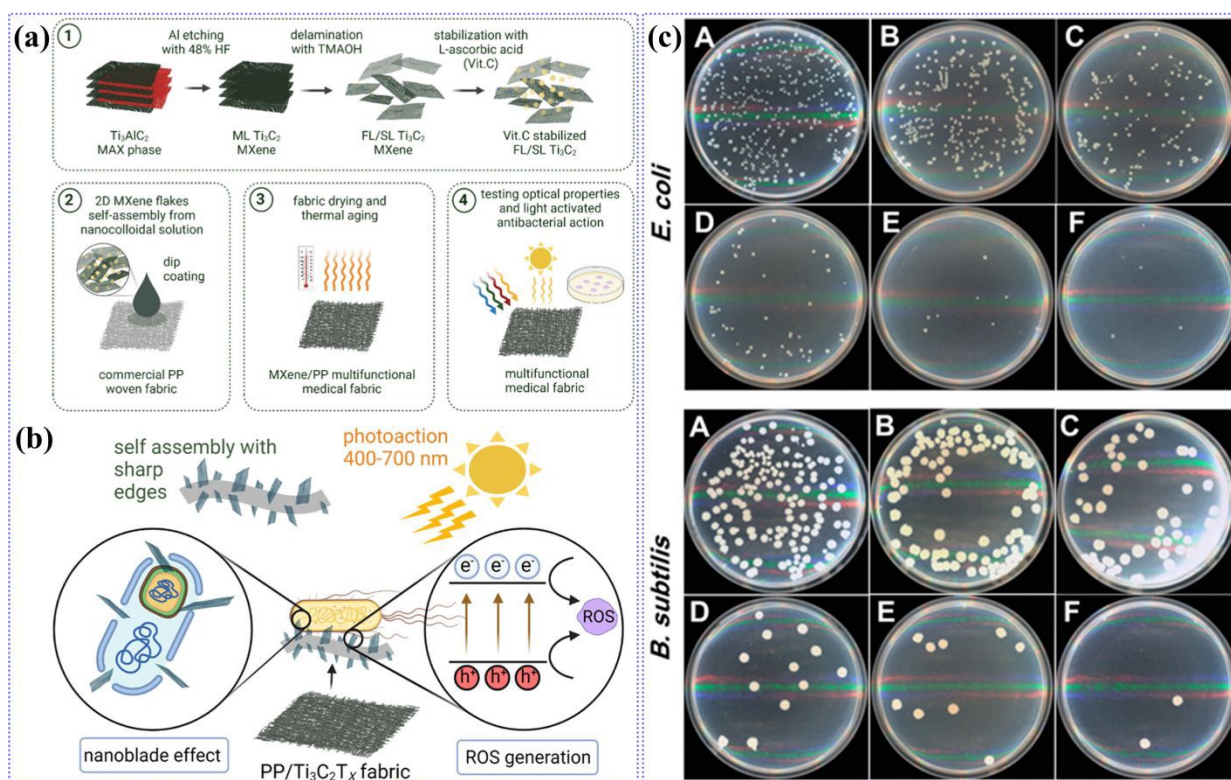25 the cell membrane, leading to the release of cytoplasmic materials.

26

Figure 18. Antibacterial activity of MXene-polymer nanocomposites. (a) Illustration showing a facile approach to obtain $Ti_3C_2T_x$-modified PP medical fabrics (PP/$Ti_3C_2T_x$ nanocomposites) with exceptional antibacterial properties, adjustable optical characteristics, and impressive thermal and chemical stability. (b) Schematic diagram showcasing the antibacterial activity in PP/$Ti_3C_2T_x$ nanocomposites, highlighting the synergistic effect of the physical nano blade action and the generation of reactive oxygen species. Reproduced with permission from ref.[75]. Copyright 2022, American Chemical Society. (c) Concentration-dependent antibacterial activities of $Ti_3C_2T_x$ in aqueous suspensions. The top frame (Right side-top, Figure A-F) shows photographs of agar plates where after a 4-hour treatment, the E. coli bacterial cells were subjected to recultivation with different concentrations of $Ti_3C_2T_x$: 0 µg/mL (A), 10 µg/mL (B), 20 µg/mL (C), 50 µg/mL (D), 100 µg/mL (E), and 200 µg/mL (F). The bottom frame (Right side-bottom, Figure A-F) displays photographs of agar plates with B. subtilis bacterial cells treated similarly. The study utilized bacterial suspensions in deionized water as a control, without the presence of $Ti_3C_2T_x$ MXene. Reproduced with permission from ref.[74]. Copyright 2016, American Chemical Society.

MXenes can be utilized for their antibacterial properties, as shown in a study where micrometer-thick $Ti_3C_2T_x$ MXene membranes were prepared by filtration onto a polyvinylidene fluoride (PVDF) support. [333]. To assess their bactericidal effects, the modified $Ti_3C_2T_x$ membranes were tested against E. coli and B. subtilis using two methods: bacterial growth on the membrane surface and exposure of the membrane to bacterial suspensions. The results showed that the fresh $Ti_3C_2T_x$ MXene membranes exhibited an antibacterial rate of over 67% against E. coli and 73% against B. subtilis, compared to the control PVDF membrane, under the same conditions. Interestingly, the

1   aged $Ti_3C_2T_x$ membrane displayed even higher efficacy, with over 99% growth inhibition observed

2   for both bacterial strains.

3   **7.7.2 Drug delivery and photothermal therapy**

4   MXene-polymer nanocomposites have promising applications in drug delivery, anticancer,

5   antibacterial biofilms, etc.[332, 334] Rabiee et al. developed an innovative nanocarrier using inorganic

6   MXene/MOF-5 (metal-organic frameworks) nanostructures for co-delivery of the drug

7   doxorubicin (DOX) and gene pCRISPR[335]. This study presents a nanocarrier approach for efficient

8   co-delivery of drugs and genes for biomedical applications. To enhance bioavailability and

9   interaction with pCRISPR, the nanomaterial was coated with alginate and chitosan. The polymer-

10   coated nano-systems doxorubicin delivery and cytotoxicity were evaluated on HEK-293, PC_{12},

11    $HepG_2$, and HeLa cell lines. The chitosan-coated nanocarriers demonstrated superior cell viability,

12   with over 60% relative cell viability in all tested cell lines. The alginate-coated nanocarriers ranked

13   second, showing more than 50% relative cell viability across all cell lines. The cytotoxicity was

14   dose-dependent, with longer treatment times leading to reduced cell viability. The nanocarriers

15   were modified to become suitable, stimuli-responsive, and equipped with a capping agent. To

16   achieve this, chitosan and alginate were used to modify the nanocarriers (Figure 19a). Polymer

17   solutions of alginate and chitosan were prepared and reacted in the dark for 7 hours. The resulting

18   suspensions were mixed with drug-free (MXene/MOF-5) and drug-loaded (MXene/MOF-5-DOX)

19   nanocarriers for 6 hours at room temperature. After 24 hours on various cell lines, MXene/MOF-

20   5 showed cell viabilities of 38.7%-14.3% at 0.1 μg/mL and 27.6%-9.9% at 10 μg/mL, with a drug

21   payload efficiency of 35.7%. Chitosan-based nanocarriers achieved a green fluorescent protein

22   (GFP)-positive efficiency of 25.8% in gene delivery studies. Yang et al. developed a clinical

23   implant based on Nb_2C MXene/titanium plate ($Nb_2C@TP$) for bacterial infection removal and for

24   regeneration of tissues[336]. This implant offers practical multimodal anti-infection functions. The

25   Nb_2C nanosheets (NSs) were decorated onto amidated TPs (TPs-NH_2) via electrostatic

26   interactions, resulting in the formation of $Nb_2C@TP$. The $Nb_2C@TP$ plays a crucial role in

27   suppressing bacteria through multiple modes (Figure 19b). When bacteria attempt to attack the

28   implant surface, $Nb_2C@TP$ activates the accessory gene regulator (Agr), which prevents bacterial

29   adherence and promotes biofilm detachment. $Nb_2C@TP$ directly induces bacterial death by

30   regulating the essential metabolic pathways such as the tricarboxylic acid (TCA) cycle and the

1 phosphotransferase system (PTS) pathway. These combined mechanisms effectively combat

2 bacterial infection.

3 Researchers have created a biodegradable nanocomposite micellar hydrogel delivery system with

4 unique functionalities of NIR-II photothermal ablation and vascular disruption, enabling

5 minimally invasive antitumor therapy using $Ti_3C_2T_x$ and poly(d,l-lactide)-poly(ethylene glycol)-

6 poly(d,l-lactide) (PDLLA-PEG-PDLLA, PLEL) triblock copolymer micelle[337]. Ti_3C_2 and CA4

7 (natural polymer) were selected as the photothermal therapy (PTT) agent and vascular disrupting

8 agent (VDA), respectively, for the development of the nanocomposite micellar hydrogel with dual

9 functionalities in minimally invasive antitumor therapy (Figure 19c).
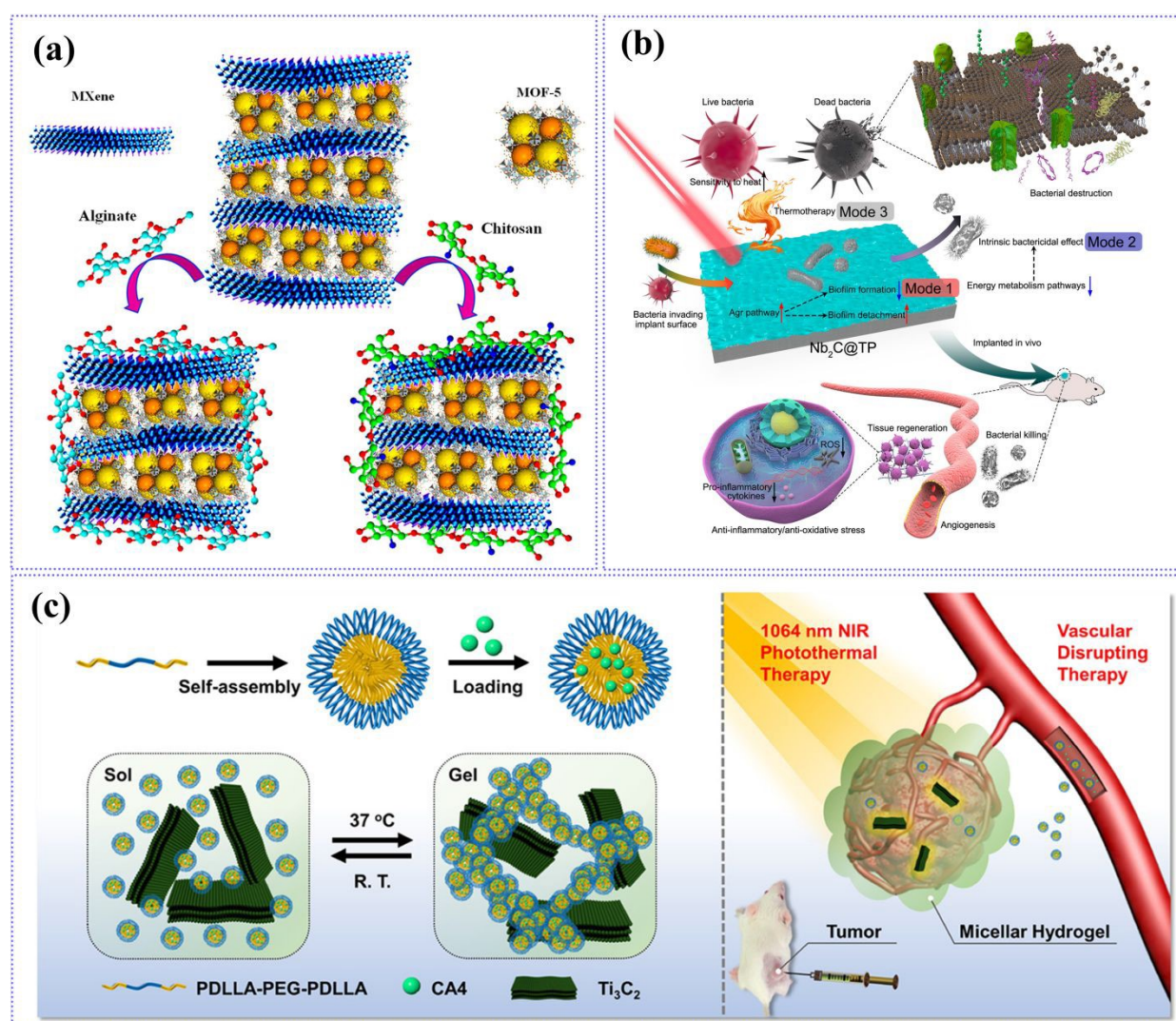
10

11 **Figure 19.** Biomedical applications of MXene polymer nanocomposites in drug delivery and
12 photothermal therapy. (a) Schematic illustration of MXene/MOF-5 and its alginate and chitosan
13 nanostructures. The modification process involves the integration of chitosan and alginate onto the

1 nanocarriers, resulting in stimuli-responsive properties and the incorporation of a capping agent.
2 Reproduced with permission from ref.[335]. Copyright 2021, American Chemical Society. (b) The
3 trimodal bacterial killing strategy of $Nb_2C@TP$. This strategy involves biofilm resistance, intrinsic
4 bactericidal effects, and thermal ablation of bacteria. Additionally, $Nb_2C@TP$ demonstrates
5 promising in vivo tissue regeneration properties. Reproduced with permission from ref.[336].
6 Copyright 2021, American Chemical Society. (c) The schematic illustration of injectable PLEL-
7 based micellar hydrogels co-delivered with CA4 and Ti_3C_2 for synergistic NIR-II photothermal
8 and vascular disrupting therapy. Reproduced with permission from ref.[337]. Copyright 2020,
9 American Chemical Society.

10 The micellar hydrogel system exhibits an impressive photothermal conversion efficiency (41.4%

11 in the 1064 nm window, utilizing a laser power of 1.0 W cm^{-2}). Additionally, hydrogel

12 demonstrates prolonged retention at the tumor site, enabling sustained release of therapeutic

13 agents, thereby facilitating comprehensive and effective treatment.

14 Additionally, MXenes can also be used to create smart 3D network nanoplatforms by integrating

15 Ti_3C_2 MXene with cellulose hydrogels showcasing light-induced bimodal photothermal/

16 chemotherapy anticancer activity[327]. When incorporating the anticancer drug doxorubicin

17 hydrochloride (DOX), the cellulose/MXene hydrogels exhibit a remarkable ability to enhance the

18 release rate of DOX, significantly accelerating its delivery. Dai et al. designed composite

19 nanosheets based on Ta_4C_3 MXene for multiple imaging-guided photothermal tumor ablation. The

20 rational selection of MXene composition and surface functionalization facilitated the achievement

21 of this innovative approach[328]. In the study, a redox reaction was initiated on the surface of Ta_4C_3

22 MXene, leading to the in-situ growth of manganese oxide nanoparticles (MnO_x/Ta_4C_3). This

23 growth was facilitated by the reducing properties of the nanosheets. Through careful selection of

24 the MXene composition and additional functionalization, the resulting MnO_x/Ta_4C_3-SP composite

25 nanosheets served as high-performance contrast agents. They enabled simultaneous use in

26 computed tomography (CT) for tantalum-based imaging, tumor microenvironment-responsive T1-

27 weighted magnetic resonance imaging (MRI) using the MnO_x component, and photoacoustic

28 imaging.

29 The advantages of MXene-polymer nanocomposites in photothermal therapy enable more

30 efficient, targeted, and controlled treatment of diseases, particularly cancer. The combination of

31 the photothermal properties of MXenes with the tunability, biocompatibility, and targeting

32 capabilities of polymers opens new possibilities for non-invasive, localized, and personalized

33 therapeutic approaches.

**7.8 Water desalination and purification membranes**

MXene-polymer composites offer many advantages in water purification and desalination applications over MXene[69]. These composites can be easily synthesized, coated onto membranes, or formed into filters or adsorbents[338]. Polymers can provide a porous and interconnected network within the composite, increasing the surface area available for adsorption[205, 339]. Numerous studies have provided evidence that laminar membranes exhibit anomalous transport phenomena, such as ultrafast and precise ion selectivity, when the d-spacing is comparable to the diameter D of hydrated ions[340].

MXene-polymer nanocomposites can be utilized to create a super-hydrophilic and underwater super-oleophobic $Ti_3C_2T_x$ MXene-based composite membrane. This can be achieved through vacuum-assisted self-assembly of MXene nanosheets on a porous polyvinylidene fluoride (PVDF) substrate, followed by in situ mineralization of the photocatalyst β-FeOOH on the membrane surface[70]. The resulting membrane was treated with HCl and dried under vacuum. The MXene@CS/TA membrane was prepared by mixing chitosan and tannic acid solutions at pH 3, immersing MXene in the solution for 12 hours, then rinsing and drying at 30°C under vacuum. The membrane was subsequently mineralized in FeCl3 solution, resulting in the MXenes/TA-FeOOH membrane, which exhibited high permeation flux and superior separation efficiency for various oil-in-water emulsions.

Wang et al. demonstrated a novel approach to stabilize the $Ti_3C_2T_x$ laminar architecture using alginate hydrogel pillars[341]. The hybrid SA-$Ti_3C_2T_x$ membrane with a lamellar structure was prepared by mixing sodium alginate (SA) solution with a diluted $Ti_3C_2T_x$ colloidal and filtered by PVDF membrane. Subsequently, the SA-$Ti_3C_2T_x$ membrane was immersed in various multivalent Mn^+ cross-linking solutions for 4 hours to obtain a cross-linked membrane having hydrogel pillars in the interlayer spacing (Figure 20a). The flexible membrane was then dried at room temperature under a vacuum, peeled from the PVDF support, and stored under a vacuum. By pillaring the membrane with Ca-alginate, the nanochannel diameters (7.4 ± 0.2 Å), resulting in a membrane that exhibited exceptional permeation cut-off and outstanding sieving properties for different valent cations. The membrane exhibited a high promise for acid recovery due to its outstanding H^+/Fe^{2+} selectivity, making it useful for traditional ion exchange membranes. Additionally, an

1 ultrathin Mn-alginate pillared membrane with the same d-spacing displayed 100% Na_2SO_4

2 rejection along with high water permeance.
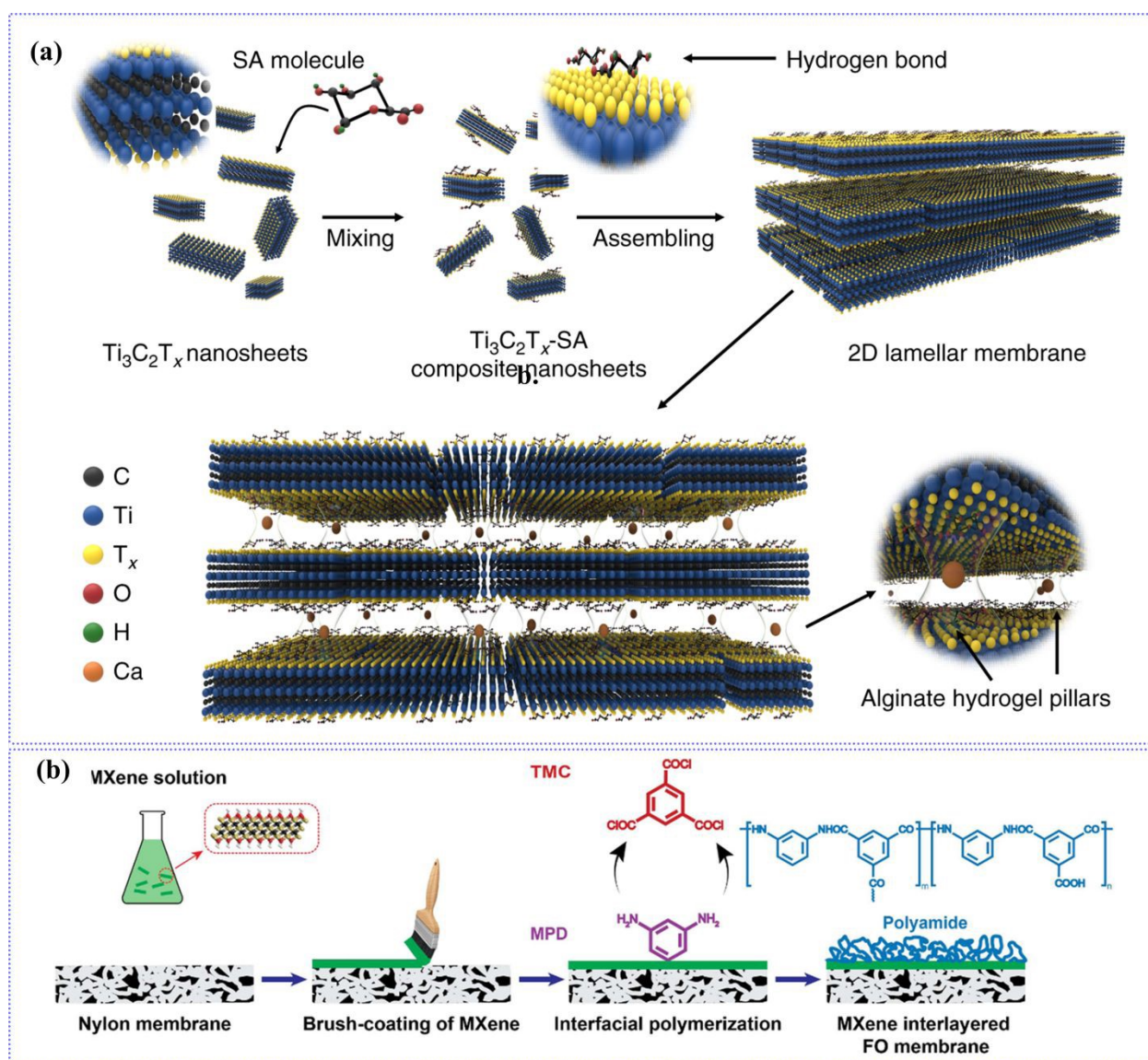
3

4 **Figure 20.** MXene-polymer nanocomposites in water purification/filtration membranes. (a)
5 Fabrication process of the sodium alginate (SA) and $Ti_3C_2T_x$ membrane. Initially, the SA solution
6 was mixed with the $Ti_3C_2T_x$ colloidal solution, leading to firm and homogeneous attachment of
7 SA molecules onto the nanosheet surface through hydrogen bonding. Subsequently, the composite
8 SA-$Ti_3C_2T_x$ nanosheets were assembled into a hybrid membrane with a lamellar structure. Finally,
9 the SA- $Ti_3C_2T_x$ membrane was immersed in various multivalent Mn^+ cross-linking solutions
10 (Ca^{2+}, Ba^{2+}, Mn^{2+}, and Al^{3+}) to obtain the cross-linked membrane with hydrogel pillars in the
11 interlayer spacing[341]. (b) Schematic of the fabrication process for MXene/nylon substrates. It
12 involves brush-coating MXene onto the surface of commercial nylon membranes, creating a thin
13 MXene layer on the nylon substrate. Subsequently, a polyamide membrane is fabricated on top of

1 the MXene/nylon substrate, resulting in the final MXene/nylon/polyamide composite membrane.
2 Reproduced with permission from ref.[338]. Copyright 2020, American Chemical Society.

3 Additionally, MXene-polymer nanocomposites can be utilized to develop a high-performance
4 forward osmosis (FO) membrane by interlayering $Ti_3C_2T_x$ MXene with polyamide[338]. The
5 fabrication process involved a scalable and straightforward brush-coating of MXene on nylon
6 substrates, followed by an interfacial polymerization step (Figure 20b). The resulting FO
7 membrane exhibited high water permeability and low specific salt flux when tested with a sodium
8 chloride draw solution. It also demonstrated exceptional performance in organic solvent forward
9 osmosis, showing a significant flux with low specific salt flux using a lithium chloride draw
10 solution. Additionally, the membrane proved effective for seawater desalination and industrial
11 textile wastewater treatment applications.

12 All-in-all, the incorporation of polymers into MXene-based materials for water purification and
13 desalination offers improved adsorption capacity, selectivity, stability, membrane performance,
14 antifouling properties, scalability, and environmental compatibility[342],[216, 343]. These advantages
15 make MXene-polymer composites promising candidates for addressing water scarcity, ensuring
16 clean water supply, and advancing sustainable water treatment technologies.

7.9 MXene-polymer nanocomposites for solar cell applications

18 MXene integrated with polymers can be ideal for solar cell applications due to their ability to
19 preserve inherent electronic properties and ensure strong interaction with polymer matrices[344].
20 This compatibility enhances electrical conductivity, making MXene-polymer composites highly
21 promising for advancing flexible electronics and photovoltaic devices. Nb_2CT_x is a significant
22 member of the MXenes family, which exhibits distinct chemical and physical characteristics as
23 well [345]. Deng et al. reported a PEDOT: PSS-Nb_2C hybrid hole transport layer (HTL) to improve
24 the device performance of organic solar cells (OSCs) [346]. They employed PEDOT: PSS-Nb_2C
25 hybrids with varying doping MXene ratios (0.05, 0.10, and 0.15 wt%) by directly mixing the Nb_2C
26 colloidal aqueous solution with PEDOT: PSS. A 40 nm-thick HTL layer was produced by spin
27 coating the ITO/glass substrates with PEDOT: PSS aqueous solution or the PEDOT: PSS-Nb_2C
28 hybrid solution for 60 seconds at 3000 rpm followed by deposition of active material, electron
29 transport layer (ETL), and electrode, respectively. Figure 21a-b presents the schematic layout of
30 the fabricated device and the chemical structures of the various non-fullerene acceptors (NFAs)
31 and polymer donor PM6. A higher WF was observed in the case of PEDOT: PSS-Nb_2C hybrid

1   film (5.3 eV), as compared to PEDOT:PSS film (5.0 eV). It is clear that the increased WF better

2   fits the WF of PM6 (5.5 eV), which decreases leakage current by suppressing charge

3   recombination and facilitating hole extraction [347]. Figure 21c-d shows J–V characteristics and

4   external quantum efficiency (EQE) spectra acquired for the OSCs with different Nb_2C MXene

5   ratios in PEDOT:PSS employing the PM6:BTP-eC9 binary active layer.
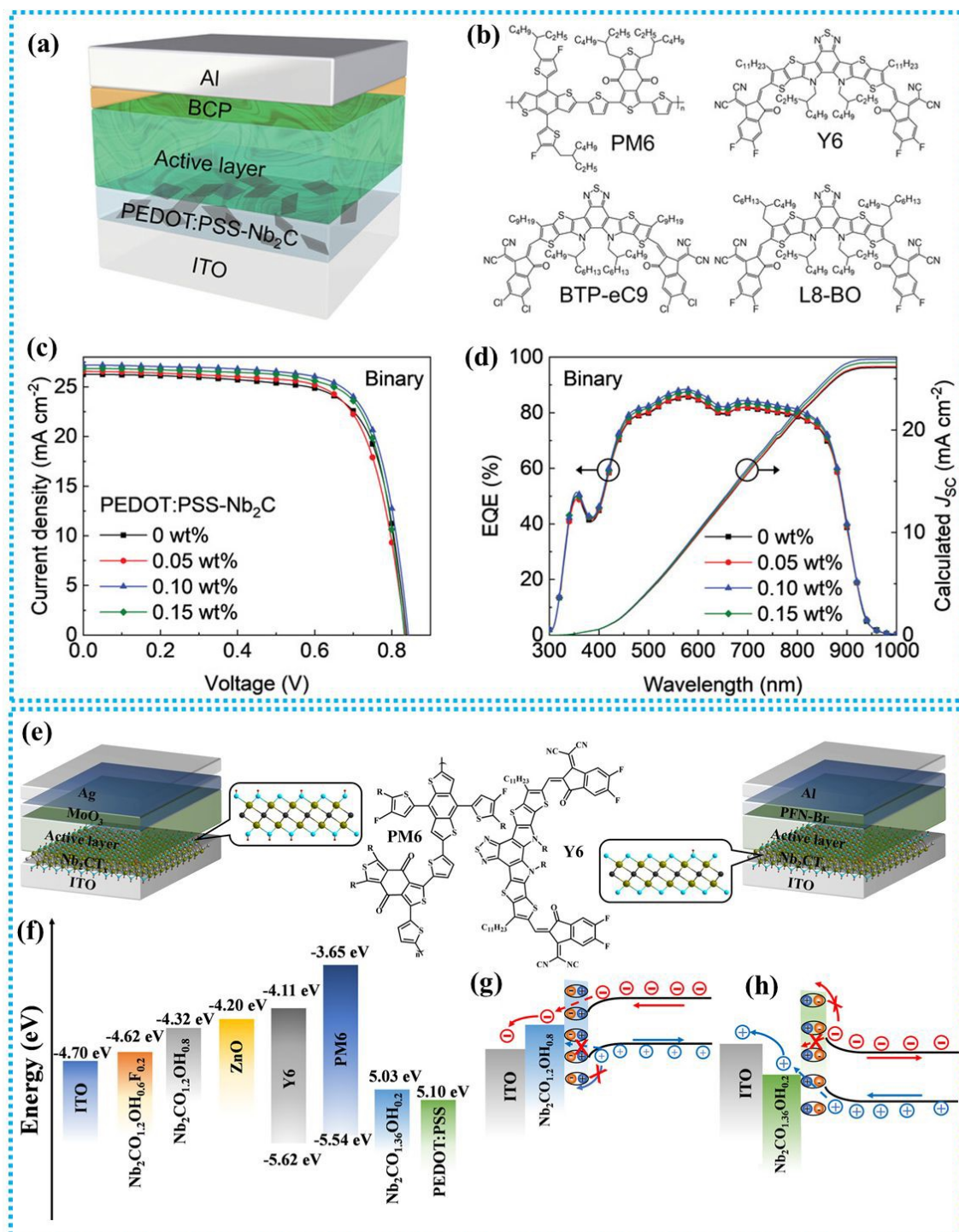
6

1   **Figure 21**. MXene-polymer-based solar cells. (a) PEDOT:PSS-Nb$_2$C hybrid HTL device
2   construction. (b) The chemical structure of various NFAs and polymer donor PM6, L8-BO, Y6,
3   and BTP-eC9. (c) J–V properties and (d) EQE spectra obtained for the solar cells using the
4   PM6:BTP-eC9 binary active layer with varying Nb$_2$C MXene doping ratios in PEDOT:PSS.
5   Reproduced with permission from ref.[346]. Copyright 2023, Wiley. (e) Diagram of the PSCs device
6   architecture showing the chemical structure of PM6, Y6, ETL, HTL, and Nb$_2$CT$_x$. (f) Nb$_2$CT$_x$ is
7   utilized as the ETL and HTL in the schematic energy level diagram of solar cells. (g) Using
8   Nb$_2$CO$_{1.2}$OH$_{0.8}$ as the ETL and (h) Nb$_2$CO$_{1.36}$OH$_{0.2}$ as the HTL, charge transfer, and extraction in
9   solar cells. Reproduced with permission from ref.[348]. Copyright 2021, American Chemical Society.

10 Through the use of solution-processable Nb$_2$C MXene and by using different NFAs (PM6:Y6,

11 PM6:BTP-eC9, PM6:BTP-eC9:L8-BO), surface treatments have improved PCE for OSCs based

12 on binary and ternary systems of active layers. It was proposed that Nb$_2$C MXene added to

13 PEDOT:PSS HTL may efficiently aid in PEDOT and PSS phase separation, enhancing

14 PEDOT:PSS's conductivity. For OSCs based on the ternary active layer of PM6:BTP-eC9:L8-BO,

15 the doping ratio of Nb$_2$C MXene in PEDOT:PSS was tuned to reach a maximal PCE of 19.33%,

16 which is currently the highest value among those of single junction OSCs employing 2D materials.

17 The hybrid HTL improves performance by reducing interface recombination, enhancing hole

18 mobility, and boosting charge extraction efficiency.

19 A similar study by Huang et al. reported the use of Nb$_2$CT$_x$ that investigated the use of additional

20 MXenes in the photovoltaic area by treating Nb$_2$CT$_x$ with alkali and annealing treatments to

21 modify its WF by controlling the surface functional groups[348]. Following a KOH treatment, −F in

22 pure Nb$_2$CT$_x$ may be substituted with −OH, and lowered the WF from 4.62 (Nb$_2$CO$_{1.2}$OH$_{0.6}$F$_{0.2}$)

23 to 4.32 eV (Nb$_2$CO$_{1.2}$OH$_{0.8}$). WF increased to 5.03 eV (Nb$_2$CO$_{1.36}$OH$_{0.2}$) as a result of the removal

24 of one part of the −OH and the transformation of another portion into −O groups upon annealing

25 at 500 °C. Additionally, this is the first time that these Nb$_2$CT$_x$ groups have been used as the ETL

26 and PM6:Y6-based polymer solar cells (PSCs) HTL, which has a stellar PCE of 15.22% (ETL)

27 and 15.03% (HTL). These Nb$_2$CT$_x$ are applied to the PSCs based on PM6:Y6 as a buffer layer,

28 where Nb$_2$CT$_x$ with KOH treatment is used as ETL, and Nb$_2$CT$_x$ with annealing treatment is used

29 as HTL. Figure 21e shows the schematic of the PSCs structures with tuned Nb$_2$CT$_x$

30 (Nb$_2$CO$_{1.2}$OH$_{0.8}$, Nb$_2$CO$_{1.36}$OH$_{0.2}$) used as the ETL and HTL. Figure 21f shows the energy level

31 diagram with Nb$_2$CT$_x$ used as the ETL and HTL. From this, it can be seen that the Nb$_2$CO$_{1.2}$OH$_{0.8}$

32 (or Nb$_2$CO$_{1.36}$OH$_{0.2}$) exhibits a well-matched energy level compared to Nb$_2$CO$_{1.2}$OH$_{0.6}$F$_{0.2}$ in PSCs,

33 which reduces the electron (or hole) barrier height. Moreover, for Nb$_2$CO$_{1.2}$OH$_{0.8}$, the dipolar

1 interlayer induced by −OH will form an electric field pointing from the active layer toward

2 Nb_2CT_x, which will facilitate the transport of the electrons but block the transport of the holes

3 (Figure 21g). On the other hand, with $Nb_2CO_{1.36}OH_{0.2}$, the dipolar interlayer created by −O will

4 provide an electric field that points from Nb_2CT_x in the direction of the active layer, facilitating

5 the movement of the holes but preventing the motion of electrons (Figure 21h).

6 V_2C MXene has also demonstrated great potential for solar cell applications due to its exceptional

7 electrical properties, superior mechanical qualities, and high transmittance[73]. V_2C MXene exhibits

8 excellent hydrophilicity, adjustable work function, strong electrical conductivity, and better

9 transparency. Gu et al. improved the properties of organic solar cells by placing a layer of V_2C

10 material between ITO and PEDOT: PSS significantly improved the performance of PM6:BTP-

11 eC9-based devices[73]. Using a 2D nanosheet material V_2C in combination with PEDOT: PSS, a

12 high-performance V_2C/PEDOT: PSS composited HTL was created, offering superior

13 transmittance and strong electrical conductivity. In addition, the V_2C/PEDOT: PSS composite

14 HTL outperformed the pure PEDOT: PSS interface layer in terms of device performance and

15 photovoltaic properties. In comparison to the 17.41% efficiency of the pure PEDOT: PSS interface

16 device, the V_2C/PEDOT: PSS-based composite interface device exhibited a notable rise to 18.17%.

17 According to the carrier dynamics study, the addition of the V_2C layer increased the number of

18 charge-transfer paths with PEDOT: PSS, which enhanced charge transfer and collection and even

19 reduced the performance of charge combinations. The findings showed that adding 2D material

20 V_2C, which has excellent conductivity and permeability, offers an efficient way to improve the

21 performance of solar cells.

22 **8. Limitations of MXenes in Polymer Nanocomposites for Various Applications**

23 There is no doubt that MXenes when added in polymers can improve the overall properties of the

24 resulting nanocomposites. However, their practical implementation across diverse applications is

25 hindered by inherent limitations such as MXene oxidation susceptibility, brittleness of polymer at

26 higher MXene concentrations, color change due to MXene, and poor dispersion of MXenes in

27 many solvents. These challenges are particularly critical when MXenes are combined with

28 polymers for specific applications, where uniform distribution and long-term stability are essential.

29 The limitations of MXenes in polymer nanocomposites for various applications are as follows:
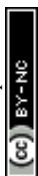
1. **Energy Storage:** Oxidation degradation in MXenes affects their conductivity and electrochemical characteristics, reducing the overall energy storage performance. Higher MXene concentration may lead to brittleness of nanocomposite which can limit mechanical flexibility, impacting stability during cyclic stability studies. Poor dispersion in polymers may also result in non-uniform coatings, lowering the specific capacitance and energy density.

2. **Sensors:** Oxidation of MXenes can reduce sensitivity and selectivity due to reduced conductivity. Beyond optimized MXene concentrations impact the mechanical durability of sensors which can limit their flexibility. Poor dispersion results in polymers may result in non-uniform sensing layers, affecting the reliability and repeatability of sensors.

3. **3D/4D Printing:** The brittleness of MXene-polymer composites restricts their flexibility and printability, posing challenges for fabricating complex structures. MXenes oxidation during post-processing can further compromise the mechanical strength and structural stability of these nanocomposites. Poor dispersion of MXenes within polymer matrices impairs resolution and uniformity, which can limit the controlled precision and performance of printed architectures.

4. **EMI Shielding:** When MXenes are incorporated into polymers, oxidation-induced degradation, mechanical brittleness, and poor dispersion can negatively impact EMI shielding performance. Oxidation at the MXene-polymer interface can reduce conductivity, lowering shielding effectiveness. Despite polymer flexibility, MXenes may still contribute to brittleness, weakening the composite under stress. Poor dispersion of MXenes leads to uneven conductivity, resulting in inhomogeneous shielding layers and reduced EMI performance. Proper dispersion and oxidation control are crucial for maximizing the effectiveness of polymer-MXene composites in EMI shielding applications.

5. **Anti-Corrosion Applications:** In anti-corrosion applications, oxidized MXenes can degrade their protective barriers, reducing efficiency. Poor dispersion of MXenes can cause uneven coatings, leading to defects and corrosion pathways. High concentrations of MXenes can lead to fragility that can result in cracks, compromising the protective performance. Effective dispersion and oxidation control are crucial for maintaining the integrity of MXene-based coatings.

6. **Flexible Electronics:** In MXene-polymer composites for flexible electronics, the overconcentration of MXenes in polymers may lead to brittleness of MXenes which limits flexibility, affecting stretchability and durability. Oxidation-induced color changes alter optical properties, restricting their use in transparent or visual devices. Poor dispersion of MXenes within the polymer matrix leads to reduced conductivity and structural inconsistencies, which degrade performance. Effective dispersion and oxidation control are crucial for enhancing the properties of MXene-based polymer composites in flexible electronic applications.

7. **Antimicrobial Applications:** When MXenes are mixed with polymers for antimicrobial applications, their susceptibility to oxidation degradation may reduce antibacterial efficacy over time. Poor dispersion in the polymer matrix leads to uneven distribution, compromising the uniformity of the antimicrobial effect. Proper dispersion and oxidation control are crucial to maintaining the long-term effectiveness of MXene-polymer-based antimicrobial composites.

8. **Drug Delivery and Photothermal Therapy:** When MXenes are added to polymers for drug delivery and photothermal therapy, their oxidation sensitivity reduces photothermal efficiency and chemical stability, affecting target delivery precision. Limited biocompatibility requires surface modifications, which may alter the structural integrity of MXenes. Dispersion challenges of MXenes in the polymer matrix hinder uniform drug loading and controlled release, impacting therapeutic effectiveness. Proper surface modification and dispersion control are essential to optimize the performance of MXene-based drug delivery and photothermal therapy systems.

9. **Water Desalination and Purification Membranes:** When MXenes are added to polymers for water desalination and purification membranes, MXene oxidation can impact ion selectivity and permeation performance, limiting their reliability and durability. The higher concentration of MXenes may lead to brittleness of the membranes under operational conditions. Limited solvent compatibility results in poor dispersion within the polymer matrix, reducing uniform pore formation and compromising membrane performance. Effective dispersion, oxidation control, and solvent compatibility are crucial for enhancing the long-term performance of MXene-based water desalination and purification membranes.

10. **Solar cells:** MXene oxidation lowers conductivity and stability, affecting solar cell efficiency. High concentrations cause agglomeration, disrupting charge transport, while poor solvent compatibility results in non-uniform films, compromising light absorption and carrier mobility. Enhanced dispersion, oxidation resistance, and solvent compatibility are crucial for improving solar cell performance.

9. Challenges and opportunities in MXene-polymer nanocomposites

9.1 Challenges

Synthesis of MXene-polymer nanocomposites poses several challenges, which can impact the final properties and performance of the materials.

1. Uniform dispersion of MXenes in polymer matrix: As MXenes tend to agglomerate due to their high surface energy, ultimately, it can lead to poor interfacial interactions and reduced mechanical properties of the nanocomposite

2. Stability: Dispersion stability is another issue that needs to be addressed. MXene-polymer nanocomposites can be sensitive to environmental factors as MXenes are prone to oxidation, leading to potential degradation or loss of functionality over time.

3. Interface compatibility: Achieving strong interactions and uniform dispersion of MXene nanosheets within polymer matrices is crucial for optimizing the properties of nanocomposites. Surface functionalization for proper interaction is itself a challenging task.

4. Scalability and reproducibility: Large-scale synthesis of MXene-polymers nanocomposites with consistent properties remains challenging, hindering widespread commercial applications. Processing techniques selection for uniform MXenes dispersion necessary for high-quality nanocomposites. High-cost instruments may be required for large-scale mixing.

5. Mechanical properties: Optimizing the ratio of MXenes and polymers is crucial for any property. MXene-polymer nanocomposites may face limitations in achieving high mechanical strength and toughness, especially in certain applications that demand robust materials if optimization is not suitable for that application.

9.2 Opportunities

Once perfect compatibility between MXenes and polymers is achieved, the MXene-polymer nanocomposites may offer enhanced mechanical, thermal, electrical, and optical properties in versatile materials, making them compatible with diverse applications.

1. Multifunctionality: The unique properties of MXene-polymer hybrids open up opportunities for developing new nanocomposites with multiple functionalities, enabling versatile applications.

2. Biomedical applications: MXene-polymer hybrids, due to their biocompatibility and antibacterial properties, hold promise in drug delivery systems, tissue engineering, and medical implants.

3. Energy-related applications: MXene-polymer nanocomposites, due to their porous structures, can be employed in energy storage devices to enhance performance and stability.

4. Environmental applications: MXene-based nanocomposites have potential in environmental remediation, sensing, and water purification membranes owing to their better adsorption and catalytic traits.

5. New-age technology integration: The combination of cutting-edge technologies, such as nanocomposite fabrication, the Internet of Things (IoT), and artificial intelligence (AI), holds tremendous potential in designing and developing future smart materials with enhanced properties and functionalities.

6. Hence, MXene-polymer nanocomposites offer exciting prospects for addressing various challenges and capitalizing on their unique properties to explore novel applications in diverse industries. However, further research is needed to overcome existing limitations and fully unlock their potential for practical utilization.

10. Future perspectives

The future of MXene-polymer nanocomposites is exceptionally promising, with vast potential across multiple domains. MXenes offer numerous beneficial properties, but these advantages are contingent on preventing oxidation. By addressing this challenge, the full spectrum of MXene's capabilities can be harnessed by integrating these with polymers, paving the way for groundbreaking applications and advancements in various fields. Ongoing advancements in MXene synthesis, functionalization, and nanocomposite fabrication are likely to yield innovative materials with enhanced properties such as lightweight structures, improved mechanical strength, superior electrical conductivity, and increased thermal stability. These developments could revolutionize industries from aerospace to electronics. Additionally, MXene-based nanocomposites show great promise in sustainable technologies, potentially leading to more efficient and eco-friendly solutions in energy storage, water purification, and environmental

1 remediation. In the biomedical field, the biocompatibility and antibacterial properties of MXene-
2 polymers hold potential for breakthroughs in drug delivery systems, tissue engineering scaffolds,
3 and bioactive coatings for implants. The tunable properties of these nanocomposites also pave the
4 way for the creation of smart materials capable of responding to external stimuli, which could
5 transform applications in sensors, actuators, and adaptive coatings. Moreover, the integration of
6 multiple functionalities within a single MXene-polymer material opens exciting possibilities for
7 multifunctional devices that perform various tasks simultaneously. Combining MXene-polymers
8 with other nanomaterials, such as graphene, metal nanoparticles, or quantum dots, may lead to new
9 synergistic effects and advanced functionalities. Furthermore, the intersection of nanocomposite
10 fabrication technologies with artificial intelligence and the Internet of Things promises to enhance
11 the design and deployment of advanced smart materials. As research and interdisciplinary
12 collaboration continue, MXene-polymer nanocomposites are set to address global challenges and
13 drive significant innovations across a range of industries.

11. Conclusions

15 In conclusion, this comprehensive review emphasizes the synthesis methods and diverse
16 applications of MXene-polymer nanocomposites while keeping in mind the serious issue of
17 MXene oxidation. The various fabrication techniques, such as solution blending, in-situ
18 polymerization, LBL assembly, and electrospinning, offer opportunities to tailor the properties of
19 these nanocomposites for specific applications. MXenes can be easily hybridized with various
20 polymers such as PVA, PDMS, PPy, PEDOT:PSS, polyaniline, polypropylene, polyurethane, and
21 many biopolymers. MXene-polymer nanocomposites exhibit conductivity, stability, flexibility,
22 biocompatibility, and ion diffusion, leading to enhanced performance and durability in various
23 devices. The incorporation of polymers in MXene-based sensors enhances sensitivity, selectivity,
24 flexibility, and response time, enabling more accurate and efficient detection of target analytes.
25 MXene-polymer composites provide EMI shielding effectiveness, lightweight, and flexible
26 characteristics, making them suitable for applications in the electronics, telecommunications, and
27 aerospace industries. The combination of MXenes with polymers offers flexibility, stretchability,
28 and improved mechanical properties, enabling the development of flexible electronic devices.
29 MXene-polymer composites inculcate higher porosity in the nanocomposite which can increase
30 the charge storage capacity. MXene-polymer composites offer enhanced photothermal conversion
31 efficiency, controlled drug delivery, enabling effective cancer treatment, and wound healing.

1 MXene-polymer composites provide enhanced adsorption capacity, selective adsorption,

2 improved stability, membrane performance, antifouling properties, scalability, and environmental

3 compatibility, making them effective materials for water purification and desalination processes.

4 These advantages highlight the potential of MXene-polymer composites in addressing various

5 challenges and advancing technological applications. The unique properties and synergistic effects

6 resulting from the combination of MXenes and polymers create exciting opportunities in various

7 fields, enabling the development of efficient, sustainable, and functional materials and devices.

8 This advancement ensures that MXene oxidation will not hinder the progress toward innovative

9 solutions.

10 **Funding**

11 This research is not supported by any funding.

12 **Author contributions:**

13 Sunil Kumar – original draft, conceptualization, and data curation; Syed Muhammad Zain Mehdi

14 – original draft, data curation, and editing; Manish Taunk – original draft and editing; Sanjeev

15 Kumar – review and editing; Amit Aherwar – review and editing; Sudhanshu Singh – review and

16 editing; Tej Singh – review and editing.

17 **Conflict of Interests**

18 The authors declare that there is no conflict of interest.

19 **Author Biographies**

20
21 **Sunil Kumar** received his B.S. and M.S. degrees in Physics from Panjab University, Chandigarh,

22 India in 2003 and 2008, respectively. He completed his Ph.D. at Thapar University, Patiala, India

23 in 2016. In 2017, he joined Sejong University as a postdoctoral fellow. Since 2022, he has been

24 working as an Assistant Professor at Sejong University, South Korea in the Department of

25 Nanotechnology and Materials Engineering. His current research interests include MXene-based

26 smart windows, flexible transparent electrodes, and energy storage devices.

27
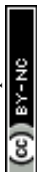
1

2 **Syed Muhammad Zain Mehdi** received his BS degree in Metallurgy and Materials Engineering
3 from the University of the Punjab, Pakistan, in 2017. He completed his MS-Ph.D. in
4 Nanotechnology at Sejong University, South Korea, in February 2024. Following this, in March
5 2024, he joined Sejong University as a Postdoctoral Fellow in the Department of Nanotechnology
6 and Materials Engineering. His research interests include doped-carbon nanotube properties in
7 field emission and the utilization of MXenes in energy storage and electrocatalysis.

8

9 **Manish Taunk** received his B.S. and M.S. degrees in Physics from Himachal Pradesh University,
10 Shimla, India in 2004 and 2008, respectively. He completed his Ph.D. at the National Institute of
11 Technology, Himachal Pradesh, India in 2012. He has worked as an Assistant Professor at various
12 universities. Currently, he is working as an Associate Professor at Chandigarh University, Mohali,
13 India, in the Department of Physics. His current research interests include MXene-based
14 nanocomposites, conducting polymers, and their applications.

15

16 **Sanjeev Kumar** earned his B.S. and M.S. degrees in Physics from GNDU University, Amritsar,
17 India, in 2005 and 2007, respectively. He completed his Ph.D. at Thapar University, Patiala, India,
18 in 2012. He has served as an Assistant Professor at Sri Guru Granth Sahib World University for
19 10 years. Currently, he is an Associate Professor in the Department of Physics at Chandigarh
20 University, Mohali, India. His research focuses on TiO_2 and ZnO-based nanocomposites and their
21 applications in photocatalysis.
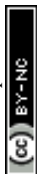
1

2

3 **Amit Aherwar** obtained his BS degree in Mechanical Engineering in 2006, and MS in Production
4 Engineering from Madhav Institute of Technology and Science (MITS) Gwalior, India in 2010.
5 He completed his Doctor of Philosophy (Ph.D.) at Malaviya National Institute of Technology
6 (MNIT) Jaipur, India in 2017. Currently, he is an Assistant Professor at MITS Gwalior. His
7 research focuses on biomaterials, tribology, composite materials, and metal casting, with an
8 emphasis on advancing material properties and manufacturing processes.

9

10 **Sudhanshu Singh** obtained his B.S. degree in Electronics & Communication from Uttar Pradesh
11 Technical University, Lucknow, India, in 2006, followed by an M.S. degree in Nanotechnology
12 from the National Institute of Technology Kurukshetra, Haryana, India, in 2008. He completed his
13 Ph.D. at Amity University Rajasthan, Jaipur, India, in 2021. With over a decade of experience as
14 an Assistant Professor at Amity University Rajasthan, he is currently serving as an Associate
15 Professor at Parul University, Gujarat, India. His research interests include the development of
16 polymers and nanocomposites for wastewater treatment, photocatalysis, and the tribological
17 properties of fiber-reinforced phenolic composites.

18

19 **Tej Singh** earned his B.S. and M.S. degrees from Panjab University, Chandigarh, India in 2003
20 and 2008, respectively, and PhD degree from the National Institute of Technology, Hamirpur,
21 India in 2013. He has gained experience at various academic institutions. Currently, Tej Singh is
22 serving as an Associate Professor at Savaria Institute of Technology, Faculty of Informatics,
23 Eötvös Loránd University, Hungary. His areas of interest and expertise include polymer
24 composites, tribology, nanoparticle synthesis, optimization methods, waste and natural renewable
25 materials utilization for potential applications, and heat transfer.

Journal of Materials Chemistry A Accepted Manuscript

1   **Declaration of generative AI and AI-assisted technologies in the writing process**

2   During the preparation of this work, the author(s) used ChatGpt to improve the grammar. After
3   using this tool/service, the author(s) reviewed and edited the content as needed and take(s) full
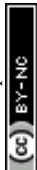4   responsibility for the content of the publication.

5   **References**

6   (1) Zhao, S. Y.; Zhang, Y. Y.; Yang, J.; Kitipornchai, S. Folded graphene reinforced
7   nanocomposites with superior strength and toughness: A molecular dynamics study. *J Mater Sci*
8   *Technol* **2022**, *120,* 196-204. DOI: 10.1016/j.jmst.2021.12.042. Zhang, Y.; Zhu, B.; Cai, X.; Yuan,
9   X. M.; Zhao, S. Y.; Yu, J. W.; Qiao, K.; Qin, R. M. Rapid In Situ Polymerization of
10   Polyacrylonitrile/Graphene Oxide Nanocomposites as Precursors for High-Strength Carbon
11   Nanofibers. *Acs Appl Mater Inter* **2021**, *13* (14), 16846-16858. DOI: 10.1021/acsami.1c02643.
12   Yan, M. L.; Jiao, W. C.; Ding, G. M.; Chu, Z. M.; Huang, Y. F.; Wang, R. G. High strength and
13   toughness epoxy nanocomposites reinforced with graphene oxide-nanocellulose micro/nanoscale
14   structures. *Appl Surf Sci* **2019**, *497*. DOI: ARTN 143802
15   10.1016/j.apsusc.2019.143802. Jankovsky, O.; Lojka, M.; Lauermannova, A. M.; Antoncik, F.;
16   Pavlikova, M.; Zaleska, M.; Pavlik, Z.; Pivak, A.; Sedmidubsky, D. Towards novel building
17   materials: High-strength nanocomposites based on graphene, graphite oxide and magnesium
18   oxychloride. *Appl Mater Today* **2020**, *20*. DOI: ARTN 100766
19   10.1016/j.apmt.2020.100766. Fan, X.; Wang, F. C.; Gao, Q.; Zhang, Y.; Huang, F.; Xiao, R. L.;
20   Qin, J. B.; Zhang, H.; Shi, X. T.; Zhang, G. C. Nature inspired hierarchical structures in nano-
21   cellular epoxy/graphene-Fe3O4 nanocomposites with ultra-efficient EMI and robust mechanical
22   strength. *J Mater Sci Technol* **2022**, *103*, 177-185. DOI: 10.1016/j.jmst.2021.06.030.
23   (2) Ryu, A.; Yim, H.; Yoo, S.; Park, J.; Lee, D. G.; Lee, J. Y.; Song, H. C.; Baek, S. H.; Nahm, S.;
24   Choi, J. W. Layer-Controlled Perovskite 2D Nanosheet Interlayer for the Energy Storage
25   Performance of Nanocomposites. *Small* **2023**. DOI: 10.1002/smll.202300526. Likhi, F. H.; Singh,
26   M.; Chavan, S. V.; Cao, T. M.; Shanbedi, M.; Karim, A. Effects of Film Confinement on Dielectric
27   and Electrical Properties of Graphene Oxide and Reduced Graphene Oxide-Based Polymer
28   Nanocomposites: Implications for Energy Storage. *Acs Appl Nano Mater* **2023**, *6* (13), 11699-
29   11714. DOI: 10.1021/acsanm.3c01674. Idumah, C. I. Phosphorene polymeric nanocomposites for
30   electrochemical energy storage applications. *J Energy Storage* **2023**, *69*. DOI: ARTN 107940
31   10.1016/j.est.2023.107940. Bera, S.; Singh, M.; Thantirige, R.; Tiwary, S. K.; Shook, B. T.;
32   Nieves, E.; Raghavan, D.; Karim, A.; Pradhan, N. R. 2D-Nanofiller-Based Polymer
33   Nanocomposites for Capacitive Energy Storage Applications. *Small Sci* **2023**, *3* (7). DOI:
34   10.1002/smsc.202300016. Prateek; Thakur, V. K.; Gupta, R. K. Recent Progress on Ferroelectric
35   Polymer-Based Nanocomposites for High Energy Density Capacitors: Synthesis, Dielectric
36   Properties, and Future Aspects. *Chem Rev* **2016**, *116* (7), 4260-4317. DOI:
37   10.1021/acs.chemrev.5b00495. Mishra, K.; Devi, N.; Siwal, S. S.; Zhang, Q. B.; Alsanie, W. F.;
38   Scarpa, F.; Thakur, V. K. Ionic Liquid-Based Polymer Nanocomposites for Sensors, Energy,
39   Biomedicine, and Environmental Applications: Roadmap to the Future. *Adv Sci* **2022**, *9* (26). DOI:
40   ARTN 2202187
41   10.1002/advs.202202187. Elemike, E. E.; Adeyemi, J.; Onwudiwe, D. C.; Wei, L.; Oyedeji, A. O.
42   The future of energy materials: A case of MXenes-carbon dots nanocomposites. *J Energy Storage*
43   **2022**, *50*. DOI: ARTN 104711
44   10.1016/j.est.2022.104711.
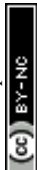
1 (3) Jouault, N.; Dalmas, F.; Said, S.; Di Cola, E.; Schweins, R.; Jestin, J.; Boue, F. Direct
2 Measurement of Polymer Chain Conformation in Well-Controlled Model Nanocomposites by
3 Combining SANS and SAXS. *Macromolecules* **2010**, *43* (23), 9881-9891. DOI:
4 10.1021/ma101682t. Faupel, F.; Zaporojtchenko, V.; Strunskus, T.; Elbahri, M. Metal-Polymer
5 Nanocomposites for Functional Applications. *Adv Eng Mater* **2010**, *12* (12), 1177-1190. DOI:
6 10.1002/adem.201000231. Su, Y. W.; Lin, W. H.; Hsu, Y. J.; Wei, K. H. Conjugated
7 Polymer/Nanocrystal Nanocomposites for Renewable Energy Applications in Photovoltaics and
8 Photocatalysis. *Small* **2014**, *10* (22), 4427-4442. DOI: 10.1002/smll.201401508. Imai, Y.;
9 Shimamoto, D.; Hotta, Y. Effect of wet jet milling of carbon nanotube on electrical properties of
10 polymer nanocomposites. *Mater Chem Phys* **2014**, *148* (3), 1178-1183. DOI:
11 10.1016/j.matchemphys.2014.09.044. Grabowski, C. A.; Koerner, H.; Meth, J. S.; Dang, A.; Hui,
12 C. M.; Matyjaszewski, K.; Bockstaller, M. R.; Durstock, M. F.; Vaia, R. A. Performance of
13 Dielectric Nanocomposites: Matrix-Free, Hairy Nanoparticle Assemblies and Amorphous
14 Polymer-Nanoparticle Blends. *Acs Appl Mater Inter* **2014**, *6* (23), 21500-21509. DOI:
15 10.1021/am506521r. Chen, L.; Du, D. H.; Sun, K.; Hou, J. H.; Ouyang, J. Y. Improved Efficiency
16 and Stability of Polymer Solar Cells Utilizing Two-Dimensional Reduced Graphene Oxide:
17 Graphene Oxide Nanocomposites as Hole-Collection Material. *Acs Appl Mater Inter* **2014**, *6* (24),
18 22334-22342. DOI: 10.1021/am506326y.
19 (4) Zhang, S. J.; Lin, W.; Wong, C. P.; Bucknall, D. G.; Kumar, S. Nanocomposites of Carbon
20 Nanotube Fibers Prepared by Polymer Crystallization. *Acs Appl Mater Inter* **2010**, *2* (6), 1642-
21 1647. DOI: 10.1021/am1001663. Flory, A. L.; Ramanathan, T.; Brinson, L. C. Physical Aging of
22 Single Wall Carbon Nanotube Polymer Nanocomposites: Effect of Functionalization of the
23 Nanotube on the Enthalpy Relaxation. *Macromolecules* **2010**, *43* (9), 4247-4252. DOI:
24 10.1021/ma901670m. Duong, H. M.; Yamamoto, N.; Bui, K.; Papavassiliou, D. V.; Maruyama,
25 S.; Wardle, B. L. Morphology Effects on Nonisotropic Thermal Conduction of Aligned Single-
26 Walled and Multi-Walled Carbon Nanotubes in Polymer Nanocomposites. *J Phys Chem C* **2010**,
27 *114* (19), 8851-8860. DOI: 10.1021/jp102138c. Basuli, U.; Chaki, T. K.; Chattopadhyay, S.;
28 Sabharwal, S. Thermal and Mechanical Properties of Polymer-Nanocomposites Based on Ethylene
29 Methyl Acrylate and Multiwalled Carbon Nanotube. *Polym Composite* **2010**, *31* (7), 1168-1178.
30 DOI: 10.1002/pc.20903. Putz, K. W.; Compton, O. C.; Palmeri, M. J.; Nguyen, S. T.; Brinson, L.
31 C. High-Nanofiller-Content Graphene Oxide-Polymer Nanocomposites via Vacuum-Assisted
32 Self-Assembly. *Adv Funct Mater* **2010**, *20* (19), 3322-3329. DOI: 10.1002/adfm.201000723. Li,
33 G. L.; Liu, G.; Li, M.; Wan, D.; Neoh, K. G.; Kang, E. T. Organo- and Water-Dispersible Graphene
34 Oxide-Polymer Nanosheets for Organic Electronic Memory and Gold Nanocomposites. *J Phys
35 Chem C* **2010**, *114* (29), 12742-12748. DOI: 10.1021/jp102640s. Kim, H.; Abdala, A. A.;
36 Macosko, C. W. Graphene/Polymer Nanocomposites. *Macromolecules* **2010**, *43* (16), 6515-6530.
37 DOI: 10.1021/ma100572e. Zare, Y.; Garmabi, H. Predictions of Takayanagi model for tensile
38 modulus of polymer/CNT nanocomposites by properties of nanoparticles and filler network.
39 *Colloid Polym Sci* **2017**, *295* (6), 1039-1047. DOI: 10.1007/s00396-017-4092-y. Ren, L. L.; Li,
40 H.; Xie, Z. L.; Ai, D.; Zhou, Y.; Liu, Y.; Zhang, S. Y.; Yang, L. J.; Zhao, X. T.; Peng, Z. R.; et al.
41 High-Temperature High-Energy-Density Dielectric Polymer Nanocomposites Utilizing Inorganic
42 Core-Shell Nanostructured Nanofillers. *Adv Energy Mater* **2021**, *11* (28). DOI: ARTN 2101297
43 10.1002/aenm.202101297. Danlee, Y.; Mederos-Henry, F.; Hermans, S.; Bailly, C.; Huynen, I.
44 Ranking Broadband Microwave Absorption Performance of Multilayered Polymer
45 Nanocomposites Containing Carbon and Metallic Nanofillers. *Front Mater* **2020**, *7*. DOI: ARTN
46 214

Journal of Materials Chemistry A Accepted Manuscript

1 10.3389/fmats.2020.00214.

2 (5) Xie, Y.; Dall'Agnese, Y.; Naguib, M.; Gogotsi, Y.; Barsoum, M. W.; Zhuang, H. L. L.; Kent,
3 P. R. C. Prediction and Characterization of MXene Nanosheet Anodes for Non-Lithium-Ion
4 Batteries. *Acs Nano* **2014**, *8* (9), 9606-9615. DOI: 10.1021/nn503921j. Shi, C. Y.; Beidaghi, M.;
5 Naguib, M.; Mashtalir, O.; Gogotsi, Y.; Billinge, S. J. L. Structure of Nanocrystalline Ti3C2
6 MXene Using Atomic Pair Distribution Function. *Phys Rev Lett* **2014**, *112* (12). DOI: ARTN
7 125501

8 10.1103/PhysRevLett.112.125501. Ghidiu, M.; Naguib, M.; Shi, C.; Mashtalir, O.; Pan, L. M.;
9 Zhang, B.; Yang, J.; Gogotsi, Y.; Billinge, S. J. L.; Barsoum, M. W. Synthesis and characterization
10 of two-dimensional Nb4C3 (MXene). *Chem Commun* **2014**, *50* (67), 9517-9520. DOI:
11 10.1039/c4cc03366c. Er, D. Q.; Li, J. W.; Naguib, M.; Gogotsi, Y.; Shenoy, V. B. Ti3C2 MXene
12 as a High Capacity Electrode Material for Metal (Li, Na, K, Ca) Ion Batteries. *Acs Appl Mater*
13 *Inter* **2014**, *6* (14), 11173-11179. DOI: 10.1021/am501144q. Gogotsi, Y.; Anasori, B. The Rise of
14 MXenes. *Acs Nano* **2019**, *13* (8), 8491-8494. DOI: 10.1021/acsnano.9b06394.

15 (6) Naguib, M.; Kurtoglu, M.; Presser, V.; Lu, J.; Niu, J. J.; Heon, M.; Hultman, L.; Gogotsi, Y.;
16 Barsoum, M. W. Two-Dimensional Nanocrystals Produced by Exfoliation of Ti3AlC2. *Adv Mater*
17 **2011**, *23* (37), 4248-4253. DOI: 10.1002/adma.201102306. Wang, X.; Garnero, C.; Rochard, G.;
18 Magne, D.; Morisset, S.; Hurand, S.; Chartier, P.; Rousseau, J.; Cabioc'h, T.; Coutanceau, C.; et
19 al. A new etching environment (FeF3/HCl) for the synthesis of two-dimensional titanium carbide
20 MXenes: a route towards selective reactivity vs. water. *J Mater Chem A* **2017**, *5* (41), 22012-
21 22023. DOI: 10.1039/c7ta01082f. Wang, C. D.; Shou, H. W.; Chen, S. M.; Wei, S. Q.; Lin, Y. X.;
22 Zhang, P. J.; Liu, Z. F.; Zhu, K. F.; Guo, X.; Wu, X. J.; et al. HCl-Based Hydrothermal Etching
23 Strategy toward Fluoride-Free MXenes. *Adv Mater* **2021**, *33* (27). DOI: ARTN 2101015

24 10.1002/adma.202101015. Mohseni-Salehi, M. S.; Taheri-Nassaj, E.; Babaei, A.; Ghazvini, A. S.;
25 Soleimanzade, M. Effect of temperature and atmosphere on V2AlC etching for V2CTx MXenes
26 synthesis used as anode for Li-ion storage systems. *J Energy Storage* **2023**, *66*. DOI: ARTN
27 107462

28 10.1016/j.est.2023.107462. Kumar, S.; Kang, D. W.; Hong, H.; Rehman, M. A.; Lee, Y. J.; Lee,
29 N. S.; Seo, Y. H. Effect of Ti3C2Tx MXenes etched at elevated temperatures using concentrated
30 acid on binder-free supercapacitors. *Rsc Adv* **2020**, *10* (68), 41837-41845. DOI:
31 10.1039/d0ra05376g.

32 (7) Gogotsi, Y.; Huang, Q. MXenes: Two-Dimensional Building Blocks for Future Materials and
33 Devices. *Acs Nano* **2021**, *15* (4), 5775-5780. DOI: 10.1021/acsnano.1c03161. Lioi, D. B.; Neher,
34 G.; Heckler, J. E.; Back, T.; Mehmood, F.; Nepal, D.; Pachter, R.; Vaia, R.; Kennedy, W. J.
35 Electron-Withdrawing Effect of Native Terminal Groups on the Lattice Structure of Ti3C2TX
36 MXenes Studied by Resonance Raman Scattering: Implications for Embedding MXenes in
37 Electronic Composites. *Acs Appl Nano Mater* **2019**, *2* (10), 6087-6091. DOI:
38 10.1021/acsanm.9b01194. Athavale, S.; Micci-Barreca, S. A.; Arole, K.; Kotasthane, V.;
39 Lutkenhaus, J. L.; Radovic, M.; Green, M. J. Effect of terminal groups on the degradation stability
40 of Ti3C2Tz MXenes. *Nanoscale* **2023**. DOI: 10.1039/d3nr02386a.

41 (8) Zeraati, A. S.; Mirkhani, S. A.; Sun, P. C.; Naguib, M.; Braun, P. V.; Sundararaj, U. Improved
42 synthesis of Ti3C2Tx MXenes resulting in exceptional electrical conductivity, high synthesis
43 yield, and enhanced capacitance. *Nanoscale* **2021**, *13* (6), 3572-3580. DOI: 10.1039/d0nr06671k.

44 (9) Lipatov, A.; Goad, A.; Loes, M. J.; Vorobeva, N. S.; Abourahma, J.; Gogotsi, Y.; Sinitskii, A.
45 High electrical conductivity and breakdown current density of individual monolayer Ti3C2Tx
46 MXene flakes. *Matter-Us* **2021**, *4* (4), 1413-1427. DOI: 10.1016/j.matt.2021.01.021.

1   (10) Zhang, B. P.; Wong, P. W.; Guo, J. X.; Zhou, Y. S.; Wang, Y.; Sun, J. W.; Jiang, M. N.;
2   Wang, Z. K.; An, A. K. Transforming Ti3C2Tx MXene's intrinsic hydrophilicity into
3   superhydrophobicity for efficient photothermal membrane desalination. *Nat Commun* **2022**, *13*
4   (1). DOI: ARTN 3315

5   10.1038/s41467-022-31028-6. Guan, Y. X.; Zhang, M. M.; Qin, J.; Ma, X. X.; Li, C.; Tang, J. L.
6   Hydrophilicity-Dependent Distinct Frictional Behaviors of Different Modified MXene
7   Nanosheets. *J Phys Chem C* **2020**, *124* (25), 13664-13671. DOI: 10.1021/acs.jpcc.0c01551.
8   (11) Li, X. L.; Huang, Z. D.; Shuck, C. E.; Liang, G. J.; Gogotsi, Y.; Zhi, C. Y. MXene chemistry,
9   electrochemistry and energy storage applications. *Nat Rev Chem* **2022**, *6* (6), 389-404. DOI:
10   10.1038/s41570-022-00384-8.
11   (12) Maleski, K.; Ren, C. E.; Zhao, M. Q.; Anasori, B.; Gogotsi, Y. Size-Dependent Physical and
12   Electrochemical Properties of Two-Dimensional MXene Flakes. *Acs Appl Mater Inter* **2018**, *10*
13   (29), 24491-24498. DOI: 10.1021/acsami.8b04662.
14   (13) Zhang, Y. J.; Xia, W. Y.; Wu, Y. B.; Zhang, P. H. Prediction of MXene based 2D tunable
15   band gap semiconductors: GW quasiparticle calculations. *Nanoscale* **2019**, *11* (9), 3993-4000.
16   DOI: 10.1039/c9nr01160a.
17   (14) Hu, C. Q.; Du, Z. J.; Wei, Z. M.; Li, L.; Shen, G. Z. Functionalized Ti3C2Tx MXene with
18   layer-dependent band gap for flexible NIR photodetectors. *Appl Phys Rev* **2023**, *10* (2). DOI: Artn
19   021402

20   10.1063/5.0140861.
21   (15) Liu, X. D.; Liu, Y.; Dong, S. L.; Zhang, X. F.; Hou, S. D. Synthesis of ultra-high specific
22   surface area aerogels with nitrogen-enriched Ti3C2Tx nanosheets as high-performance
23   supercapacitor electrodes. *J Mater Chem C* **2022**, *10* (40), 14929-14938. DOI:
24   10.1039/d2tc01987f. Ren, C. E.; Zhao, M. Q.; Makaryan, T.; Halim, J.; Boota, M.; Kota, S.;
25   Anasori, B.; Barsoum, M. W.; Gogotsi, Y. Porous Two-Dimensional Transition Metal Carbide
26   (MXene) Flakes for High-Performance Li-Ion Storage. *Chemelectrochem* **2016**, *3* (5), 689-693.
27   DOI: 10.1002/celc.201600059.
28   (16) Ling, Z.; Ren, C. E.; Zhao, M. Q.; Yang, J.; Giammarco, J. M.; Qiu, J. S.; Barsoum, M. W.;
29   Gogotsi, Y. Flexible and conductive MXene films and nanocomposites with high capacitance. *P*
30   *Natl Acad Sci USA* **2014**, *111* (47), 16676-16681. DOI: 10.1073/pnas.1414215111.
31   (17) Zhang, W. Y.; Jin, H. X.; Zhang, J. X. Nb2CTx MXene as High-Performance Energy Storage
32   Material with Na, K, and Liquid K-Na Alloy Anodes. *Langmuir* **2021**, *37* (3), 1102-1109. DOI:
33   10.1021/acs.langmuir.0c02957.
34   (18) Dall'Agnese, Y.; Taberna, P. L.; Gogotsi, Y.; Simon, P. Two-Dimensional Vanadium Carbide
35   (MXene) as Positive Electrode for Sodium-Ion Capacitors. *J Phys Chem Lett* **2015**, *6* (12), 2305-
36   2309. DOI: 10.1021/acs.jpclett.5b00868.
37   (19) Liu, D.; Wang, R. W.; Chang, W.; Zhang, L.; Peng, B. Q.; Li, H. D.; Liu, S. Q.; Yan, M.;
38   Guo, C. S. Ti3C2 MXene as an excellent anode material for high-performance microbial fuel cells.
39   *J Mater Chem A* **2018**, *6* (42), 20887-20895. DOI: 10.1039/c8ta07305h. Fei, M. M.; Lin, R. Z.;
40   Deng, Y. M.; Xian, H. X.; Bian, R. J.; Zhang, X. L.; Cheng, J. G.; Xu, C. X.; Cai, D. Y.
41   Polybenzimidazole/Mxene composite membranes for intermediate temperature polymer
42   electrolyte membrane fuel cells. *Nanotechnology* **2018**, *29* (3). DOI: ARTN 035403
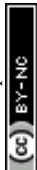43   10.1088/1361-6528/aa9ab0.

1   (20) Kolubah, P. D.; Mohamed, H. O.; Ayach, M.; Hari, A. R.; Alshareef, H. N.; Saikaly, P.; Chae,
2   K. J.; Castano, P. W2N-MXene composite anode catalyst for efficient microbial fuel cells using
3   domestic wastewater. *Chem Eng J* **2023**, *461*. DOI: ARTN 141821

4   10.1016/j.cej.2023.141821. Jiang, D. M.; Zhu, C. Y.; He, Y.; Xing, C. C.; Xie, K.; Xu, Y.; Wang,
5   Y. Q. Polyaniline-MXene-coated carbon cloth as an anode for microbial fuel cells. *J Solid State*
6   *Electr* **2022**, *26* (11), 2435-2443. DOI: 10.1007/s10008-022-05255-2. Chen, J. F.; Zhang, Y. W.;
7   Wu, Y. Q.; Wang, J. Y.; Zhao, Y. Y.; Wang, M. K.; Yang, J. Q.; Liu, J. Y.; Wang, R. J.; Yang, Y.
8   W.; et al. Enhanced bioelectrochemical performance by NiCoAl-LDH/MXene hybrid as cathode
9   catalyst for microbial fuel cell. *Int J Hydrogen Energ* **2023**, *48* (15), 6056-6066. DOI:
10 10.1016/j.ijhydene.2022.11.173.
11 (21) Chen, J. X.; Li, Z. L.; Ni, F. L.; Ouyang, W. X.; Fang, X. S. Bio-inspired transparent MXene
12 electrodes for flexible UV photodetectors. *Mater Horiz* **2020**, *7* (7), 1828-1833. DOI:
13 10.1039/d0mh00394h. Xu, H.; Ren, A. B.; Wu, J.; Wang, Z. M. Recent Advances in 2D MXenes
14 for Photodetection. *Adv Funct Mater* **2020**, *30* (24). DOI: ARTN 2000907
15 10.1002/adfm.202000907.
16 (22) Yao, L. J.; Tian, X.; Cui, X. X.; Zhao, R. J.; Xiao, X. C.; Wang, Y. D. Partially oxidized
17 Ti3C2Tx MXene-sensitive material-based ammonia gas sensor with high-sensing performances
18 for room temperature application. *J Mater Sci-Mater El* **2021**, *32* (23), 27837-27848. DOI:
19 10.1007/s10854-021-07166-w. Pei, Y. Y.; Zhang, X. L.; Hui, Z. Y.; Zhou, J. Y.; Huang, X.; Sun,
20 G. Z.; Huang, W. Ti3C2TX MXene for Sensing Applications: Recent Progress, Design Principles,
21 and Future Perspectives. *Acs Nano* **2021**, *15* (3), 3996-4017. DOI: 10.1021/acsnano.1c00248.
22 Lorencova, L.; Bertok, T.; Filip, J.; Jerigova, M.; Velic, D.; Kasak, P.; Mahmoud, K. A.; Tkac, J.
23 Highly stable Ti3C2Tx (MXene)/Pt nanoparticles-modified glassy carbon electrode for H2O2 and
24 small molecules sensing applications. *Sensor Actuat B-Chem* **2018**, *263*, 360-368. DOI:
25 10.1016/j.snb.2018.02.124.
26 (23) Zhang, C. F.; McKeon, L.; Kremer, M. P.; Park, S. H.; Ronan, O.; Seral-Ascaso, A.; Barwich,
27 S.; Coileain, C. O.; McEvoy, N.; Nerl, H. C.; et al. Additive-free MXene inks and direct printing
28 of micro-supercapacitors. *Nat Commun* **2019**, *10*. DOI: ARTN 1795

29 10.1038/s41467-019-09398-1. Guo, T. Z.; Zhou, D.; Deng, S. G.; Jafarpour, M.; Avaro, J.; Neels,
30 A.; Heier, J.; Zhang, C. F. Rational Design of Ti3C2Tx MXene Inks for Conductive, Transparent
31 Films. *Acs Nano* **2023**, *17* (4), 3737-3749. DOI: 10.1021/acsnano.2c11180. Shao, Y. Z.; Wei, L.
32 S.; Wu, X. Y.; Jiang, C. M.; Yao, Y.; Peng, B.; Chen, H.; Huangfu, J. T.; Ying, Y. B.; Zhang, C.
33 A. F. O.; et al. Room-temperature high-precision printing of flexible wireless electronics based on
34 MXene inks. *Nat Commun* **2022**, *13* (1). DOI: ARTN 3223
35 10.1038/s41467-022-30648-2.
36 (24) Aakyiir, M.; Tanner, B.; Yap, P. L.; Rastin, H.; Tung, T. T.; Losic, D.; Meng, Q. S.; Ma, J.
37 3D printing interface-modified PDMS/MXene nanocomposites for stretchable conductors. *J Mater*
38 *Sci Technol* **2022**, *117*, 174-182. DOI: 10.1016/j.jmst.2021.11.048.
39 (25) Orangi, J.; Hamade, F.; Davis, V. A.; Beidaghi, M. 3D Printing of Additive-Free 2D Ti3C2Tx
40 (MXene) Ink for Fabrication of Micro-Supercapacitors with Ultra-High Energy Densities. *Acs*
41 *Nano* **2020**, *14* (1), 640-650. DOI: 10.1021/acsnano.9b07325. Zhang, S. P.; Rana, S. S.; Bhatta,
42 T.; Pradhan, G. B.; Sharma, S.; Song, H. Y. S.; Jeong, S.; Park, J. Y. 3D printed smart glove with
43 pyramidal MXene/Ecoflex composite-based toroidal triboelectric nanogenerators for wearable
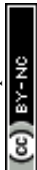44 human-machine interaction applications. *Nano Energy* **2023**, *106*. DOI: ARTN 108110

1   10.1016/j.nanoen.2022.108110. Yuan, M. M.; Wang, L. B.; Liu, X. Q.; Du, X. Y.; Zhang, G. B.;
2   Chang, Y. K.; Xia, Q. X.; Hu, Q. K.; Zhou, A. G. 3D printing quasi-solid-state micro-
3   supercapacitors with ultrahigh areal energy density based on high concentration MXene sediment.
4   *Chem Eng J* **2023**, *451*. DOI: ARTN 138686
5   10.1016/j.cej.2022.138686.
6   (26) Li, L.; Meng, J.; Bao, X. R.; Huang, Y. P.; Yan, X. P.; Qian, H. L.; Zhang, C.; Liu, T. X.
7   Direct-Ink-Write 3D Printing of Programmable Micro-Supercapacitors from MXene-Regulating
8   Conducting Polymer Inks. *Adv Energy Mater* **2023**, *13* (9). DOI: 10.1002/aenm.202203683.
9   (27) Nguyen, V. T.; Min, B. K.; Kim, S. K.; Yi, Y.; Choi, C. G. A flexible and high-performance
10 electrochromic smart window produced by WO3/Ti3C2Tx MXene hybrids. *J Mater Chem C* **2021**,
11 *9* (9), 3183-3192. DOI: 10.1039/d0tc05547f. Li, Y. Y.; Wang, Y. Q.; Lu, J.; Wang, W. W.; Wang,
12 D. Synergistically photothermal Au Nanoprisms@MXene enable adaptive solar modulation of
13 HA-PNIPAM hydrogels for smart window br. *Chem Eng J* **2023**, *457*. DOI: ARTN 141299
14 10.1016/j.cej.2023.141299. Li, Y. Y.; Wang, Y. Q.; Lu, J.; Wang, W. W.; Wang, D.
15 Synergistically photothermal Au Nanoprisms@MXene enable adaptive solar modulation of HA-
16 PNIPAM hydrogels for smart window (vol 457, 142119, 2023). *Chem Eng J* **2023**, *462*. DOI:
17 ARTN 142119
18 10.1016/j.cej.2023.142119. Kumar, S.; Park, H. M.; Nguyen, V. H.; Kim, M.; Nasir, N.; Kumar,
19 M.; Seo, Y. Application dependent stability of Ti3C2Tx MXene in PDLC-based smart-windows.
20 *Ceram Int* **2022**, *48* (23), 35092-35099. DOI: 10.1016/j.ceramint.2022.08.099. Kumar, S.; Kang,
21 D.; Nguyen, V.; Nasir, N.; Hong, H.; Kim, M.; Nguyen, D. C.; Lee, Y. J.; Lee, N.; Seo, Y.
22 Application of Titanium-Carbide MXene-Based Transparent Conducting Electrodes in Flexible
23 Smart Windows. *Acs Appl Mater Inter* **2021**, *13* (34), 40976-40985. DOI:
24 10.1021/acsami.1c12100.
25 (28) Dai, Y.; Wu, X. Y.; Li, L. L.; Zhang, Y.; Deng, Z. M.; Yu, Z. Z.; Zhang, H. B. 3D printing of
26 resilient, lightweight and conductive MXene/reduced graphene oxide architectures for broadband
27 electromagnetic interference shielding. *J Mater Chem A* **2022**, *10* (21), 11375-11385. DOI:
28 10.1039/d2ta01388f. Han, M. K.; Shuck, C. E.; Rakhmanov, R.; Parchment, D.; Anasori, B.; Koo,
29 C. M.; Friedman, G.; Gogotsi, Y. Beyond Ti3C2Tx: MXenes for Electromagnetic Interference
30 Shielding. *Acs Nano* **2020**, *14* (4), 5008-5016. DOI: 10.1021/acsnano.0c01312.
31 (29) Shahzad, F.; Alhabeb, M.; Hatter, C. B.; Anasori, B.; Hong, S. M.; Koo, C. M.; Gogotsi, Y.
32 Electromagnetic interference shielding with 2D transition metal carbides (MXenes). *Science* **2016**,
33 *353* (6304), 1137-1140. DOI: 10.1126/science.aag2421.
34 (30) Lai, S.; Jeon, J.; Jang, S. K.; Xu, J.; Choi, Y. J.; Park, J. H.; Hwang, E.; Lee, S. Surface group
35 modification and carrier transport properties of layered transition metal carbides (Ti2CTx, T: -OH,
36 -F and -O) (vol 7, pg 19390, 2015). *Nanoscale* **2016**, *8* (2), 1216-1216. DOI: 10.1039/c5nr90214b.
37 Rakhi, R. B.; Ahmed, B.; Hedhili, M. N.; Anjum, D. H.; Alshareef, H. N. Effect of Postetch
38 Annealing Gas Composition on the Structural and Electrochemical Properties of Ti2CTx MXene
39 Electrodes for Supercapacitor Applications. *Chem Mater* **2015**, *27* (15), 5314-5323. DOI:
40 10.1021/acs.chemmater.5b01623.
41 (31) Zhao, J. X.; Lu, H. Y.; Wei, X. J.; Gao, Y. Y.; Song, Y. Z.; Xu, B. A. Direct writing additive-
42 free V2CTx MXene architectures enables Zn-ion hybrid capacitor with ultrahigh energy density.
43 *J Energy Storage* **2023**, *66*. DOI: ARTN 107481
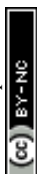44 10.1016/j.est.2023.107481.

Journal of Materials Chemistry A Accepted Manuscript

1 (32) Selvam, S. P.; Cho, S. B. Silver chalcogenide loaded V2CTx MXene-molecularly imprinted
2 polymer-based novel ratiometric sensor for the early predictive cancer marker: L-Fucose. *Chem*
3 *Eng J* **2023**, *469*. DOI: ARTN 144016

4 10.1016/j.cej.2023.144016.
5 (33) Halim, J.; Cook, K. M.; Naguib, M.; Eklund, P.; Gogotsi, Y.; Rosen, J.; Barsoum, M. W. X-
6 ray photoelectron spectroscopy of select multi-layered transition metal carbides (MXenes). *Appl*
7 *Surf Sci* **2016**, *362*, 406-417. DOI: 10.1016/j.apsusc.2015.11.089. Yan, Y. F.; Han, H.; Dai, Y. J.;
8 Zhu, H.; Liu, W. H.; Tang, X.; Gan, W.; Li, H. Nb2CTx MXene Nanosheets for Dye Adsorption.
9 *Acs Appl Nano Mater* **2021**, *4* (11), 11763-11769. DOI: 10.1021/acsanm.1c02339.
10 (34) Zhang, Y. K.; Zhang, G. F.; Zhao, S.; Gao, A. L.; Cui, J.; Yan, Y. H. Three-Dimensional
11 MXene-Based Functional Materials for Water Treatment: Preparation, Functional Tailoring, and
12 Applications. *Ind Eng Chem Res* **2023**, *62* (19), 7297-7335. DOI: 10.1021/acs.iecr.3c00306. Li,
13 M.; Dai, X. G.; Wang, M. N.; Bai, H. Bioinspired Macroporous Materials of MXene Nanosheets:
14 Ice-Templated Assembly and Multifunctional Applications. *Small Methods* **2023**. DOI:
15 10.1002/smtd.202300213. Korkmaz, H.; Hasar, U. C.; Ramahi, O. M. Thin-film MXene-based
16 metamaterial absorber design for solar cell applications. *Opt Quant Electron* **2023**, *55* (6). DOI:
17 ARTN 530
18 10.1007/s11082-023-04810-z. Khot, A. C.; Dongale, T. D.; Nirmal, K. A.; Deepthi, J. K.; Sutar,
19 S. S.; Kim, T. G. 2D Ti3C2Tx MXene-derived self-assembled 3D TiO2nanoflowers for
20 nonvolatile memory and synaptic learning applications. *J Mater Sci Technol* **2023**, *150*, 1-10. DOI:
21 10.1016/j.jmst.2023.01.003.
22 (35) Szuplewska, A.; Kulpińska, D.; Dybko, A.; Jastrzębska, A. M.; Wojciechowski, T.;
23 Rozmysłowska, A.; Chudy, M.; Grabowska-Jadach, I.; Ziemkowska, W.; Brzózka, Z.; et al. 2D
24 Ti2C (MXene) as a novel highly efficient and selective agent for photothermal therapy. *Materials*
25 *Science and Engineering: C* **2019**, *98*, 874-886. DOI: https://doi.org/10.1016/j.msec.2019.01.021.
26 (36) Tian, M.; Gan, W.; Oh, E.-S. MXene Clay (Ti2C)-Containing In Situ Polymerized Hollow
27 Core–Shell Binder for Silicon-Based Anodes in Lithium-Ion Batteries. *Acs Omega* **2023**, *8* (51),
28 49302-49310. DOI: 10.1021/acsomega.3c07752.
29 (37) Wu, Y.; Li, J.; Sui, G.; Chai, D.-F.; Li, Y.; Guo, D.; Chu, D.; Liang, K. Interface and doping
30 engineering of V2C-MXene-based electrocatalysts for enhanced electrocatalysis of overall water
31 splitting. *Carbon Energy* **2024**, *6* (10), e583. DOI: https://doi.org/10.1002/cey2.583.
32 (38) Jenitha, M.; Durgalakshmi, D.; Balakumar, S.; Rakkesh, R. A. Vanadium-based MXenes:
33 synthesis, structural insights, and electrochemical properties for Zn-ion battery applications: a
34 beginner's guide. *Emergent Materials* **2024**. DOI: 10.1007/s42247-024-00916-6.
35 (39) Ponnalagar, D.; Hang, D.-R.; Islam, S. E.; Liang, C.-T.; Chou, M. M. C. Recent progress in
36 two-dimensional Nb2C MXene for applications in energy storage and conversion. *Mater Design*
37 **2023**, *231*, 112046. DOI: https://doi.org/10.1016/j.matdes.2023.112046.
38 (40) Palisaitis, J.; Persson, I.; Halim, J.; Rosen, J.; Persson, P. O. Å. On the Structural Stability of
39 MXene and the Role of Transition Metal Adatoms. *Nanoscale* **2018**, *10* (23), 10850-10855,
40 10.1039/C8NR01986J. DOI: 10.1039/C8NR01986J.
41 (41) Yang, L.; Du, J.; Deng, J.; Sulaiman, N. H. M.; Feng, X.; Liu, C.; Zhou, X. Defective Nb2C
42 MXene Cocatalyst on TiO2 Microsphere for Enhanced Photocatalytic CO2 Conversion to
43 Methane. *Small* **2024**, *20* (19), 2307007. DOI: https://doi.org/10.1002/smll.202307007.
44 (42) Cheng, Y.-W.; Dai, J.-H.; Zhang, Y.-M.; Song, Y. Two-Dimensional, Ordered, Double
45 Transition Metal Carbides (MXenes): A New Family of Promising Catalysts for the Hydrogen
46 Evolution Reaction. *The Journal of Physical Chemistry C* **2018**, *122* (49), 28113-28122. DOI:

1 10.1021/acs.jpcc.8b08914. He, M.; Zhou, Y.; Luo, Q.; Yang, J. Platinum monolayer dispersed on
2 MXenes for electrocatalyzed hydrogen evolution: a first-principles study. *Nanoscale* **2024**, *16*
3 (33), 15670-15676, 10.1039/D4NR01864H. DOI: 10.1039/D4NR01864H.
4 (43) Gao, Y.; Cao, Y.; Zhuo, H.; Sun, X.; Gu, Y.; Zhuang, G.; Deng, S.; Zhong, X.; Wei, Z.; Li,
5 X.; et al. Mo2TiC2 MXene: A Promising Catalyst for Electrocatalytic Ammonia Synthesis.
6 *Catalysis Today* **2020**, *339*, 120-126. DOI: https://doi.org/10.1016/j.cattod.2018.12.029.
7 (44) Hua, S.; Huang, B.; Le, Z.; Huang, Q. Mo-based Mo2Ti2C3 MXene as photothermal
8 nanoagents to eradicating methicillin-resistant Staphylococcus aureus with photothermal therapy.
9 *Mater Design* **2023**, *231*, 112033. DOI: https://doi.org/10.1016/j.matdes.2023.112033.
10 (45) Saraf, M.; Chacon, B.; Ippolito, S.; Lord, R. W.; Anayee, M.; Wang, R.; Inman, A.; Shuck,
11 C. E.; Gogotsi, Y. Enhancing Charge Storage of Mo2Ti2C3 MXene by Partial Oxidation. *Adv*
12 *Funct Mater* **2024**, *34* (1), 2306815. DOI: https://doi.org/10.1002/adfm.202306815.
13 (46) Yoon, J.; Kim, S.; Park, K. H.; Lee, S.; Kim, S. J.; Lee, H.; Oh, T.; Koo, C. M. Biocompatible
14 and Oxidation-Resistant Ti3C2Tx MXene with Halogen-Free Surface Terminations. *Small*
15 *Methods* **2023**. DOI: ARTN 2201579

16 10.1002/smtd.202201579. Fan, Q.; Yi, M. J.; Chai, C. X.; Li, W. W.; Qi, P.; Wang, J. H.; Hao, J.
17 C. Oxidation stability enhanced MXene-based porous materials derived from water-in-ionic liquid
18 Pickering emulsions for wearable piezoresistive sensor and oil/water separation applications. *J*
19 *Colloid Interf Sci* **2022**, *618*, 311-321. DOI: 10.1016/j.jcis.2022.03.073. Habib, T.; Zhao, X. F.;
20 Shah, S. A.; Chen, Y. X.; Sun, W. M.; An, H.; Lutkenhaus, J. L.; Radovic, M.; Green, M. J.
21 Oxidation stability of Ti3C2Tx MXene nanosheets in solvents and composite films. *Npj 2d Mater*
22 *Appl* **2019**, *3*. DOI: ARTN 8
23 10.1038/s41699-019-0089-3.
24 (47) Zhang, C. F. J.; Pinilla, S.; McEyoy, N.; Cullen, C. P.; Anasori, B.; Long, E.; Park, S. H.;
25 Seral-Ascaso, A.; Shmeliov, A.; Krishnan, D.; et al. Oxidation Stability of Colloidal Two-
26 Dimensional Titanium Carbides (MXenes). *Chem Mater* **2017**, *29* (11), 4848-4856. DOI:
27 10.1021/acs.chemmater.7b00745.
28 (48) Kim, J.; Yoon, Y.; Kim, S. K.; Park, S.; Song, W.; Myung, S.; Jung, H. K.; Lee, S. S.; Yoon,
29 D. H.; An, K. S. Chemically Stabilized and Functionalized 2D-MXene with Deep Eutectic
30 Solvents as Versatile Dispersion Medium. *Adv Funct Mater* **2021**, *31* (13). DOI: ARTN 2008722

31 10.1002/adfm.202008722.
32 (49) Zhao, X. F.; Cao, H. X.; Coleman, B. J.; Tan, Z. Y.; Echols, I. J.; Pentzer, E. B.; Lutkenhaus,
33 J. L.; Radovic, M.; Green, M. J. The Role of Antioxidant Structure in Mitigating Oxidation in
34 Ti3C2Tx and Ti2CTx MXenes. *Adv Mater Interfaces* **2022**, *9* (20). DOI: ARTN 2200480

35 10.1002/admi.202200480.
36 (50) Lee, S.; Kim, E. H.; Yu, S.; Kim, H.; Park, C.; Lee, S. W.; Han, H.; Jin, W.; Lee, K.; Lee, C.
37 E.; et al. Polymer-Laminated Ti3C2Tx MXene Electrodes for Transparent and Flexible Field-
38 Driven Electronics. *Acs Nano* **2021**, *15* (5), 8940-8952. DOI: 10.1021/acsnano.1c01621.
39 (51) Shamsabadi, A. A.; Isfahani, A. P.; Salestan, S. K.; Rahimpour, A.; Ghalei, B.; Sivaniah, E.;
40 Soroush, M. Pushing Rubbery Polymer Membranes To Be Economic for CO2 Separation:
41 Embedment with Ti3C2Tx MXene Nanosheets. *Acs Appl Mater Inter* **2020**, *12* (3), 3984-3992.
42 DOI: 10.1021/acsami.9b19960. Amin, I.; van den Brekel, H.; Nemani, K.; Batyrev, E.; de Vooys,
43 A.; van der Weijde, H.; Anasori, B.; Shiju, N. R. Ti3C2Tx MXene Polymer Composites for
44 Anticorrosion: An Overview and Perspective. *Acs Appl Mater Inter* **2022**. DOI:
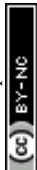45 10.1021/acsami.2c11953.

1   (52) Natu, V.; Hart, J. L.; Sokol, M.; Chiang, H.; Taheri, M. L.; Barsoum, M. W. Edge Capping
2   of 2D-MXene Sheets with Polyanionic Salts To Mitigate Oxidation in Aqueous Colloidal
3   Suspensions. *Angew Chem Int Edit* **2019**, *58* (36), 12655-12660. DOI: 10.1002/anie.201906138.
4   (53) Wu, C. W.; Unnikrishnan, B.; Chen, I. W. P.; Harroun, S. G.; Chang, H. T.; Huang, C. C.
5   Excellent oxidation resistive MXene aqueous ink for micro-supercapacitor application. *Energy*
6   *Storage Mater* **2020**, *25*, 563-571. DOI: 10.1016/j.ensm.2019.09.026.
7   (54) Shi, Y. Q.; Liu, C.; Duan, Z. P.; Yu, B.; Liu, M. H.; Song, P. A. Interface engineering of
8   MXene towards super-tough and strong polymer nanocomposites with high ductility and excellent
9   fire safety. *Chem Eng J* **2020**, *399*. DOI: ARTN 125829

10 10.1016/j.cej.2020.125829.
11 (55) Liu, M. F.; Zhuo, Y. L.; Sarycheva, A.; Gogotsi, Y.; Bissett, M. A.; Young, R. J.; Kinloch, I.
12 A. Deformation of and Interfacial Stress Transfer in Ti3C2 MXene-Polymer Composites. *Acs Appl*
13 *Mater Inter* **2022**, *14* (8), 10681-10690. DOI: 10.1021/acsami.1c21611. Wan, S. J.; Li, X.; Wang,
14 Y. L.; Chen, Y.; Xie, X.; Yang, R.; Tomsia, A. P.; Jiang, L.; Cheng, Q. F. Strong sequentially
15 bridged MXene sheets. *P Natl Acad Sci USA* **2020**, *117* (44), 27154-27161. DOI:
16 10.1073/pnas.2009432117.
17 (56) Soomro, R. A.; Zhang, P.; Fan, B. M.; Wei, Y.; Xu, B. Progression in the Oxidation Stability
18 of MXenes. *Nano-Micro Lett* **2023**, *15* (1). DOI: ARTN 108

19 10.1007/s40820-023-01069-7.
20 (57) Mozafari, M.; Soroush, M. Surface functionalization of MXenes. *Materials Advances* **2021**,
21 *2* (22), 7277-7307, 10.1039/D1MA00625H. DOI: 10.1039/D1MA00625H.
22 (58) Fu, Z. H.; Wang, N.; Legut, D.; Si, C.; Zhang, Q. F.; Du, S. Y.; Germann, T. C.; Francisco, J.
23 S.; Zhang, R. F. Rational Design of Flexible Two-Dimensional MXenes with Multiple
24 Functionalities. *Chem Rev* **2019**, *119* (23), 11980-12031. DOI: 10.1021/acs.chemrev.9b00348.
25 (59) Zhang, X. S.; Wang, X. F.; Lei, Z. W.; Wang, L. L.; Tian, M. W.; Zhu, S. F.; Xiao, H.; Tang,
26 X. N.; Qu, L. J. Flexible MXene-Decorated Fabric with Interwoven Conductive Networks for
27 Integrated Joule Heating, Electromagnetic Interference Shielding, and Strain Sensing
28 Performances. *Acs Appl Mater Inter* **2020**, *12* (12), 14459-14467. DOI: 10.1021/acsami.0c01182.
29 (60) Li, L.; Fu, X. Y.; Chen, S.; Uzun, S.; Levitt, A. S.; Shuck, C. E.; Han, W.; Gogotsi, Y.
30 Hydrophobic and Stable MXene-Polymer Pressure Sensors for Wearable Electronics. *Acs Appl*
31 *Mater Inter* **2020**, *12* (13), 15362-15369. DOI: 10.1021/acsami.0c00255.
32 (61) Chen, K.; Hu, Y. P.; Wang, F.; Liu, M. X.; Liu, P.; Li, C.; Yu, Y. S.; Xiao, X. F.; Feng, Q.
33 Ultra-stretchable, adhesive, and self-healing MXene/polyampholytes hydrogel as flexible and
34 wearable epidermal sensors. *Colloid Surface A* **2022**, *645*. DOI: ARTN 128897

35 10.1016/j.colsurfa.2022.128897.
36 (62) Cui, Y. L.; Zhu, J.; Tong, H.; Zou, R. Advanced perspectives on MXene composite
37 nanomaterials: Types synthetic methods, thermal energy utilization and 3D-printed techniques.
38 *Iscience* **2023**, *26* (1). DOI: ARTN 105824

39 10.1016/j.isci.2022.105824.
40 (63) Li, T.; Chen, T. H.; Shen, X. C.; Shi, H. H.; Jabari, E.; Naguib, H. E. A binder jet 3D printed
41 MXene composite for strain sensing and energy storage application. *Nanoscale Adv* **2022**, *4* (3),
42 916-925. DOI: 10.1039/d1na00698c.
43 (64) Liu, H. D.; Du, C. F.; Liao, L. L.; Zhang, H. J.; Zhou, H. Q.; Zhou, W. C.; Ren, T. N.; Sun,
44 Z. C.; Lu, Y. F.; Nie, Z. T.; et al. Approaching intrinsic dynamics of MXenes hybrid hydrogel for

1 3D printed multimodal intelligent devices with ultrahigh superelasticity and temperature
2 sensitivity. *Nat Commun* **2022**, *13* (1). DOI: ARTN 3420

3 10.1038/s41467-022-31051-7.
4 (65) Adekoya, G. J.; Adekoya, O. C.; Sadiku, R. E.; Hamam, Y.; Ray, S. S. Applications of
5 MXene-Containing Polypyrrole Nanocomposites in Electrochemical Energy Storage and
6 Conversion. *Acs Omega* **2022**. DOI: 10.1021/acsomega.2c02706. Liu, S.-M.; Chen, M.-X.; Xie,
7 Y.; Liu, D.-H.; Zheng, J.-F.; Xiong, X.; Jiang, H.; Wang, L.-C.; Luo, H.; Han, K. Nb2CTx MXene
8 boosting PEO polymer electrolyte for all-solid-state Li-S batteries: two birds with one stone
9 strategy to enhance Li+ conductivity and polysulfide adsorptivity. *Rare Metals* **2023**, *42* (8), 2562-
10 2576. DOI: 10.1007/s12598-022-02260-2.
11 (66) Yan, H.; Li, W.; Li, H.; Fan, X. Q.; Zhu, M. H. Ti3C2 MXene nanosheets toward high-
12 performance corrosion inhibitor for epoxy coating. *Prog Org Coat* **2019**, *135*, 156-167. DOI:
13 10.1016/j.porgcoat.2019.06.013.
14 (67) He, X.; Wu, J.; Huang, X.; Chen, Y.; Zhang, L.; Sheng, X. Three-in-one polymer
15 nanocomposite coating via constructing tannic acid functionalized MXene/BP hybrids with
16 superior corrosion resistance, friction resistance, and flame-retardancy. *Chemical Engineering*
17 *Science* **2024**, *283*, 119429. DOI: https://doi.org/10.1016/j.ces.2023.119429.
18 (68) Li, L.; Liu, X. Y.; Wang, J. F.; Yang, Y. Y.; Cao, Y. X.; Wang, W. J. New application of
19 MXene in polymer composites toward remarkable anti-dripping performance for flame retardancy.
20 *Compos Part a-Appl S* **2019**, *127*. DOI: ARTN 105649

21 10.1016/j.compositesa.2019.105649.
22 (69) Jin, Y.; Fan, Y. Y.; Meng, X. X.; Li, J. Y.; Li, C.; Sunarso, J.; Yang, N. T.; Meng, B.; Zhang,
23 W. M. Modeling of hydrated cations transport through 2D MXene (Ti3C2Tx) membranes for
24 water purification. *J Membrane Sci* **2021**, *631*. DOI: ARTN 119346

25 10.1016/j.memsci.2021.119346.
26 (70) Hu, J. X.; Zhan, Y. Q.; Zhang, G. Y.; Feng, Q. Y.; Yang, W.; Chiao, Y. H.; Zhang, S. R.; Sun,
27 A. Durable and super-hydrophilic/underwater super-oleophobic two-dimensional MXene
28 composite lamellar membrane with photocatalytic self-cleaning property for efficient oil/water
29 separation in harsh environments. *J Membrane Sci* **2021**, *637*. DOI: ARTN 119627

30 10.1016/j.memsci.2021.119627.
31 (71) Ren, C. E.; Hatzell, K. B.; Alhabeb, M.; Ling, Z.; Mahmoud, K. A.; Gogotsi, Y. Charge- and
32 Size-Selective Ion Sieving Through Ti3C2Tx MXene Membranes. *J Phys Chem Lett* **2015**, *6* (20),
33 4026-4031. DOI: 10.1021/acs.jpclett.5b01895. Han, R. L.; Ma, X. F.; Xie, Y. L.; Teng, D.; Zhang,
34 S. H. Preparation of a new 2D MXene/PES composite membrane with excellent hydrophilicity
35 and high flux. *Rsc Adv* **2017**, *7* (89), 56204-56210. DOI: 10.1039/c7ra10318b.
36 (72) Deng, B.; Lian, H.; Xue, B.; Song, R.; Chen, S.; Wang, Z.; Xu, T.; Dong, H.; Wang, S.
37 Niobium-Carbide MXene Modified Hybrid Hole Transport Layer Enabling High-Performance
38 Organic Solar Cells Over 19%. *Small* **2023**, *19* (23), 2207505. DOI:
39 https://doi.org/10.1002/smll.202207505. Assunção, J. P. F.; Lemos, H. G.; Rossato, J. H. H.;
40 Nogueira, G. L.; Lima, J. V. M.; Fernandes, S. L.; Nishihora, R. K.; Fernandes, R. V.; Lourenço,
41 S. A.; Bagnis, D.; et al. Interface passivation with Ti3C2Tx-MXene doped PMMA film for highly
42 efficient and stable inverted perovskite solar cells. *J Mater Chem C* **2024**, *12* (2), 562-574,
43 10.1039/D3TC03810F. DOI: 10.1039/D3TC03810F.

Journal of Materials Chemistry A Accepted Manuscript

1   (73) Gu, Q.; Wang, J.; Peng, R.; Song, W.; Xie, L.; Zhou, R.; Ge, Z. Nonfullerene Organic Solar
2   Cells with 18.17% Efficiency Obtained Using a V2C/PEDOT:PSS Composite Hole-Transport
3   Layer. *ACS Applied Energy Materials* **2023**, *6* (3), 1982-1988. DOI: 10.1021/acsaem.2c03883.
4   (74) Rasool, K.; Helal, M.; Ali, A.; Ren, C. E.; Gogotsi, Y.; Mahmoud, K. A. Antibacterial Activity
5   of Ti3C2Tx MXene. *Acs Nano* **2016**, *10* (3), 3674-3684. DOI: 10.1021/acsnano.6b00181.
6   (75) Purbayanto, M. A. K.; Jakubczak, M.; Bury, D.; Nair, V. G.; Birowska, M.; Moszczynska,
7   D.; Jastrzebska, A. Tunable Antibacterial Activity of a Polypropylene Fabric Coated with Bristling
8   Ti3C2Tx MXene Flakes Coupling the Nanoblade Effect with ROS Generation. *Acs Appl Nano*
9   *Mater* **2022**, *5* (4), 5373-5386. DOI: 10.1021/acsanm.2c00365.
10 (76) Gao, Y. J.; Dong, Y. H.; Yang, S. T.; Mo, A. C.; Zeng, X.; Chen, Q. M.; Peng, Q. Size-
11 dependent photothermal antibacterial activity of Ti3C2Tx MXene nanosheets against methicillin-
12 resistant Staphylococcus aureus. *J Colloid Interf Sci* **2022**, *617*, 533-541. DOI:
13 10.1016/j.jcis.2022.03.032.
14 (77) Pan, Y.; Hang, Y. T.; Zhao, X. H.; Liu, G. P.; Jin, W. Q. Optimizing separation performance
15 and interfacial adhesion of PDMS/PVDF composite membranes for butanol recovery from
16 aqueous solution. *J Membrane Sci* **2019**, *579*, 210-218. DOI: 10.1016/j.memsci.2019.03.008.
17 (78) Shi, X. Y.; Gao, M. H.; Hu, W. W.; Luo, D.; Hu, S. Z.; Huang, T.; Zhang, N.; Wang, Y.
18 Largely enhanced adsorption performance and stability of MXene through in-situ depositing
19 polypyrrole nanoparticles. *Sep Purif Technol* **2022**, *287*. DOI: ARTN 120596

20 10.1016/j.seppur.2022.120596.
21 (79) Sharma, P. K.; Pradhan, S. K.; Pramanik, M.; Limaye, M. V.; Singh, S. B. MXene Based
22 Electrospun Polymer Electrolyte fibers: Fabrication and Enhanced Ionic Conductivity.
23 *Chemistryselect* **2022**, *7* (40). DOI: ARTN e202201986

24 10.1002/slct.202201986.
25 (80) Mayerberger, E. A.; Urbanek, O.; McDaniel, R. M.; Street, R. M.; Barsoum, M. W.; Schauer,
26 C. L. Preparation and characterization of polymer-Ti3C2Tx (MXene) composite nanofibers
27 produced via electrospinning. *J Appl Polym Sci* **2017**, *134* (37). DOI: Artn 45295

28 10.1002/App.45295.
29 (81) Boota, M.; Anasori, B.; Voigt, C.; Zhao, M. Q.; Barsoum, M. W.; Gogotsi, Y.
30 Pseudocapacitive Electrodes Produced by Oxidant-Free Polymerization of Pyrrole between the
31 Layers of 2D Titanium Carbide (MXene). *Adv Mater* **2016**, *28* (7), 1517-1522. DOI:
32 10.1002/adma.201504705.
33 (82) Wang, Q. W.; Zhang, H. B.; Liu, J.; Zhao, S.; Xie, X.; Liu, L. X.; Yang, R.; Koratkar, N.; Yu,
34 Z. Z. Multifunctional and Water-Resistant MXene-Decorated Polyester Textiles with Outstanding
35 Electromagnetic Interference Shielding and Joule Heating Performances. *Adv Funct Mater* **2019**,
36 *29* (7). DOI: ARTN 1806819

37 10.1002/adfm.201806819.
38 (83) Yi, P.; Zou, H. H.; Yu, Y. H.; Li, X. F.; Li, Z. Y.; Deng, G.; Chen, C. Y.; Fang, M.; He, J. Z.;
39 Sun, X.; et al. MXene-Reinforced Liquid Metal/Polymer Fibers via Interface Engineering for
40 Wearable Multifunctional Textiles. *Acs Nano* **2022**. DOI: 10.1021/acsnano.2c04863.
41 (84) Zhou, T. Z.; Yu, Y. Z.; He, B.; Wang, Z.; Xiong, T.; Wang, Z. X.; Liu, Y. T.; Xin, J. W.; Qi,
42 M.; Zhang, H. Z.; et al. Ultra-compact MXene fibers by continuous and controllable synergy of
43 interfacial interactions and thermal drawing-induced stresses. *Nat Commun* **2022**, *13* (1). DOI:
44 ARTN 4564

1   10.1038/s41467-022-32361-6.

2   (85) Tan, K. H.; Samylingam, L.; Aslfattahi, N.; Saidur, R.; Kadirgama, K. Optical and
3   conductivity studies of polyvinyl alcohol-MXene (PVA-MXene) nanocomposite thin films for
4   electronic applications. *Opt Laser Technol* **2021**, *136*. DOI: ARTN 106772

5   10.1016/j.optlastec.2020.106772. Yu, W. J.; Li, Y.; Xin, B. J.; Lu, Z. MXene/PVA Fiber-based
6   Supercapacitor with Stretchability for Wearable Energy Storage. *Fiber Polym* **2022**, *23* (11), 2994-
7   3001. DOI: 10.1007/s12221-022-4389-4. Yi, Y.; Chiao, M.; Mahmoud, K. A.; Wang, B. An
8   MXene-doped PVA/PVP hydrogel-based strain sensor applicable in liquid environment. *Smart*
9   *Mater Struct* **2023**, *32* (2). DOI: ARTN 025010

10   10.1088/1361-665X/acafbc. Li, L. M.; Ji, X. F.; Chen, K. Conductive, self-healing, and
11   antibacterial Ag/MXene-PVA hydrogel as wearable skin-like sensors. *J Biomater Appl* **2023**, *37*
12   (7), 1169-1181. DOI: Artn 08853282221131137

13   10.1177/08853282221131137. Li, C. X.; Zheng, A.; Zhou, J. Y.; Huang, W. W.; Zhang, Y.; Han,
14   J. X.; Cao, L. Y.; Yang, D. Y. A self-adhesive, self-healing and antibacterial hydrogel based on
15   PVA/MXene-Ag/sucrose for fast-response, high-sensitivity and ultra-durable strain sensors. *New*
16   *J Chem* **2023**, *47* (14), 6621-6630. DOI: 10.1039/d3nj00586k. Haataja, R.; Myllymaki, S.;
17   Laitinen, O.; Jantunen, H.; Liimatainen, H. Controlling the cell and surface architecture of
18   cellulose nanofiber/PVA/ Ti3C2TX MXene hybrid cryogels for optimized permittivity and EMI
19   shielding performance. *Mater Design* **2023**, *228*. DOI: ARTN 111855
20   10.1016/j.matdes.2023.111855.

21   (86) Wang, D. Z.; Lin, Y.; Hu, D. W.; Jiang, P. K.; Huang, X. Y. Multifunctional 3D-
22   MXene/PDMS nanocomposites for electrical, thermal and triboelectric applications. *Compos Part*
23   *a-Appl S* **2020**, *130*. DOI: ARTN 105754

24   10.1016/j.compositesa.2019.105754. Lu, W. G.; Mustafa, B.; Wang, Z. Y.; Lian, F. Z.; Yu, G. L.
25   PDMS-Encapsulated MXene@Polyester Fabric Strain Sensor for Multifunctional Sensing
26   Applications. *Nanomaterials-Basel* **2022**, *12* (5). DOI: ARTN 871

27   10.3390/nano12050871. Liu, H. B.; Fu, R. L.; Su, X. Q.; Wu, B. Y.; Wang, H.; Xu, Y.; Liu, X. H.
28   Electrical insulating MXene/PDMS/BN composite with enhanced thermal conductivity for
29   electromagnetic shielding application. *Compos Commun* **2021**, *23*. DOI: ARTN 100593
30   10.1016/j.coco.2020.100593.

31   (87) Faruk, O.; Adak, B. Recent advances in PEDOT:PSS integrated graphene and MXene-based
32   composites for electrochemical supercapacitor applications. *Synthetic Met* **2023**, *297*. DOI: ARTN
33   117384

34   10.1016/j.synthmet.2023.117384. Chetana, S.; Upadhyay, S.; Joshi, N. C.; Kumar, N.; Choudhary,
35   P.; Sharma, N.; Thakur, V. N. A facile supercritical fluid synthesis of cobalt sulfide integrated with
36   MXene and PANI/PEDOT nanocomposites as electrode material for supercapacitor applications.
37   *Flatchem* **2023**, *37*. DOI: ARTN 100456

38   10.1016/j.flatc.2022.100456. Zhang, M. Y.; Yang, W. K.; Wang, Z. Q.; Liu, H.; Yin, R.; Liu, C.
39   T.; Shen, C. Y. Highly compressible and thermal insulative conductive
40   MXene/PEDOT:PSS@melamine foam for promising wearable piezoresistive sensor. *Appl Phys*
41   *Lett* **2023**, *122* (4). DOI: Artn 043507

42   10.1063/5.0137571. Jin, X. Z.; Yang, Z. Y.; Huang, C. H.; Yang, J. H.; Wang, Y.
43   PEDOT:PSS/MXene/PEG composites with remarkable thermal management performance and
44   excellent HF-band & X-band electromagnetic interference shielding efficiency for electronic
45   packaging. *Chem Eng J* **2022**, *448*. DOI: ARTN 137599

Journal of Materials Chemistry A Accepted Manuscript

10.1016/j.cej.2022.137599.

(88) Cheng, T.; Yang, X. L.; Yang, S.; Li, L.; Liu, Z. T.; Qu, J.; Meng, C. F.; Li, X. C.; Zhang, Y. Z.; Lai, W. Y. Flexible Transparent Bifunctional Capacitive Sensors with Superior Areal Capacitance and Sensing Capability based on PEDOT:PSS/MXene/Ag Grid Hybrid Electrodes. *Adv Funct Mater* **2023**, *33* (5). DOI: ARTN 2210997

10.1002/adfm.202210997.

(89) He, Z. W.; Xie, H. M.; Wu, H. Q.; Chen, J. H.; Ma, S. Y.; Duan, X.; Chen, A. Q.; Kong, Z. Recent Advances in MXene/Polyaniline-Based Composites for Electrochemical Devices and Electromagnetic Interference Shielding Applications. *Acs Omega* **2021**, *6* (35), 22468-22477. DOI: 10.1021/acsomega.1c02996. Elancheziyan, M.; Eswaran, M.; Shuck, C. E.; Senthilkumar, S.; Elumalai, S.; Dhanusuraman, R.; Ponnusamy, V. K. Facile synthesis of polyaniline/titanium carbide (MXene) nanosheets/palladium nanocomposite for efficient electrocatalytic oxidation of methanol for fuel cell application. *Fuel* **2021**, *303*. DOI: 10.1016/j.fuel.2021.121329.

(90) Yang, C. Q.; Zhang, D. Z.; Wang, D. Y.; Luan, H. X.; Chen, X. Y.; Yan, W. Y. In Situ Polymerized MXene/Polypyrrole/Hydroxyethyl Cellulose- Based Flexible Strain Sensor Enabled by Machine Learning for Handwriting Recognition. *Acs Appl Mater Inter* **2023**, *15* (4), 5811-5821. DOI: 10.1021/acsami.2c18989. Wang, L.; Wu, H.; Zhai, X.; Shi, J.; Zhou, Q. Q.; Li, H.; Wan, J. M. Ti3C2Tx MXene/dopamine-modified polypyrrole flexible composite electrodes with application in energy storage devices. *J Alloy Compd* **2023**, *946*. DOI: ARTN 169347

10.1016/j.jallcom.2023.169347. Luo, W. L.; Sun, Y.; Han, Y. Q.; Ding, J. X.; Li, T. X.; Hou, C. P.; Ma, Y. Flexible Ti3C2Tx MXene/polypyrrole composite films for high-performance all-solid asymmetric supercapacitors. *Electrochim Acta* **2023**, *441*. DOI: ARTN 141818

10.1016/j.electacta.2023.141818. Liu, Z. L.; Zhang, R.; Xiong, H. L.; Zhang, L. L.; Li, J. Z.; Wang, L. Q.; Qiao, Z. A. Swelling-Induced Structural Transformation Strategy: Controllable Synthesis of 2D Porous Polypyrrole/MXene Heterostructures with Tunable Pore Structures. *Adv Mater Interfaces* **2023**, *10* (11). DOI: 10.1002/admi.202202501.

(91) Wu, Z. T.; Shang, T. X.; Deng, Y. Q.; Tao, Y.; Yang, Q. H. The Assembly of MXenes from 2D to 3D. *Adv Sci* **2020**, *7* (7). DOI: ARTN 1903077

10.1002/advs.201903077.

(92) He, S.; Sun, X.; Zhang, H.; Yuan, C.; Wei, Y.; Li, J. Preparation Strategies and Applications of MXene-Polymer Composites: A Review. *Macromolecular Rapid Communications* **2021**, *42* (19), 2100324. DOI: https://doi.org/10.1002/marc.202100324.

(93) Riazi, H.; Nemani, S. K.; Grady, M. C.; Anasori, B.; Soroush, M. Ti3C2 MXene–polymer nanocomposites and their applications. *J Mater Chem A* **2021**, *9* (13), 8051-8098, 10.1039/D0TA08023C. DOI: 10.1039/D0TA08023C.

(94) Gong, K.; Zhou, K.; Qian, X.; Shi, C.; Yu, B. MXene as emerging nanofillers for high-performance polymer composites: A review. *Composites Part B: Engineering* **2021**, *217*, 108867. DOI: https://doi.org/10.1016/j.compositesb.2021.108867.

(95) Chen, X.; Zhao, Y.; Li, L.; Wang, Y.; Wang, J.; Xiong, J.; Du, S.; Zhang, P.; Shi, X.; Yu, J. MXene/Polymer Nanocomposites: Preparation, Properties, and Applications. *Polymer Reviews* **2021**, *61* (1), 80-115. DOI: 10.1080/15583724.2020.1729179. Carey, M.; Barsoum, M. W. MXene polymer nanocomposites: a review. *Materials Today Advances* **2021**, *9*, 100120. DOI: https://doi.org/10.1016/j.mtadv.2020.100120. Aghamohammadi, H.; Amousa, N.; Eslami-Farsani, R. Recent advances in developing the MXene/polymer nanocomposites with multiple properties:

1 A review study. *Synthetic Met* **2021**, *273*, 116695. DOI:
2 https://doi.org/10.1016/j.synthmet.2020.116695.

3 (96) Naguib, M.; Kurtoglu, M.; Presser, V.; Lu, J.; Niu, J.; Heon, M.; Hultman, L.; Gogotsi, Y.;
4 Barsoum, M. W. Two-Dimensional Nanocrystals Produced by Exfoliation of Ti3AlC2. *Adv Mater*
5 **2011**, *23* (37), 4248-4253.

6 (97) Oyehan, T. A.; Salami, B. A.; Abdulrasheed, A. A.; Hambali, H. U.; Gbadamosi, A.; Valsami-
7 Jones, E.; Saleh, T. A. MXenes: Synthesis, properties, and applications for sustainable energy and
8 environment. *Appl Mater Today* **2023**, *35*, 101993. DOI:
9 https://doi.org/10.1016/j.apmt.2023.101993.

10 (98) Shuck, C. E.; Han, M.; Maleski, K.; Hantanasirisakul, K.; Kim, S. J.; Choi, J.; Reil, W. E. B.;
11 Gogotsi, Y. Effect of Ti3AlC2 MAX Phase on Structure and Properties of Resultant Ti3C2Tx
12 MXene. *Acs Appl Nano Mater* **2019**, *2* (6), 3368-3376. DOI: 10.1021/acsanm.9b00286.

13 (99) Natu, V.; Pai, R.; Sokol, M.; Carey, M.; Kalra, V.; Barsoum, M. W. 2D Ti3C2Tz MXene
14 Synthesized by Water-free Etching of Ti3AlC2 in Polar Organic Solvents. *Chem* **2020**, *6* (3), 616-
15 630. DOI: https://doi.org/10.1016/j.chempr.2020.01.019.

16 (100) Yang, S.; Zhang, P.; Wang, F.; Ricciardulli, A. G.; Lohe, M. R.; Blom, P. W. M.; Feng, X.
17 Fluoride-Free Synthesis of Two-Dimensional Titanium Carbide (MXene) Using A Binary
18 Aqueous System. *Angewandte Chemie International Edition* **2018**, *57* (47), 15491-15495. DOI:
19 https://doi.org/10.1002/anie.201809662.

20 (101) Liu, L.; Orbay, M.; Luo, S.; Duluard, S.; Shao, H.; Harmel, J.; Rozier, P.; Taberna, P.-L.;
21 Simon, P. Exfoliation and Delamination of Ti3C2Tx MXene Prepared via Molten Salt Etching
22 Route. *Acs Nano* **2022**, *16* (1), 111-118.

23 (102) Li, T.; Yao, L.; Liu, Q.; Gu, J.; Luo, R.; Li, J.; Yan, X.; Wang, W.; Liu, P.; Chen, B.; et al.
24 Fluorine-Free Synthesis of High-Purity Ti3C2T (T=OH, O) via Alkali Treatment. *Angewandte*
25 *Chemie International Edition* **2018**, *57* (21), 6115-6119. DOI:
26 https://doi.org/10.1002/anie.201800887.

27 (103) Wang, D.; Zhou, C.; Filatov, A. S.; Cho, W.; Lagunas, F.; Wang, M.; Vaikuntanathan, S.;
28 Liu, C.; Klie, R. F.; Talapin, D. V. Direct synthesis and chemical vapor deposition of 2D carbide
29 and nitride MXenes. *Science* **2023**, *379* (6638), 1242-1247. DOI: doi:10.1126/science.add9204.

30 (104) Halim, J.; Kota, S.; Lukatskaya, M. R.; Naguib, M.; Zhao, M.-Q.; Moon, E. J.; Pitock, J.;
31 Nanda, J.; May, S. J.; Gogotsi, Y.; et al. Synthesis and Characterization of 2D Molybdenum
32 Carbide (MXene). *Adv Funct Mater* **2016**, *26* (18), 3118-3127. DOI:
33 https://doi.org/10.1002/adfm.201505328.

34 (105) Rems, E.; Anayee, M.; Fajardo, E.; Lord, R. L.; Bugallo, D.; Gogotsi, Y.; Hu, Y.-J.
35 Computationally Guided Synthesis of MXenes by Dry Selective Extraction. *Adv Mater* **2023**, *35*
36 (45), 2305200. DOI: https://doi.org/10.1002/adma.202305200.

37 (106) Xiao, X.; Yu, H.; Jin, H.; Wu, M.; Fang, Y.; Sun, J.; Hu, Z.; Li, T.; Wu, J.; Huang, L.; et al.
38 Salt-Templated Synthesis of 2D Metallic MoN and Other Nitrides. *Acs Nano* **2017**, *11* (2), 2180-
39 2186. DOI: 10.1021/acsnano.6b08534.

40 (107) Ding, H.; Li, Y.; Li, M.; Chen, K.; Liang, K.; Chen, G.; Lu, J.; Palisaitis, J.; Persson, P. O.
41 Å.; Eklund, P.; et al. Chemical scissor–mediated structural editing of layered transition metal
42 carbides. *Science* **2023**, *379* (6637), 1130-1135. DOI: doi:10.1126/science.add5901.

43 (108) Kumar, S.; Kumari, N.; Seo, Y. MXenes: Versatile 2D materials with tailored surface
44 chemistry and diverse applications. *Journal of Energy Chemistry* **2024**, *90*, 253-293. DOI:
45 https://doi.org/10.1016/j.jechem.2023.11.031.

Journal of Materials Chemistry A Accepted Manuscript

1   (109) Schultz, T.; Frey, N. C.; Hantanasirisakul, K.; Park, S.; May, S. J.; Shenoy, V. B.; Gogotsi,
2   Y.; Koch, N. Surface Termination Dependent Work Function and Electronic Properties of
3   Ti3C2Tx MXene. *Chem Mater* **2019**, *31* (17), 6590-6597. DOI: 10.1021/acs.chemmater.9b00414.
4   Caffrey, N. M. Effect of mixed surface terminations on the structural and electrochemical
5   properties of two-dimensional Ti3C2T2 and V2CT2 MXenes multilayers. *Nanoscale* **2018**, *10*
6   (28), 13520-13530, 10.1039/C8NR03221A. DOI: 10.1039/C8NR03221A.
7   (110) Su, T. M.; Ma, X. H.; Tong, J. H.; Ji, H. B.; Qin, Z. Z.; Wu, Z. L. Surface engineering of
8   MXenes for energy and environmental applications. *J Mater Chem A* **2022**, *10* (19), 10265-10296.
9   DOI: 10.1039/d2ta01140a.
10 (111) Mohammadi, A. V.; Rosen, J.; Gogotsi, Y. The world of two-dimensional carbides and
11 nitrides (MXenes). *Science* **2021**, *372* (6547), 1165-+. DOI: ARTN abf1581

12 10.1126/science.abf1581.
13 (112) Zhu, Y. D.; Ma, X. Y.; Li, L. P.; Yang, Q. J.; Jin, F.; Chen, Z. N.; Wu, C. P.; Shi, H. B.;
14 Feng, Z. Q.; Yin, S. K.; et al. Surface Functional Modification by Ti3C2Tx MXene on PLLA
15 Nanofibers for Optimizing Neural Stem Cell Engineering. *Adv Healthc Mater* **2023**. DOI:
16 10.1002/adhm.202300731. Zhang, J. B.; Tang, S.; Ding, N.; Ma, P.; Zhang, Z. T. Surface-modified
17 Ti3C2 MXene nanosheets for mesenchymal stem cell osteogenic differentiation via photothermal
18 conversion. *Nanoscale Adv* **2023**, *5* (11), 2921-2932. DOI: 10.1039/d3na00187c. Yuan, W. K.;
19 Zhu, L. L.; Zheng, Y. J.; Guo, W. Y.; Min, Y. L.; Fan, J. C. Surface Engineering with Interfacial
20 Poly(glutamic acid)/MXene/Aramid Nanofibers Protective Layer for Dendrite-Free Zinc Anodes.
21 *Energ Fuel* **2023**, *37* (11), 8031-8041. DOI: 10.1021/acs.energyfuels.3c01058. Tokmedash, M.
22 A.; Nagpal, N.; Chen, P. Y.; VanEpps, J. S.; Min, J. H. Stretchable, Nano-Crumpled MXene
23 Multilayers Impart Long-Term Antibacterial Surface Properties. *Adv Mater Interfaces* **2023**, *10*
24 (16). DOI: 10.1002/admi.202202350. Sharma, V.; Sardana, S.; Dhiman, R.; Mahajan, A. Surface
25 engineered MXene with multi-electroactive sites for developing durable and efficient water-
26 splitting electrolyzer. *Appl Phys Lett* **2023**, *122* (19). DOI: Artn 191601
27 10.1063/5.0142311. Schultz, T.; Barmann, P.; Longhi, E.; Meena, R.; Geerts, Y.; Gogotsi, Y.;
28 Barlow, S.; Marder, S. R.; Petit, T.; Koch, N. Work function and energy level alignment tuning at
29 Ti3C2Tx MXene surfaces and interfaces using (metal-)organic donor/acceptor molecules. *Phys
30 Rev Mater* **2023**, *7* (4). DOI: ARTN 045002
31 10.1103/PhysRevMaterials.7.045002. Mustafa, M. N.; Abdah, M. A. A. M.; Numan, A.; Sulaiman,
32 Y.; Walvekar, R.; Khalid, M. Development of high-performance MXene/nickel cobalt phosphate
33 nanocomposite for electrochromic energy storage system using response surface methodology. *J
34 Energy Storage* **2023**, *68*. DOI: ARTN 107880
35 10.1016/j.est.2023.107880. Guo, J. L.; Shang, Z. L.; Sun, Y.; Li, C. H.; Xia, J. Y.; Zou, Y. X.; Du,
36 K.; Liu, G. Q.; Zhou, F.; Liu, W. M. Surface-modified Ti3C2Tx MXene as anti-wear and extreme
37 pressure additive for PFPE supramolecular gel. *Tribol Int* **2023**, *186*. DOI: ARTN 108611
38 10.1016/j.triboint.2023.108611. Di, H. X.; Zhao, D.; Hui, X. B.; Wang, Z. X.; Yin, L. W.; Qian,
39 Z.; Guo, E. Y.; Wang, C. X. Surface Ti vacancy passivation of Ti3C2O2 MXene via transition
40 metal atoms as high-performance potassium-ion batteries anodes. *Appl Surf Sci* **2023**, *630*. DOI:
41 ARTN 157504
42 10.1016/j.apsusc.2023.157504. Bark, H.; Thangavel, G.; Liu, R. J.; Chua, D. H. C.; Lee, P. S.
43 Effective Surface Modification of 2D MXene toward Thermal Energy Conversion and
44 Management. *Small Methods* **2023**. DOI: ARTN 2300077
45 10.1002/smtd.202300077. Almarzooqi, N.; Hong, S. H. Y.; Verma, P.; Shaheen, A.; Schiffer, A.;
46 AlMarzooqi, F. Photothermal Surface Heating Membrane Distillation Using 3D-Printed Ti3C2TX

MXene-Based Nanocomposite Spacers. *Acs Appl Mater Inter* **2023**, *15* (17), 20998-21007. DOI: 10.1021/acsami.3c00830.

(113) Kumar, S.; Mehdi, S. M. Z.; Ali, M.; Choi, S. R.; Yoo, S.; Kim, M.; Suleman, M.; Singh, T.; Seo, Y. Supercapacitors with enhanced energy storage and hydrogen evolution reaction performance via sequential alkali-modified MXenes. *Journal of Materials Chemistry C* **2024**, *12* (46), 18732-18745.

(114) Arole, K.; Blivin, J. W.; Saha, S.; Holta, D. E.; Zhao, X.; Sarmah, A.; Cao, H.; Radovic, M.; Lutkenhaus, J. L.; Green, M. J. Water-dispersible Ti3C2Tz MXene nanosheets by molten salt etching. *iScience* **2021**, *24* (12), 103403. DOI: https://doi.org/10.1016/j.isci.2021.103403. Liu, L. Y.; Orbay, M.; Luo, S.; Duluard, S.; Shao, H.; Harmel, J.; Rozier, P.; Taberna, P. L.; Simon, P. Exfoliation and Delamination of Ti

C

T

 MXene Prepared

 Molten Salt Etching Route. *ACS Nano* **2022**, *16* (1), 111-118. DOI: 10.1021/acsnano.1c08498.

(115) Li, M.; Lu, J.; Luo, K.; Li, Y. B.; Chang, K. K.; Chen, K.; Zhou, J.; Rosen, J.; Hultman, L.; Eklund, P.; et al. Element Replacement Approach by Reaction with Lewis Acidic Molten Salts to Synthesize Nanolaminated MAX Phases and MXenes. *Journal of the American Chemical Society* **2019**, *141* (11), 4730-4737. DOI: 10.1021/jacs.9b00574.

(116) Natu, V.; Barsoum, M. W. MXene Surface Terminations: A Perspective. *The Journal of Physical Chemistry C* **2023**, *127* (41), 20197-20206. DOI: 10.1021/acs.jpcc.3c04324.

(117) Natu, V.; Barsoum, M. W. MXene Surface Terminations: A Perspective. *The Journal of Physical Chemistry C* **2023**. DOI: 10.1021/acs.jpcc.3c04324.

(118) Persson, I.; Naslund, L. A.; Halim, J.; Barsoum, M. W.; Darakchieva, V.; Palisaitis, J.; Rosen, J.; Persson, P. O. A. On the organization and thermal behavior of functional groups on Ti3C2 MXene surfaces in vacuum. *2d Mater* **2018**, *5* (1). DOI: ARTN 015002

10.1088/2053-1583/aa89cd.

(119) Xiong, K. W.; Wang, P. H.; Yang, G.; Liu, Z. F.; Zhang, H. J.; Jin, S. W.; Xu, X. Functional Group Effects on the Photoelectronic Properties of MXene (Sc2CT2, T = O, F, OH) and Their Possible Photocatalytic Activities. *Sci Rep-Uk* **2017**, *7*. DOI: ARTN 15095

10.1038/s41598-017-15233-8.

(120) Hassan, M.; Ali, A.; Rasool, K.; Mahmoud, K. Ion conduction in polyvinylidene fluoride (PVDF)/MXene nanolayers membrane for water treatment applications. *Abstr Pap Am Chem S* **2016**, *251*.

(121) Qu, D. Y.; Jian, Y. Y.; Guo, L. H.; Su, C.; Tang, N.; Zhang, X. M.; Hu, W. W.; Wang, Z.; Zhao, Z. H.; Zhong, P.; et al. An Organic Solvent-Assisted Intercalation and Collection (OAIC) for Ti3C2Tx MXene with Controllable Sizes and Improved Yield. *Nano-Micro Lett* **2021**, *13* (1). DOI: ARTN 188

10.1007/s40820-021-00705-4.

(122) Li, X.; Yin, X.; Han, M.; Song, C.; Sun, X.; Xu, H.; Cheng, L.; Zhang, L. A controllable heterogeneous structure and electromagnetic wave absorption properties of Ti2CTx MXene. *J Mater Chem C* **2017**, *5* (30), 7621-7628, 10.1039/C7TC01991B. DOI: 10.1039/C7TC01991B.

1   (123) Doo, S.; Chae, A.; Kim, D.; Oh, T.; Ko, T. Y.; Kim, S. J.; Koh, D.-Y.; Koo, C. M. Mechanism
2   and Kinetics of Oxidation Reaction of Aqueous Ti3C2Tx Suspensions at Different pHs and
3   Temperatures. *Acs Appl Mater Inter* **2021**, *13* (19), 22855-22865. DOI: 10.1021/acsami.1c04663.
4   (124) Natu, V.; Hart, J. L.; Sokol, M.; Chiang, H.; Taheri, M. L.; Barsoum, M. W. Edge Capping
5   of 2D-MXene Sheets with Polyanionic Salts To Mitigate Oxidation in Aqueous Colloidal
6   Suspensions. *Angewandte Chemie International Edition* **2019**, *58* (36), 12655-12660. DOI:
7   https://doi.org/10.1002/anie.201906138.
8   (125) Zhang, C. J.; Pinilla, S.; McEvoy, N.; Cullen, C. P.; Anasori, B.; Long, E.; Park, S.-H.; Seral-
9   Ascaso, A.; Shmeliov, A.; Krishnan, D.; et al. Oxidation Stability of Colloidal Two-Dimensional
10 Titanium Carbides (MXenes). *Chem Mater* **2017**, *29* (11), 4848-4856. DOI:
11 10.1021/acs.chemmater.7b00745.
12 (126) Huang, S.; Mochalin, V. N. Hydrolysis of 2D Transition-Metal Carbides (MXenes) in
13 Colloidal Solutions. *Inorganic Chemistry* **2019**, *58* (3), 1958-1966. DOI:
14 10.1021/acs.inorgchem.8b02890.
15 (127) Xia, F. J.; Lao, J. C.; Yu, R. H.; Sang, X. H.; Luo, J. Y.; Li, Y.; Wu, J. S. Ambient oxidation
16 of Ti3C2 MXene initialized by atomic defects. *Nanoscale* **2019**, *11* (48), 23330-23337. DOI:
17 10.1039/c9nr07236e.
18 (128) Sang, X. H.; Xie, Y.; Lin, M. W.; Alhabeb, M.; Van Aken, K. L.; Gogotsi, Y.; Kent, P. R.
19 C.; Xiao, K.; Unocic, R. R. Atomic Defects in Monolayer Titanium Carbide (Ti3C2Tx) MXene.
20 *Acs Nano* **2016**, *10* (10), 9193-9200. DOI: 10.1021/acsnano.6b05240.
21 (129) Ibragimova, R.; Rinke, P.; Komsa, H.-P. Native Vacancy Defects in MXenes at Etching
22 Conditions. *Chem Mater* **2022**, *34* (7), 2896-2906. DOI: 10.1021/acs.chemmater.1c03179.
23 Khaledialidusti, R.; Mishra, A. K.; Barnoush, A. Atomic defects in monolayer ordered double
24 transition metal carbide (Mo2TiC2Tx) MXene and CO2 adsorption. *J Mater Chem C* **2020**, *8* (14),
25 4771-4779, 10.1039/C9TC06046D. DOI: 10.1039/C9TC06046D.
26 (130) Doo, S.; Chae, A.; Kim, D.; Oh, T.; Ko, T. Y.; Kim, S. J.; Koh, D. Y.; Koo, C. M. Mechanism
27 and Kinetics of Oxidation Reaction of Aqueous Ti3C2Tx Suspensions at Different pHs and
28 Temperatures. *Acs Appl Mater Inter* **2021**, *13* (19), 22855-22865. DOI: 10.1021/acsami.1c04663.
29 Kim, D.; Ko, T. Y.; Kim, H.; Lee, G. H.; Cho, S.; Koo, C. M. Nonpolar Organic Dispersion of 2D
30 Ti3C2Tx MXene Flakes via Simultaneous Interfacial Chemical Grafting and Phase Transfer
31 Method. *Acs Nano* **2019**, *13* (12), 13818-13828. DOI: 10.1021/acsnano.9b04088.
32 (131) Li, J. B.; Qin, R. Z.; Yan, L.; Chi, Z.; Yu, Z. H.; Li, N. T.; Hu, M. J.; Chen, H. L.; Shan, G.
33 C. Plasmonic Light Illumination Creates a Channel To Achieve Fast Degradation of Ti3C2TX
34 Nanosheets. *Inorganic Chemistry* **2019**, *58* (11), 7285-7294. DOI:
35 10.1021/acs.inorgchem.9b00329.
36 (132) Zhao, X.; Vashisth, A.; Blivin, J. W.; Tan, Z.; Holta, D. E.; Kotasthane, V.; Shah, S. A.;
37 Habib, T.; Liu, S.; Lutkenhaus, J. L.; et al. pH, Nanosheet Concentration, and Antioxidant Affect
38 the Oxidation of Ti3C2Tx and Ti2CTx MXene Dispersions. *Adv Mater Interfaces* **2020**, *7* (20),
39 2000845. DOI: https://doi.org/10.1002/admi.202000845.
40 (133) Kumar, S.; Park, H. M.; Singh, T.; Kumar, M.; Seo, Y. Long-Term Stability Studies and
41 Applications of Ti$_3$C$_2$T$_x$ MXene. *International Journal of Energy Research* **2023**, *2023*, 5275439.
42 DOI: 10.1155/2023/5275439.
43 (134) Huang, S. H.; Mochalin, V. N. Hydrolysis of 2D Transition-Metal Carbides (MXenes) in
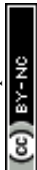44 Colloidal Solutions. *Inorg Chem* **2019**, *58* (3), 1958-1966. DOI: 10.1021/acs.inorgchem.8b02890.

1   (135) Li, X.; Xue, N.; Yao, Q.; Han, L.; Zhao, X.; Li, B.; He, T.; Tao, X. Obtaining Ambient-
2   Stable MXene Ti3C2T through Avoidance of Surface Oxidation Active Sites. *Adv Mater*
3   *Interfaces* **2022**, *9* (24), 2200991. DOI: https://doi.org/10.1002/admi.202200991.
4   (136) Chertopalov, S.; Mochalin, V. N. Environment-Sensitive Photoresponse of Spontaneously
5   Partially Oxidized Ti3C2 MXene Thin Films. *Acs Nano* **2018**, *12* (6), 6109-6116. DOI:
6   10.1021/acsnano.8b02379.
7   (137) Hope, M. A.; Forse, A. C.; Griffith, K. J.; Lukatskaya, M. R.; Ghidiu, M.; Gogotsi, Y.; Grey,
8   C. P. NMR reveals the surface functionalisation of Ti3C2 MXene. *Phys Chem Chem Phys* **2016**,
9   *18* (7), 5099-5102. DOI: 10.1039/c6cp00330c.
10 (138) Kamysbayev, V.; Filatov, A. S.; Hu, H.; Rui, X.; Lagunas, F.; Wang, D.; Klie, R. F.; Talapin,
11 D. V. Covalent surface modifications and superconductivity of two-dimensional metal carbide
12 MXenes. *Science* **2020**, *369* (6506), 979-983. DOI: doi:10.1126/science.aba8311. Yoon, J.; Kim,
13 S.; Park, K. H.; Lee, S.; Kim, S. J.; Lee, H.; Oh, T.; Koo, C. M. Biocompatible and Oxidation-
14 Resistant Ti3C2Tx MXene with Halogen-Free Surface Terminations. *Small Methods* **2023**, *7* (8),
15 2201579. DOI: https://doi.org/10.1002/smtd.202201579. Dash, A.; Vaßen, R.; Guillon, O.;
16 Gonzalez-Julian, J. Molten salt shielded synthesis of oxidation prone materials in air. *Nature*
17 *Materials* **2019**, *18* (5), 465-470. DOI: 10.1038/s41563-019-0328-1.
18 (139) Karlsson, L. H.; Birch, J.; Halim, J.; Barsoum, M. W.; Persson, P. O. A. Atomically Resolved
19 Structural and Chemical Investigation of Single MXene Sheets. *Nano Lett* **2015**, *15* (8), 4955-
20 4960. DOI: 10.1021/acs.nanolett.5b00737.
21 (140) Zheng, Y.; Chen, W.; Sun, Y.; Huang, C.; Wang, Z.; Zhou, D. High conductivity and stability
22 of polystyrene/MXene composites with orientation-3D network binary structure. *Journal of*
23 *Colloid and Interface Science* **2021**, *595*, 151-158.
24 (141) Lee, S.; Kim, E. H.; Yu, S.; Kim, H.; Park, C.; Lee, S. W.; Han, H.; Jin, W.; Lee, K.; Lee,
25 C. E. Polymer-laminated Ti3C2TX MXene electrodes for transparent and flexible field-driven
26 electronics. *ACS nano* **2021**, *15* (5), 8940-8952.
27 (142) Hao, Z.; Zhang, S.; Yang, S.; Li, X.; Gao, Y.; Peng, J.; Li, L.; Bao, L.; Li, X. Bridged Ti3C2T
28 x MXene film with superior oxidation resistance and structural stability for high-performance
29 flexible supercapacitors. *ACS Applied Energy Materials* **2022**, *5* (3), 2898-2908.
30 (143) Xu, Z.; Ding, X.; Li, S.; Huang, F.; Wang, B.; Wang, S.; Zhang, X.; Liu, F.; Zhang, H.
31 Oxidation-resistant MXene-based melamine foam with ultralow-percolation thresholds for
32 electromagnetic-infrared compatible shielding. *Acs Appl Mater Inter* **2022**, *14* (35), 40396-40407.
33 (144) Chae, A.; Murali, G.; Lee, S. Y.; Gwak, J.; Kim, S. J.; Jeong, Y. J.; Kang, H.; Park, S.; Lee,
34 A. S.; Koh, D. Y. Highly oxidation-resistant and self-healable MXene-based hydrogels for
35 wearable strain sensor. *Advanced Functional Materials* **2023**, *33* (24), 2213382.
36 (145) Amin, I.; Brekel, H. v. d.; Nemani, K.; Batyrev, E.; de Vooys, A.; van der Weijde, H.;
37 Anasori, B.; Shiju, N. R. Ti3C2T x MXene polymer composites for anticorrosion: an overview
38 and perspective. *ACS Applied Materials & Interfaces* **2022**, *14* (38), 43749-43758.
39 (146) Zhao, K.; Lee, J. W.; Yu, Z. G.; Jiang, W.; Oh, J. W.; Kim, G.; Han, H.; Kim, Y.; Lee, K.;
40 Lee, S. Humidity-tolerant moisture-driven energy generator with MXene aerogel–organohydrogel
41 bilayer. *ACS nano* **2023**, *17* (6), 5472-5485.
42 (147) Liu, L.-X.; Chen, W.; Zhang, H.-B.; Ye, L.; Wang, Z.; Zhang, Y.; Min, P.; Yu, Z.-Z. Super-
43 tough and environmentally stable aramid. Nanofiber@ MXene coaxial fibers with outstanding
44 electromagnetic interference shielding efficiency. *Nano-Micro Letters* **2022**, *14* (1), 111.

1 (148) Lee, G. S.; Yun, T.; Kim, H.; Kim, I. H.; Choi, J.; Lee, S. H.; Lee, H. J.; Hwang, H. S.; Kim,
2 J. G.; Kim, D.-w. Mussel inspired highly aligned Ti3C2T x MXene film with synergistic
3 enhancement of mechanical strength and ambient stability. *Acs Nano* **2020**, *14* (9), 11722-11732.
4 (149) Liu, N.; Li, Q.; Wan, H.; Chang, L.; Wang, H.; Fang, J.; Ding, T.; Wen, Q.; Zhou, L.; Xiao,
5 X. High-temperature stability in air of Ti3C2T x MXene-based composite with extracted
6 bentonite. *Nature Communications* **2022**, *13* (1), 5551.
7 (150) Zhang, H.-W.; Yang, L.-Y.; Huang, M.-L.; Cheng, M.-H.; Feng, Z.-S.; Meng, F.; Lin, Z.;
8 Wang, Y. Flexible MXene/sodium alginate composite fabric with high structural stability and
9 oxidation resistance for electromagnetic interference shielding. *Nano Research* **2024**, 1-10.
10 (151) Habib, T.; Zhao, X.; Shah, S. A.; Chen, Y.; Sun, W.; An, H.; Lutkenhaus, J. L.; Radovic,
11 M.; Green, M. J. Oxidation stability of Ti3C2Tx MXene nanosheets in solvents and composite
12 films. *Npj 2d Mater Appl* **2019**, *3* (1), 8. DOI: 10.1038/s41699-019-0089-3.
13 (152) Kumar, S.; Park, H. M.; Kim, M.; Nasir, N.; Kumar, M.; Seo, Y. Application dependent
14 stability of Ti3C2Tx MXene in PDLC-based smart-windows. *Ceramics International* **2022**, *48*
15 (23), 35092-35099.
16 (153) Zheng, Y.; Chen, W.; Wang, Z.; Wang, Q. Polystyrene/rGO composites with orientation-3d
17 network binary structure and its surprising conductivity. *Macromolecules* **2018**, *51* (20), 7993-
18 8000. Yang, L.; Wang, Z.; Ji, Y.; Wang, J.; Xue, G. Highly ordered 3D graphene-based polymer
19 composite materials fabricated by "particle-constructing" method and their outstanding
20 conductivity. *Macromolecules* **2014**, *47* (5), 1749-1756.
21 (154) Alhabeb, M.; Maleski, K.; Anasori, B.; Lelyukh, P.; Clark, L.; Sin, S.; Gogotsi, Y.
22 Guidelines for synthesis and processing of two-dimensional titanium carbide (Ti3C2T x MXene).
23 *Chem Mater* **2017**, *29* (18), 7633-7644.
24 (155) Natu, V.; Hart, J. L.; Sokol, M.; Chiang, H.; Taheri, M. L.; Barsoum, M. W. Edge capping
25 of 2D-MXene sheets with polyanionic salts to mitigate oxidation in aqueous colloidal suspensions.
26 *Angewandte Chemie* **2019**, *131* (36), 12785-12790.
27 (156) Wu, F.; Ye, Y.; Chen, R.; Zhao, T.; Qian, J.; Zhang, X.; Li, L.; Huang, Q.; Bai, X.; Cui, Y.
28 Gluing Carbon Black and Sulfur at Nanoscale: A Polydopamine-Based'Nano-Binder'for Double-
29 Shelled Sulfur Cathodes. *Advanced Energy Materials* **2017**, *7* (3).
30 (157) Kim, I. H.; Yun, T.; Kim, J. E.; Yu, H.; Sasikala, S. P.; Lee, K. E.; Koo, S. H.; Hwang, H.;
31 Jung, H. J.; Park, J. Y. Mussel-Inspired Defect Engineering of Graphene Liquid Crystalline Fibers
32 for Synergistic Enhancement of Mechanical Strength and Electrical Conductivity. *Advanced*
33 *Materials* **2018**, *30* (40), 1803267.
34 (158) Tian, W.; VahidMohammadi, A.; Wang, Z.; Ouyang, L.; Beidaghi, M.; Hamedi, M. M.
35 Layer-by-layer self-assembly of pillared two-dimensional multilayers. *Nature Communications*
36 **2019**, *10* (1), 2558.
37 (159) Dong, M.; Hu, Y.; Yu, X.; Liu, M.; Bilotti, E.; Zhang, H.; Papageorgiou, D. G. Probing
38 Interfacial Interactions in Ternary Nanocomposites of Ti3C2Tx MXene Nanoplatelets,
39 Multiwalled Carbon Nanotubes, and Poly(vinyl alcohol) toward Synergistic Reinforcement. *Acs*
40 *Appl Polym Mater* **2024**, *6* (1), 207-217. DOI: 10.1021/acsapm.3c01816.
41 (160) Zhan, Y.; Zheng, X.; Nan, B.; Lu, M.; Shi, J.; Wu, K. Flexible MXene/aramid nanofiber
42 nanocomposite film with high thermal conductivity and flame retardancy. *European Polymer*
43 *Journal* **2023**, *186*, 111847. DOI: https://doi.org/10.1016/j.eurpolymj.2023.111847.
44 (161) Li, N.; Wang, X.; Liu, Y.; Li, Y.; Li, J.; Qin, Z.; Jiao, T. Ultrastretchable, Self-Adhesive and
45 conductive MXene nanocomposite hydrogel for body-surface temperature distinguishing and
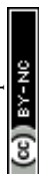
electrophysiological signal monitoring. *Chem Eng J* **2024**, *483*, 149303. DOI: https://doi.org/10.1016/j.cej.2024.149303.

(162) Bisht, N.; Jaiswal, S.; Vishwakarma, J.; Gupta, S. K.; Yeo, R. J.; Sankaranarayanan, S. K. R. S.; Dhand, C.; Dwivedi, N. MXene enhanced Shape Memory Polymer Composites: The rise of MXenes as fillers for stimuli-responsive materials. *Chem Eng J* **2024**, *498*, 155154. DOI: https://doi.org/10.1016/j.cej.2024.155154.

(163) Ling, Z.; Ren, C. E.; Zhao, M.-Q.; Yang, J.; Giammarco, J. M.; Qiu, J.; Barsoum, M. W.; Gogotsi, Y. Flexible and conductive MXene films and nanocomposites with high capacitance. *Proceedings of the National Academy of Sciences* **2014**, *111* (47), 16676-16681.

(164) Wan, S.; Li, X.; Wang, Y.; Chen, Y.; Xie, X.; Yang, R.; Tomsia, A. P.; Jiang, L.; Cheng, Q. Strong sequentially bridged MXene sheets. *Proceedings of the National Academy of Sciences* **2020**, *117* (44), 27154-27161. DOI: doi:10.1073/pnas.2009432117.

(165) Wang, L.; Qiu, H.; Song, P.; Zhang, Y.; Lu, Y.; Liang, C.; Kong, J.; Chen, L.; Gu, J. 3D Ti3C2Tx MXene/C hybrid foam/epoxy nanocomposites with superior electromagnetic interference shielding performances and robust mechanical properties. *Composites Part A: Applied Science and Manufacturing* **2019**, *123*, 293-300.

(166) Liu, J.; Zhang, H.-B.; Xie, X.; Yang, R.; Liu, Z.; Liu, Y.; Yu, Z.-Z. Multifunctional, Superelastic, and Lightweight MXene/Polyimide Aerogels. *Small* **2018**, *14* (45), 1802479. DOI: https://doi.org/10.1002/smll.201802479.

(167) Luo, J.-Q.; Zhao, S.; Zhang, H.-B.; Deng, Z.; Li, L.; Yu, Z.-Z. Flexible, stretchable and electrically conductive MXene/natural rubber nanocomposite films for efficient electromagnetic interference shielding. *Composites Science and Technology* **2019**, *182*, 107754.

(168) Zhang, H.; Wang, L.; Zhou, A.; Shen, C.; Dai, Y.; Liu, F.; Chen, J.; Li, P.; Hu, Q. Effects of 2-D transition metal carbide Ti 2 CT x on properties of epoxy composites. *RSC advances* **2016**, *6* (90), 87341-87352.

(169) Liu, R.; Miao, M.; Li, Y.; Zhang, J.; Cao, S.; Feng, X. Ultrathin biomimetic polymeric Ti3C2T x MXene composite films for electromagnetic interference shielding. *ACS applied materials & interfaces* **2018**, *10* (51), 44787-44795.

(170) Pan, Y.; Fu, L.; Zhou, Q.; Wen, Z.; Lin, C. T.; Yu, J.; Wang, W.; Zhao, H. Flammability, thermal stability and mechanical properties of polyvinyl alcohol nanocomposites reinforced with delaminated Ti3C2Tx (MXene). *Polymer Composites* **2020**, *41* (1), 210-218.

(171) Zhi, W.; Xiang, S.; Bian, R.; Lin, R.; Wu, K.; Wang, T.; Cai, D. Study of MXene-filled polyurethane nanocomposites prepared via an emulsion method. *Composites Science and Technology* **2018**, *168*, 404-411.

(172) Sheng, X.; Zhao, Y.; Zhang, L.; Lu, X. Properties of two-dimensional Ti3C2 MXene/thermoplastic polyurethane nanocomposites with effective reinforcement via melt blending. *Composites Science and Technology* **2019**, *181*, 107710.

(173) Mazhar, S.; Qarni, A. A.; Haq, Y. U.; Haq, Z. U.; Murtaza, I. Promising PVC/MXene based flexible thin film nanocomposites with excellent dielectric, thermal and mechanical properties. *Ceramics International* **2020**, *46* (8), 12593-12605.

(174) Liu, S.; Wang, L.; Wang, X.; Liu, L.; Zhou, A.; Cao, X. Preparation, mechanical and thermal characteristics of d-Ti3C2/PVA film. *Materials Today Communications* **2020**, *22*, 100799.

(175) Hatter, C. B.; Shah, J.; Anasori, B.; Gogotsi, Y. Micromechanical response of two-dimensional transition metal carbonitride (MXene) reinforced epoxy composites. *Composites Part B: Engineering* **2020**, *182*, 107603.

Journal of Materials Chemistry A Accepted Manuscript

(176) Wang, L.; Chen, L.; Song, P.; Liang, C.; Lu, Y.; Qiu, H.; Zhang, Y.; Kong, J.; Gu, J. Fabrication on the annealed Ti3C2Tx MXene/Epoxy nanocomposites for electromagnetic interference shielding application. *Composites Part B: Engineering* **2019**, *171*, 111-118.

(177) Shi, Y.; Liu, C.; Liu, L.; Fu, L.; Yu, B.; Lv, Y.; Yang, F.; Song, P. Strengthening, toughing and thermally stable ultra-thin MXene nanosheets/polypropylene nanocomposites via nanoconfinement. *Chemical Engineering Journal* **2019**, *378*, 122267.

(178) Shayesteh Zeraati, A.; Mirkhani, S. A.; Sun, P.; Naguib, M.; Braun, P. V.; Sundararaj, U. Improved synthesis of Ti3C2Tx MXenes resulting in exceptional electrical conductivity, high synthesis yield, and enhanced capacitance. *Nanoscale* **2021**, *13* (6), 3572-3580, 10.1039/D0NR06671K. DOI: 10.1039/D0NR06671K.

(179) Naguib, M.; Saito, T.; Lai, S.; Rager, M. S.; Aytug, T.; Parans Paranthaman, M.; Zhao, M.-Q.; Gogotsi, Y. Ti3C2Tx (MXene)–polyacrylamide nanocomposite films. *Rsc Adv* **2016**, *6* (76), 72069-72073, 10.1039/C6RA10384G. DOI: 10.1039/C6RA10384G.

(180) Hadi, Z.; Yeganeh, J. K.; Zare, Y.; Munir, M. T.; Rhee, K. Y. Predicting of electrical conductivity for Polymer-MXene nanocomposites. *Journal of Materials Research and Technology* **2024**, *28*, 4229-4238. DOI: https://doi.org/10.1016/j.jmrt.2024.01.014.

(181) Yu, Y.; Yi, P.; Xu, W.; Sun, X.; Deng, G.; Liu, X.; Shui, J.; Yu, R. Environmentally Tough and Stretchable MXene Organohydrogel with Exceptionally Enhanced Electromagnetic Interference Shielding Performances. *Nano-Micro Lett* **2022**, *14* (1), 77. DOI: 10.1007/s40820-022-00819-3.

(182) Cao, W.-T.; Chen, F.-F.; Zhu, Y.-J.; Zhang, Y.-G.; Jiang, Y.-Y.; Ma, M.-G.; Chen, F. Binary Strengthening and Toughening of MXene/Cellulose Nanofiber Composite Paper with Nacre-Inspired Structure and Superior Electromagnetic Interference Shielding Properties. *Acs Nano* **2018**, *12* (5), 4583-4593. DOI: 10.1021/acsnano.8b00997.

(183) Wang, D.; Lin, Y.; Hu, D.; Jiang, P.; Huang, X. Multifunctional 3D-MXene/PDMS nanocomposites for electrical, thermal and triboelectric applications. *Composites Part A: Applied Science and Manufacturing* **2020**, *130*, 105754.

(184) Mayerberger, E. A.; Urbanek, O.; McDaniel, R. M.; Street, R. M.; Barsoum, M. W.; Schauer, C. L. Preparation and characterization of polymer-Ti3C2Tx (MXene) composite nanofibers produced via electrospinning. *Journal of Applied Polymer Science* **2017**, *134* (37), 45295.

(185) Naguib, M.; Saito, T.; Lai, S.; Rager, M. S.; Aytug, T.; Paranthaman, M. P.; Zhao, M.-Q.; Gogotsi, Y. Ti 3 C 2 T x (MXene)–polyacrylamide nanocomposite films. *RSC advances* **2016**, *6* (76), 72069-72073.

(186) Sobolčiak, P.; Ali, A.; Hassan, M. K.; Helal, M. I.; Tanvir, A.; Popelka, A.; Al-Maadeed, M. A.; Krupa, I.; Mahmoud, K. A. 2D Ti3C2Tx (MXene)-reinforced polyvinyl alcohol (PVA) nanofibers with enhanced mechanical and electrical properties. *PLoS One* **2017**, *12* (8), e0183705.

(187) Sun, R.; Zhang, H. B.; Liu, J.; Xie, X.; Yang, R.; Li, Y.; Hong, S.; Yu, Z. Z. Highly conductive transition metal carbide/carbonitride (MXene)@ polystyrene nanocomposites fabricated by electrostatic assembly for highly efficient electromagnetic interference shielding. *Advanced Functional Materials* **2017**, *27* (45), 1702807.

(188) Tu, S.; Jiang, Q.; Zhang, X.; Alshareef, H. N. Large dielectric constant enhancement in MXene percolative polymer composites. *ACS nano* **2018**, *12* (4), 3369-3377.

(189) Han, C.; Zhang, H.; Chen, Q.; Li, T.; Kong, L.; Zhao, H.; He, L. A directional piezoelectric sensor based on anisotropic PVDF/MXene hybrid foam enabled by unidirectional freezing. *Chem Eng J* **2022**, *450*, 138280. DOI: https://doi.org/10.1016/j.cej.2022.138280.
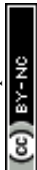
(190) Safarkhani, M.; Far, B. F.; Huh, Y.; Rabiee, N. Thermally Conductive MXene. *ACS Biomaterials Science & Engineering* **2023**, *9* (12), 6516-6530. DOI: 10.1021/acsbiomaterials.3c01420.

(191) Liu, R.; Li, W. High-Thermal-Stability and High-Thermal-Conductivity Ti3C2Tx MXene/Poly(vinyl alcohol) (PVA) Composites. *Acs Omega* **2018**, *3* (3), 2609-2617. DOI: 10.1021/acsomega.7b02001.

(192) Cao, Y.; Deng, Q.; Liu, Z.; Shen, D.; Wang, T.; Huang, Q.; Du, S.; Jiang, N.; Lin, C.-T.; Yu, J. Enhanced thermal properties of poly(vinylidene fluoride) composites with ultrathin nanosheets of MXene. *Rsc Adv* **2017**, *7* (33), 20494-20501, 10.1039/C7RA00184C. DOI: 10.1039/C7RA00184C.

(193) Ji, C.; Wang, Y.; Ye, Z.; Tan, L.; Mao, D.; Zhao, W.; Zeng, X.; Yan, C.; Sun, R.; Kang, D. J.; et al. Ice-Templated MXene/Ag–Epoxy Nanocomposites as High-Performance Thermal Management Materials. *Acs Appl Mater Inter* **2020**, *12* (21), 24298-24307. DOI: 10.1021/acsami.9b22744.

(194) Wang, M.; Liu, Y.; Zhang, H.; Wu, Y.; Pan, L. Thermal conductivities of Ti3C2Tx MXenes and their interfacial thermal performance in MXene/epoxy composites – a molecular dynamics simulation. *International Journal of Heat and Mass Transfer* **2022**, *194*, 123027. DOI: https://doi.org/10.1016/j.ijheatmasstransfer.2022.123027.

(195) Gholivand, H.; Fuladi, S.; Hemmat, Z.; Salehi-Khojin, A.; Khalili-Araghi, F. Effect of surface termination on the lattice thermal conductivity of monolayer Ti3C2Tz MXenes. *Journal of Applied Physics* **2019**, *126* (6). DOI: 10.1063/1.5094294 (acccessed 10/22/2024).

(196) Cao, Y.; Deng, Q.; Liu, Z.; Shen, D.; Wang, T.; Huang, Q.; Du, S.; Jiang, N.; Lin, C.-T.; Yu, J. Enhanced thermal properties of poly (vinylidene fluoride) composites with ultrathin nanosheets of MXene. *RSC advances* **2017**, *7* (33), 20494-20501.

(197) Liu, R.; Li, W. High-thermal-stability and high-thermal-conductivity Ti3C2T x MXene/poly (vinyl alcohol)(PVA) composites. *ACS omega* **2018**, *3* (3), 2609-2617.

(198) Yan, C.; Ji, C.; Zeng, X.; Sun, R.; Wong, C.-P. Interconnecting the promising MXenes via Ag nanowire in epoxy nanocomposites for high-performance thermal management applications. In *2018 19th International Conference on Electronic Packaging Technology (ICEPT)*, 2018; IEEE: pp 510-512.

(199) Kang, R.; Zhang, Z.; Guo, L.; Cui, J.; Chen, Y.; Hou, X.; Wang, B.; Lin, C.-T.; Jiang, N.; Yu, J. Enhanced thermal conductivity of epoxy composites filled with 2D transition metal carbides (MXenes) with ultralow loading. *Scientific reports* **2019**, *9* (1), 9135.

(200) Huang, Z. Y.; Wang, S. J.; Kota, S.; Pan, Q. W.; Barsoum, M. W.; Li, C. Y. Structure and crystallization behavior of poly(ethylene oxide)/Ti3C2Tx MXene nanocomposites. *Polymer* **2016**, *102*, 119-126. DOI: 10.1016/j.polymer.2016.09.011.

(201) Carey, M.; Hinton, Z.; Natu, V.; Pai, R.; Sokol, M.; Alvarez, N. J.; Kalra, V.; Barsoum, M. W. Dispersion and Stabilization of Alkylated 2D MXene in Nonpolar Solvents and Their Pseudocapacitive Behavior. *Cell Rep Phys Sci* **2020**, *1* (4). DOI: ARTN 100042

10.1016/j.xcrp.2020.100042.

(202) Wei, L. F.; Ma, J. Z.; Zhang, W. B.; Pan, Z. Y.; Ma, Z. L.; Kang, S. L.; Fan, Q. Q. Enhanced Antistatic and Self-Heatable Wearable Coating with Self-Tiered Structure Caused by Amphiphilic MXene in Waterborne Polymer. *Langmuir* **2020**, *36* (23), 6580-6588. DOI: 10.1021/acs.langmuir.9b03943.

(203) Srivatsa, S.; Packo, P.; Mishnaevsky, L.; Uhl, T.; Grabowski, K. Deformation of Bioinspired MXene-Based Polymer Composites with Brick and Mortar Structures: A Computational Analysis. *Materials* **2020**, *13* (22). DOI: ARTN 5189

10.3390/ma13225189. Mao, H. W.; Gu, C.; Yan, S. Q.; Xin, Q.; Cheng, S.; Tan, P.; Wang, X. J.; Xiu, F.; Liu, X. Q.; Liu, J. Q.; et al. MXene Quantum Dot/Polymer Hybrid Structures with Tunable Electrical Conductance and Resistive Switching for Nonvolatile Memory Devices. *Adv Electron Mater* **2020**, *6* (1). DOI: ARTN 1900493

10.1002/aelm.201900493. Jin, X.; Zhang, W. S.; Liu, S. Y.; Zhang, T. P.; Song, Z. H.; Shao, W. L.; Mao, R. Y.; Yao, M.; Jian, X. G.; Hu, F. Y. Highly stable Ti3C2Tx MXene-based sandwich-like structure via interfacial self-assembly of nitrogen-rich polymer network for superior sodium-ion storage performance. *Chem Eng J* **2023**, *451*. DOI: ARTN 138763

10.1016/j.cej.2022.138763. Sun, F. C.; Wang, X. Z.; Wu, D. C.; El-Khouly, M.; Zheng, T. A.; Zhang, B.; Chen, Y. Conjugated Polymer-Functionalized 2D MXene Nanosheets for Nonvolatile Memory Devices with High Environmental Stability. *Acs Appl Nano Mater* **2023**, *6* (9), 7186-7195. DOI: 10.1021/acsanm.3c00220.

(204) Lan, C. T.; Jia, H.; Qiu, M. H.; Fu, S. H. Ultrathin MXene/Polymer Coatings with an Alternating Structure on Fabrics for Enhanced Electromagnetic Interference Shielding and Fire-Resistant Protective Performances. *Acs Appl Mater Inter* **2021**, *13* (32), 38761-38772. DOI: 10.1021/acsami.1c11638.

(205) Cao, Y. W.; Jia, Y. C.; Meng, X. D.; Fan, X. Y.; Zhang, J.; Zhou, J.; Matoga, D.; Bielawski, C. W.; Geng, J. X. Covalently grafting conjugated porous polymers to MXene offers a two-dimensional sandwich-structured electrocatalytic sulfur host for lithium-sulfur batteries. *Chem Eng J* **2022**, *446*. DOI: ARTN 137365

10.1016/j.cej.2022.137365.

(206) Guan, Q. Y.; Yan, H. J.; Cai, Y. Q. Strongly Modulated Exfoliation and Functionalization of MXenes with Rationally Designed Groups in Polymer: A Theoretical Study. *Chem Mater* **2022**, *34* (21), 9414-9424. DOI: 10.1021/acs.chemmater.2c01721.

(207) Zhang, P.; Yang, X. J.; Li, P.; Zhao, Y. Y.; Niu, Q. J. Fabrication of novel MXene (Ti3C2)/polyacrylamide nanocomposite hydrogels with enhanced mechanical and drug release properties. *Soft Matter* **2020**, *16* (1), 162-169. DOI: 10.1039/c9sm01985e.

(208) Lee, J. T.; Wyatt, B. C.; Davis, G. A.; Masterson, A. N.; Pagan, A. L.; Shah, A.; Anasori, B.; Sardar, R. Covalent Surface Modification of Ti3C2Tx MXene with Chemically Active Polymeric Ligands Producing Highly Conductive and Ordered Microstructure Films. *Acs Nano* **2021**, *15* (12), 19600-19612. DOI: 10.1021/acsnano.1c06670.

(209) Guo, Q. Q.; Zhang, X. X.; Zhao, F. Y.; Song, Q. C.; Su, G. H.; Tan, Y. X.; Tao, Q. C.; Zhou, T.; Yu, Y. M.; Zhou, Z. H.; et al. Protein-Inspired Self-Healable Ti3C2 MXenes/Rubber-Based Supramolecular Elastomer for Intelligent Sensing. *Acs Nano* **2020**, *14* (3), 2788-2797. DOI: 10.1021/acsnano.9b09802.

(210) Tu, S. B.; Jiang, Q.; Zhang, J. W.; He, X.; Hedhili, M. N.; Zhang, X. X.; Alshareef, H. N. Enhancement of Dielectric Permittivity of Ti3C2Tx, MXene/Polymer Composites by Controlling Flake Size and Surface Termination. *Acs Appl Mater Inter* **2019**, *11* (30), 27358-27362. DOI: 10.1021/acsami.9b09137. Idumah, C. I. Influence of surfaces and interfaces on MXene and MXene hybrid polymeric nanoarchitectures, properties, and applications. *J Mater Sci* **2022**, *57* (31), 14579-14619. DOI: 10.1007/s10853-022-07526-9.

(211) Jiao, C. Y.; Deng, Z. M.; Min, P.; Lai, J. J.; Gou, Q. Q.; Gao, R.; Yu, Z. Z.; Zhang, H. B. Photothermal healable, stretchable, and conductive MXene composite films for efficient electromagnetic interference shielding. *Carbon* **2022**, *198*, 179-187. DOI: 10.1016/j.carbon.2022.07.017.

(212) Eom, W.; Shin, H.; Ambade, R. B.; Lee, S. H.; Lee, K. H.; Kang, D. J.; Han, T. H. Large-scale wet-spinning of highly electroconductive MXene fibers. *Nat Commun* **2020**, *11* (1). DOI: 10.1038/s41467-020-16671-1.

(213) Tian, W. Q.; VahidMohammadi, A.; Wang, Z.; Ouyang, L. Q.; Beidaghi, M.; Hamedi, M. M. Layer-by-layer self-assembly of pillared two-dimensional multilayers. *Nat Commun* **2019**, *10*. DOI: ARTN 2558

10.1038/s41467-019-10631-0.

(214) Wu, X. Y.; Han, B. Y.; Zhang, H. B.; Xie, X.; Tu, T. X.; Zhang, Y.; Dai, Y.; Yang, R.; Yu, Z. Z. Compressible, durable and conductive polydimethylsiloxane-coated MXene foams for high-performance electromagnetic interference shielding. *Chem Eng J* **2020**, *381*. DOI: ARTN 122622

10.1016/j.cej.2019.122622.

(215) Pan, Y.; He, M.; Wu, J.; Qi, H.; Cheng, Y. One-step synthesis of MXene-functionalized PEDOT:PSS conductive polymer hydrogels for wearable and noninvasive monitoring of sweat glucose. *Sensors and Actuators B: Chemical* **2024**, *401*, 135055. DOI: https://doi.org/10.1016/j.snb.2023.135055.

(216) Yin, J. J.; Zhan, F. K.; Jiao, T. F.; Deng, H. Z.; Zou, G. D.; Bai, Z. H.; Zhang, Q. R.; Peng, Q. M. Highly efficient catalytic performances of nitro compounds via hierarchical PdNPs-loaded MXene/polymer nanocomposites synthesized through electrospinning strategy for wastewater treatment. *Chinese Chem Lett* **2020**, *31* (4), 992-995. DOI: 10.1016/j.cclet.2019.08.047. Huang, X. X.; Wang, R.; Jiao, T. F.; Zou, G. D.; Zhan, F. K.; Yin, J. J.; Zhang, L. X.; Zhou, J. X.; Peng, Q. M. Facile Preparation of Hierarchical AgNP-Loaded MXene/Fe3O4/Polymer Nanocomposites by Electrospinning with Enhanced Catalytic Performance for Wastewater Treatment. *Acs Omega* **2019**, *4* (1), 1897-1906. DOI: 10.1021/acsomega.8b03615.

(217) Jiang, C. M.; Wu, C.; Li, X. J.; Yao, Y.; Lan, L. Y.; Zhao, F. N.; Ye, Z. Z.; Ying, Y. B.; Ping, J. F. All-electrospun flexible triboelectric nanogenerator based on metallic MXene nanosheets. *Nano Energy* **2019**, *59*, 268-276. DOI: 10.1016/j.nanoen.2019.02.052.

(218) Yun, J.; Echols, I.; Flouda, P.; Wang, S. Y.; Easley, A.; Zhao, X. F.; Tan, Z. Y.; Prehn, E.; Zi, G.; Radovic, M.; et al. Layer-by-Layer Assembly of Polyaniline Nanofibers and MXene Thin-Film Electrodes for Electrochemical Energy Storage. *Acs Appl Mater Inter* **2019**, *11* (51), 47929-47938. DOI: 10.1021/acsami.9b16692.

(219) Zhang, H.; Wang, L. B.; Zhou, A. G.; Shen, C. J.; Dai, Y. H.; Liu, F. F.; Chen, J. F.; Li, P.; Hu, Q. K. Effects of 2-D transition metal carbide Ti2CTx on properties of epoxy composites. *Rsc Adv* **2016**, *6* (90), 87341-87352. DOI: 10.1039/c6ra14560d.

(220) Zhang, S. S.; Tu, T. T.; Li, T. Y.; Cai, Y.; Wang, Z. Y.; Zhou, Y.; Wang, D.; Fang, L.; Ye, X. S.; Liang, B. 3D MXene/PEDOT:PSS Composite Aerogel with a Controllable Patterning Property for Highly Sensitive Wearable Physical Monitoring and Robotic Tactile Sensing. *Acs Appl Mater Inter* **2022**, *14* (20), 23877-23887. DOI: 10.1021/acsami.2c03350.

(221) Chen, Y. C.; Lin, Y. F.; Liu, C. T.; Liu, Y. C.; Lin, M. H.; Lan, G. Y.; Cheng, Y. S.; Yu, H. L.; Huang, C. C.; Chang, H. T.; et al. Facilitation of Osteogenic Differentiation of hASCs on PEDOT:PSS/MXene Composite Sponge with Electrical Stimulation. *Acs Appl Polym Mater* **2023**, *5* (7), 4753-4766. DOI: 10.1021/acsapm.3c00146.

Journal of Materials Chemistry A Accepted Manuscript
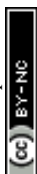
Journal of Materials Chemistry A Accepted Manuscript

1   (222) Liu, K.; Du, H. S.; Liu, W.; Zhang, M.; Wang, Y. X.; Liu, H. Y.; Zhang, X. Y.; Xu, T.; Si,
2   C. L. Strong, flexible, and highly conductive cellulose nanofibril/PEDOT:PSS/MXene
3   nanocomposite films for efficient electromagnetic interference shielding. *Nanoscale* **2022**, *14* (40),
4   14902-14912. DOI: 10.1039/d2nr00468b.
5   (223) Chang, G. J.; Zeng, L. J.; Xie, L.; Xue, B.; Zheng, Q. Ultrathin multifunctional
6   electromagnetic interference shielding MXene/ AgNWs/PEDOT:PSS coatings with superior
7   electro/photo-thermal transition ability and water repellency. *Chem Eng J* **2023**, *470*. DOI: ARTN
8   144033

9   10.1016/j.cej.2023.144033.
10 (224) Gu, Q.; Wang, J.; Peng, R. X.; Song, W.; Zhou, R.; Ge, Z. Y. Nonfullerene Organic Solar
11 Cells with 18.17% Efficiency Obtained Using a V2C/PEDOT:PSS Composite Hole-Transport
12 Layer. *Acs Applied Energy Materials* **2023**. DOI: 10.1021/acsaem.2c03883.
13 (225) Deng, B. Z.; Lian, H.; Xue, B. T.; Song, R. C.; Chen, S.; Wang, Z. H.; Xu, T.; Dong, H. L.;
14 Wang, S. H. Niobium-Carbide MXene Modified Hybrid Hole Transport Layer Enabling High-
15 Performance Organic Solar Cells Over 19%. *Small* **2023**, *19* (23). DOI: 10.1002/smll.202207505.
16 (226) Nguyen, V. T.; Min, B. K.; Yi, Y.; Kim, S. J.; Choi, C. G.
17 MXene(Ti3C2TX)/graphene/PDMS composites for multifunctional broadband electromagnetic
18 interference shielding skins. *Chem Eng J* **2020**, *393*. DOI: ARTN 124608

19 10.1016/j.cej.2020.124608.
20 (227) Zhu, W. B.; Luo, H. S.; Tang, Z. H.; Zhang, H.; Fan, T.; Wang, Y. Y.; Huang, P.; Li, Y. Q.;
21 Fu, S. Y. Ti3C2Tx MXene/Bamboo Fiber/PDMS Pressure Sensor with Simultaneous Ultrawide
22 Linear Sensing Range, Superb Environmental Stability, and Excellent Biocompatibility. *Acs*
23 *Sustain Chem Eng* **2022**, *10* (11), 3546-3556. DOI: 10.1021/acssuschemeng.1c07994.
24 (228) Xu, X. M.; Wu, H.; He, X.; Hota, M. K.; Liu, Z. X.; Zhuo, S. F.; Kim, H.; Zhang, X. X.;
25 Alshareef, H. N. Iontronics Using V2CTx MXene-Derived Metal-Organic Framework Solid
26 Electrolytes. *Acs Nano* **2020**, *14* (8), 9840-9847. DOI: 10.1021/acsnano.0c02497.
27 (229) Nguyen, V. T.; Nguyen, Q. D.; Min, B. K.; Yi, Y.; Choi, C. G. Ti3C2Tx MXene/carbon
28 nanotubes/waterborne polyurethane based composite ink for electromagnetic interference
29 shielding and sheet heater applications. *Chem Eng J* **2022**, *430*. DOI: ARTN 133171

30 10.1016/j.cej.2021.133171.
31 (230) Jing, J. Y.; Ma, Z. L.; Jiang, R. C.; Zhang, Y.; Shao, L. Flexible
32 Polyurethane@Ti3C2Tx/Silver Nanowires Composite Films with Cocontinuous Segregated
33 Structures for Superior Electromagnetic Interference Shielding and Joule Heating. *Adv Eng Mater*
34 **2023**, *25* (11). DOI: ARTN 2201938

35 10.1002/adem.202201938.
36 (231) Zhao, C. C.; Zhou, M.; Yu, H. B. High water and oxygen reactivity inducing excellent anti-
37 corrosive performance in waterborne Ti2CTx/epoxy composite coating. *Appl Surf Sci* **2022**, *586*.
38 DOI: ARTN 152880

39 10.1016/j.apsusc.2022.152880.
40 (232) Liang, W. Y.; Zhitomirsky, I. MXene-polypyrrole electrodes for asymmetric
41 supercapacitors. *Electrochim Acta* **2022**, *406*. DOI: ARTN 139843

42 10.1016/j.electacta.2022.139843.

1 (233) Liu, G. Y.; Zou, J. H.; Tang, Q. Y.; Yang, X. Y.; Zhang, Y. W.; Zhang, Q.; Huang, W.;
2 Chen, P.; Shao, J. J.; Dong, X. C. Surface Modified Ti3C2 MXene Nanosheets for Tumor
3 Targeting Photothermal/Photodynamic/Chemo Synergistic Therapy. *Acs Appl Mater Inter* **2017**,
4 *9* (46), 40077-40086. DOI: 10.1021/acsami.7b13421.
5 (234) Mayerberger, E. A.; Street, R. M.; McDaniel, R. M.; Barsoum, M. W.; Schauer, C. L.
6 Antibacterial properties of electrospun Ti3C2Tz (MXene)/chitosan nanofibers. *Rsc Adv* **2018**, *8*
7 (62), 35386-35394. DOI: 10.1039/c8ra06274a.
8 (235) Yousaf, T.; Areeb, A.; Murtaza, M.; Munir, A.; Khan, Y.; Waseem, A. Silane-Grafted
9 MXene (Ti3C2TX) Membranes for Enhanced Water Purification Performance. *Acs Omega* **2022**,
10 *7* (23), 19502-19512. DOI: 10.1021/acsomega.2c01143.
11 (236) Likitaporn, C.; Okhawilai, M.; Kasemsiri, P.; Qin, J. Q.; Potiyaraj, P.; Uyama, H. High
12 electrolyte uptake of MXene integrated membrane separators for Zn-ion batteries. *Sci Rep-Uk*
13 **2022**, *12* (1). DOI: ARTN 19915

14 10.1038/s41598-022-24578-8.
15 (237) Basara, G.; Saeidi-Javash, M.; Ren, X.; Bahcecioglu, G.; Wyatt, B. C.; Anasori, B.; Zhang,
16 Y. L.; Zorlutuna, P. Electrically conductive 3D printed Ti (3) C (2) T x MXene-PEG composite
17 constructs for cardiac tissue engineering. *Acta Biomater* **2022**, *139*, 179-189. DOI:
18 10.1016/j.actbio.2020.12.033.
19 (238) Jiang, C. G.; Xie, W. Y.; Wu, D. F. Balancing the Overall Performance of Poly(vinyl
20 alcohol)/MXene Composite Organohydrogels for Flexible Strain Sensors. *Acs Appl Polym Mater*
21 **2023**, *5* (1), 370-380. DOI: 10.1021/acsapm.2c01546370.
22 (239) Liu, J. H.; Meng, X. J.; Dong, F.; Ren, S. Y.; Wang, B.; Tan, F. Highly Stretchable and
23 Sensitive Ti3C2TX MXene/Sodium Alginate/ Acrylamide Hydrogel for Flexible Electronic
24 Sensors. *Acs Appl Polym Mater* **2022**. DOI: 10.1021/acsapm.2c01169.
25 (240) Tang, T. T.; Wang, S. C.; Jiang, Y.; Xu, Z. G.; Chen, Y.; Peng, T. S.; Khan, F.; Feng, J. B.;
26 Song, P. G.; Zhao, Y. Flexible and flame-retarding phosphorylated MXene/polypropylene
27 composites for efficient electromagnetic interference shielding. *J Mater Sci Technol* **2022**, *111*,
28 66-75. DOI: 10.1016/j.jmst.2021.08.091.
29 (241) Zhang, Y. K.; Chen, C.; Chen, Z. F.; Zhang, T. T.; Wang, Y. L.; Cao, S. Y.; Ma, J. Superior
30 Anticorrosion Performance of Well-Dispersed MXene- Polymer Composite Coatings Enabled by
31 Covalent Modification and Ambient Electron-Beam Curing. *Acs Appl Mater Inter* **2023**, *15* (8),
32 11099-11110. DOI: 10.1021/acsami.2c22184.
33 (242) Qian, Y.; Zhong, J.; Ou, J. P. Improvement in alkali-resistance of basalt fiber-reinforced
34 polymer by Ti3C2TX (MXene) modified matrix. *Polym Composite* **2023**, *44* (4), 2581-2591. DOI:
35 10.1002/pc.27265. Hou, K.; Yang, Y. F.; Zhou, H.; Chen, X. M.; Ge, S. B. Enhanced Yield of
36 Large-Sized Ti3C2Tx MXene Polymers Nanosheets via Cyclic Ultrasonic-Centrifugal Separation.
37 *Polymers-Basel* **2023**, *15* (6). DOI: ARTN 1330
38 10.3390/polym15061330.
39 (243) Kim, T. M.; Ryplida, B.; Lee, G. B.; Park, S. Y. Cancer cells targeting H2O2-responsive
40 MXene-integrated hyaluronic acid polymer dots coated sensor. *J Ind Eng Chem* **2023**, *120*, 188-
41 194. DOI: 10.1016/j.jiec.2022.12.025.
42 (244) Zhou, Y.; Zou, Y. B.; Peng, Z. Y.; Yu, C. Y.; Zhong, W. B. Arbitrary deformable and high-
43 strength electroactive polymer/MXene anti-exfoliative composite films assembled into high
44 performance, flexible all-solid-state supercapacitors. *Nanoscale* **2020**, *12* (40), 20797-20810. DOI:
45 10.1039/d0nr04980h.

(245) Deng, Q. H.; Feng, Y. F.; Li, W.; Xu, X. Q.; Peng, C.; Wu, Q. Strong interface effect induced high-k property in polymer based ternary composites filled with 2D layered Ti3C2 MXene nanosheets. *J Mater Sci-Mater El* **2019**, *30* (10), 9106-9113. DOI: 10.1007/s10854-019-01239-7.

(246) Zheng, X. H.; Shen, J. K.; Hu, Q. L.; Nie, W. Q.; Wang, Z. Q.; Zou, L. H.; Li, C. L. Vapor phase polymerized conducting polymer/MXene textiles for wearable electronics. *Nanoscale* **2021**, *13* (3), 1832-1841. DOI: 10.1039/d0nr07433k. Sharma, S.; Chhetry, A.; Ko, S.; Park, J. Y. Highly Sensitive and Stable Pressure Sensor Based on Polymer-Mxene Composite Nanofiber Mat for Wearable Health Monitoring. *Proc Ieee Micr Elect* **2020**, 810-813. Kim, K. N.; Kim, S. Y.; Choi, S. H.; Lee, M.; Song, W.; Lim, J.; Lee, S. S.; Myung, S. All-Printed Wearable Triboelectric Nanogenerator with Ultra-Charged Electron Accumulation Polymers Based on MXene Nanoflakes. *Adv Electron Mater* **2022**, *8* (12). DOI: 10.1002/aelm.202200819.

(247) Zhang, R. N.; Liu, Q.; Wang, Z. Z.; Yang, X. D.; Guo, Y. X. Conductive polymer doped two-dimensional MXene materials: opening the channel of magnesium ion transport. *Rsc Adv* **2022**, *12* (7), 4329-4335. DOI: 10.1039/d1ra08690a. Parajuli, D.; Murali, N.; Devendra, K. C.; Karki, B.; Samatha, K.; Kim, A. A.; Park, M.; Pant, B. Advancements in MXene-Polymer Nanocomposites in Energy Storage and Biomedical Applications. *Polymers-Basel* **2022**, *14* (16). DOI: ARTN 3433

10.3390/polym14163433.

(248) Zhou, Z. H.; Panatdasirisuk, W.; Mathis, T. S.; Anasori, B.; Lu, C. H.; Zhang, X. X.; Liao, Z. W.; Gogotsi, Y.; Yang, S. Layer-by-layer assembly of MXene and carbon nanotubes on electrospun polymer films for flexible energy storage. *Nanoscale* **2018**, *10* (13), 6005-6013. DOI: 10.1039/c8nr00313k.

(249) Liu, Y. Q.; Xu, D. R.; Ding, Y.; Lv, X. X.; Huang, T. T.; Yuan, B. L.; Jiang, L.; Sun, X. Y.; Yao, Y. Q.; Tang, J. A conductive polyacrylamide hydrogel enabled by dispersion-enhanced MXene@chitosan assembly for highly stretchable and sensitive wearable skin. *J Mater Chem B* **2021**, *9* (42), 8862-8870. DOI: 10.1039/d1tb01798e. Maleski, K.; Mochalin, V. N.; Gogotsi, Y. Dispersions of Two-Dimensional Titanium Carbide MXene in Organic Solvents. *Chem Mater* **2017**, *29* (4), 1632-1640. DOI: 10.1021/acs.chemmater.6b04830.

(250) Li, K.; Wang, X. H.; Li, S.; Urbankowski, P.; Li, J. M.; Xu, Y. X.; Gogotsi, Y. An Ultrafast Conducting Polymer@MXene Positive Electrode with High Volumetric Capacitance for Advanced Asymmetric Supercapacitors. *Small* **2020**, *16* (4). DOI: ARTN 1906851

10.1002/smll.201906851.

(251) Bao, W. Z.; Liu, L.; Wang, C. Y.; Choi, S.; Wang, D.; Wang, G. X. Facile Synthesis of Crumpled Nitrogen-Doped MXene Nanosheets as a New Sulfur Host for Lithium-Sulfur Batteries. *Adv Energy Mater* **2018**, *8* (13). DOI: ARTN 1702485

10.1002/aenm.201702485. Mehdi, S. M. Z.; Ghulam Abbas, H.; Ali, M.; Rizvi, S. B. H.; Choi, S. R.; Goak, J. C.; Seo, Y.; Kumar, S.; Lee, N. Enhanced Electrochemical Performance and Theoretical Insights of Ni-Intercalated Ti3C2T x MX ene. *Energy & Environmental Materials*, e12876.

(252) Harris, J. K.; Ratcliff, E. L. Ion diffusion coefficients in poly(3-alkylthiophenes) for energy conversion and biosensing: role of side-chain length and microstructure. *J Mater Chem C* **2020**, *8* (38), 13319-13327. DOI: 10.1039/d0tc03690k.

(253) Chen, C.; Boota, M.; Xie, X. Q.; Zhao, M. Q.; Anasori, B.; Ren, C. E.; Miao, L.; Jiang, J. J.; Gogotsi, Y. Charge transfer induced polymerization of EDOT confined between 2D titanium carbide layers. *J Mater Chem A* **2017**, *5* (11), 5260-5265. DOI: 10.1039/c7ta00149e.

1 (254) Xue, H.; Huang, P.-H.; Göthelid, M.; Strömberg, A.; Niklaus, F.; Li, J. Ultrahigh-Rate On-
2 Paper PEDOT:PSS-Ti2C Microsupercapacitors with Large Areal Capacitance. *Adv Funct Mater*
3 **2024**, *34* (49), 2409210. DOI: https://doi.org/10.1002/adfm.202409210.
4 (255) Yao, Y.; Feng, W.; Chen, M.; Zhong, X.; Wu, X.; Zhang, H.; Yu, Y. Boosting the
5 Electrochemical Performance of Li–S Batteries with a Dual Polysulfides Confinement Strategy.
6 *Small* **2018**, *14* (42), 1802516. DOI: https://doi.org/10.1002/smll.201802516.
7 (256) Qin, L. Q.; Tao, Q. Z.; Liu, X. J.; Fahlman, M.; Halim, J.; Perssona, P. O. A.; Rosen, J.;
8 Zhang, F. L. Polymer-MXene composite films formed by MXene-facilitated electrochemical
9 polymerization for flexible solid-state microsupercapacitors. *Nano Energy* **2019**, *60*, 734-742.
10 DOI: 10.1016/j.nanoen.2019.04.002.
11 (257) Liu, S. M.; Chen, M. X.; Xie, Y.; Liu, D. H.; Zheng, J. F.; Xiong, X.; Jiang, H.; Wang, L.
12 C.; Luo, H.; Han, K. Nb2CTx MXene boosting PEO polymer electrolyte for all-solid-state Li-S
13 batteries: two birds with one stone strategy to enhance Li+ conductivity and polysulfide
14 adsorptivity. *Rare Metals* **2023**. DOI: 10.1007/s12598-022-02260-2. Zhang, Y. X.; Wu, F.; Huang,
15 Y. X.; Li, S. J.; Li, C.; Wang, Z. H.; Xie, M. A novel gel polymer electrolyte doped with MXene
16 enables dendrite-free cycling for high-performance sodium metal batteries. *J Mater Chem A* **2022**,
17 *10* (21), 11553-11561. DOI: 10.1039/d2ta00452f. Xu, H. S.; Zhang, H.; Wang, Y. F.; Tang, C.;
18 Xiao, T. Y.; Xu, Z.; Li, H.; Xu, F. G.; Mai, Y. Y. Two-dimensional sandwich-like MXene-
19 conductive polymer nanocomposite with in-plane cylindrical mesopores for long cycling lithium-
20 sulfur batteries. *2d Mater* **2023**, *10* (2). DOI: ARTN 024006
21 10.1088/2053-1583/acbec4. Pan, Q. W.; Zheng, Y. W.; Kota, S.; Huang, W. C.; Wang, S. J.; Qi,
22 H.; Kim, S.; Tu, Y. F.; Barsoum, M. W.; Li, C. Y. 2D MXene-containing polymer electrolytes for
23 all-solid-state lithium metal batteries. *Nanoscale Adv* **2019**, *1* (1), 395-402. DOI:
24 10.1039/c8na00206a.
25 (258) Liu, C. K.; Tian, Y.; An, Y. L.; Yang, Q. L.; Xiong, S. L.; Feng, J. K.; Qian, Y. T. Robust
26 and flexible polymer/MXene-derived two dimensional TiO2 hybrid gel electrolyte for dendrite-
27 free solid-state zinc-ion batteries. *Chem Eng J* **2022**, *430*. DOI: ARTN 132748

28 10.1016/j.cej.2021.132748.
29 (259) Li, X.; Lu, Y. L.; Shi, Z. H.; Liu, G.; Xu, G.; An, Z. J.; Xing, H.; Chen, Q. M.; Han, R. P.
30 S.; Liu, Q. J. Onion-inspired MXene/chitosan-quercetin multilayers: Enhanced response to H2O
31 molecules for wearable human physiological monitoring. *Sensor Actuat B-Chem* **2021**, *329*. DOI:
32 ARTN 129209

33 10.1016/j.snb.2020.129209.
34 (260) Zhou, J.; Shokouh, S. H. H.; Komsa, H. P.; Rieppo, L.; Cui, L. F.; Lv, Z. P.; Kordas, K.
35 MXene-Polymer Hybrid for High-Performance Gas Sensor Prepared by Microwave-Assisted In-
36 Situ Intercalation. *Adv Mater Technol-Us* **2022**, *7* (9). DOI: ARTN 2101565

37 10.1002/admt.202101565.
38 (261) Sharma, S.; Chhetry, A.; Sharifuzzaman, M.; Yoon, H.; Park, J. Y. Wearable capacitive
39 pressure sensor based on MXene composite nanofibrous scaffolds for reliable human physiological
40 signal acquisition. *ACS applied materials & interfaces* **2020**, *12* (19), 22212-22224.
41 (262) Wang, K.; Lou, Z.; Wang, L. L.; Zhao, L. J.; Zhao, S. F.; Wang, D. Y.; Han, W.; Jiang, K.;
42 Shen, G. Z. Bioinspired Interlocked Structure-Induced High Deformability for Two-Dimensional
43 Titanium Carbide (MXene)/Natural Microcapsule-Based Flexible Pressure Sensors. *Acs Nano*
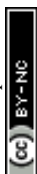44 **2019**, *13* (8), 9139-9147. DOI: 10.1021/acsnano.9b03454.

Journal of Materials Chemistry A Accepted Manuscript

(263) Qin, R. Z.; Hu, M. J.; Li, X.; Liang, T.; Tan, H. Y.; Liu, J. Z.; Shan, G. C. A new strategy for the fabrication of a flexible and highly sensitive capacitive pressure sensor. *Microsyst Nanoeng* **2021**, *7* (1). DOI: ARTN 100

10.1038/s41378-021-00327-1.

(264) Riazi, H.; Taghizadeh, G.; Soroush, M. MXene-Based Nanocomposite Sensors. *Acs Omega* **2021**, *6* (17), 11103-11112. DOI: 10.1021/acsomega.0c05828.

(265) Jin, L.; Wu, C. L.; Wei, K.; He, L. F.; Gao, H.; Zhang, H. X.; Zhang, K.; Asiri, A. M.; Alamry, K. A.; Yang, L.; et al. Polymeric Ti3C2Tx MXene Composites for Room Temperature Ammonia Sensing. *Acs Appl Nano Mater* **2020**, *3* (12), 12071-12079. DOI: 10.1021/acsanm.0c02577.

(266) Ge, G.; Zhang, Y. Z.; Zhang, W. L.; Yuan, W.; El-Demellawi, J. K.; Zhang, P.; Di Fabrizio, E.; Dong, X. C.; Alshareef, H. N. Ti3C2Tx MXene-Activated Fast Gelation of Stretchable and Self-Healing Hydrogels: A Molecular Approach. *Acs Nano* **2021**, *15* (2), 2698-2706. DOI: 10.1021/acsnano.0c07998.

(267) Li, X. B.; He, L. Z.; Li, Y. F.; Chao, M. Y.; Li, M. K.; Wan, P. B.; Zhang, L. Q. Healable, Degradable, and Conductive MXene Nanocomposite Hydrogel for Multifunctional Epidermal Sensors. *Acs Nano* **2021**, *15* (4), 7765-7773. DOI: 10.1021/acsnano.1c01751.

(268) Shao, Y. M.; Zhu, Y.; Zheng, R.; Wang, P.; Zhao, Z. Z.; An, J. Highly sensitive and selective surface molecularly imprinted polymer electrochemical sensor prepared by Au and MXene modified glassy carbon electrode for efficient detection of tetrabromobisphenol A in water. *Adv Compos Hybrid Ma* **2022**, *5* (4), 3104-3116. DOI: 10.1007/s42114-022-00562-8. Peng, Z. Q.; Zhang, X. D.; Zhao, C. M.; Gan, C. S.; Zhu, C. H. Hydrophobic and stable MXene/ reduced graphene oxide/polymer hybrid materials pressure sensors with an ultrahigh sensitive and rapid response speed pressure sensor for health monitoring. *Mater Chem Phys* **2021**, *271*. DOI: ARTN 124729

10.1016/j.matchemphys.2021.124729. Gong, L. G.; Qi, X. X.; Yu, K.; Gao, J. Q.; Zhou, B. B.; Yang, G. Y. Covalent conductive polymer chain and organic ligand ethylenediamine modified MXene-like-{AlW12O40} compounds for fully symmetric supercapacitors, electrochemical sensors and photocatalysis mechanisms. *J Mater Chem A* **2020**, *8* (11), 5709-5720. DOI: 10.1039/c9ta14103k.

(269) Tran, M. H.; Brilmayer, R.; Liu, L.; Zhuang, H.; Hess, C.; Andrieu-Brunsen, A.; Birkel, C. S. Synthesis of a smart hybrid MXene with switchable conductivity for temperature sensing. *ACS Applied Nano Materials* **2020**, *3* (5), 4069-4076.

(270) Zhang, Y.; Chen, K.; Li, Y.; Lan, J.; Yan, B.; Shi, L.; Ran, R. High-strength, self-healable, temperature-sensitive, MXene-containing composite hydrogel as a smart compression sensor. *ACS applied materials & interfaces* **2019**, *11* (50), 47350-47357.

(271) Echols, I. J.; An, H.; Zhao, X.; Prehn, E. M.; Tan, Z.; Radovic, M.; Green, M. J.; Lutkenhaus, J. L. pH-Response of polycation/Ti 3 C 2 T x MXene layer-by-layer assemblies for use as resistive sensors. *Molecular Systems Design & Engineering* **2020**, *5* (1), 366-375.

(272) Sharma, S.; Chhetry, A.; Zhang, S.; Yoon, H. Md. Sharifuzzaman, X. Hui, JY Park. *ACS Nano* **2021**, *15*, 4380.

(273) Li, L.; Fu, X.; Chen, S.; Uzun, S.; Levitt, A. S.; Shuck, C. E.; Han, W.; Gogotsi, Y. Hydrophobic and stable MXene–polymer pressure sensors for wearable electronics. *ACS applied materials & interfaces* **2020**, *12* (13), 15362-15369.

Journal of Materials Chemistry A Accepted Manuscript
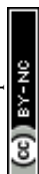
1   (274) Shi, X.; Wang, H.; Xie, X.; Xue, Q.; Zhang, J.; Kang, S.; Wang, C.; Liang, J.; Chen, Y.
2   Bioinspired ultrasensitive and stretchable MXene-based strain sensor via nacre-mimetic
3   microscale "brick-and-mortar" architecture. *ACS nano* **2018**, *13* (1), 649-659.
4   (275) Lu, Y.; Qu, X.; Zhao, W.; Ren, Y.; Si, W.; Wang, W.; Wang, Q.; Huang, W.; Dong, X.
5   Highly stretchable, elastic, and sensitive MXene-based hydrogel for flexible strain and pressure
6   sensors. *Research* **2020**.
7   (276) Li, X.; He, L.; Li, Y.; Chao, M.; Li, M.; Wan, P.; Zhang, L. Healable, degradable, and
8   conductive MXene nanocomposite hydrogel for multifunctional epidermal sensors. *ACS nano*
9   **2021**, *15* (4), 7765-7773.
10 (277) Wang, Q.; Pan, X.; Lin, C.; Gao, H.; Cao, S.; Ni, Y.; Ma, X. Modified Ti3C2TX (MXene)
11 nanosheet-catalyzed self-assembled, anti-aggregated, ultra-stretchable, conductive hydrogels for
12 wearable bioelectronics. *Chemical Engineering Journal* **2020**, *401*, 126129.
13 (278) Luo, J. Q.; Zhao, S.; Zhang, H. B.; Deng, Z. M.; Li, L. L.; Yu, Z. Z. Flexible, stretchable
14 and electrically conductive MXene/natural rubber nanocomposite films for efficient
15 electromagnetic interference shielding. *Compos Sci Technol* **2019**, *182*. DOI: ARTN 107754
16 10.1016/j.compscitech.2019.107754. Yang, H. T.; Li, J. L.; Xiao, X.; Wang, J. H.; Li, Y. F.; Li,
17 K. R.; Li, Z. P.; Yang, H. C.; Wang, Q.; Yang, J.; et al. Topographic design in wearable MXene
18 sensors with in-sensor machine learning for full-body avatar reconstruction. *Nat Commun* **2022**,
19 *13* (1). DOI: ARTN 5311
20 10.1038/s41467-022-33021-5. Sun, J. L.; Chang, Y.; Dong, L.; Zhang, K. K.; Hua, Q. L.; Zang, J.
21 H.; Chen, Q. S.; Shang, Y. Y.; Pan, C. F.; Shan, C. X. MXene enhanced self-powered alternating
22 current electroluminescence devices for patterned flexible displays. *Nano Energy* **2021**, *86*. DOI:
23 ARTN 106077
24 10.1016/j.nanoen.2021.106077.
25 (279) Wan, Y. J.; Li, X. M.; Zhu, P. L.; Sun, R.; Wong, C. P.; Liao, W. H. Lightweight, flexible
26 MXene/polymer film with simultaneously excellent mechanical property and high-performance
27 electromagnetic interference shielding. *Compos Part a-Appl S* **2020**, *130*. DOI: ARTN 105764
28 10.1016/j.compositesa.2020.105764.
29 (280) Han, R.; Zheng, L.; Li, G.; Chen, G.; Ma, S.; Cai, S.; Li, Y. Self-poled poly (vinylidene
30 fluoride)/MXene piezoelectric energy harvester with boosted power generation ability and the
31 roles of crystalline orientation and polarized interfaces. *ACS Applied Materials & Interfaces* **2021**,
32 *13* (39), 46738-46748.
33 (281) Zhao, Q.; Yang, L.; Ma, Y.; Huang, H.; He, H.; Ji, H.; Wang, Z.; Qiu, J. Highly sensitive,
34 reliable and flexible pressure sensor based on piezoelectric PVDF hybrid film using MXene
35 nanosheet reinforcement. *Journal of Alloys and Compounds* **2021**, *886*, 161069.
36 (282) Zhao, L. J.; Wang, L. L.; Zheng, Y. Q.; Zhao, S. F.; Wei, W.; Zhang, D. W.; Fu, X. Y.; Jiang,
37 K.; Shen, G. Z.; Han, W. Highly-stable polymer-crosslinked 2D MXene-based flexible
38 biocompatible electronic skins for in vivo biomonitoring. *Nano Energy* **2021**, *84*. DOI: ARTN
39 105921
40 10.1016/j.nanoen.2021.105921.
41 (283) Wu, X. M.; Huang, B.; Lv, R. Y.; Wang, Q. G.; Wang, Y. Highly flexible and low
42 capacitance loss supercapacitor electrode based on hybridizing decentralized conjugated polymer
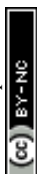43 chains with MXene. *Chem Eng J* **2019**, *378*. DOI: ARTN 122246

10.1016/j.cej.2019.122246. Raagulan, K.; Braveenth, R.; Kim, B. M.; Lim, K. J.; Lee, S. B.; Kim, M.; Chai, K. Y. An effective utilization of MXene and its effect on electromagnetic interference shielding: flexible, free-standing and thermally conductive composite from MXene-PAT-poly(p-aminophenol)-polyaniline co-polymer. *Rsc Adv* **2020**, *10* (3), 1613-1633. DOI: 10.1039/c9ra09522e. Kong, N.; Lv, K.; Chen, W. T.; Guan, J.; Zhao, P. F.; Tao, J. L.; Zhang, J. Z. Natural Polymer Template for Low-Cost Producing HighPerformance Ti3C2Tx MXene Electrodes for Flexible Supercapacitors. *Acs Appl Mater Inter* **2022**, *14* (51), 56877-56885. DOI: 10.1021/acsami.2c18559. Gund, G. S.; Park, J. H.; Harpalsinh, R.; Kota, M.; Shin, J. H.; Kim, T. I.; Gogotsi, Y.; Park, H. S. MXene/Polymer Hybrid Materials for Flexible AC-Filtering Electrochemical Capacitors. *Joule* **2019**, *3* (1), 164-176. DOI: 10.1016/j.joule.2018.10.017.

(284) Yun, J.; Park, J.; Ryoo, M.; Kitchamsetti, N.; Goh, T. S.; Kim, D. Piezo-triboelectric hybridized nanogenerator embedding MXene based bifunctional conductive filler in polymer matrix for boosting electrical power. *Nano Energy* **2023**, *105*, 108018.

(285) Wang, S.; Shao, H.-Q.; Liu, Y.; Tang, C.-Y.; Zhao, X.; Ke, K.; Bao, R.-Y.; Yang, M.-B.; Yang, W. Boosting piezoelectric response of PVDF-TrFE via MXene for self-powered linear pressure sensor. *Composites Science and Technology* **2021**, *202*, 108600.

(286) Guo, M.; Jiang, J.; Qian, J.; Liu, C.; Ma, J.; Nan, C. W.; Shen, Y. Flexible robust and high-density FeRAM from array of organic ferroelectric nano-lamellae by self-assembly. *Advanced Science* **2019**, *6* (6), 1801931.

(287) Martins, P.; Lopes, A.; Lanceros-Mendez, S. Electroactive phases of poly (vinylidene fluoride): Determination, processing and applications. *Progress in polymer science* **2014**, *39* (4), 683-706.

(288) Mokhtari, F.; Usman, K. A. S.; Zhang, J.; Komljenovic, R.; Simon, Z. a.; Dharmasiri, B.; Rezk, A.; Sherrell, P. C.; Henderson, L. C.; Varley, R. J. Enhanced Acoustoelectric Energy Harvesting with Ti3C2T x MXene in an All-Fiber Nanogenerator. *ACS Applied Materials & Interfaces* **2025**.

(289) Rana, S. S.; Rahman, M. T.; Salauddin, M.; Sharma, S.; Maharjan, P.; Bhatta, T.; Cho, H.; Park, C.; Park, J. Y. Electrospun PVDF-TrFE/MXene nanofiber mat-based triboelectric nanogenerator for smart home appliances. *ACS applied materials & interfaces* **2021**, *13* (4), 4955-4967.

(290) Kou, L.; Haque, R.; Sadri, R.; Auliya, R. Z.; Kaur, M.; Roberts, E. P.; Gan, W. C.; Mohammad Haniff, M. A. S.; Dee, C. F.; Ooi, P. C. Enhanced Piezoelectric Nanogenerator Based on Tridoped Graphene and Ti3CNT x MXene Quasi-3D Heterostructure. *Industrial & Engineering Chemistry Research* **2024**, *63* (36), 15853-15868.

(291) Kim, Y.; Wu, X.; Lee, C.; Oh, J. H. Characterization of PI/PVDF-TrFE composite nanofiber-based triboelectric nanogenerators depending on the type of the electrospinning system. *ACS Applied Materials & Interfaces* **2021**, *13* (31), 36967-36975.

(292) Min, G.; Pullanchiyodan, A.; Dahiya, A. S.; Hosseini, E. S.; Xu, Y.; Mulvihill, D. M.; Dahiya, R. Ferroelectric-assisted high-performance triboelectric nanogenerators based on electrospun P (VDF-TrFE) composite nanofibers with barium titanate nanofillers. *Nano Energy* **2021**, *90*, 106600.

(293) Wang, D.; Zhang, D.; Li, P.; Yang, Z.; Mi, Q.; Yu, L. Electrospinning of flexible poly (vinyl alcohol)/MXene nanofiber-based humidity sensor self-powered by monolayer molybdenum diselenide piezoelectric nanogenerator. *Nano-micro letters* **2021**, *13*, 1-13.

1 (294) Zheng, W.; Li, T.; Jin, F.; Qian, L.; Ma, J.; Wei, Z.; Ma, X.; Wang, F.; Sun, J.; Yuan, T.
2 Interfacial Polarization Locked Flexible β-Phase Glycine/Nb2CTx Piezoelectric Nanofibers. *Small*
3 **2024**, 2308715.
4 (295) Kim, J.; Jang, M.; Jeong, G.; Yu, S.; Park, J.; Lee, Y.; Cho, S.; Yeom, J.; Lee, Y.; Choe, A.
5 MXene-enhanced β-phase crystallization in ferroelectric porous composites for highly-sensitive
6 dynamic force sensors. *Nano Energy* **2021**, *89*, 106409.
7 (296) Auliya, R. Z.; Ooi, P. C.; Sadri, R.; Talik, N. A.; Yau, Z. Y.; Mohammad Haniff, M. A. S.;
8 Goh, B. T.; Dee, C. F.; Aslfattahi, N.; Al-Bati, S. Exploration of 2D Ti3C2 MXene for all solution
9 processed piezoelectric nanogenerator applications. *Scientific Reports* **2021**, *11* (1), 17432.
10 (297) Bhatta, T.; Maharjan, P.; Cho, H.; Park, C.; Yoon, S. H.; Sharma, S.; Salauddin, M.; Rahman,
11 M. T.; Rana, S. S.; Park, J. Y. High-performance triboelectric nanogenerator based on MXene
12 functionalized polyvinylidene fluoride composite nanofibers. *Nano Energy* **2021**, *81*, 105670.
13 (298) Li, X.; Wang, W.; Cai, W.; Liu, H.; Liu, H.; Han, N.; Zhang, X. Mxene/multiwalled carbon
14 nanotube/polymer hybrids for tribopiezoelectric nanogenerators. *ACS Applied Nano Materials*
15 **2022**, *5* (9), 12836-12847.
16 (299) Shepelin, N. A.; Sherrell, P. C.; Skountzos, E. N.; Goudeli, E.; Zhang, J.; Lussini, V. C.;
17 Imtiaz, B.; Usman, K. A. S.; Dicinoski, G. W.; Shapter, J. G. Interfacial piezoelectric polarization
18 locking in printable Ti3C2T x MXene-fluoropolymer composites. *Nature communications* **2021**,
19 *12* (1), 3171.
20 (300) Wu, W.; Zhao, W.; Sun, Q.; Yu, B.; Yin, X.; Cao, X.; Feng, Y.; Li, R. K.; Qu, J. Surface
21 treatment of two dimensional MXene for poly (vinylidene fluoride) nanocomposites with tunable
22 dielectric permittivity. *Composites Communications* **2021**, *23*, 100562.
23 (301) Tu, S.; Qiu, L.; Liu, C.; Zeng, F.; Yuan, Y.-Y.; Hedhili, M. N.; Musteata, V.; Ma, Y.; Liang,
24 K.; Jiang, N. Suppressing Dielectric Loss in MXene/Polymer Nanocomposites through Interfacial
25 Interactions. *ACS nano* **2024**, *18* (14), 10196-10205.
26 (302) Li, Y.; Bai, X.; Liu, J.; Yang, B. Stretchable MXene/PVDF Piezoelectric Sensor for Finger
27 Motion Detection and Tactile Recognition. In *2024 IEEE 37th International Conference on Micro*
28 *Electro Mechanical Systems (MEMS)*, 2024; IEEE: pp 113-116.
29 (303) Ji, X.; Ge, L.; Liu, C.; Tang, Z.; Xiao, Y.; Chen, W.; Lei, Z.; Gao, W.; Blake, S.; De, D.
30 Capturing functional two-dimensional nanosheets from sandwich-structure vermiculite for cancer
31 theranostics. *Nature communications* **2021**, *12* (1), 1124.
32 (304) Feng, W.; Wang, R.; Zhou, Y.; Ding, L.; Gao, X.; Zhou, B.; Hu, P.; Chen, Y. Ultrathin
33 molybdenum carbide MXene with fast biodegradability for highly efficient theory-oriented
34 photonic tumor hyperthermia. *Advanced Functional Materials* **2019**, *29* (22), 1901942.
35 (305) Fu, Y.; Li, C.; Cheng, Y.; He, Y.; Zhang, W.; Wei, Q.; Li, D. Biomass aerogel composite
36 containing BaTiO3 nanoparticles and MXene for highly sensitive self-powered sensor and
37 photothermal antibacterial applications. *Composites Part A: Applied Science and Manufacturing*
38 **2023**, *173*, 107663.
39 (306) McLellan, K.; Li, T. R.; Sun, Y. C.; Jakubinek, M. B.; Naguib, H. E. 4D Printing of MXene
40 Composites for Deployable Actuating Structures. *Acs Appl Polym Mater* **2022**. DOI:
41 10.1021/acsapm.2c01192XXX-XXX.
42 (307) McLellan, K.; Li, T. R.; Sun, Y. C.; Jakubinek, M. B.; Naguib, H. E. 4D Printing of MXene
43 Composites for Deployable Actuating Structures. *Acs Appl Polym Mater* **2022**, *4* (12), 8774-8785.
44 DOI: 10.1021/acsapm.2c01192.
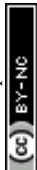
Journal of Materials Chemistry A Accepted Manuscript

1 (308) Cao, W. T.; Ma, C.; Mao, D. S.; Zhang, J.; Ma, M. G.; Chen, F. MXene-Reinforced Cellulose
2 Nanofibril Inks for 3D-Printed Smart Fibres and Textiles. *Adv Funct Mater* **2019**, *29* (51). DOI:
3 ARTN 1905898

4 10.1002/adfm.201905898.
5 (309) Li, K.; Zhao, J.; Zhussupbekova, A.; Shuck, C. E.; Hughes, L.; Dong, Y. Y.; Barwich, S.;
6 Vaesen, S.; Shvets, I. V.; Mobius, M.; et al. 4D printing of MXene hydrogels for high-efficiency
7 pseudocapacitive energy storage. *Nat Commun* **2022**, *13* (1). DOI: ARTN 6884

8 10.1038/s41467-022-34583-0.
9 (310) Li, Y. W.; Peng, S. Q.; Kankala, R. K.; Wu, L. X.; Chen, A. Z.; Wang, S. B. 3D printing of
10 mechanically robust MXene-encapsulated polyurethane elastomer. *Compos Part a-Appl S* **2022**,
11 *163*. DOI: ARTN 107182

12 10.1016/j.compositesa.2022.107182.
13 (311) Liu, H. B.; Huang, Z. Y.; Chen, T.; Su, X. Q.; Liu, Y. N.; Fu, R. L. Construction of 3D
14 MXene/Silver nanowires aerogels reinforced polymer composites for extraordinary
15 electromagnetic interference shielding and thermal conductivity. *Chem Eng J* **2022**, *427*. DOI:
16 ARTN 131540

17 10.1016/j.cej.2021.131540. Chu, X.; Wang, Y. H.; Cai, L. C.; Huang, H. C.; Xu, Z.; Xie, Y. T.;
18 Yan, C.; Wang, Q.; Zhang, H. T.; Li, H.; et al. Boosting the energy density of aqueous MXene-
19 based supercapacitor by integrating 3D conducting polymer hydrogel cathode. *Susmat* **2022**, *2* (3),
20 379-390. DOI: 10.1002/sus2.61.
21 (312) Bora, P. J.; Anil, A. G.; Ramamurthy, P. C.; Tan, D. Q. MXene interlayered crosslinked
22 conducting polymer film for highly specific absorption and electromagnetic interference shielding.
23 *Materials Advances* **2020**, *1* (2). DOI: 10.1039/d0ma00005a. Sun, R. H.; Zhang, H. B.; Liu, J.;
24 Xie, X.; Yang, R.; Li, Y.; Hong, S.; Yu, Z. Z. Highly Conductive Transition Metal
25 Carbide/Carbonitride(MXene)@polystyrene Nanocomposites Fabricated by Electrostatic
26 Assembly for Highly Efficient Electromagnetic Interference Shielding. *Adv Funct Mater* **2017**, *27*
27 (45). DOI: ARTN 1702807
28 10.1002/adfm.201702807.
29 (313) Li, R. S.; Ding, L.; Gao, Q.; Zhang, H. M.; Zeng, D.; Zhao, B. A.; Fan, B. B.; Zhang, R.
30 Tuning of anisotropic electrical conductivity and enhancement of EMI shielding of polymer
31 composite foam via CO2-assisted delamination and orientation of MXene. *Chem Eng J* **2021**, *415*.
32 DOI: ARTN 128930

33 10.1016/j.cej.2021.128930.
34 (314) Liu, J.; Zhang, H. B.; Sun, R. H.; Liu, Y. F.; Liu, Z. S.; Zhou, A. G.; Yu, Z. Z. Hydrophobic,
35 Flexible, and Lightweight MXene Foams for High-Performance Electromagnetic-Interference
36 Shielding. *Adv Mater* **2017**, *29* (38). DOI: ARTN 1702367

37 10.1002/adma.201702367. Sun, Y.; Ding, R.; Hong, S. Y.; Lee, J.; Seo, Y. K.; Nam, J. D.; Suhr,
38 J. MXene-xanthan nanocomposite films with layered microstructure for electromagnetic
39 interference shielding and Joule heating. *Chem Eng J* **2021**, *410*. DOI: ARTN 128348
40 10.1016/j.cej.2020.128348.
41 (315) Zhang, Q. M.; Wang, Q.; Cui, J.; Zhao, S.; Zhang, G. F.; Gao, A. L.; Yan, Y. H. Structural
42 design and preparation of Ti3C2Tx MXene/polymer composites for absorption-dominated

electromagnetic interference shielding. *Nanoscale Adv* **2023**, *5* (14), 3549-3574. DOI: 10.1039/d3na00130j.

(316) Chang, G.; Zeng, L.; Xie, L.; Xue, B.; Zheng, Q. Ultrathin multifunctional electromagnetic interference shielding MXene/AgNWs/PEDOT:PSS coatings with superior electro/photo-thermal transition ability and water repellency. *Chem Eng J* **2023**, *470*, 144033. DOI: https://doi.org/10.1016/j.cej.2023.144033.

(317) Zeng, Z. H.; Wu, N.; Wei, J. J.; Yang, Y. F.; Wu, T. T.; Li, B.; Hauser, S. B.; Yang, W. D.; Liu, J. R.; Zhao, S. Y. Porous and Ultra-Flexible Crosslinked MXene/Polyimide Composites for Multifunctional Electromagnetic Interference Shielding. *Nano-Micro Lett* **2022**, *14* (1). DOI: ARTN 59

10.1007/s40820-022-00800-0.

(318) Hussain, K.; Mehboob, S.; Ahmad, I.; Mumtaz, M.; Khan, A. R.; Mujtaba-ul-Hassan, S.; Mehran, M. T.; Iqbal, Z.; Ahmad, J.; Mehmood, M.; et al. Terahertz time-domain spectroscopy of thin and flexible CNT-modified MXene/polymer composites. *Appl Phys a-Mater* **2021**, *127* (5). DOI: ARTN 382

10.1007/s00339-021-04525-6.

(319) Monastyreckis, G.; Mishnaevsky, L.; Hatter, C. B.; Aniskevich, A.; Gogotsi, Y.; Zeleniakiene, D. Micromechanical modeling of MXene-polymer composites. *Carbon* **2020**, *162*, 402-409. DOI: 10.1016/j.carbon.2020.02.070.

(320) Liu, R. T.; Miao, M.; Li, Y. H.; Zhang, J. F.; Cao, S. M.; Feng, X. Ultrathin Biomimetic Polymeric Ti3C2Tx MXene Composite Films for Electromagnetic Interference Shielding. *Acs Appl Mater Inter* **2018**, *10* (51), 44787-44795. DOI: 10.1021/acsami.8b18347.

(321) Nie, Y.; Huang, J. K.; Ma, S. Y.; Li, Z. C.; Shi, Y. K.; Yang, X. F.; Fang, X.; Zeng, J. B.; Bi, P. Y.; Qi, J. T.; et al. MXene-hybridized silane films for metal anticorrosion and antibacterial applications. *Appl Surf Sci* **2020**, *527*. DOI: ARTN 146915

10.1016/j.apsusc.2020.146915.

(322) Zhang, F. Y.; Liu, W. Q.; Wang, S.; Liu, C. H.; Shi, H. Y.; Liang, L. Y.; Pi, K. Surface functionalization of Ti3C2Tx and its application in aqueous polymer nanocomposites for reinforcing corrosion protection. *Compos Part B-Eng* **2021**, *217*. DOI: ARTN 108900

10.1016/j.compositesb.2021.108900.

(323) He, D. M.; Cai, M.; Yan, H.; Lin, Q. L.; Fan, X. Q.; Zhang, L.; Zhu, M. H. Tribological properties of Ti3C2Tx MXene reinforced interpenetrating polymers network coating. *Tribol Int* **2021**, *163*. DOI: ARTN 107196

10.1016/j.triboint.2021.107196.

(324) Zou, Y.; Jin, X.; Zhang, X. P.; Kong, X. L.; Zhang, Q.; Xie, X. H.; Liu, C. J.; Ke, L. N.; Liu, W. G.; Wang, W. A multifunctional biomedical patch based on hyperbranched epoxy polymer and MXene. *Sci China Technol Sc* **2021**, *64* (12), 2744-2754. DOI: 10.1007/s11431-021-1843-3.

(325) Chen, K.; Chen, Y. H.; Deng, Q. H.; Jeong, S. H.; Jang, T. S.; Du, S. Y.; Kim, H. E.; Huang, Q.; Han, C. M. Strong and biocompatible poly(lactic acid) membrane enhanced by Ti3C2Tz (MXene) nanosheets for Guided bone regeneration. *Mater Lett* **2018**, *229*, 114-117. DOI: 10.1016/j.matlet.2018.06.063.

(326) Li, Z. L.; Zhang, H.; Han, J.; Chen, Y.; Lin, H.; Yang, T. Surface Nanopore Engineering of 2D MXenes for Targeted and Synergistic Multitherapies of Hepatocellular Carcinoma (vol 30, 1706981, 2018). *Adv Mater* **2019**, *31* (27). DOI: ARTN 1902282

1   10.1002/adma.201902282. Murugan, C.; Sharma, V.; Murugan, R. K.; Malaimegu, G.;
2   Sundaramurthy, A. Two-dimensional cancer theranostic nanomaterials: Synthesis, surface
3   functionalization and applications in photothermal therapy. *J Control Release* **2019**, *299*, 1-20.
4   DOI: 10.1016/j.jconrel.2019.02.015. Lin, H.; Gao, S. S.; Dai, C.; Chen, Y.; Shi, J. L. A Two-
5   Dimensional Biodegradable Niobium Carbide (MXene) for Photothermal Tumor Eradication in
6   NIR-I and NIR-II Biowindows (vol 139, pg 16235, 2017). *J Am Chem Soc* **2020**, *142* (23), 10567-
7   10567. DOI: 10.1021/jacs.0c04999.
8   (327) Xing, C. Y.; Chen, S. Y.; Liang, X.; Liu, Q.; Qu, M. M.; Zou, Q. S.; Li, J. H.; Tan, H.; Liu,
9   L. P.; Fan, D. Y.; et al. Two-Dimensional MXene (Ti3C2)-Integrated Cellulose Hydrogels:
10   Toward Smart Three-Dimensional Network Nanoplatforms Exhibiting Light-Induced Swelling
11   and Bimodal Photothermal/Chemotherapy Anticancer Activity. *Acs Appl Mater Inter* **2018**, *10*
12   (33), 27631-27643. DOI: 10.1021/acsami.8b08314.
13   (328) Dai, C.; Chen, Y.; Jing, X. X.; Xiang, L. H.; Yang, D. Y.; Lin, H.; Liu, Z.; Han, X. X.; Wu,
14   R. Two-Dimensional Tantalum Carbide (MXenes) Composite Nanosheets for Multiple Imaging-
15   Guided Photothermal Tumor Ablation. *Acs Nano* **2017**, *11* (12), 12696-12712. DOI:
16   10.1021/acsnano.7b07241.
17   (329) Liu, A. P.; Liu, Y.; Liu, G. J.; Zhang, A. T.; Cheng, Y. J.; Li, Y.; Zhang, L.; Wang, L. S.;
18   Zhou, H.; Liu, J. Q.; et al. Engineering of surface modified Ti3C2Tx MXene based dually
19   controlled drug release system for synergistic multitherapies of cancer. *Chem Eng J* **2022**, *448*.
20   DOI: ARTN 137691

21   10.1016/j.cej.2022.137691.
22   (330) Yao, B.; Zhang, J.; Fan, Z. Q.; Ding, Y. D.; Zhou, B.; Yang, R. L.; Zhao, J. F.; Zhang, K.
23   Rational Engineering of the DNA Walker Amplification Strategy by Using a Au@Ti3C2@PEI-
24   Ru(dcbpy)(3)(2+) Nanocomposite Biosensor for Detection of the SARS-CoV-2 RdRp Gene. *Acs*
25   *Appl Mater Inter* **2021**, *13* (17), 19816-19824. DOI: 10.1021/acsami.1c04453. Lei, Y. J.; Zhao, E.
26   N.; Zhang, Y. Z.; Jiang, Q.; He, J. H.; Baeumner, A.; Wolfbeis, O. S.; Wang, Z. L.; Salama, K. N.;
27   Aishareef, H. N. A MXene-Based Wearable Biosensor System for High-Performance In Vitro
28   Perspiration Analysis. *Small* **2019**, *15* (19). DOI: ARTN 1901190
29   10.1002/smll.201901190.
30   (331) Lin, B.; Yuen, A. C. Y.; Oliver, S.; Liu, J. J.; Yu, B.; Yang, W.; Wu, S. Y.; Yeoh, G. H.;
31   Wang, C. H. Dual functionalisation of polyurethane foam for unprecedented flame retardancy and
32   antibacterial properties using layer-by-layer assembly of MXene chitosan with antibacterial metal
33   particles. *Compos Part B-Eng* **2022**, *244*. DOI: ARTN 110147

34   10.1016/j.compositesb.2022.110147.
35   (332) Liu, L.; Zhu, M. H.; Ma, Z. W.; Xu, X. D.; Seraji, S. M.; Yu, B.; Sun, Z. Q.; Wang, H.;
36   Song, P. G. A reactive copper-organophosphate-MXene heterostructure enabled antibacterial, self-
37   extinguishing and mechanically robust polymer nanocomposites. *Chem Eng J* **2022**, *430*. DOI:
38   ARTN 132712

39   10.1016/j.cej.2021.132712.
40   (333) Rasool, K.; Mahmoud, K. A.; Johnson, D. J.; Helal, M.; Berdiyorov, G. R.; Gogotsi, Y.
41   Efficient Antibacterial Membrane based on Two-Dimensional Ti3C2Tx (MXene) Nanosheets. *Sci*
42   *Rep-Uk* **2017**, *7*. DOI: ARTN 1598

43   10.1038/s41598-017-01714-3.

Journal of Materials Chemistry A Accepted Manuscript

1   (334) Yang, H. G.; Zheng, Q.; Zhang, P.; Nie, G. C.; Ali, T.; Raza, S. Fabrication of MXene
2   (Ti2C3Tx) based conducting polymer materials and their applications as anticancer and metal ions
3   removal from wastewater. *Surf Interfaces* **2023**, *36*. DOI: ARTN 102493

4   10.1016/j.surfin.2022.102493.
5   (335) Rabiee, N.; Bagherzadeh, M.; Jouyandeh, M.; Zarrintaj, P.; Saeb, M. R.; Mozafari, M.;
6   Shokouhimehr, M.; Varma, R. S. Natural Polymers Decorated MOF-MXene Nanocarriers for Co-
7   delivery of Doxorubicin/pCRISPR. *Acs Appl Bio Mater* **2021**, *4* (6), 5106-5121. DOI:
8   10.1021/acsabm.1c00332.
9   (336) Yang, C.; Luo, Y.; Lin, H.; Ge, M.; Shi, J. L.; Zhang, X. L. Niobium Carbide MXene
10   Augmented Medical Implant Elicits Bacterial Infection Elimination and Tissue Regeneration. *Acs*
11   *Nano* **2021**, *15* (1), 1086-1099. DOI: 10.1021/acsnano.0c08045.
12   (337) Tao, N.; Liu, Y. D.; Wu, Y. J.; Li, X. L.; Li, J.; Sun, X. Y.; Chen, S.; Liu, Y. N. Minimally
13   Invasive Antitumor Therapy Using Biodegradable Nanocomposite Micellar Hydrogel with
14   Functionalities of NIR-II Photothermal Ablation and Vascular Disruption. *Acs Appl Bio Mater*
15   **2020**, *3* (7), 4531-4542. DOI: 10.1021/acsabm.0c00465.
16   (338) Wu, X.; Ding, M. M.; Xu, H.; Yang, W.; Zhang, K. S.; Tian, H. L.; Wang, H. T.; Xie, Z. L.
17   Scalable Ti3C2Tx MXene Interlayered Forward Osmosis Membranes for Enhanced Water
18   Purification and Organic Solvent Recovery. *Acs Nano* **2020**, *14* (7), 9125-9135. DOI:
19   10.1021/acsnano.0c04471.
20   (339) Ihsanullah, I. MXenes (two-dimensional metal carbides) as emerging nanomaterials for
21   water puri fication: Progress, challenges and prospects. *Chem Eng J* **2020**, *388*. DOI: ARTN
22   124340

23   10.1016/j.cej.2020.124340.
24   (340) Abraham, J.; Vasu, K. S.; Williams, C. D.; Gopinadhan, K.; Su, Y.; Cherian, C. T.; Dix, J.;
25   Prestat, E.; Haigh, S. J.; Grigorieva, I. V.; et al. Tunable sieving of ions using graphene oxide
26   membranes. *Nat Nanotechnol* **2017**, *12* (6), 546-+. DOI: 10.1038/Nnano.2017.21. Thomas, M.;
27   Corry, B.; Hilder, T. A. What Have We Learnt About the Mechanisms of Rapid Water Transport,
28   Ion Rejection and Selectivity in Nanopores from Molecular Simulation? *Small* **2014**, *10* (8), 1453-
29   1465. DOI: 10.1002/smll.201302968. Richards, L. A.; Schafer, A. I.; Richards, B. S.; Corry, B.
30   The Importance of Dehydration in Determining Ion Transport in Narrow Pores. *Small* **2012**, *8* (11),
31   1701-1709. DOI: 10.1002/smll.201102056.
32   (341) Wang, J.; Zhang, Z. J.; Zhu, J. N.; Tian, M. T.; Zheng, S. C.; Wang, F. D.; Wang, X. D.;
33   Wang, L. Ion sieving by a two-dimensional Ti3C2Tx alginate lamellar membrane with stable
34   interlayer spacing. *Nat Commun* **2020**, *11* (1). DOI: ARTN 3540

35   10.1038/s41467-020-17373-4.
36   (342) Zeng, Y. X.; Wang, P.; He, B. L.; Liu, S. J.; Ye, Q.; Zhou, F. Fabrication of zwitterionic
37   polymer-functionalized MXene nanosheets for anti-bacterial and anti-biofouling applications.
38   *Prog Org Coat* **2023**, *183*. DOI: ARTN 107727

39   10.1016/j.porgcoat.2023.107727.
40   (343) Khosla, A.; Sonu; Awan, H. T. A.; Singh, K.; Gaurav; Walvekar, R.; Zhao, Z. H.; Kaushik,
41   A.; Khalid, M.; Chaudhary, V. Emergence of MXene and MXene-Polymer Hybrid Membranes as
42   Future- Environmental Remediation Strategies. *Adv Sci* **2022**, *9* (36). DOI:
43   10.1002/advs.202203527.

1 (344) Hou, C.; Huang, C.; Yu, H.; Shi, S. Surface-Engineered Ti3C2T with Tunable Work
2 Functions for Highly Efficient Polymer Solar Cells. *Small* **2022**, *18* (21), 2201046. DOI:
3 https://doi.org/10.1002/smll.202201046. Wen, J.; Sun, Z.; Qiao, Y.; Zhou, Y.; Liu, Y.; Zhang, Q.;
4 Liu, Y.; Jiao, S. Ti3C2 MXene-Reduced Graphene Oxide Composite Polymer-Based Printable
5 Electrolyte for Quasi-Solid-State Dye-Sensitized Solar Cells. *ACS Applied Energy Materials* **2022**,
6 *5* (3), 3329-3338. DOI: 10.1021/acsaem.1c03928.
7 (345) Liu, Y.; Xiao, H.; Goddard III, W. A. Schottky-barrier-free contacts with two-dimensional
8 semiconductors by surface-engineered MXenes. *Journal of the American Chemical Society* **2016**,
9 *138* (49), 15853-15856. Li, G.; Li, N.; Peng, S.; He, B.; Wang, J.; Du, Y.; Zhang, W.; Han, K.;
10 Dang, F. Highly efficient Nb2C MXene cathode catalyst with uniform O-terminated surface for
11 lithium–oxygen batteries. *Advanced Energy Materials* **2021**, *11* (1), 2002721.
12 (346) Deng, B.; Lian, H.; Xue, B.; Song, R.; Chen, S.; Wang, Z.; Xu, T.; Dong, H.; Wang, S.
13 Niobium-Carbide MXene Modified Hybrid Hole Transport Layer Enabling High-Performance
14 Organic Solar Cells Over 19%. *Small* **2023**, *19* (23), 2207505.
15 (347) Yang, T.; Wang, M.; Duan, C.; Hu, X.; Huang, L.; Peng, J.; Huang, F.; Gong, X. Inverted
16 polymer solar cells with 8.4% efficiency by conjugated polyelectrolyte. *Energy & Environmental*
17 *Science* **2012**, *5* (8), 8208-8214.
18 (348) Huang, C.; Shi, S.; Yu, H. Work function adjustment of Nb2CT x nanoflakes as hole and
19 electron transport layers in organic solar cells by controlling surface functional groups. *ACS*
20 *Energy Letters* **2021**, *6* (10), 3464-3472.

21

Data Availability Statement:

No new data was created in this review. All data referenced are from previously published sources and are available in the respective cited articles.